Durham E-Theses

Magnetic properties of metallic fine particle systems

Lambrick, David Brynne

How to cite:

Lambrick, David Brynne (1986) *Magnetic properties of metallic fine particle systems*, Durham theses, Durham University. Available at Durham E-Theses Online: http://etheses.dur.ac.uk/7087/

Use policy

The full-text may be used and/or reproduced, and given to third parties in any format or medium, without prior permission or charge, for personal research or study, educational, or not-for-profit purposes provided that:

- a full bibliographic reference is made to the original source
- a link is made to the metadata record in Durham E-Theses
- the full-text is not changed in any way

The full-text must not be sold in any format or medium without the formal permission of the copyright holders.

Please consult the full Durham E-Theses policy for further details.

MAGNETIC PROPERTIES OF METALLIC FINE

PARTICLE SYSTEMS

David Brynne Lambrick, B.Sc., G.I.M.A.

Thesis submitted to the University of Durham
in candidature for the Degree of
Doctor of Philosophy

September 1986

13. FEB 1987

Thesis
1986/LAM

ABSTRACT

A study of the magnetic properties of metallic fine particle systems in the form of magnetic fluids has been made. The fluids were prepared utilising the organometallic decomposition route (detailed separately by N. Mason, Ph.D. thesis, Durham University 1986) and single metal systems containing Fe, Co and Ni were prepared from new precursors. The properties of the first hydrocarbon based mixed metal particle systems are also reported. For systems prepared with Fe precursors it is thought that the fine particles are not in the α-Fe phase but may be amorphous and/or consist of iron carbides. Co and Ni systems result in particles with bulk-metal like structures although Co usually forms in the f.c.c. phase. The h.c.p. is also observed. The mixed metal systems were of FeCo and Ni_3Fe and a tendency to form the superlattice or ordered structures was observed. In both cases Fe has been lost to the particles and this is thought to be due to the formation of volatile iron compounds during preparation and/or surfactant complexes. Narrow size distributions have been obtained in all cases with mean particle diameters in the range 4-10 nm and standard deviations of between 0.8 and 1.9. The form of the size distribution has been found to be Gaussian. A study of the anisotropy of the particles using torque and magnetisation measurements has found uniaxial anisotropy with the first anisotropy constant of the order $10^5 Jm^{-3}$.

The values observed are too large to be ascribed solely to shape anisotropy. Low temperature magnetisation measurements have revealed the existence of a paramagnetic component in the fluids. Loss of magnetisation has occurred in all systems and is thought to be due to oxidation of the metal.

STATEMENT ON JOINT WORK

The magnetic fluids project at Durham is a co-operative study between the Departments of Physics and Chemistry. All the fluids examined in this study were prepared by members of the Chemistry Department. The author is responsible for all the magnetic measurements (except when indicated otherwise) made upon the fluids. A large proportion of the particle size distributions in Chapter 4 were collected on the image size analyser by Mr. N. Mason of the Chemistry Department. The analysis and interpretation of this and all other data is due to the author.

D.B. Lambrick

September 1986.

ACKNOWLEDGEMENTS

PUBLICATIONS

Some of the material in this thesis has already been

published in the following:-

(1)   Preparation and Properties of Metallic Iron Ferrofluids
       M. Kilner, S.R. Hoon, D.B. Lambrick, J.A. Potton,
       B.K. Tanner
       IEEE Trans. Magn. MAG20 1735 (1984).

(2)   Magnetic Properties of Textured Magnetic Fluids
       J. Szpunar, D.B. Lambrick, S.R. Hoon, D.M. Paige,
       B. Szpunar.
       Proc. 7th ICOTOM 701 (1984).
       Netherlands Society for Materials Science, Zwijndrecht.

(3)   An automated micrograph image size analyser
       S.R. Hoon, D.B. Lambrick, D.M. Paige
       J. Phys. E : Sci. Inst. 18 389 (1985).

(4)   Mixed Metal Ferrofluids
       S.R. Hoon, D.B. Lambrick, N. Mason
       I.E.E. Colloq. Elec. Active Fl. (Digest 14) p9/14
       (1985).

(5)   An Iron-Cobalt 'Alloy' Magnetic Fluid
       D.B. Lambrick, N. Mason, N.J. Harris, G.J. Russell,
       S.R. Hoon, M. Kilner
       IEEE Trans. Magn. MAG21 1891 (1985).

(6)   Preparation and Properties of Ni-Fe Magnetic Fluids
       D.B. Lambrick, N. Mason, S.R. Hoon, M. Kilner
       J. Magn. Mag. Mat. (in press) (1986).

CONTENTS   Page

CHAPTER FIVE : TEXTURE STUDIES

CHAPTER SIX : NEW MAGNETIC FLUIDS

CHAPTER SEVEN : CONCLUSIONS AND FUTURE WORK

CHAPTER ONE

FINE PARTICLES AND MAGNETISM

1.1 Introduction

Systems of fine magnetic particles, where fine is permitted to range from 1 nm to $\sim$1 μm, appear in many different areas of science. Principal amongst these is undoubtedly magnetic information technology (MINT) where the particles have sizes of the order of a micron and are composed of materials such as γ-Fe_2O_3 or CrO_2. Appearances are also made, however, in the fields of geophysics (rock magnetism), electrical engineering (permanent magnets), chemistry (catalysis), the life sciences (magneto tatic bacteria) and medicine (cancer research). The fine particle systems described in this study are magnetic fluids ("ferrofluids") which have particle sizes of the order of a nanometer and whose particle material was usually metallic. These fine particles are thus at the smallest end of the 'fine' scale and probably bear closest resemblance to the catalytic particles which are also often composed of transition metals in the zero valence state. Magnetic fluids have striking properties unique to themselves.

1.2 Magnetic Fluids

1.2.1 Description

Although it may be theoretically possible (Handrich and Kobe 1970), the spontaneous ordering of magnetic moments in a single phase fluid has not yet been observed. The terms "magnetic fluid" or "ferrofluid" are used to describe colloidal suspensions of fine particles of magnetic material dispersed in a liquid (at room temperature) carrier.

By virtue of their stability against settling out in the gravitational field and in magnetic field gradients, magnetic fluids are distinct from the suspensions prepared by Bitter (1932) or Elmore (1938) for domain observations, those used for magnetic clutches (Rabinow 1949) or those used for crack detection in steels (Tanner et al. 1986).

A colloidal suspension is, by definition, a suspension in which the particles remain suspended in the presence of the gravitational field. For this to be possible, the Brownian motion of the particles must overcome their settling velocity (Shliomis 1974). This requires particles no larger than ~ 1 μm. The magnetostatic interaction between the particles causes them to form aggregates which exceed this size and hence settle out. In order for thermal activation of the solid particles to overcome the magnetostatic interaction, the moments and hence the particle volumes (assuming particle moment $m_p = v_p M_b^\infty$ where v_p is the particle volume and M_b^∞ is the saturation

magnetization of the bulk material) must be even smaller, typically of the order 10nm. This is easily small enough for each particle to be a single magnetic domain. Particles of this size, brought together, may still aggregate due to the short range, attractive, van der Waals/London forces. To prevent this the particles must be coated with dispersant molecules, usually surface active agents (surfactants or SAA). These are carrier soluble long chain hydrocarbon molecules with active sites (e.g. cationic groups such as NH_2^+) which adhere to the particle surface and hence prevent the particles from approaching too closely.

Magnetic fluids should also retain their magnetic properties with time. Oxidation of metallic particles or a slow chemical reaction between particle and surfactant molecule can reduce the magnetic moments of the particles. In commercial systems this stability is achieved by using the chemically stable oxides of iron. In addition, technological utility requires carrier liquids that are themselves stable, for example, high vapour pressure oils.

Magnetic fluids are thus three component systems; solid phase magnetic particles of about 1-10 nm in diameter, surfactant molecules adhering to their surfaces and a liquid phase carrier. (Figure 1.1). They behave in many respects as would a uniform (single phase) magnetic liquid.

1.2.2 Applications of Magnetic Fluids

Although it may be said that the first attempt at

Free Surfactant   Bound Surfactant

Carrier Liquid   Magnetic Material
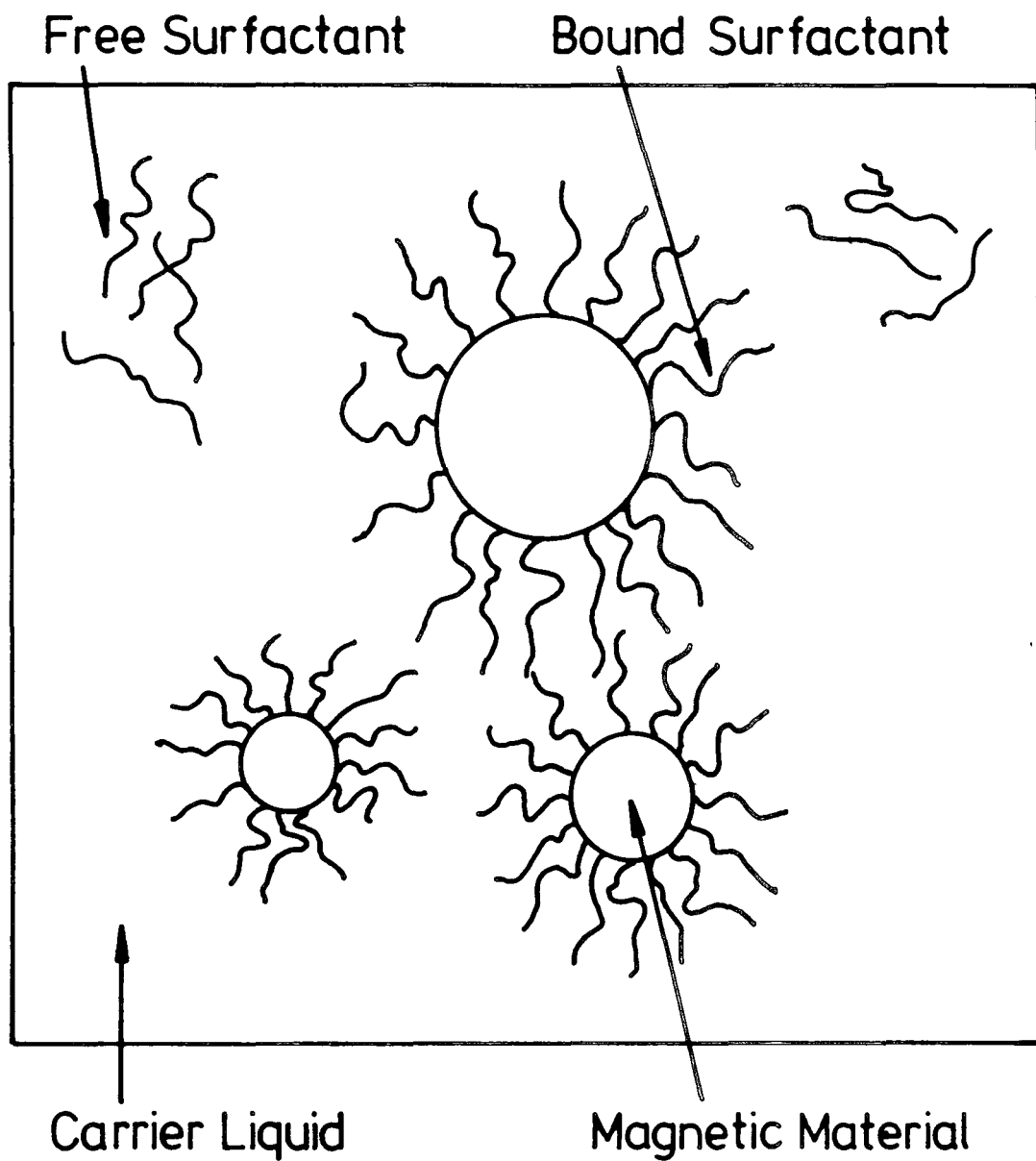
FIGURE 1.1
The components of a magnetic fluid;
magnetic material, surfactant and
carrier liquid.

producing a magnetic fluid was made by Knight (1779), the study of stable fluids as defined above is now about 20 years old. The original impetus was the U.S. space program, where it was hoped to utilise magnetic fluids to control the flow of fuels in weightless conditions (Papell 1965). Another potential space application was a heat-to-mechanical energy converter using the Curie temperature of the fluid (Rosenweig et al. 1965). These lead to the commercial fluids manufactured by Ferrofluidics Corporation of Nashua, New Hampshire. The major application of these fluids is as pressure seals for high speed rotating shafts (Figure 1.2). A magnetic fluid is constrained between the poles of a circular magnet and the metal shaft, forming a liquid 'O' ring seal. These seals can withstand pressure differentials of 0.4 MPa (600 p.s.i.) whilst the shaft rotates at 10,000 r.p.m. These seals find application in large computer disc drives and in crystal growers. Other applications of magnetic fluids include damping stepper motors, mechanical damping and heat dissapation in moving coil loudspeakers, magnetic separation (Rosenweig 1979) and magnetic ink jet printing (Maruno 1983). For reviews of applications see Bailey (1983) or Charles and Popplewell (1980).

All commercial fluids use magnetite (Fe_3O_4) as the particle material. This has a saturation magnetization, σ^∞ of ~ 91 $JT^{-1}kg^{-1}$ and a Curie temperature of ~ 860 K. Most ferrites have similar Curie temperatures and lower σ^∞. Metallic iron has a saturation magnetization of 217 $JT^{-1}kg^{-1}$

Soft Iron Pole Pieces

Permanent Magnet

P_1

P_2

ω

S   N

S   N

Magnetically
Permeable
Shaft
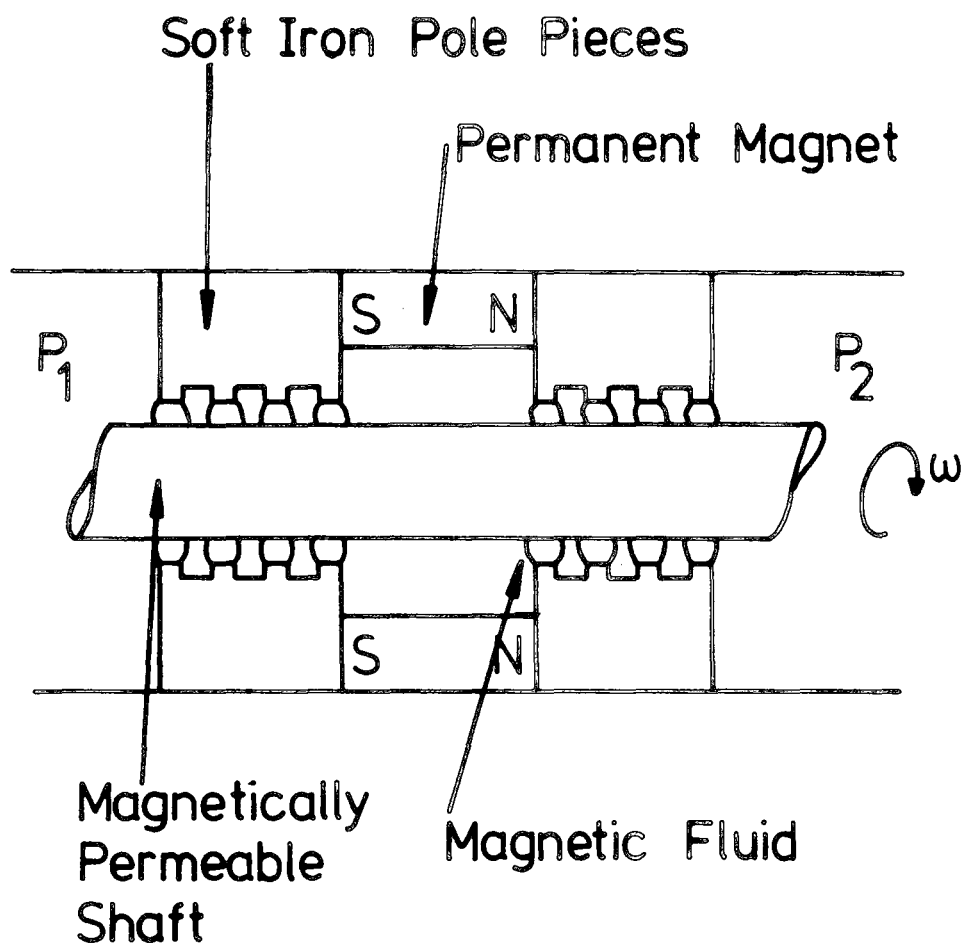
Magnetic Fluid

$P_1 \neq P_2$

FIGURE 1.2
The elements of a rotary pressure
seal utilising a magnetic fluid.

and metallic Ni has a Curie temperature of 627 K. The NiFe alloys have Curie temperatures ranging from 523 K to 1043 K and the FeCo alloys have a magnetization greater than that of pure iron in the composition range > 0 wt% Co to ∿62 wt% Co. Thus in order to vary the intrinsic magnetic properties of magnetic fluids and hence extend and/or improve their utility, the preparation of metallic and alloy systems is desirable. This requirement motivated the present study. The direct ancestors of the systems studied herein were the cobalt suspensions first prepared by Thomas (1966) and Hess & Parker (1966) by the decomposition of dicobalt octacarbonyl in the presence of polymeric dispersants.

In this study the properties of new preparations of Fe, Co and Ni fluids, as well as those of the first intermetallic systems prepared via this route, are described.

1.3 Magnetism

1.3.1 Introduction

The first manifestations of magnetic phenomena were the forces, observed centuries B.C., between lodestone (magnetite) and iron. During the nineteenth century similar forces were found to exist between electric currents. The effect of one current element (there being, as yet, no incontrovertible evidence for the existence of magnetic "charges" or monopoles) on another is described in terms of a vector field, the magnetic induction $\underline{B}$ (or flux density/

B-field). The force on a circuit C due to another circuit C' (see Figure 1.3a) may be expressed as

$$\underline{F}_{c' \to c} = \oint_C I \, d\underline{s} \wedge \underline{B}(\underline{r})$$ (1.1)

The unit of induction is the Tesla (T) and $1T = 1N/Am^{-1}$.

A magnetic dipole moment (usually referred to simply as magnetic moment) arises from the circulatory motion of a filamentary current. If this current is i and it encloses an area $\underline{S}$ (see Figure 1.3b) then the dipole moment produced is given by

$$\underline{m} = i \, \underline{S}$$ (1.2)

and thus has units $Am^2 = JT^{-1}$.

For a single electron, this may be written in terms of the angular momentum, $\underline{p}$, of the electron

$$\underline{m}_\ell = (e/2m) \, \underline{p}$$ (1.3)

This classical moment corresponds to the orbital motion of the electron. From quantum theory we know that the electron also possesses a spin motion which results in a dipole moment given by,

$$\underline{m}_s = (e/m) \, \underline{s}$$ (1.4)

where $\underline{s}$ is the spin momentum of the electron and e and m are the charge and mass respectively of the electron. The integral unit of magnetic moment for electrons, the Bohr
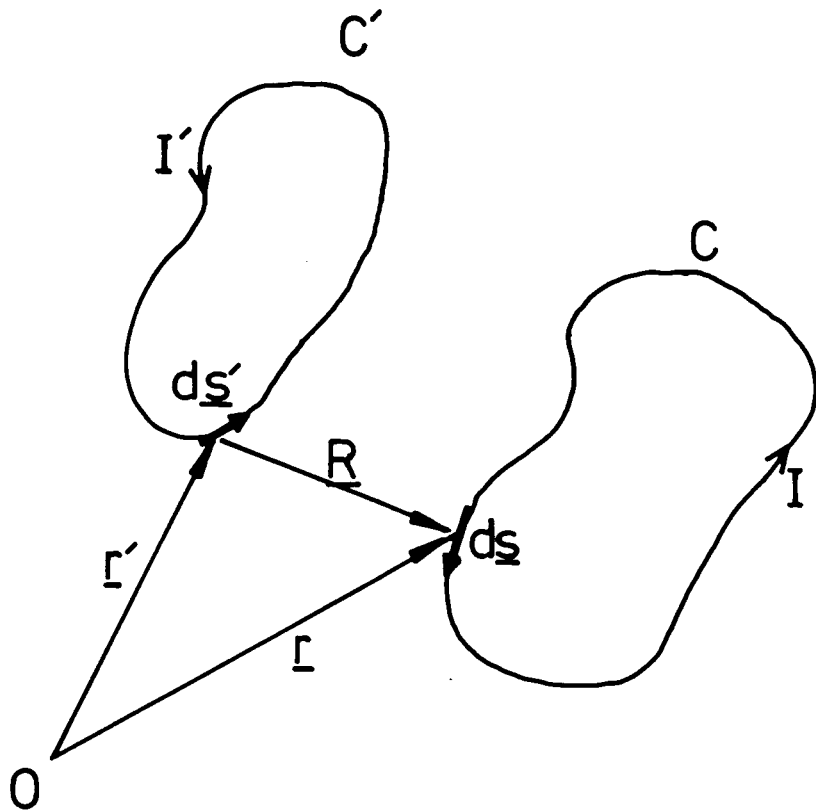
(a)
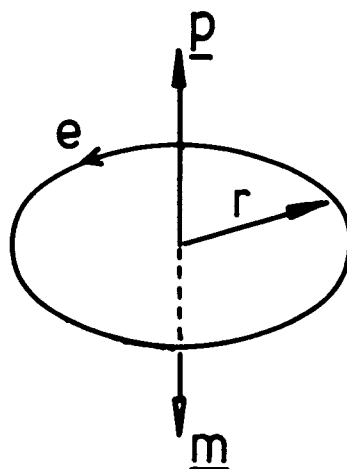
(b)

FIGURE 1.3
(a) Geometry of the force between
    two electric circuits.
(b) The angular momentum and magnetic
    moment of an orbital electron.

magneton, μ_B , is thus that for the lowest orbital state,
$l = 0$ i.e. $\mu_B = (e\hbar/2m)$. The magnetic moments which occur
in materials and are responsible for the forces between
them, arise from these two sources. The magnetic dipole
moment per unit volume of material is denoted the
magnetization of the material and is expressed in Am^{-1} or JT^{-1}
m^{-3}. The specific or per unit mass magnetization, σ, is
given by M/ρ, where ρ is the density of the material.

The total induction at any point is derived from two
components, the magnetization currents in materials and the
'free' currents in circuits (those driven by batteries
etc.). The contribution of the latter is described by the
vector field $\underline{H}$ (magnetic field strength) which is defined to
have the same dimensions as the magnetization $\underline{M}$. An ideal
solenoid with n turns per unit length, carrying a current I
will give rise to an $\underline{H}$-field of:

$$\underline{H} = nI\,\hat{\underline{z}} \qquad\qquad (1.5)$$

where $\hat{\underline{z}}$ is the axial unit vector.

The total induction may thus be expressed as

$$\underline{B} = \mu_0(\underline{H} + \underline{M}) \qquad\qquad (1.6a)$$
$$= \underline{B}_0 + \mu_0\underline{M} \qquad\qquad (1.6b)$$

where μ_0 is a constant of proportionality, the permeability
of free space and has the value $4\pi \times 10^{-7}$ Hm^{-1}.

1.3.2 Types of Magnetic Behaviour

Magnetic materials are usually classified according to their susceptibility, κ, defined by

$$\kappa = \underline{M}/\underline{H} \qquad (1.7)$$

although other definitions are often used, e.g. the differential susceptibility, dM/dH. In this study $\kappa = M/B_0$ will be used. The susceptibility has related quantities, the relative and absolute permeabilities defined respectively by

$$\mu_r = (1 + \kappa) \qquad (1.8a)$$

$$\mu = \mu_0 \mu_r \qquad (1.8b)$$

The magnetic behaviour of materials is usually divided into three categories:-

(i)   diamagnetic

(ii)   paramagnetic

(iii) ferro- or ferrimagnetic.

The first of these arises from the change induced in the orbital motion of the electrons by the application of a magnetic field. In a manner analogous to Lenz' law, this change produces a small moment opposing the applied field and hence κ is small and negative. As all materials contain electrons with orbital momentum, this occurs in all materials. The second and third categories require the existence of permanent dipole moments in the material. Paramagnetism, characterised by small positive susceptibilities, is the tendency of these moments to align

parallel to the magnetic field and hence minimize their
potential energy

$$U = -\underline{m} . \underline{B}_0 \qquad\qquad (1.9)$$

against the disordering produced by thermal excitation.
This applies to insulators containing ions with partially
filled shells and was first suggested in the classical limit
by Langevin, other sources of paramagnetism are the
conduction electrons in metals (Pauli paramagnetism) and
excited states in unfilled shells of insulators (van Vleck
paramagnetism). The final category contains materials with
very large positive susceptibilities. The fundamental
nature of these materials, however, is the spontaneous
ordering of the atomic moments (below some critical
temperature T_c) even in the absence of any applied field.
The three main types of ordering are ferromagnetic,
ferrimagnetic and antiferromagnetic. In the first, all the
magnetic moments tend to align parallel to each other. In
the other two, two sets of moments align antiparallel,
ferrimagnetism being the uncompensated case where one of
these has a larger net moment and antiferromagnetism the
case where they have equal net moment. The metals iron,
cobalt and nickel and their alloys are ferromagnetic whilst
magnetite is ferrimagnetic and so all the fine particles
described herein have intrinsically ordered atomic moments.

1.3.3 Magnetic Order and Exchange Interaction

For magnetic dipole moments to order spontaneously they must interact in some way. This interaction is not the dipole-dipole interaction. In 1907 Weiss proposed an internal field (molecular field) which aligned the moments and obtained a phenomenological description of ferromagnetism. This internal field would need to be equivalent to $\sim 10^3$ T, whilst dipole interactions can only provide ~ 0.1 T. An interaction of sufficient energy was only discovered with the advent of quantum theory (which also provided the necessary concept of electron spin).

The responsibility for magnetic order lies with the exchange interaction. The Pauli exclusion principle or antisymmetry requirement for many electron systems links the spin state of a system to its spatial wavefunction. Heisenberg (1928) first demonstrated how this could lead to magnetic order when he considered the hydrogen molecule. He approximated the two electron wavefunction by combining single, atomic states. Thus if $\psi_a(1)$, $\psi_b(2)$ are the spatial wavefunctions for atomic electrons 1,2 in states a,b then the two electron system has wavefunctions,

$$\varphi_\pm = (1/\sqrt{2})(\psi_a(1)\psi_b(2) \pm \psi_a(2)\psi_b(1)) \qquad (1.10)$$

where φ_+ is symmetrical under coordinate exchange and φ_- is antisymmetrical. The Hamiltonian for the two electron system is composed of the two single atom Hamiltonians together with an interaction term,

$$\mathcal{H} = \mathcal{H}_1 + \mathcal{H}_2 + \mathcal{H}_{int} \qquad (1.11)$$

Associated with the antisymmetric spatial wavefunction are three symmetric spin states all with total spin S = 1 (parallel spins). The symmetric spatial wavefunction has only one possible antisymmetric spin state which has S = 0 (antiparallel spins). There are thus two possible total wavefunctions ($\Psi_\pm$) for the system and the part of the total energy dependent on the interactions may be expressed

$$E_\pm = A_\pm^2 (K_{12} + J_{12}) \qquad (1.12)$$

where K_{12} is called the Coulomb integral, $A_\pm$ are normalizing constants and

$$J_{12} = \int \psi_a^0(1) \psi_b^0(2) H_{int} \psi_a(2) \psi_b(1) dv \qquad (1.13)$$

is the exchange integral. If this is positive then the state Ψ_- has lower energy and hence a total spin S = 1 results. In practice it is extremely difficult to evaluate exchange integrals, even the sign being difficult to predict. This type of exchange is known as direct exchange as it occurs between electrons on neighbouring atoms. It is suited only to systems where the atoms are so well separated that they retain free-atom characteristics. Since 1928 other types of exchange have been proposed. Indirect exchange occurs between conduction electrons and localized magnetic electrons and is used to describe rare earth metals. Superexchange occurs by the simultaneous coupling of the spins on magnetic atoms with the non-magnetic atoms between them and is used to describe ferrites. Itinerant

exchange is that between electrons which are able to move throughout the crystal lattice. This is appropriate to the transition metals.

The elementary magnetic moments in the transition metals arise from the spins of the electrons in the unfilled 3-d energy bands. The orbital contribution is "quenched" by the crystalline fields. There is much evidence (for example specific heat or non-integral number of Bohr magnetons per atom) to suggest that the 3-d carriers of magnetic moment are itinerant. Different models have been proposed to describe the magnetic behaviour of the transition metals Fe, Co and Ni, that most widely applied to real materials being the Stoner model.

1.3.4 Band Theory of Magnetism

The itinerant or band theory of magnetism assumes that the electrons responsible for the magnetic moment may be described using Bloch-type wavefunctions and thus energy bands. These electrons are not localized to specific atoms, unlike those in the Heisenberg model. This description is applicable to metals and alloys of the transition series, in particular the 3d-metals. This theory was initiated by Bloch (1929), Slater (1936) and Stoner (1933, 1938, 1939). That due to Stoner will be briefly outlined here, to give some indication of the manner in which ferromagnetism may arise in the metals from which the fine particles discussed herein are composed. Fuller details may be found in Stoner

(1948, 1951) and Wohlfarth (1981).

Stoner's approximations were:-

(a)   the set of electrons/holes are in a partially filled
      energy band which has a parabolic shape near the Fermi
      level.

(b)   the exchange interaction may be introduced in terms of
      a molecular field proportional to the magnetization.

(c)   Fermi-Dirac statistics describe the distribution of
      electrons amongst the energy states.

These allowed him to develop a statistical mechanical
description of the spontaneous magnetization at absolute
zero and its dependence on temperature. Implicit equations
involving a parameter related to the Gibbs free energy were
obtained. These required numerical solution which gave
results much in accordance with experiment. The greatest
success of this model was its natural explanation of the
non-integral number of Bohr magnetons per atom obtained
experimentally for the magnetization of Fe, Co and Ni at OK.
How this arises may be seen as follows.

In the absence of any exchange interaction, the
electrons will fill the energy band in pairs of opposite
spin up to the Fermi level. In the d-metals the narrow
d-band and wide s-bands overlap (see Figure 1.4a). This
means that although there is an integral number of electrons
per atom in the outer two shells, they will start to fill
the s-band before the d-band is completely full. For
example, Ni has 10 electrons per atom to distribute between

(a)

(b)
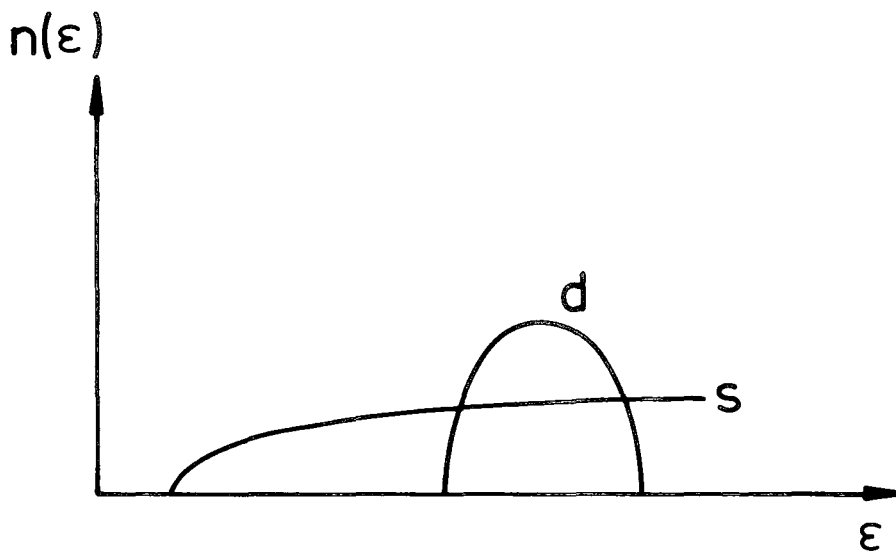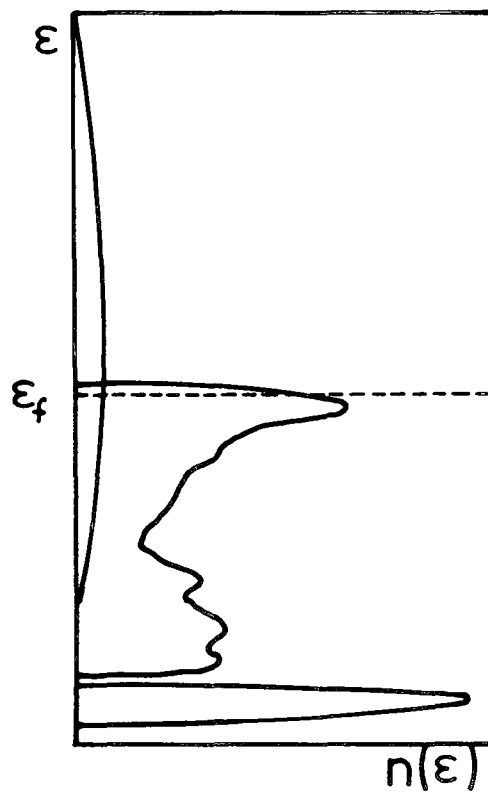
ε - Energy
$n(\varepsilon)$ - Density of states
ε_f - Fermi energy

FIGURE 1.4
(a) The overlap between the s and d
    bands in 3d metals.
(b) The Fermi level in 3d metals

the 3-d and 4-s bands. The Fermi level (see Figure 1.4b) is such that when it is reached there are 0.6 electrons (per atom) in the 4s-band and 9.4 in the 3d-band. The 0.6 hole in the 3d-band gives rise to the magnetization of Ni, which at OK corresponds to 0.6 μ_b per atom.

The magnetic moment arises from unequal numbers of electrons with up and down spins. This excess of up (say) spins is a consequence of the exchange interaction. A decrease in this energy is obtained by parallel alignment of spins. However, for an electron to move from a down spin state to an up spin state, it would have to move to an unoccupied energy level above the highest filled level occurring in the absence of exchange. That is, its kinetic energy would be increased. An equilibrium between these two opposite tendencies is established which leaves an excess of up spins. In terms of the molecular field, the two sub-bands corresponding to the two spin states are split, those electrons with spin parallel to the molecular field have their energy decreased by $\mu_b \cdot \underline{H}_m$ whilst the antiparallel spins have theirs increased by the same amount. This is illustrated in Figure 1.5.

Other theories have been proposed to explain the fractional Bohr magneton number in Fe, Co and Ni. Van Vleck (1953), for example, (describing a model of Hurwitz) considers Ni metal to have 40% of the atoms in the 3d↑ state and 60% in the 3d↓ with these constantly being redistributed amongst all the atoms. These and other
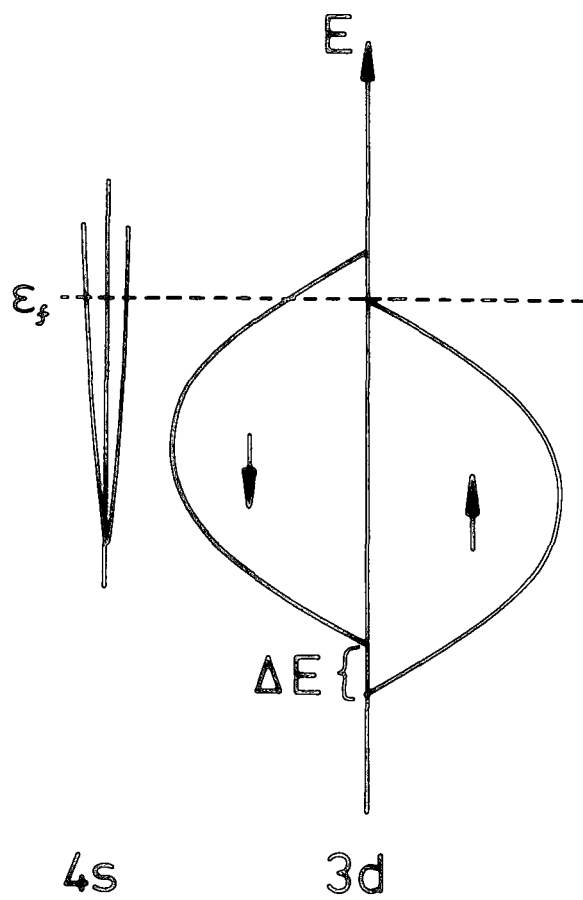
FIGURE 1.5
The band splitting caused by the
exchange energy.

approaches are described in the Symposium on Exchange (Rev. Mod. Phys. <u>25</u> 199 (1953)) of the 1953 Washington Magnetics Conference. Theories of magnetism remain under much discussion and a modern review is given by Moriya (1979).

1.4 Fine Particle Magnetism

1.4.1 Domains

The magnetization curve of a bulk ferromagnetic material is shown in Figure 1.6. In zero applied field it is possible for the material to have no macroscopic magnetization, yet a rapid rise to saturation will occur if relatively small fields are applied. To explain this phenomenon, Weiss (1907) suggested that ferromagnetic materials were composed of regions, called domains, each of which possessed the spontaneous magnetization due to the molecular field but arranged in such a manner that their net vector sum of magnetizations can be zero. The existence of domains is now well established, indeed they have been observed directly by Parpia et al. (1984).

1.4.2 Single Domain Particles

Domains arise in order to minimize the magnetostatic energy of a material in its own <u>B</u>-field. However, exchange energy demands that parallel spin arrangements are taken up. There is thus a region between domains, called the domain wall, over which the spin orientation changes and this has an increase in exchange energy associated with it. The

M

B_o

M^∞

$(B_o)_C$
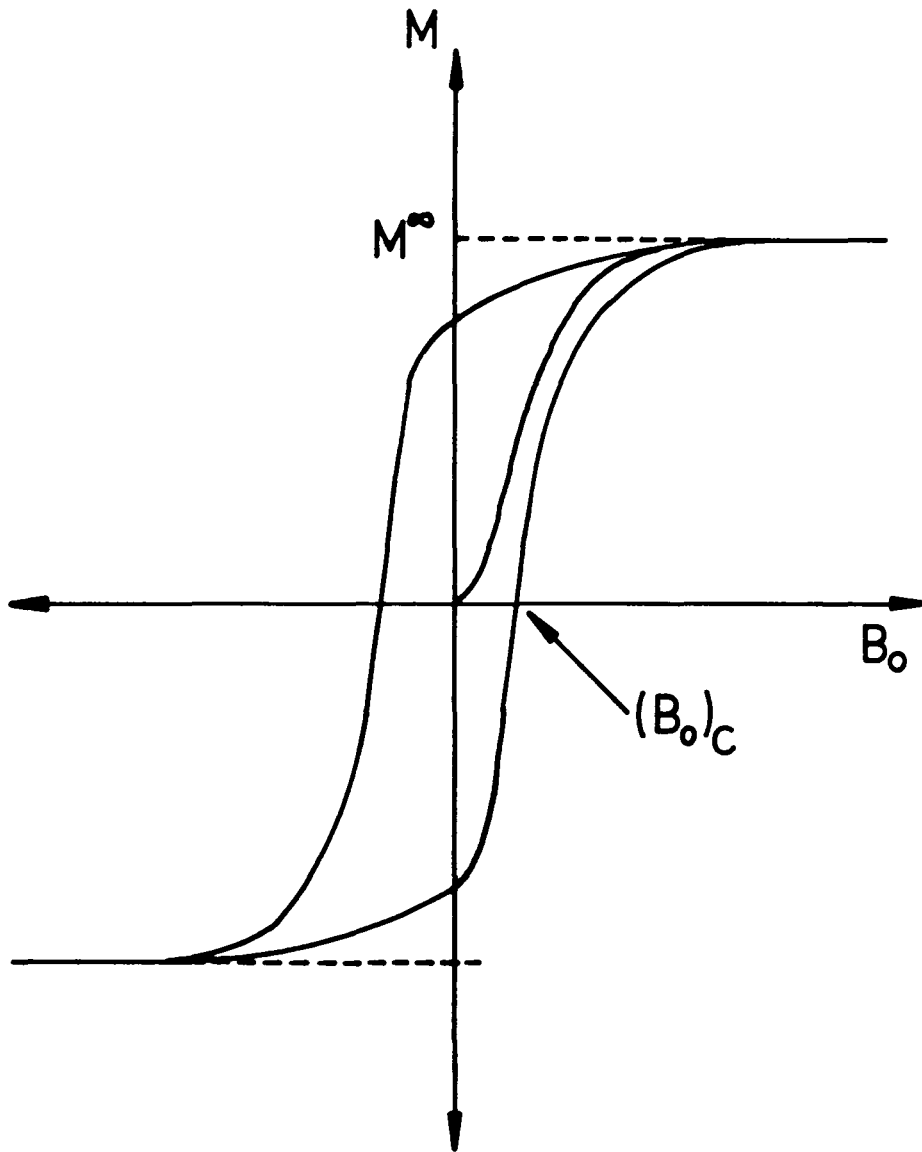
(B_o) – Coercivity
M^∞ – Saturation Magnetisation

FIGURE 1.6
The magnetisation curve and hysteresis
loop of a ferromagnetic material.

number and size of domains in a specimen will be a result of
the trade-off between decreasing magnetostatic energy and
increasing exchange energy. As a specimen of material is
made smaller the relative contribution of these sources of
energy changes and below some critical size it becomes
possible for a single domain particle to exist. Calculation
of the critical size is made by equating the magnetostatic
energies of single and (minimum energy) multidomain
configurations in the absence of any field. Results of such
calculations by Kittel (1946) for iron cubes/spheres were
15nm diameters. More rigorous calculations consider how the
magnetization changes from a uniform to a non-uniform
configuration in the domain (Brown 1957) but obtain critical
diameters of the same order. Values of 29nm for iron and
60nm for Ni have also been obtained (Brailsford 1966). The
fine particles studied herein have diameters 5-8nm and hence
are certainly all single domain.

1.4.3 Particle Anisotropies

Single domain particles have a uniform magnetization
(ignoring surface effects) which may be represented by a
single vector through the centre of the particle. The
magnetic state of the particle is altered by changing the
direction of this vector, its magnitude remaining constant.
The energy of the magnetization within the particle is not
isotropic. Certain directions have less energy associated

with them and are known as the easy directions. The
magnetization tends to lie along these directions in the
absence of any applied field. This anisotropy may be
represented in terms of phenomenological anisotropy
constants; for a uniaxial anisotropy the energy of the
magnetization vector may be written,

$$E = \sum K_n \sin^{2n} \vartheta \qquad (1.14)$$

where θ is the angle of the vector from the easy axis and K_n
are the anisotropy constants. It is usually sufficient to
consider only the first two terms. For three easy axes as
in the cubic crystals the energy may be expressed as

$$E_K = K_0 + K_1 (\alpha_1^2 \alpha_2^2 + \alpha_2^2 \alpha_3^2 + \alpha_1^2 \alpha_3^2) + ... \qquad (1.15)$$

where the α_i are the direction cosines of the vector with
respect to the three easy axes. Net anisotropies are
usually uniaxial in fine particle systems. Four mechanisms
for anisotropy are discussed below.

(i) Magnetocrystalline Anisotropy

     This is the effect observed in the bulk material.
Interactions between electron orbital motions in the crystal
lower the energy in certain directions. Fe which has a body
centred cubic structure, has easy axes along the cube edges,
<100> directions, whilst Ni with a face centred cubic
structure has easy axes (below 320K) along the cube
diagonals, <111> directions. In Co, which is hexagonal, the
single easy axis is along the c axis. (In fine particle

form, Co usually adopts its high temperature, fcc phase).
Magnetocrystalline anisotropy constants are of the order $\sim 10^3$
-10^4 Jm^{-3} in the cubic cases and $\sim 10^5$ Jm^{-3} in the hexagonal
case.

(ii) Shape Anisotropy

This is due to the demagnetizing field produced within
a specimen in opposition to its magnetization. It depends
on the magnitude of $\underline{M}$ and the specimen geometry. The
demagnetizing field is given by

$$(\underline{B}_0)_D = - D\underline{M} \tag{1.16}$$

where D is known as the demagnetizing factor. This leads to
an energy term for the specimen of,

$$E = \tfrac{1}{2} D M^2 \tag{1.17}$$

For an infinitely long, narrow cylinder, D along the long
axis tends to zero and hence the magnetization vector will
lie along the long axis of an elongated particle. For a
prolate ellipsoid (Figure 1.7) an effective anisotropy
constant may be calculated as

$$K_S = (M_b^\infty)^2 (D_w - D_l) \tag{1.18}$$

For Fe particles with an aspect ratio (l/w) of 1.1,
$K_S = \sim 10^5$ Jm^{-3}. Thus even for quite small elongations,
shape anisotropy dominates magnetocrystalline. Figure 1.8
shows K_S as a function of elongation for Fe, Co and Ni. For
all of the fine particles systems studied herein, a uniaxial
anisotropy has been observed.
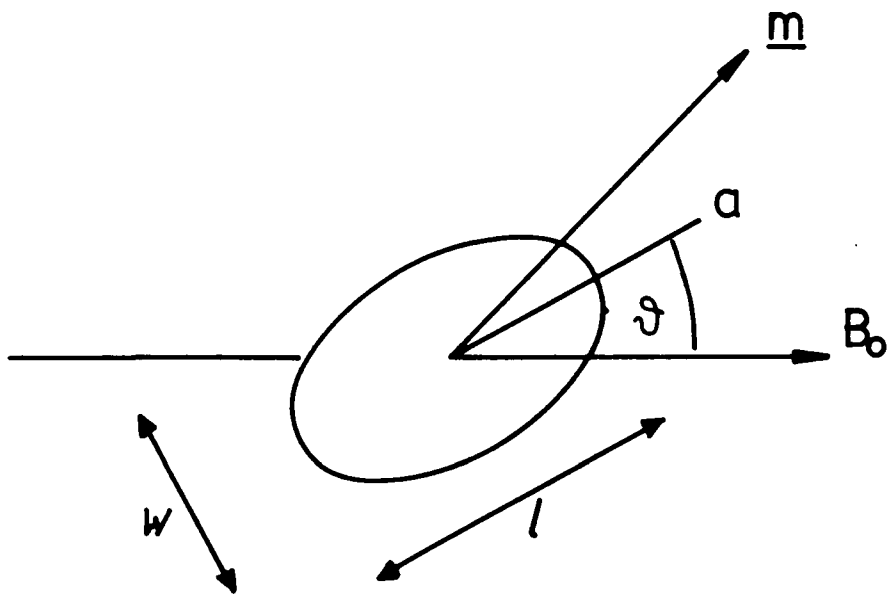
a – easy axis

m – magnetic moment

FIGURE 1.7
Definition of angles for prolate
sphere in uniform magnetic field.
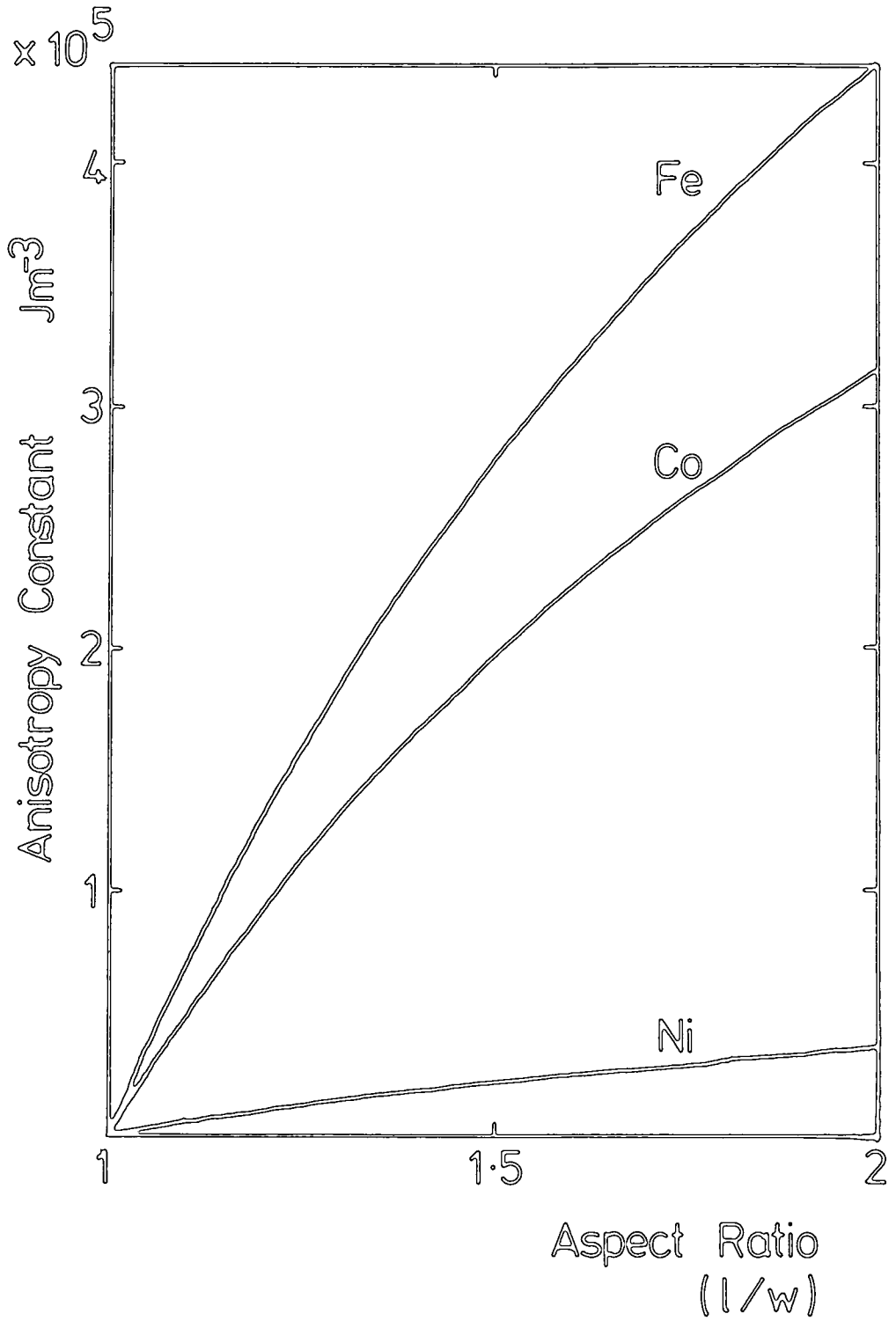
FIGURE 1.8
Shape anisotropy as a function of
aspect ratio for prolate spheres of
Fe,Co and Ni

(iii)   Strain Anisotropy

The application of anisotropic strain to a crystal will alter the interatomic spacing along the strain direction and thus alter the magnetic interaction energy along that direction. As a result anisotropy develops. This may occur in magnetic fluids when they are frozen if the coefficients of expansion of the particle material and carrier liquid are very different. The presence of the surfactant layer may, however, reduce this effect.

(iv)   Exchange Anisotropy

This occurs via the interaction between a ferromagnetic core and an antiferromagnetic surface layer. Mieklejohn and Bean (1956) first observed this for a Co/CoO interface at 77K. The hysteresis loop of the system is displaced along the field axis. This effect has been observed in this study for Co particles and is reported in Chapter 6.

1.4.4   Magnetization Reversal mechanisms

The magnetization of a single domain particle can only change (at fixed temperature) by rotation of the spin directions. This may occur in three ways (Frei et al. 1957):-

(i)   Rotation in Unison

This is represented in Figure 1.9a. All the individual spins rotate simultaneously and by the same amount in the same direction. This process leads to square hysteresis loops with coercivity,
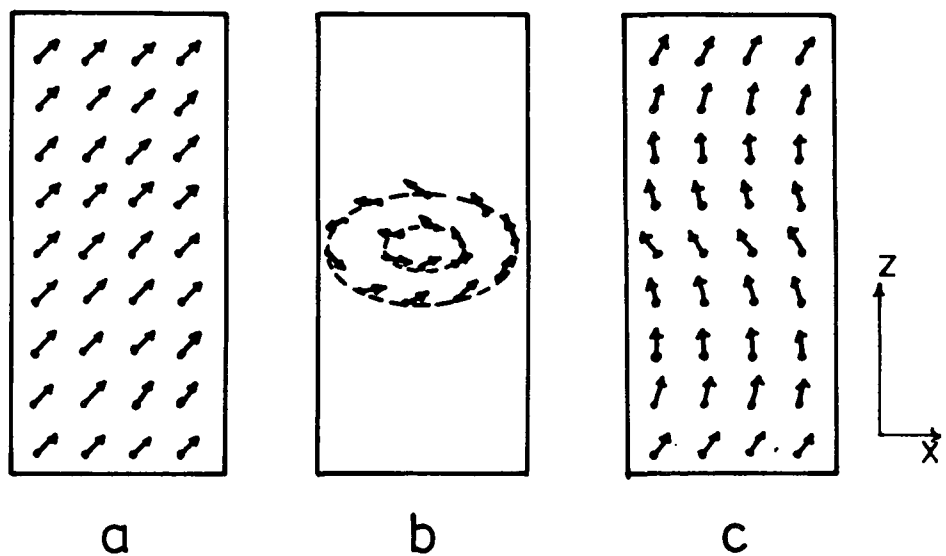
a - Rotation in Unison
b - Curling
c - Buckling

FIGURE 1.9
Magnetisation reversal mechanisms in single domain particles.

$$(B_0)_c = \tfrac{1}{2}\mu_0 M_b^\infty \qquad\qquad (1.19)$$

(ii) Magnetization Curling

This is illustrated in Figure 1.9b. The spins rotate in planes perpendicular to the radius of the cylinder. Again a rectangular hysteresis loop will be obtained with coercivity,

$$(B_0)_c = 1.08(R_0/R)^2 \mu_0 M_b^\infty \qquad\qquad (1.20)$$

where R is the radius of the cylinder, $R_0 = A/M_b^\infty$ and A is related to the exchange integral.

(iii) Magnetization Buckling

This is shown in figure 1.9c. The spin rotations occur in planes parallel to the x-plane and the deviation from the z-axis is a periodic function of z. For large values of (R/R_0) the coercivity is given by

$$(B_0)_c = -1.29(R_0/R)^{\tfrac{2}{3}} \mu_0 M_b^\infty \qquad\qquad (1.21)$$

The mechanism occurring in a cylinder depends on the parameter $S = (R/R_0)$. Frei et al. find that Curling occurs for S > 1.1, Buckling for S < 1.1, whilst Buckling becomes Rotation in Unison for S << 1. For a sphere, assuming curling, they obtain $(B_0)_c = \tfrac{2}{3} - 1.39S^{-2}$ which yields the critical diameter for single domain state as $S_c = 1.44$. For prolate ellipsoids they calculate $1.04 < S_c < 1.44$.

In addition to the above mechanisms for single particles, Jacobs and Luborsky (1957) suggested non-coherent

reversal mechanisms for chains of spheres. These are illustrated in Figure 1.10. They may apply to large single domain particles which have a morphology similar to a chain of spheres.

1.4.5 Superparamagnetism

Coercivity as a function of particle size for fine particles embedded in a solid matrix is shown in Figure 1.11. As the particle size decreases the increase in coercivity is explained by the transition from multi- to single domain particles and the subsequent reversal mechanisms above replacing domain wall movement. Eventually, however, for particles below about 10nm diameter the coercivity begins to decrease and finally falls to zero. This is explained by the phenomenon of superparamagnetism. Whilst investigating the magnetization of geological samples, Neel (1949a,b) noted that if a single domain particle became small enough, its magnetization vector could fluctuate in a Brownian manner under the influence of thermal energy. Rotation in unison is assumed.

(i) Fixed Isotropic Particles

Consider an assembly of identical, spherical particles, each possessing moment m_p and having no anisotropy. The energy of each particle in the presence of an applied field, $\underline{B}_o$, is given by

$$E = -\underline{m}_p \cdot \underline{B}_o = -m_p B_o \cos \vartheta \qquad (1.22)$$

where θ is the angle between the moment and the field
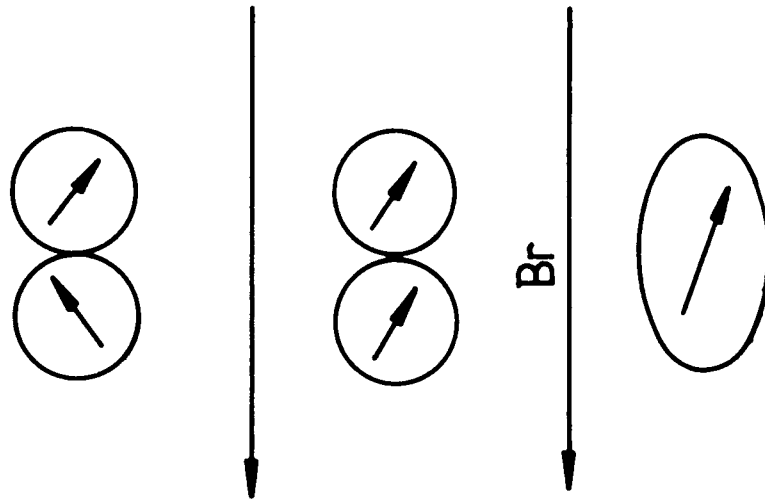
Br – Reversing Field

FIGURE 1.10
Chain of Spheres model for reversal
of magnetisation.
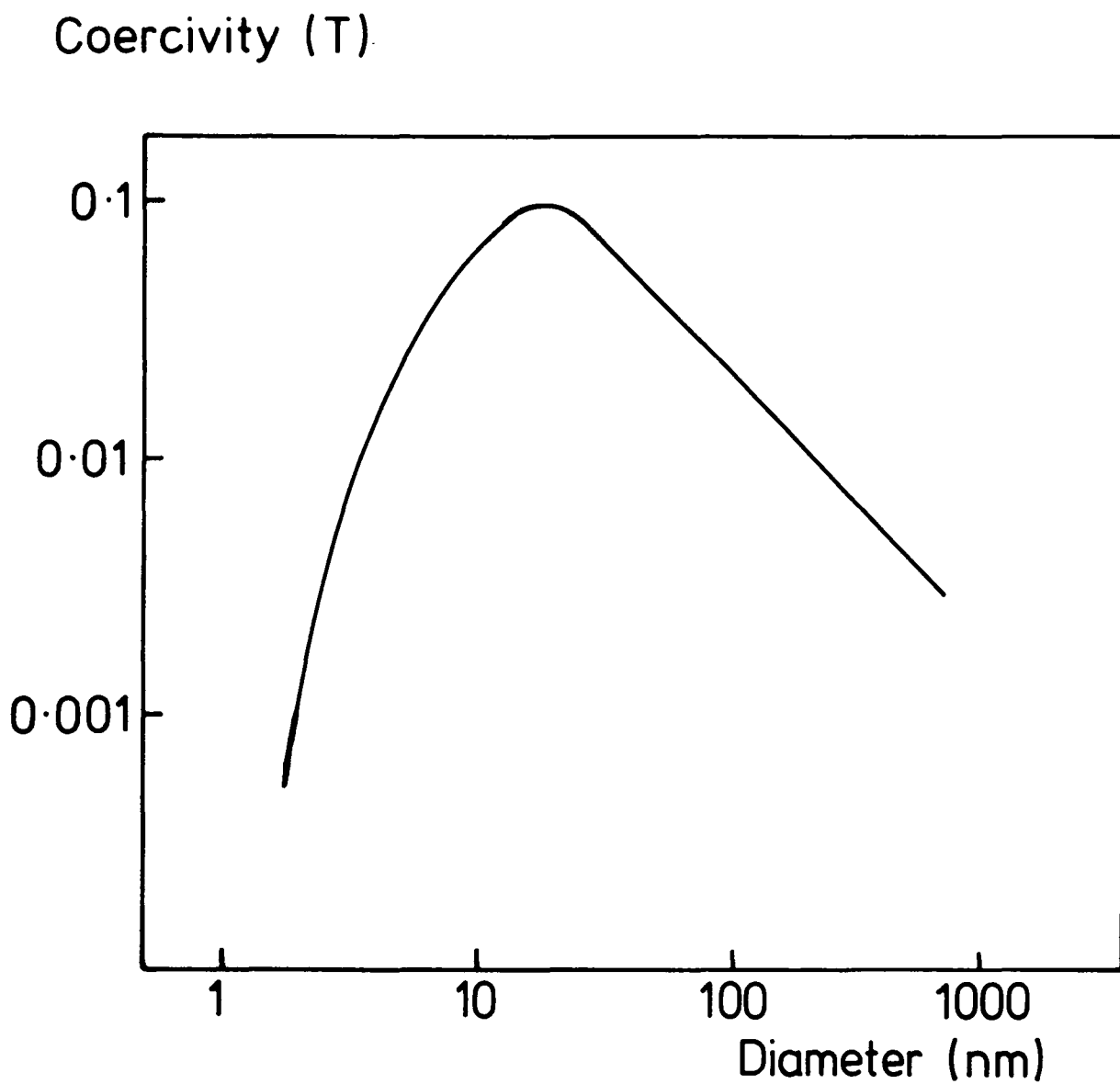
Coercivity (T)

FIGURE 1.11
Coercivity as a function of particle
size. (After Luborsky 1959).

direction. If these moments are allowed to fluctuate thermally and the system attains thermal equilibrium then the component, in the field direction, of the magnetization of the assembly is given by averaging over a Boltzmann distribution. That is, we have the classical Langevin paramagnetism but instead of each moment being of the order μ_b , they are of the order $10^5 \mu_b$. Bean (1955) christened this "superparamagnetism". The magnetization of the system may thus be described in terms of the Langevin function;

$$M(B_o) = (n_p m_p / V) L(x) = (n_p m_p / V)(\coth(x) - 1/x) \qquad (1.23)$$

where $x = m_p B_o / kT$, $L(x)$ is the Langevin function, n_p is the number of particles and V is the total volume of the system.
 This equation has two distinguishing characteristics;
(a) the magnetization curve shows no hysteresis.
(b) in the absence of dipole interactions between the particles, magnetization curves taken at different temperatures will superimpose when plotted as a function of B_o/T.
These provide an empirical definition of superparamagnetism. The low and high field approximations of equation (1.23) are easily found to be,

$$M(B_o) = (n_p m_p / V) \, m_p B_o / 3kT \qquad (1.24a)$$

$$M(B_o) = (n_p m_p / V)(1 - kT / m_p B_o) \qquad (1.24b)$$

(ii) Fixed Anisotropic Particles
    Real particles are usually anisotropic. In the case of

magnetic fluids, the particles often have uniaxial
anisotropy due to shape. The energy (per unit volume) of
uniaxial particles in an applied field B_o is given by

$$E = -\underline{m}_p \cdot \underline{B}_o + K \sin^2 \varphi \qquad (1.25)$$

where φ is the angle between the magnetization direction and
the easy axis. If this is used instead of (1.22) to average
over the Boltzmann distribution of energies, the simple
Langevin function will not result.

Assuming that all the particles have their easy axis
parallel to the field, West (1961) found the magnetization
of the system to be given by

$$M = (n_p m_p / V) \{ a^{-\frac{1}{2}} (e^b y(\alpha_1) + e^{-b} y(\alpha_2)) \}^{-1} \sinh(b) - \frac{b}{2a}) \qquad (1.26)$$

where $a = K v_p / kT$, $b = m_p B_o / kT$, $\alpha_1 = (1 + b/2a) a^{\frac{1}{2}}$ and $\alpha_2 =$
$(1 - b/2a) a^{\frac{1}{2}}$. Figure 1.12 shows M as a function of b for
different values of a. West found that for a = 0.01,
b = 0.01 the magnetizations were $\sim$12% greater than the
Langevin values. For large values of a, Bean (1955) found

$$M \simeq \frac{n_p m_p}{V} \tanh(m_p B_o / kT) \qquad (1.27)$$

If $kT \gg K v_p$ then Langevin behaviour will result.

(iii) Conditions for Thermal Fluctuation of the Moment

The above analyses assumed that the magnetization
vector of each particle fluctuated thermally. We must now
consider the circumstances under which this will occur. The
case of uniaxially anisotropic particles is once more
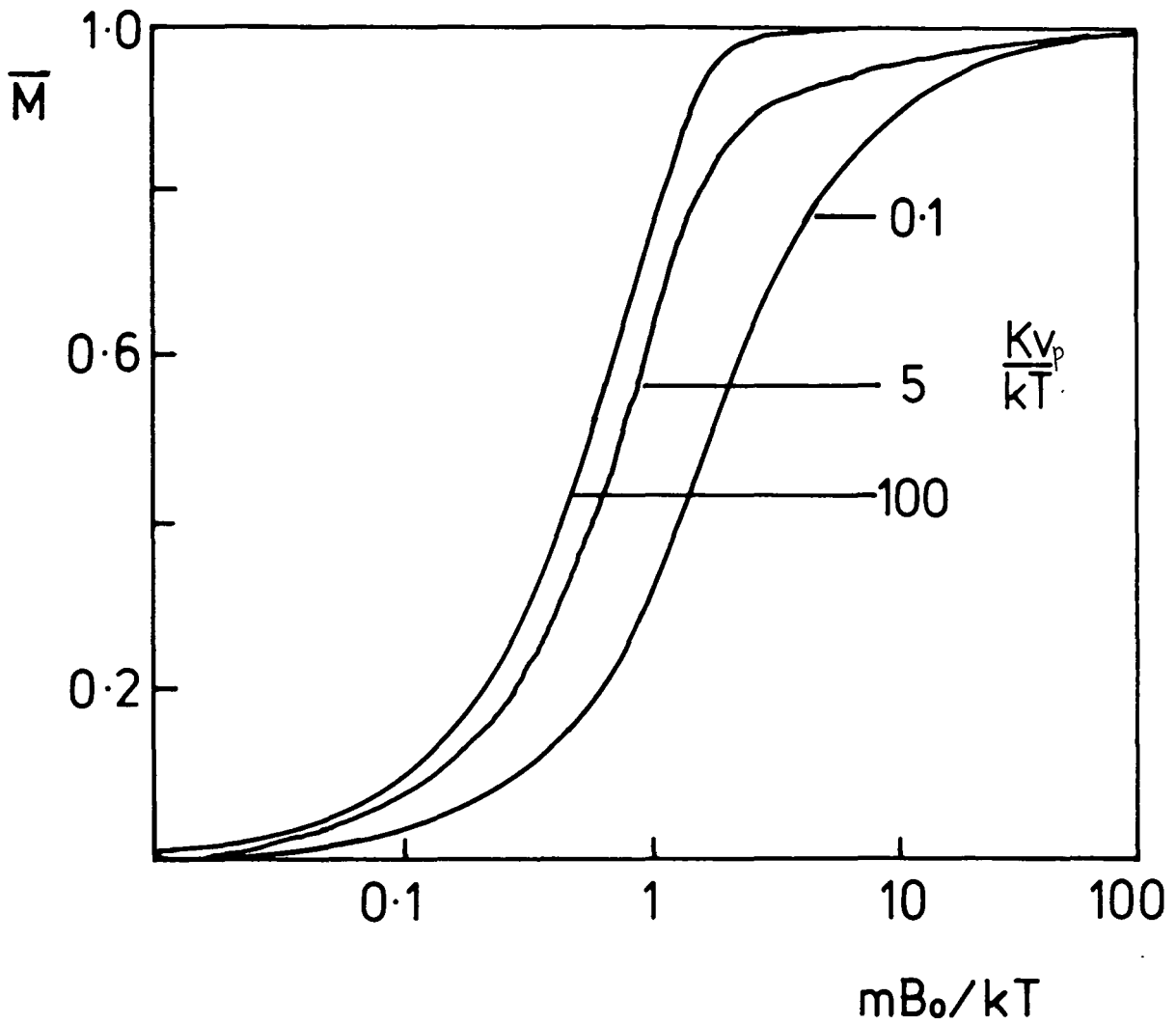
FIGURE 1.12
Magnetisation curves for fixed
anisotropic particles.
(After West 1961).

assumed. The energy of such a particle is given by equation (1.25). If we consider the case in which the easy axis is aligned parallel to the field, then in equilibrium the magnetization vector will adopt a minimum energy position given by

$$\frac{\partial E}{\partial \varphi} = -B_0 M_b^\infty \sin\varphi + K \sin 2\varphi = 0 \qquad (1.28)$$

For small fields, where the vector will tend to lie parallel to the easy axis, having either direction along it and we obtain

$$(B_0)_K = 2K / M_b^\infty \qquad (1.29)$$

as an upper limit for the field. This is known as the anisotropy field of the particle. Between the two minima positions ($\varphi = 0°$, 180°) of equation (1.28) there is an energy barrier, $\Delta E = Kv_p$, which can be overcome by thermal energy. In equilibrium at temp T_1, field B_1, there will be n_1 vectors in the $\varphi = 0°$ direction and n_2 in the $\varphi = 180°$. If the temperature or field is changed then these two populations will redistribute themselves until a new equilibrium is established. This will take some time, τ, known as the relaxation time. If w_{12} is the probability of a transition from state 1 ($\varphi = 0°$ say) to state 2 ($\varphi = 180°$) then the relaxation time is given by Neel (1949) and Brown (1959) as

$$\tau = (w_{12} + w_{21})^{-1} \qquad (1.30a)$$

and

$$w_{ij} = f_{ij} \exp(-\Delta E / kT) \qquad (1.30b)$$

PAGE 24

The theory as developed by Brown (1959, 1963) assumes a two state system. This has been shown to be a good approximation as long as $\Delta E/kT > 2$. (Aharoni 1964). This relaxation of the moment within its crystal habit is termed the Néel relaxation and the characteristic relaxation time is denoted τ_N.

For example, the decay in remanence with time may be written (Kneller 1969)

$$M^r(t) = M^r(0) \exp(-t/\tau_N) \qquad (1.31)$$

where t = 0 corresponds to the moment (in time) when the saturating field was removed. The relaxation time is then given by

$$\tau_N = (1/2f_o) \exp(Kv_p/kT) \qquad (1.32)$$

where f_{ij} has here been taken to be the precessional frequency $(= m_p H_{eff}/(2\pi \underline{p})$ of the magnetization vector. (Brown 1959), f_{ij} is usually taken to have the value $\sim 10^9$ Hz. Brown (1963) treated the problem more rigorously, obtaining more accurate expressions for the f_{ij} but the numerical results are much the same as those obtained from the intuitive approach above.

The time taken for an experimental measurement must now be compared to the relaxation time of the system in order to discover whether thermal fluctuations will produce superparamagnetic behaviour. Inserting $K = M_b(B_o)_K/2$ into

equation (1.32) reveals that the relaxation time is strongly dependent on the volume of the particles and the temperature. If the time of the experiment is Δt then:-

(a) if $\Delta t > \tau_N$ - the system is always measured in thermodynamic equilibrium and hence superparamagnetism will be observed.

(b) if $\Delta t < \tau_N < 10^9$ - then time dependent effects will be observed for example remanence decay.

(c) if $\Delta t << \tau_N$ - then the magnetization of the system is essentially constant over time. Geological timescales can be attained.

Condition (a) yields

$$\ln(2 \Delta t\, f_0)\, kT/(K v_p) > 1 \qquad (1.33)$$

as the requirement for observation of superparamagnetism. For laboratory measurements t = 100s may be assumed (Kneller 1969), for which the logarithmic term is approximately 25. The critical volume for superparamagnetic behaviour is then

$$V < V_c = \frac{25kT}{K} \qquad (1\,34)$$

Alternatively, given particles of a certain volume, (1.34) defines the critical temperature for thermal activation of the moment. These are known as the blocking volume (or diameter) and temperature of the particle.

(iv) Free Anisotropic Particles

In the above it has been assumed that the particles

have been spatially fixed. For magnetic fluids above their freezing point, this is not the case. The particle body is free to rotate. A Brownian motion of the particle will occur in the liquid carrier and this provides another mechanism for relaxation of the magnetization.

If large anisotropic particles are assumed ($Kv_p \gg kT$) with magnetic moment locked into the easy axis, then the relaxation time of the moment is equal to the Brownian rotational-diffusion time of the particle body and is given by Shliomis (1974) as

$$\tau_B = \frac{3v_p\eta}{kT} \tag{1.35}$$

where η is the viscosity of the carrier liquid. This equation does not take into account the effect of the adsorbed surfactant layers. It should be noted that this is not a magnetic equation, it is valid for the mechanical relaxation of the particle in the carrier and hence does not take into account any applied field.

Relaxation of the magnetic moments will occur via the mechanism with the shortest relaxation time. The critical volume (at fixed temperature) at which one process takes over from the other is given by equating the relaxation times, $\tau_N = \tau_B$

$$f_i \exp(Kv_p/kT) = \frac{3v_p\eta}{kT} \tag{1.36}$$

and solving for v_p. Using magnetocrystalline values for K, Shliomis obtains critical diameters, D_s, of 8.5 nm for Fe and 4.0 nm for Co at room temperature. For particle

diameters less than D_s the Neel relaxation process dominates.

When a field, $(B_0)_a$, is applied to a system of particles which relax via the Brownian mechanism, their moments tend to align their easy axes parallel to the field. This process has a characteristic time given by Shliomis for the limiting cases $(B_0)_a \gg (B_0)_K (i = a)$ and $(B_0)_a \ll (B_0)_K$, $(i = k)$ as

$$\tau_t = \frac{6\eta}{M_b^\infty (B_0)_i} \qquad (1.37)$$

In the latter case this may be written as $\tau_t = \eta 3/K$. Hoon et al. (1980) have taken into account the effect of the surfactant layer and obtain

$$\tau_t = \frac{6\eta}{M_b^\infty (B_0)_a} (1 + \frac{\delta}{r}) \qquad (1.38)$$

where r is the radius of the particle and δ is the length of the surfactant molecules.

If the 100s criterion is applied to Brownian relaxation and η is taken to be 10^{-3} Nsm^{-2} then equation (1.35) gives,

$$V_p \leqslant \frac{kT \Delta t}{3\eta} = 1.38 \times 10^{-16} m^3 \qquad (1.39)$$

that is, a particle diameter of 6.4 microns. Magnetic fluids in carrier liquids such as toluene will thus always exhibit superparamagnetism at room temperature. Deviation from Langevin behaviour will occur, however, due to magnetostatic interactions and particle size distributions. These effects are discussed in Chapters 2 and 4.

CHAPTER TWO

MAGNETIC FLUIDS AND COLLOIDS

2.1 Introduction

Magnetic fluids are lyophobic (solvent resisting) colloids. That is, the dispersed material does not form a solution with the dispersing medium. Lyophobic colloids are prepared via two techniques, dispersion and condensation. Dispersion methods mechanically fragment the colloid material whilst condensation methods form particles from molecular solutions. In the case of magnetic colloids these methods usually proceed in the presence of a dispersing agent, e.g. a surfactant, which acts as a steric stabilizer. The fine particles produced may be redispersed into another carrier liquid. Principal preparative routes are outlined below.

Many of the properties of magnetic fluids are those of lyophobic colloids, for example, flocculation and sedimentation. Their magnetic nature, however, reveals itself in several striking properties such as the normal field surface instability (see Figure 2.1) and anisotropic viscosity in magnetic fields. Colloidal and magnetic properties are discussed below.

FIGURE 2·1

The normal field surface
instability
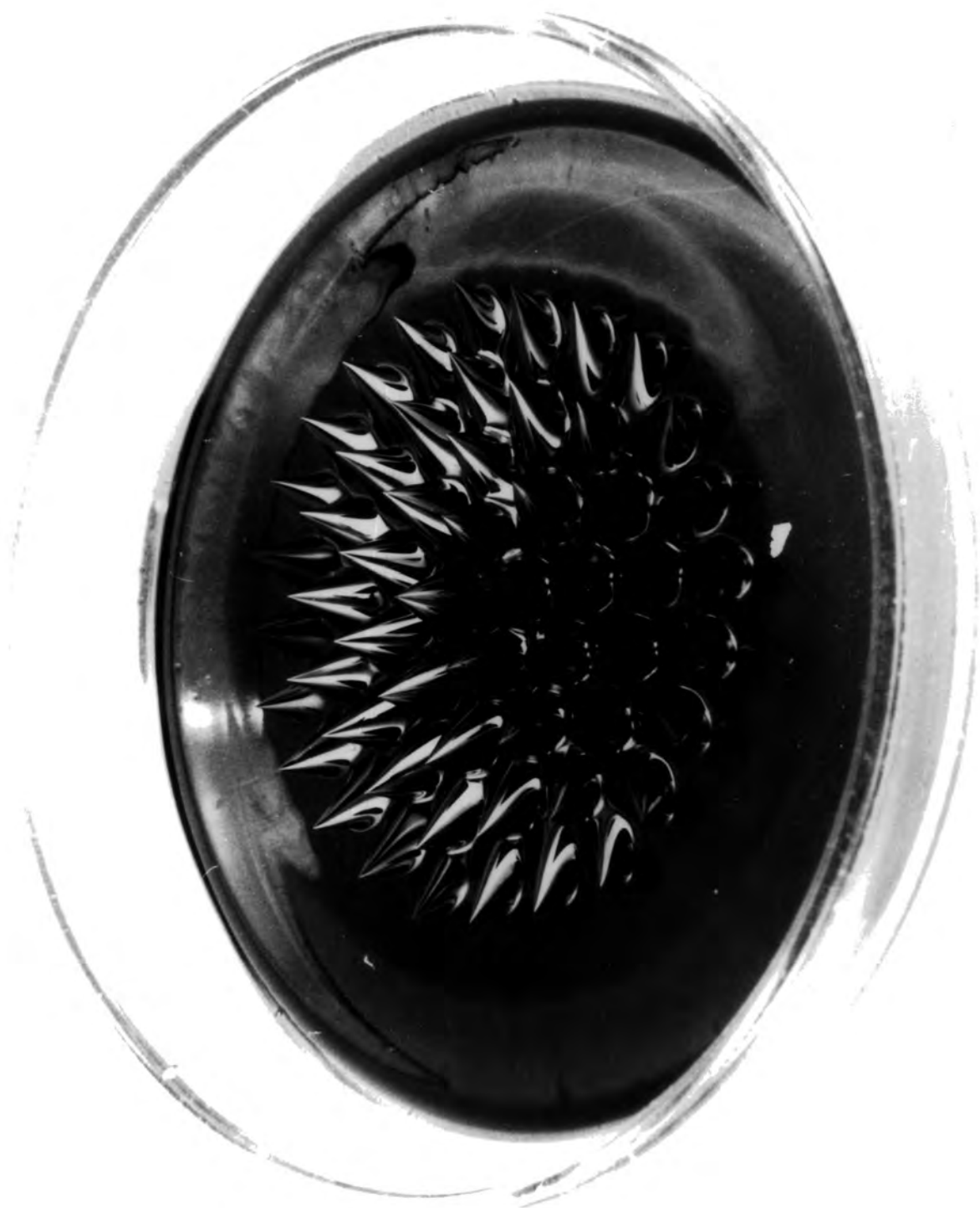
2.2 Preparative Routes

2.2.1 Non-metallic Particles

(a) Dispersion Techniques

Mechanical fragmentation of coarse material is accomplished by ball-milling. The grinding takes place in a dispersant/carrier liquid solution and may continue for several weeks. Centrifuging is then used to remove the larger particles. The particle material is usually magnetite (Fe_3O_4) or $\gamma\text{-}Fe_2O_3$ and a typical dispersant/carrier combination is Aerosol C61 in water. This method was first proposed by Papell (1963, 1965) and has been developed by Rosensweig and co-workers (Rosenweig et al., 1965, Kaiser and Rosensweig 1969, Kaiser and Miskolczy 1970). Commercial manufacture of magnetic fluids by the Ferrofluidics Corporation utilises this technique.

Refinements to the process were introduced by Khalafalla and Reimer (1973) and Rosensweig (1975). The former reduced grinding time by using an antiferromagnetic material (wustite) during grinding and then converting it to a magnetic form by refluxing. Rosensweig found that by removing the dispersant from a fluid prepared as above, drying the then flocculated particles and redispersing them into another dispersant/carrier solution, fluids with larger saturation magnetizations and lower viscosities could be obtained. Commercially prepared magnetic fluids have saturation magnetizations in the range 8-48 $JT^{-1}kg^{-1}$

(100-600G). Particle sizes are usually about 10nm. Typical

carrier liquids are water, light mineral oil, kerosene or

silicate esters. Grinding techniques lead to broad particle

size distributions which are well represented by the

log-normal distribution (see Chapter 4).

(b) Condensation Techniques

The essence of these methods is precipitation from

solution. Elmore (1938a,b) first prepared a colloidal

magnetite suspension by adding NaOH to a solution of Fe^{2+}/Fe^{3+}

ions and peptizing the precipitate with HCl. Larger

particles may be removed by centrifuging before the smaller

particles are dispersed by ball-milling or boiling with a

surfactant such as oleic acid. By varying the rate of

change of pH or by simultaneous addition of hydroxide and

ion solutions to warm water, the particle size may be

varied. (A. Wooding priv. comm.). The preparation of

β-FeOOH particles by these methods and their subsequent

conversion to γ-Fe_2O_3 is an important technique in the

magnetic media industry. Smaller particle sizes than those

obtained by ball-milling are achieved, typically around 8nm.

Although the initial preparation is in aqueous solution, the

particles may be filtered, washed, dried and redispersed

into other carrier lqiuids, for example petroleum ether.

The texture studies reported in Chapter 5 were carried

out on materials prepared by this technique.

2.2.2 Metallic Particles

Fine metallic particles are prepared almost exclusively

by condensation techniques. Although there are many methods available, e.g. inert gas evaporation (Kusaka et al., 1969), elecrodeposition in two-layer bath (Myalkovskii et al. 1984), electroless plating techniques (Akimoto et al., 1972) and spark erosion (Berkowitz and Walker 1983), only two have been extensively used to prepare particles for magnetic fluids. These are electrodeposition and organometallic decomposition and are described below.

(a)   Electrodeposition into Mercury

This technique has its origins in permanent magnet research in the 1950's when it was used to prepare elongated single particles (ESD) of Fe (Mayer and Vogt 1952) Ni (Mieklejohn 1958), Co (Deryugin and Sigel 1962), Fe/Co (Luborsky and Paine 1960), Ni/Co (Falk and Hooper 1961).

Salts of the required metals, dissolved in water or alcohol, are reduced and deposited into a liquid metal cathode by passing a current through the solution. In order to obtain small spherical particles the cathode must be agitated by physical stirring and magnetic agitation with an AC field. Liquid metals other than mercury have been proposed as carriers, e.g. 'Ingas' an indium-gallium-tin alloy (Kagan, 1970).

The preparation of magnetic fluids by this method has been pursued by Shepherd et al., (1971, 1972), Hoon (1978, 1979, 1980) and Popplewell et al., (1976, 1980). Mercury based fluids are prone to aggregation (Hoon 1980) due to the absence of a completely satisfactory dispersant.

(b) <u>Organometallic Decomposition</u>

Thomas (1966) first prepared fine particles of metallic cobalt by the thermolysis of dicobalt octacarbonyl, $Co_2(CO)_8$, in the presence of dispersants. This work was extended by Hess and Parker (1966) who studied a range of polymer dispersants. It has since been expanded to include Fe particles (Griffiths et al., 1979, Smith and Wychick 1980, Kilner et al., 1984 and this thesis), Ni particles (Hoon et al. 1983 and this study) and to the mixed metal systems, Fe-Co and Fe-Ni reported herein (Lambrick et al., 1985, 1986).

In common with many other organometallic compounds dicobalt octacarbonyl decomposes to the metal when heated above its critical temperature. The use of Ni and Fe carbonyls to prepare NiFe films was proposed by Edelman in 1958. Thomas discovered that in the presence of polymer dispersants, fine particles formed rather than a thin film of the metal. In his original work and that of Hess and Parker, use was made of polymers of vinyl pyrolidine or vinyl chloride-vinyl acetate as dispersants. These have now been superseded by commercial surfactants (R.W. Chantrell, 1977, K. O'Grady 1982 and this work) such as Sarkosyl (Ciba-Geigy), Duomeen-TDO (Akzo-Chemie) or Solsperse 3000 (ICI). (See Section 2.3.1 B(i)).

Figure 2.2 shows the experimental apparatus used by N. Mason in the Department of Chemistry, Durham University, to prepare the fluids studied in this thesis. The carrier

Stirrer
Motor

Bubbler

Stirrer
Seal

Condensor

N$_2$

Adapted
Shlenk Tube

Heating
Bath

Paddle

Jack
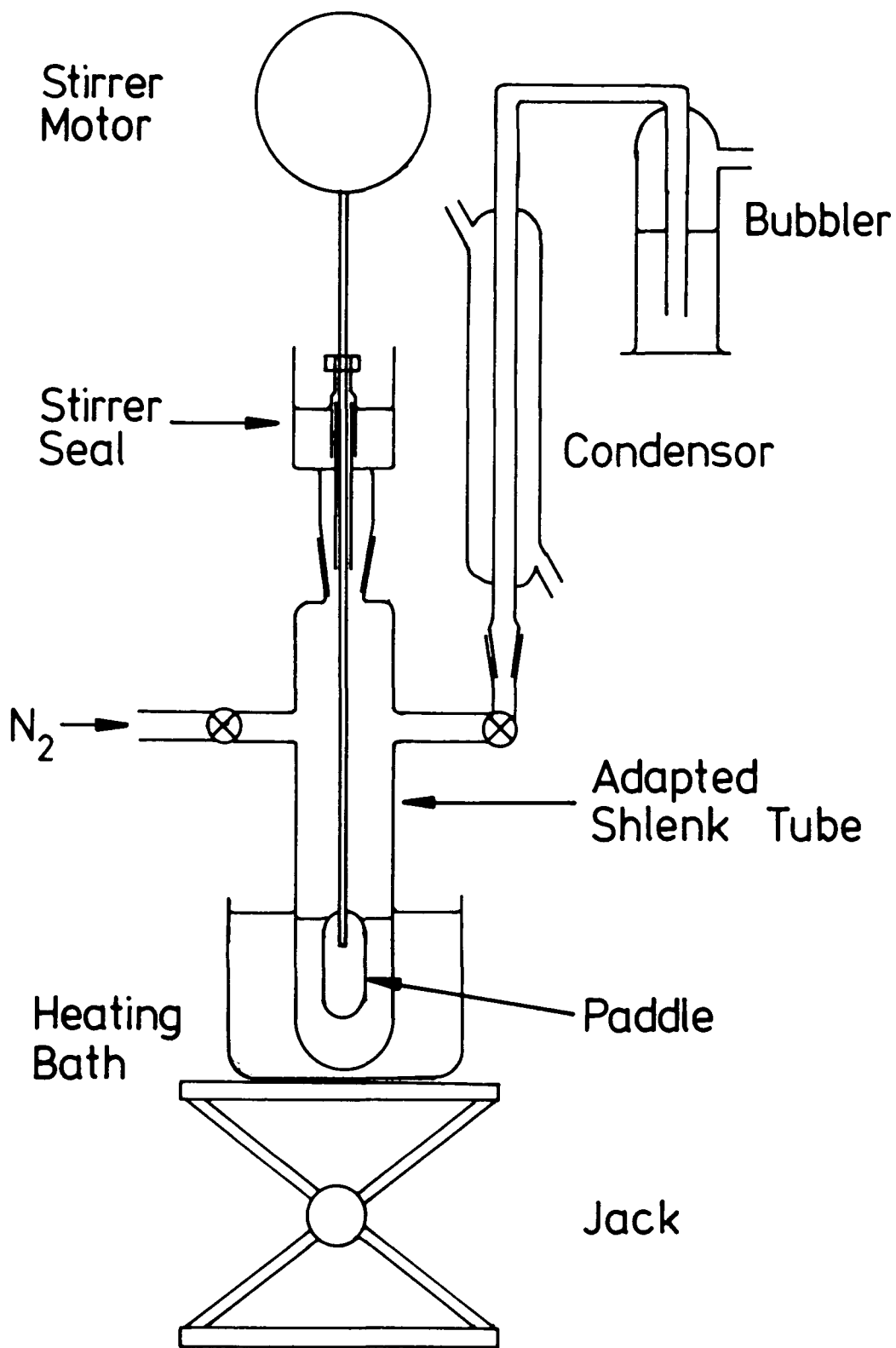
FIGURE 2.2
Fluid preparation apparatus used by
N.Mason (Chemistry Dept.,Durham
University) to prepare the fluids
for this study.

liquid, usually toluene (CH-⟨_⟩), is dried with sodium
wire and the surfactant dissolved into it. This solution is
then degassed and placed into the adapted Schlenk tube. The
apparatus is purged with dried N_2 before the carbonyl is
introduced. The mixture is then stirred for about ½ hour
before the preheated oil or metal bath is raised and
thermolysis begun. Heating is continued for approximately
1-3 hours after which the resulting black fluid is removed
and stored under N_2. Some typical quantities are shown in
Table 2.1.

Unlike dicobalt octacarbonyl which may be purchased,
the precursors used to prepare the FeCo, FeNi and some of
the Fe and Ni systems had first to be prepared. These
systems were not simple carbonyls, as the cyclopentadiene
ligand, (π-C_5H_5) was also present, e.g. (π-C_5H_5)Fe(CO)$_2$
Co(CO)$_4$. Mason (1986) describes details of their
preparations and those of the fluids themselves.

The chemistry of particle formation has been
investigated by Papirer et al., (1983) and Smith and Wychick
(1980). Their results imply that the process is complex,
involving the formation of intermediate higher order (that
is a larger number of metal atoms) carbonyls and
surfactant-metal complexes which act as nucleation sites for
particle growth. The mechanism is not completely
understood.

Decomposition by Ultra-Violet light was used by Hoon
et al. (1983) to prepare Ni systems. The other carbonyls

Fluid	Surfactant	Carrier	Mass of Complex (g)	Mass of Surf. (g)	Vol. Carrier liquid (cm^3)	Metal Bath Temp. °C	Heating Time hrs
NiFe3	Manoxol OT	1-M-N	0.7018	0.4542	10	170	3
FeCo2	Solsperse	Toluene	1.4973	1.4962	10	130	2
MK34	Duomeen-TDO	Toluene	3.5	0.69	10	130	3

1-M-N = 1-methyl-napthalene

Manoxol OT = Dioctyl sulphosuccinate, sodium salt

Sarkosyl O = N-methyl-N-(1-oxo)-9-octadecenyl glycine

TABLE 2.1
Typical preparation details

are not as susceptible as Ni(CO)$_4$ to UV decomposition and the technique has not been pursued.

General features of the organometallic route are the small particle sizes and their narrow distribution. Particle sizes are usually in the range 4-10nm and standard deviations of ~1nm have been obtained consistently during this study from electron microscopy data. Although the vapour pressure of toluene renders it impractical for commercial use, O'Grady (1982) has reported the successful transfer of fine particles of Co from toluene to diffusion pump oil. Other carrier liquids such as 1-methyl-napthalene and petroleum ether have been used to prepare fluids at Durham. Metallic systems should be capable of much higher saturation magnetizations than oxide systems and O'Grady (1982) prepared Co fluids with magnetizations of 10-24 JT^{-1} kg^{-1} (150-300G) comparable with commercial oxide systems. In this study, the incorporation of large quantities of the metals has been secondary to the preparation of new materials and routes and thus typical saturation magnetizations are 0.5 - 2.5 $JT^{-1}kg^{-1}$(5-30G). The viscosities (zero field) and densities of these fluids are comparable to those of their carrier liquids.

2.3 Colloidal Properties

2.3.1 Stability Considerations

Colloids may be defined (Kruyt 1952) as dispersions in which one substance has at least one dimension lying in the

range 1nm - 1μm. They fall between small molecule solutions
and coarse suspensions. Molecules which are large enough
(e.g. proteins, polymers) and which are in true solution
also fall into the colloidal category and are known as
lyophilic ("solvent-loving") colloids. They are
thermodynamically stable in the sense that they are in
equilibrium with minimum free energy. Lyophobic
("solvent-hating") colloids are not stable in this respect
as the free energy associated with the surface area of the
particles could be reduced by combining them into a single
large particle. However, the time taken for a lyophobic
system to reach its minimum free energy state can be vastly
greater (~ years) than the time over which it is observed.

The principal stability consideration for lyophobic
colloids such as magnetic fluids is the rate at which
particles aggregate and sediment out. This is most
conveniently discussed with the aid of a qualitative
representation of the interaction energy between two
particles. This net energy is the result of various
attractive and repulsive terms which are outlined below and
is shown in Figure 2.3. Particles are constantly being
brought together by Brownian motion with an energy of the
order of kT. The stability of the colloid depends on the
energy of the barrier B. If E_b < kT then the particles will
fall into the primary well and aggregate irreversibly. Of
course the particles cannot approach indefinitely and
eventually Born repulsion (due to overlap of electron

Steric Repulsion

NET

Secondary Well

E_b

v.d. Waals attraction

Magnetic attraction

Potential Energy

Surface Separation
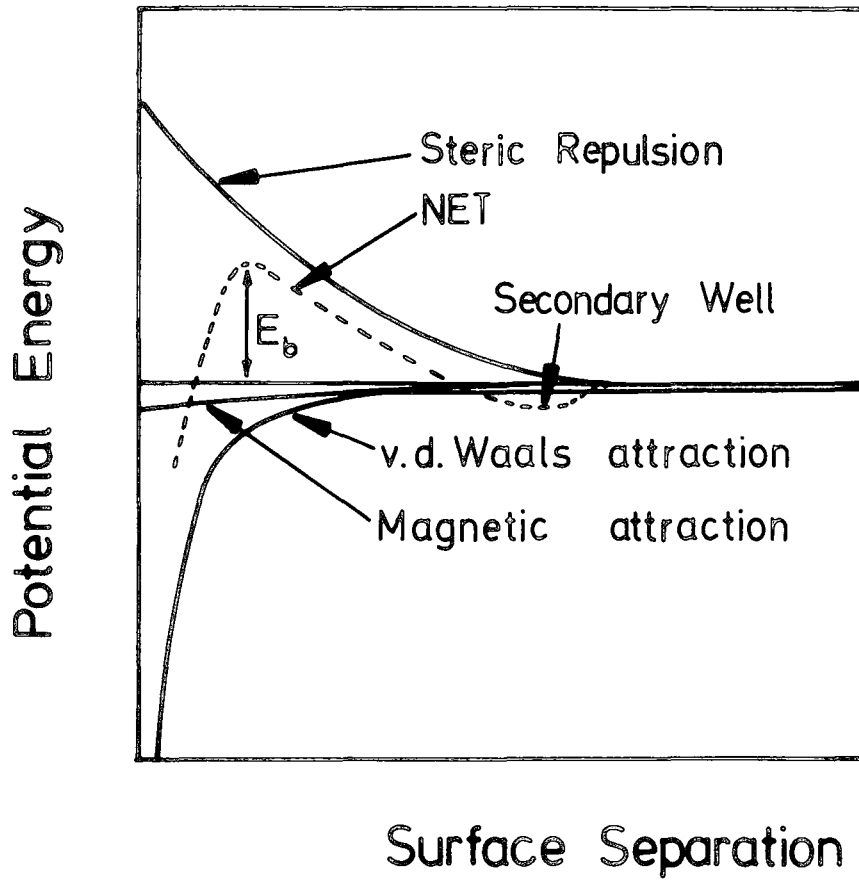
FIGURE 2.3
Schematic representation of the
potential energy between two
particles in a magnetic fluid.

clouds) keeps the particles separate. However, long before
such small separations are reached the particles will have
sedimented, destroying the colloid. The secondary well
which exists in lyophobic colloids (Kruyt 1952) is usually <
kT and represents reversible flocculations explaining
properties like thixotropy. At infinite separation the
interaction energy must tend to zero. For a colloid to be
stable over a long period, the energy barrier E_b must be
large (>> kT).

The attractive and repulsive component energies in
magnetic fluids are now discussed. The most important
repulsive term in the majority of lyophobic colloids is
electrostatic repulsion due to the double charge layer at
the particle surface. This is not present in the magnetic
fluids of this study as they had non-polar carrier liquids
and so is not discussed.

A. Attractive Forces

(i) Molecular Dispersion Forces

Neutral atoms or molecules with permanent electric
dipole moments may attract one another via the induction
(Debye 1920) or orientation (Keesom 1921) effects. Wang
(1927) showed that attractive forces may also exist between
neutral, non-polar atoms and London (1930a,b, 1937,
Eisenschitz and London 1930) formalised this theory of
dispersion forces. Israelachvili and Tabor (1973) state
that dispersion forces may be thought of as
quantum-mechanical induction forces. Metallic particles in

non-polar media are neutral and do not possess appreciable permanent electric moments and so the molecular forces between them must be ascribed to dispersion effects.

Instantaneous dipoles are produced by rapid fluctuations (zero-point motion) of the electron charge distribution in molecules. These dipoles propagate synchronized electric fields which induce dipoles in nearby polarizable molecules which are in phase with the generating fluctuations if the molecules are sufficiently close. London treated the molecules as isotropic harmonic oscillators and derived a formula for the interaction energy between two molecules which, for molecules characterized by a single oscillator frequency, may be written in terms of the static polarizability, $\alpha_i = \alpha_i(0) = \frac{2p_i^2}{3h\nu_i}$, as;

$$U_{12} = -\left(\frac{1}{4\pi\varepsilon_0}\right)^2 \frac{3h}{2R^6} \alpha_1 \alpha_2 \frac{\nu_1 \nu_2}{\nu_1 + \nu_2} = \frac{-C_{12}}{R^6} \qquad (2\cdot1)$$

where ν_i is the characteristic frequency of atom i and p its electric dipole moment at that frequency. C_{12} is the London constant and the molecules are assumed to be in vacuo.

Casimir and Polder (1948) have shown that when the molecule separation is greater than $\lambda_i/2$, where λ_i is the characteristic absorption wavelength of atom i, the phase coherence between induced and inducing dipoles is lost and the interaction energy becomes;

$$U_{12} = -\left(\frac{1}{4\pi\varepsilon_0}\right)^2 \frac{23}{4\pi} \hbar c \frac{\alpha_1 \alpha_2}{R^7} = -K_{12}/R^7 \qquad (2\cdot2)$$

the molecular forces are said to be retarded at these separations.

McLachlan (1963a,b, 1965) derived an expression for the interaction between two atom/molecules in the presence of a third medium which for non-retarded forces is

$$U_{12} = -\left(\frac{1}{4\pi\varepsilon_0}\right)^2 \frac{3\hbar}{\pi R^6} \int_0^\infty \frac{\alpha_1^0 \alpha_2^a}{\varepsilon_3^2} \, d\xi \qquad (2\cdot3)$$

where α_i^* and ε_3 are functions of the complex frequency $i\xi$, α_i^* is the polarizability of atom i in medium 3 and ε_3 is the dielectric constant of medium 3. McLachlan also showed that at finite temperatures there is a temperature dependent term in the total interaction energy.

For particles which are composed of many atoms, the total energy may be calculated by microscopic or macroscopic means. For small particles whose separation is much larger than their radii , their polarizabilities may be calculated by a continuum method (Strattan 1941) and then inserted into the microscopic equation (2.3) giving the expression

$$U_{12} = -\left(\frac{1}{4\pi\varepsilon_0}\right)^2 \frac{3\hbar r_1^3 r_2^3}{\pi R^6} \int_0^\infty \frac{(\varepsilon_1-\varepsilon_3)(\varepsilon_2-\varepsilon_3)}{(\varepsilon_1+2\varepsilon_3)(\varepsilon_2+2\varepsilon_3)} \, d\xi \qquad r \gg R \quad (2\cdot4)$$

where $\varepsilon_j = \varepsilon_j(i\xi)$ = dielectric constants of particles (j = 1,2) or medium (j = 3). For large particles, the microscopic approach involves adding pairwise the interaction between the atoms in each body (Hamaker 1937). Altenatively, Lifschitz (1956) and Langbein (1969, 1971) approach the problem using the macroscopic dielectric function of the materials. Both of these approaches lead to

expressions which may be written

$$U_{12} = -\frac{A_{132}\, r_1\, r_2}{6R\,(r_1 + r_2)}$$

(2·5)

where A_{132} is the Hamaker constant which is $\pi n_1 n_2 C_{12}$ in the microscopic case (n_i = no. of polarizable atoms) and r_i are the radii of the spherical particles. From the macroscopic approach

$$A \doteq \frac{3\hbar}{4\pi} \left(\frac{1}{4\pi\varepsilon_0}\right)^2 \int_0^\infty \sum_{n=1}^\infty \frac{1}{n^3} \left(\frac{\varepsilon_1 - \varepsilon_3}{\varepsilon_1 + \varepsilon_3}\right)^n \left(\frac{\varepsilon_2 - \varepsilon_3}{\varepsilon_2 + \varepsilon_3}\right)^n d\xi$$

(2·6)

from which it may be seen that for identical particles ($\varepsilon_1 = \varepsilon_2$), A > 0 and the dispersion forces are always attractive. Langbein also considered the case of two coated particles and obtained an approximate expression which to first order retains the 1/R dependence.

At separations of ~0.4nm or less the dispersion forces are superseded by exchange forces. Fluctuating magnetic moments and higher order electric multipole moments contribute energies smaller by a factor of ~10^{-4} than the electric dipole term and hence may be ignored. Permanent magnetic moments are considered in the next section. The attractive molecular dispersion forces between two particles may be summarized;

$$U \propto \begin{cases} -\dfrac{1}{R} & 0\cdot4\,nm < R \ll r \\[4mm] -\dfrac{1}{R^6} & R \gg r \end{cases}$$

(2·7)

(ii) <u>Magnetic Forces</u>

Each particle in a magnetic fluid consists of a single magnetic domain and hence has a permanent magnetic dipole

moment. Assuming these to be point dipoles, the interaction

energy between two particles may be written

$$U_{12} = \left(\frac{\mu_0}{4\pi}\right)\left[\frac{(\underline{m}_1 \cdot \underline{m}_2) - 3(\underline{m}_1 \cdot \hat{\underline{R}})(\underline{m}_2 \cdot \hat{\underline{R}})}{R^3}\right] \qquad (2\cdot 8)$$

where $\underline{m}$ is magnetic moment and $\underline{R}$ is the vector joining

particle centres. With respect to colloidal stability we

are concerned with coagulation, that is particles coming

into irreversible contact. For two identical particles in

contact, the energy minimum given when $\underline{m}_1 \wedge \underline{m}_2 = 0$, is

$$U_{12} = -\left(\frac{\mu_0}{4\pi}\right)\frac{2 m_p^2}{8 r_p^3} = -\left(\frac{\mu_0}{4\pi}\right)\frac{m_p^2}{4 r_p^3} \qquad (2\cdot 9)$$

where r_p is the particle radius. Assuming the particle

moment is given by

$$m_p = v_p M_b^\infty \qquad (2\cdot 10)$$

where M_b^∞ is the bulk magnetization of the particle material

and v_p is particle volume, the energy becomes

$$U_{12} = -\left(\frac{\mu_0}{4\pi}\right)\frac{4}{9} M_b^{\infty 2}\pi^2 r^3 \qquad (2\cdot 11)$$

If this is to be overcome by thermal energy, we may

define a critical radius by

$$r_c = \left(\frac{9kT}{\mu_0 \pi M_b^{\infty 2}}\right)^{\frac{1}{3}} \qquad (2\cdot 12)$$

At 300K, $M_b^\infty = 1.6 \times 10^6$ $JT^{-1}m^{-3}$ (approx. Fe or Co) this

gives $r \sim 1.5nm$ whilst for $M_b^\infty = 0.4 \times 10^6$ $JT^{-1}m^{-3}$ (Ni,

Fe_3O_4) $r \sim 3.9nm$. This energy would increase by a factor

of 20 if one of the particles radius was doubled. Thus the

effect of a few large particles in a magnetic fluid will be

to seed aggregation. For systems with the mean particle
radius < r_c, aggregations will be due to molecular
dispersion forces. Decreasing temperature has the effect of
reducing the critical radius and will enhance aggregate
formation. Particles coated with surfactants cannot come
into contact and so the critical radius may be greater than
r_c above. It should also be noted that this equation refers
to the "magnetic size" of the particle which is usually
smaller than the physical size.

B. Repulsive Forces

Metallic particles in non-polar solvents cannot be
stabilized by electric double layers as particles in aqueous
solvents (Massart 1981) and Faraday (Au/H_2O) sols may be.
These are very sensitive to ionic concentration/pH and can
be sedimented and by adding very small quantities of
electrolyte. The systems described herein required steric
barriers to achieve stability which were provided by surface
active agents.

(i) Surfactants

Surface active agents (surfactants, SAA's) are
substances which absorb onto the interfaces of a system and
alter the interfacial free energy considerably even when
present in small concentrations. The interfacial free
energy is usually reduced by surfactants which act as
detergents, emulsifiers, foamers, wetters and dispersants.

To act as a surfactant a molecule has to be
amphipathic, i.e. consist of two parts; a lyophobic group

which concentrates at the interface and lyophilic group which remains in the solvent. Whether a particular molecular group will act as lyophobic or lyophilic depends on the solvent and the conditions (temp., pH) of use. Surfactants usually consist of a long hydrocarbon chain with an active group at one end. There are four types:-

(i)   Anionic - the active head is negatively charged,

$$e.g. \quad R - \overset{\overset{\textstyle O}{\|}}{C} - O^- \ Na^+ \ (soaps).$$
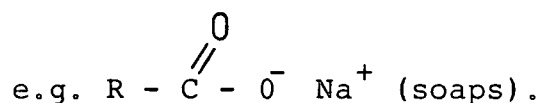
(ii) Cationic -the active head is positively charged,

$$e.g. \quad R - NH_3^+ \ Cl^- \ (amine \ salts)$$
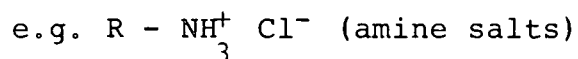
(iii)Zwitterionic -there are both positively and negatively

charged groups on the chain,

$$e.g. \quad R - NH_2^+ - CH_2 - COO^- \ (amino$$

acids)
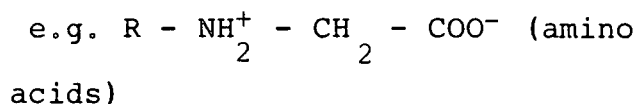
(iv)   Non-ionic -no charged groups

$$e.g. \quad RCOOCH_2CHOHCH_2OH \ (monoglyceride$$

of fatty acid)
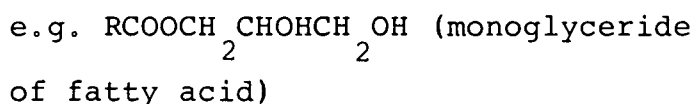
A surfactant which has been found most useful in preparing the fluids in this study is Duomeen-TDO (Akzo-Chemie) a long chain alkyl propylene diamine dioleate

$$R - NH_2 - CH_2 - CH_2 - CH_2 - NH_3^{++} \quad 2(C_{17}H_{33}COO)^-$$

and is a cationic surfactant.
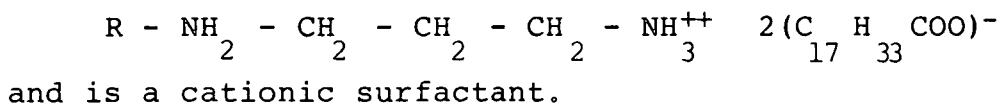
The behaviour of surfactants in non-polar media is not clearly understood. Metal salts may form complexes with metallic surfaces (Black 1969). The role of surfactants in the thermal decomposition of organometallics is not just to

stabilize the particles, they also act to catalyse and nucleate particle growth. Surfactants provide repulsive forces via the interactions of the long chains extending from the particle surface (see Figure 1.1). Two repulsion mechanisms are thought to act and are outlined below.

(ii) Entropic (Steric) Repulsion

Consider two particles, coated with long chain surfactants whose "head" group is firmly attached to the particle and whose "tail" is free to move in the carrier liquid. As the particles approach and the tails begin to occupy the same volume, the possible configurations each tail may adopt becomes severely restricted. To overcome this loss of entropy, energy must be supplied and this is equivalent to a repulsive force between the particles. Mackor (1951) adopted a statistical approach, treating the long chain "tails" as rigid rods attached by a ball joint to the particle. Scholten (1978) obtained a simple expression for this entropic energy

$$U_S = \frac{2}{3} \pi \Gamma k T \left(\delta - \frac{x}{2} \right)^2 \left(1 \cdot 5 d + 2 \delta + \frac{x}{2} \right) / \delta \qquad (2 \cdot 13)$$

by considering the reductions in volume available to the tails and applying the ideal gas law. Here (see Figure 2.4a) δ = thickness of surfactant layer (length of chains), x = distance between particle surfaces, Γ = surface density of surfactant molecules. For δ = 2nm, Γ = $10^{15}\,m^{-2}$ this provides repulsive energies of ~ 20kT for x~2nm. This is more than sufficient to stabilize against the attractive
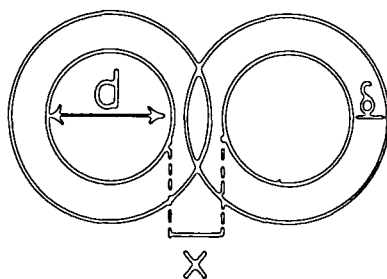
(a)
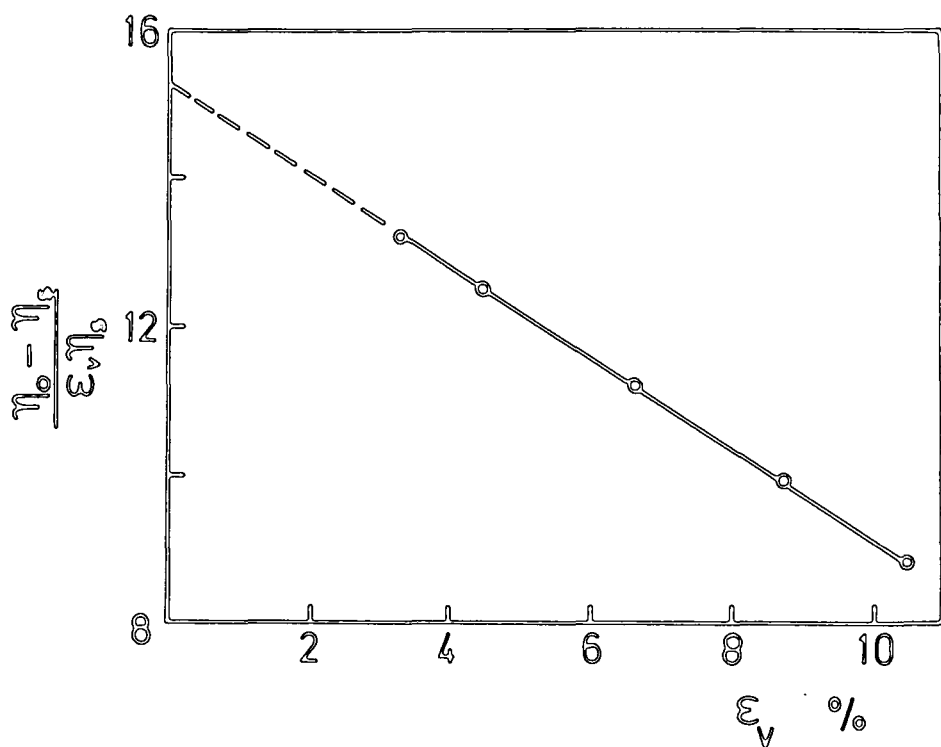
(b)

FIGURE 2.4
(a) Surfactant layer on particle
    surface. (Eqn. 2.13)
(b) Viscosity of a magnetic fluid
    taking surfactant layer into
    account. (Rosensweig etal 1965)

forces.

(iii) Enthalpic Repulsion

If the long chain tails have an exothermic heat of
solution in the carrier liquid, then on approach of the two
particles, the local increase in chain concentrations will
require energy. (Bagchi 1972). This again is equivalent to
a repulsive energy. Bagchi estimates that this energy is an
order of magnitude smaller than the entropic term and so not
a major contributor to repulsive energy.

The various attractive and repulsive energies are shown
as solid lines in Figure 2.3. They sum to total energies
of the form of the dotted line. Stable colloids require
large energy barriers. Stability in magnetic fields is
considered in Section 2.4.1.

2.3.2 Rheological Properties

Einstein (1920, 1906) provided a basis for the
discussion of the viscosity of colloids. Assuming
incompressibility, no slipping, turbulence or inertia
effects, he derived an expression for the viscosity of a
dilute suspension of rigid spheres

$$\eta_s = \eta_o (1 + 2 \cdot 5 \phi) \qquad (2 \cdot 14)$$

where η_o is the viscosity of the suspending medium and ϕ is
the volume fraction of the solid phase. This equation is
valid for $\phi < 0.01$ and non-interacting particles. At higher
concentrations, terms in ϕ^2 or higher must be added to the
bracketed term. For non-spherical particles, Simha (1949,

1950) has shown that viscosity may be written

$$\eta_s = \eta_o (1 + a\phi + k_1 a^2 \phi^2 \ldots)$$
(2·15)

where the k_i are the numerical factors depending on the axial ratios of the particles. Eirich et al. (1936) found that the k_i did not depend on the size or concentration of the particles. Vand (1948) found empirically

$$\eta_s = \eta_o (1 + 2\cdot 5\phi + 7\cdot 17 k_1 \phi^2 + \ldots)$$
(2·16)

whereas Eirich obtained $8k_1 \phi^2$. In the case of coated particles, the coating increases the size of the particle and must be taken into account. After de Bruyn (1949), Rosensweig et al. (1965) obtained an expression for particles of radius r, whose uncoated volume fraction is ε and coating thickness δ

$$\frac{\eta_s - \eta_o}{\varepsilon \eta_s} = 2\cdot 5 \left(1 + \frac{\delta}{r}\right)^3 - \left(\frac{2\cdot 5\phi_c - 1}{\phi_c^2}\right) \left(1 + \frac{\delta}{r}\right)^6 \varepsilon$$
(2·17)

which they verified (Figure 2.4b) for ferrite particles coated with oleic acid. They point out that to reduce the viscosity of a fluid, at fixed ε, δ/r must be reduced.

Weser and Stierstadt (1985) point out that the presence of excess surfactant in the carrier liquid requires η_o to be replaced with η_o' which includes the effect of this surfactant. They also correct ϕ to include particles which may be too small to be detected magnetically when ϕ is

determined. The viscosity of magnetic fluids in the
presence of a magnetic fluid is discussed in 2.4.2.

2.3.3 Optical Behaviour

Characteristic optical behaviour in colloid systems are
Tyndall scattering, double refraction and dichroism.
Tyndall scattering (Rayleigh scattering) is not observed in
the concentrated mangetic fluids studied herein and they are
black. Double refraction and dichroism are usually induced
in colloids by external means, e.g. V_2O_5 sols become doubly
refracting when set in laminar flow. Both of these
properties are present in magnetic fluids subjected to
applied magnetic fields and are discussed in Section 2.4.3.

2.3.4 Gravitational and Diffusional Phenomena

Suspensions of solid material in a liquid will be
subject to diffusional and gravitational forces. The
diffusion constant for spherical particles may be written

$$D = \frac{kT}{6\pi\eta r} \qquad (2 \cdot 18)$$

where r is the radius of the particle. The criterion for
colloidal stability in a gravitatinal field is

$$kT > m^* gh \qquad (2 \cdot 19)$$

where $m^* = \frac{4}{3}\pi r^3 \Delta\rho$ and $\Delta\rho = |\rho_p - \rho_l|$, ρ_p = density of particles.
This defines a critical radius, r_c, for stability against
settling in the gravitational field. The radius, r, must be
less than r_c, where

$$r_c = \left(\frac{kT}{gh} \cdot \frac{3}{4\pi} \cdot \frac{1}{\Delta\rho} \right)^{\frac{1}{3}} \qquad (2 \cdot 20)$$

Shliomis (1974) equates the Brownian velocity and Stokes settling velocity to obtain an upper limit for the particle radius,

$$r_< \lesssim \left(\frac{\eta^2 kT}{\rho_p (\Delta\rho)^2 g^2} \right)^{\frac{1}{7}} \qquad (2\cdot21)$$

For Fe particles in toluene at 300K this implies a radius of $1.7\mu m$. Note that cooling the system reduces the critical radius.

Even if the above criterion is satisfied, the gravitational field will induce a variation in the height distribution of particle sizes. Shliomis gives this as

$$n(h) \simeq \exp\left[\frac{-(\Delta\rho) v_p gh}{kT}\right] \qquad (2\cdot22)$$

If $\Delta\rho = 8000$ kgm^{-3}, $T = 300K$ and $r = 10$nm then this implies a maximum height of ~ 0.01m for there to be no discernible concentration gradient across it. It should be noted that the time taken to establish equilibrium may be large thus allowing this maximum height to be much greater. This time may be estimated as $t' \sim h^2/D$ where D is the diffusional constant (Shliomis 1974) and for the figures quoted above may be several weeks. Magnetic field gradients will be considered in 2.4.4.

2.4 Magneto-Colloidal Properties

2.4.1 Stability in Magnetic Fields

(a) Uniform Field

A uniform magnetic field applied to a magnetic fluid

will tend to align the particle dipole moments. As the

magnetostatic energy is a minimum for collinear moments

(equation 2.9) this will promote aggregation. This effect

is analogous to decreasing the temperature in equation 2.12.

This enhancement of the magnetostatic interaction promotes

the formation of chains and clusters. De Gennes and Pincus

(1970) found that the application of an external magnetic

field will induce chain and ring (flux closure) structures

in very dilute magnetic fluids. They did not take molecular

dispersion forces or steric repulsion into account. More

recently Menear et al. (1984) have developed a Monte-Carlo

computer model for monodisperse two dimensional systems.

They take entropic repulsion into account and include

magnetic interactions over a range of 5 particle diameters,

long range interactions being approximated by a uniform

magnetization. Their results are valid for fluids within

ellipsoidal holders. They find, for 2.5nm radii particles,

a tendency towards dimer formation even in zero applied

field. For 3.75nm radii particles in a 0.5T applied field

they obtain strong chain formation as illustrated in Figure

2.5a. They also find a limited increase in the average

interaction energy for particles in a magnetic field. For r

= 3.75nm cobalt particles this increase in attraction

between particles is small. The field induced agglomeration

observed by Peterson (1977), Krueger (1980) and Hayes (1975,

1977) was on systems with much larger particles.

Bradbury et al. (1986) have extended this work to
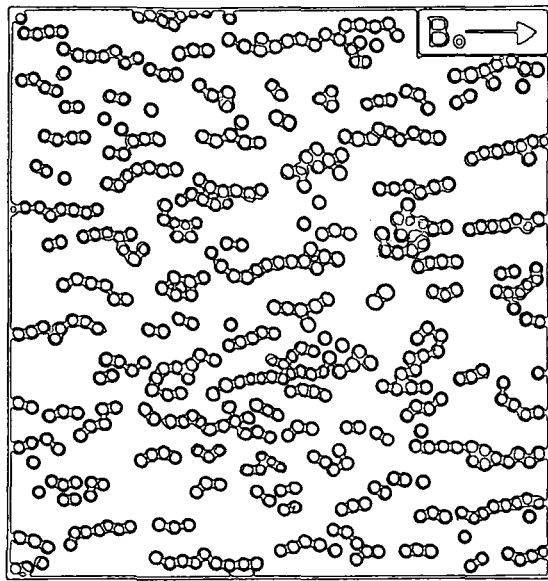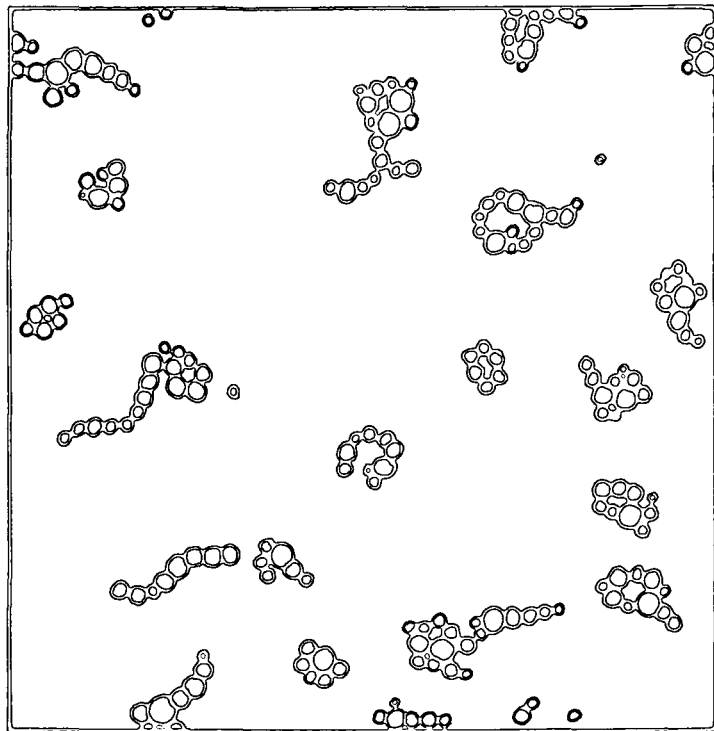
FIGURE 2.5
(a) Chain formation for 3.75nm
    Co particles in 0.5T.
    (2-D computer model Menear
    etal 1984)
(b) Aggregation induced by larger
    particles in zero field.
    (Bradbury etal 1986)

include a particle size distribution. For median particle diameters of 5nm of cobalt they observe some short range ordering involving the larger particles even in zero applied field. As the median diameter is increased they find that the larger particles seed aggegation. In an applied field of 0.5T they find that a system with 5nm median diameter exhibits chaining (anisotropy) in the field direction. For median diameter = 15nm in zero field they find that almost all the particles are already in aggregates (Figure 2.5b).

(b)   Non-uniform field

A magnetic moment $\underline{m}_p$ in a field gradient $\nabla \underline{B}_o$ will experience a force given by

$$\underline{F}_m = \underline{m}_p \cdot \nabla \underline{B}_o \qquad (2 \cdot 23)$$

If $\underline{m}_p = v_p \underline{M}_b^\infty$ and equating the magnetic force $\underline{F}_m$ to the Stokes force $\underline{F}_s = 6\pi\eta r \underline{u}$ we obtain the terminal velocity for the particle as

$$\underline{u} = \frac{2 r_p^3 M_b^\infty \nabla \underline{B}_o}{3\eta} \qquad (2 \cdot 24)$$

Rosensweig et al. (1965) point out that the creation of a concentration gradient, ∇n, will be opposed by diffusion of particles against it. The flux of particles along the magnetic field gradient, $N_m = n|\underline{u}|$ where n = number concentration, will in equilibrium be equal to the diffusional flux $N_D = - D\nabla n$. The particle radius is then

$$r^3 = \frac{3}{4\pi} \frac{kT}{M_b^\infty \nabla B_o} \frac{\nabla n}{n} \qquad (2 \cdot 25)$$

As a criterion for stability against settling out, ∇n /n may be taken as 0.01 m^{-1} (i.e. 100% change in concentration over 1cm) and for ferrite particles with diameters of 2-20nm, field gradients of 1-100 Tm^{-1} can be withstood. For metallic particles these diameters have to be reduced by factors of $\frac{1}{2}$ to $\frac{1}{3}$ to be stable in the same gradients.

Shliomis (1974) notes that the ratio of magnetic force $v_p M_b^\infty |\nabla \underline{B}_o|$ to Archimedean force $\nabla \rho v_p g$ is independent of particle size. Magnetic forces will dominate when $|\nabla \underline{B}_o| >$ $g\Delta \rho / M_b^\infty$.

2.4.2 Magnetoviscosity

In the presence of a magnetic field, the rotational motion of ferromagnetic particles is constrained. Einstein's formula (2.14) is valid only when the rotational velocity, $\underline{\omega}$, of the particles coincides with the local angular velocity or vorticity, $\underline{\Omega}$, of the carrier liquid. When a magnetic fluid is placed in a magnetic field, partial alignment of the particle moments occurs, each particle experiencing a torque, $\underline{\tau} = \underline{m}_p \wedge \underline{B}_o$ If $\underline{B}_o$ is not parallel to $\underline{\Omega}$, this will hinder the rotation of the particle within the carrier and increase the viscosity.

Hall and Busenberg (1969) consider a dilute magnetic suspension ignoring Brownian effects and obtain the viscosity as

$$\eta_s = \eta_o (1 + 2 \cdot 5 \phi + 1 \cdot 5 \phi \sin^2 \alpha_s) \qquad (2 \cdot 26)$$

where $\sin^2 \alpha_s$ is given by

$$\sin^2 \alpha_s = \frac{1}{2}\left[1 + \left(\frac{\mu m_p B_o}{\eta r_p^3 \kappa}\right)^2\right] - \left\{\frac{1}{4}\left[1 + \left(\frac{\mu m_p B_o}{\eta r_p^3 \kappa}\right)^2\right]^2\right.$$

$$\left. - \left(\frac{\mu m_p B_o}{4\pi \eta r_p^3 \kappa}\right)\sin^2 \gamma\right\}^{\frac{1}{2}} \qquad (2\cdot27)$$

where γ = angle between $\underline{B}_o$ and the axis of rotation, κ is
the velocity gradient and μ the permeability of the carrier
liquid. McTague (1969) found that the viscosity of a
magnetic fluid was increased by the presence of a magnetic
field. The increase was greater when the applied field was
parallel to the flow than when perpendicular, (see Figure
2.6). His results were broadly in line with the theory of
Hall and Busenberg but the rate of increase in viscosity
with applied field was not as rapid as the theory predicts.
This is due to the fact that it does not account for
Brownian motion. Shliomis (1972) takes Brownian motion into
account and obtains

$$\eta = \eta_o (1 + 2\cdot5\phi)\left(1 + \frac{3}{2}\phi \frac{b - \tanh b}{b + \tanh b} \sin^2 \alpha\right) \qquad (2\cdot28)$$

where $b = m_p B_o / kT$ and α is the angle between $\underline{\Omega}$ and $\underline{B}_o$. This
equation accounts for the experimentally observed fields of
0.1T required to reach saturation of the magnetoviscosity.
A similar analysis by Levi et al. (1973) provides the same
results. It should be noted that the size of particle in
this instance is the hydrodynamic size, i.e. metallic core
plus surfactant coating.

Weser and Stierstadt (1985) also examine the
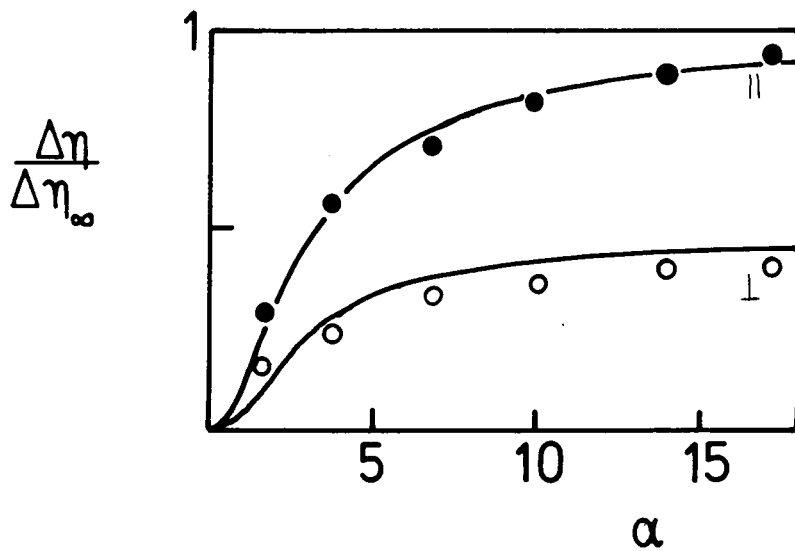
$$\alpha = \frac{mB_0}{kT}$$

FIGURE 2.6
Magnetoviscosity of a magnetic
fluid perpendicular and parallel
to the applied field. (McTague 1969)

magnetoviscosity of magnetic fluids using the Shliomis theory. They found it necessary to correct for interactions using a mean field $\underline{B}_{loc}$ in place of $\underline{B}_o$. They also correct for the presence of excess surfactant and find that the hydrodynamic particle size is smaller than the magnetic particle size plus surfactant length. This may be evidence for a magnetically "dead" layer at the particle surface, however as they do not obtain a physical size from electron microscopy this cannot be estimated. Viscosity measurements together with electron microscope measurements provide a means of calculating the surfactant thickness.

Particle interactions will also have an effect on the fluid viscosity but as yet this effect has not been quantified.

2.4.3 Optical Properties

The application of a magnetic field to a magnetic fluid induces optical anisotropy in the fluid. The two main effects are dichroism and birefringence (double refraction or Cotton-Mouton effect). Dichroism is an anisotropy in the absorption of light whilst birefringence is an anisotropy in the refractive index. Light with its electric vector parallel to the applied field is absorbed more strongly and has a larger refractive index than that with its vector perpendicular to the field. This anisotropy may be associated with orientation of individual particles or chaining of the particles. Dichroism and brirefringence has been observed in magnetic fluids by many workers, e.g.

Scholten (1975, 1980), Martinet (1978), Davies and Llewellyn
(1979a,b). Davies and Llewellyn (1979a) and Scholten
(1980) find that at low fields the difference in refractive
index parallel and perpendicular to the applied field, $\Delta n = |n_{11}$
$-n_\perp|$ varies linearly with $\underline{B}_O^2$, in accord with the
theoretical work of O'Konski et al. (1959). At higher
fields a Langevin type behaviour is found as also observed
by Scholten (1975). Scholten (1980) has shown that the form
of the variation of dichroism with applied field is the same
as that for birefringence. The work of Davies and Llewellyn
with pulsed fields and the decay of birefringence with time
suggested that birefringence is due to the alignment of
particle body (i.e. particles with blocked moments) with the
applied field. For small metallic cobalt particles in
toluene, Llewellyn (1983) has shown that the observed
dichroism and birefringence variation with wavelength
requires particle elongations of 1.3:1. As this is much
larger than any elongation observed by electron microscopy,
he concludes that particle chaining is responsible for the
optical effects as suggested by Scholten (1980). Davies and
Llewellyn (1980) have also observed Faraday rotation in
magnetic fluids. They also discuss the deviation of
magnetic and hydrodynamic particle sizes from birefringence
measurements which will be discussed in Chapter 4.

2.4.4 Ferrohydrodynamics

Ferrohydrodynamics is to be distinguished from
magnetohydrodynamics in that magnetic fluids are usually

good insulators so that there are no forces due to currents of free charge as in the latter.

A recent survey of ferrohydrodynamics has been given by Rosensweig (1985) who gives the set of continuum equations for magnetic fluids as:

$$\frac{\partial \rho}{\partial t} + \underline{\nabla}\cdot(\rho\underline{v}) = 0 \qquad (2\cdot29a)$$

$$\frac{\partial(\rho\underline{v})}{\partial t} + \underline{\nabla}\cdot(\rho\underline{v}.\underline{v}) = \underline{\nabla}.\underline{T} + \rho\underline{F} \qquad (2\cdot29b)$$

$$\frac{\partial(\rho\underline{s})}{\partial t} + \underline{\nabla}\cdot(\rho\underline{v}.\underline{s}) = \underline{\nabla}.\underline{C} + \underline{A} + \rho\underline{G} \qquad (2\cdot29c)$$

where the first two equations are the same as those in ordinary fluid mechanics and represent conservation of mass and momentum balance respectively. The third equation represents angular momentum balance where ρ is the fluid mass density, $\underline{v}$ velocity, $\underline{s}$ spin angular momentum (p.unit mass), $\underline{T}$ is the surface stress tensor, $\underline{F}$ the gravitational force (p.u.m.), $\underline{G}$ the body couple (p.u.m.) and $\underline{A}$ is the rate of conversion of external angular momentum to spin angular momentum.

If the applied magnetic field is quasi-static relative to the motion of the fluid elements and incompressibility is assumed then equations (2.29a) and (2.29b) become

$$\underline{\nabla}\cdot\underline{v} = 0 \qquad (2\cdot30a)$$

$$\frac{\partial\underline{v}}{\partial t} + \underline{v}\cdot\underline{\nabla}\underline{v} = -\nabla p^{*} + \mu_{0}M\nabla H + \eta\nabla^{2}v + \rho g \qquad (2\cdot30b)$$

where $p^{*} = p - \mu_{0}\int_{0}^{H}\rho^{2}\left(\frac{\partial M(\rho)}{\partial\rho}\right)_{H,T}dH$ and $p = p(\rho,T)$. If the

fluid is inviscid (η = 0) irrotational ($\underline{\Omega}$ = 0) isothermal (T = constant) and steady ($\frac{\partial}{\partial t}$ = 0) then equation (2.30b) becomes

$$p^{*} + \tfrac{1}{2}\rho v^{2} + \rho g h - \mu_0 \overline{M} H = const. \qquad (2\cdot31)$$

which is Bernoulli's equation with an extra magnetic term. Hence $\overline{M} = \frac{1}{H}\int_{o}^{H}$ MdH is the field averaged magnetization. A non-magnetic body immersed in a magnetic fluid subjected to a non-uniform field gradient will experience a force which Rosensweig (1985) calculates is given by

$$F_m = - V \mu_0 M \nabla H \qquad (2\cdot32)$$

if the field is sufficiently intense. This property is exploited in the separation of materials, e.g. scrap recovery separating Al from Zn . A magnetic body immersed in a magnetic fluid will self levitate under this force, a unique property of magnetic fluids.

The Normal Field Instability

Figure 2.1 shows the surface instability induced by a magnetic field of sufficient strength applied normal to an interface between a magnetic fluid and a non-magnetic fluid (air). This surface arises because in the presence of the magnetic field any peaks in the perturbed surface will have flux concentrated through them which gives rise to forces that drive the peaks further. Surface tension and gravitational forces oppose this and provide the stabilizing co-forces. The formation of a stable, strongly perturbed

surface with large peak heights when the flat surface cannot
be supported is unique to magnetic fluids. Cowley and
Rosensweig (1967) and Rosensweig (1985) detail the
ferrohydrodynamics of the normal field instability. Bacri
and Salin (1984) show that the transition from flat surface
to peaked surface is discontinuous and hysteretic,
disappearing at a lower critical field than that at which it
appears. The critical magnetization is given by Cowley and
Rosensweig as

$$M_c^2 = \frac{2}{\mu_o}\left(1 + \frac{\mu_o}{\mu}\right)\left(\rho g \sigma\right)^{1/2} \qquad (2.33)$$

for linear media where $B = \mu H$ and σ = interfacial tension
and is

$$M_c^2 = \frac{2}{\mu_o}\left(1 + \frac{1}{r_o}\right)\left(g \Delta\rho \sigma\right)^{\frac{1}{2}} \qquad (2.34)$$

for non-linear media where

$$r_o = \left(\frac{\mu_c \mu_t}{\mu_o^2}\right)^{\frac{1}{2}} \qquad (2.35)$$

and $\mu_c = B_o/H_o$ a chord permeability and $\mu_t = (\frac{\partial M}{\partial H})_o$ is the
tangent permeability. $\Delta\rho$ is the difference in density of
the two fluids. The critical field is given by

$$B_{o_c} = \frac{(1 + D\kappa)M_c}{\kappa} \qquad (2.36)$$

where D is the demagnetization factor and $\kappa = \mu_r - 1$ ($B = \mu_o\mu_r$
H). Bacri and Salin are also able to explain the heights of
the peaks, previously unexplained.

2.5 The Magnetization Curve

2.5.1 In the Liquid State

In the liquid state, the fine particles in a magnetic fluid are free anisotropic particles as discussed in Section 1.4.5(iv) and the magnetization curve is superparmagnetic, as discussed in 1.4.5. Particles whose moment relaxes within the crystal habit may be said to be intrinsically superparamagnetic at the temperature of concern whilst those that relax via rotary diffusion of the entire particle are extrinsically superparamgentic. In the liquid state both types of particle lead to a mangetization curve given by (1.23);

$$M_{ff}(B_o) = M_{ff}^{\infty} \, L(b) \qquad\qquad (2.37)$$

where $M_{ff}^{\infty} = n_p m_p / V_{ff}$ is the saturation magnetization of the monodisperse system and $b = m_p B_o / kT$. Assuming there is no loss of magnetic moment due to surface effects, the volume fraction of material is given by

$$\varepsilon_v = M_{ff}^{\infty} / M_b^{\infty}$$

$$= \rho_{ff} \, \sigma_{ff}^{\infty} / M_b^{\infty} \qquad\qquad (2.38)$$

where ρ_{ff} is the density of the magnetic fluid and σ_{ff}^{∞} its saturation mass magnetization.

2.5.2 The Effect of a Particle Size Distribution

All magnetic fluids possess a particle size distribution and so both intrinsically and extrinsically superparamagnetic particles may be present. The relaxation

time for the two are very different; Bogardus et. al. (1975) observed times of < $1\mu s$ for intrinsic and ~ 4ms for extrinsic particles. Hydrodynamic sizes can be obtained from measurements of the relaxation time of extrinsic particles (Davies and Llewellyn 1980).

For a polydisperse system, equation (1.23) becomes

$$M_{ff}(B_o) = \frac{1}{V_{ff}} \sum m_i L\left(\frac{m_i B_o}{kT}\right) \qquad (2\cdot39)$$

or if there are $n(m_k)$ particles with moment m_k then

$$M_{ff}(B_o) = \frac{1}{V_{ff}} \sum n(m_k) m_k L\left(\frac{m_k B_o}{kT}\right) \qquad (2\cdot40)$$

or if $f(m_k)$ is the fraction of the total moment which has m_k moment in $(m_k, m_k + \Delta m_k)$ then

$$M_{ff}(B_o) = M_{ff}^{\infty} \sum_k f(m_k) \Delta m_k L\left(\frac{m_k B_o}{kT}\right) \qquad (2\cdot41)$$

where $M_{ff}^{\infty} = \frac{\sum n(m_k) m_k}{V_{ff}}$. The large number of particles per unit volume (~ $10^{22} m^{-3}$ for this study) permits use of the integral;

$$M_{ff}(B_o) = M_{ff}^{\infty} \int_0^{\infty} f(m) dm \, L\left(\frac{m B_o}{kT}\right) \qquad (2\cdot42)$$

and the magnetization curve deviates from the simple Langevin curve. This is discussed further in Chapter 4.

2.5.3 In the solid state

The magnetization curve of a frozen fluid depends on the magnetic history of the sample. The important parameters are:- the magnetic field applied during freezing, the freezing point of the fluid, the critical superparamagnetic temperature of the particles, their anisotropy and the measurement temperature.

(i) Freezing in Zero Field

Freezing in the absence of a field, whether the freezing point of the fluid is above or below the blocking temperature of the particles may be expected to solidify the particles with a random arrangement of easy axes. (Solidification may be achieved by freezing or by setting the particles in an epoxy resin, in which case the measurement temperature can be above the "freezing" point). If magnetization curves are now recorded above the blocking temperature then superparamagnetic curves will result and B_o /T superposition (Section 1.4.5(i)) may be applied. Below the blocking temperature a hysteresis loop will develop with coercivity and remanance, which for monodisperse systems with each particle having the same aspect ratio (l/w, Section 1.4.3(ii)) Stoner and Wohlfarth (1948) calculated as

$$(B_o)_c = 0.479 (D_w - D_l) M_{ff}^\infty \qquad (2.43a)$$

$$M^r = 0.5 M_{ff}^\infty \qquad (2.43b)$$

and the initial susceptibility

$$K_i = \frac{2}{3} \frac{1}{D_w - D_l} \qquad (2.44)$$

The effect of a particle size distribution on the coercivity and remnance was considered by Chantrell et al. (1977, 1980) for the case in which all the easy axes are aligned parallel to the measuring field. The magnetization curve of such a system is given by

$$M_{ff}(B_o) = M_{ff}^{\infty} \left[\int_0^{y_c} f(y) L(b) \, dy + \int_{y_c}^{\infty} f(y) F(y, B_o) \, dy \right] \quad (2.45)$$

where the second term is due to the blocked particles and F(y,Bo) is not the Langevin function but may be represented by equation 1.26, f(y) is the particle size distribution where $y = d/\bar{d}_{\frac{1}{2}}$ and $\bar{d}_{\frac{1}{2}}$ is the median particle diameter. It is the second term that gives rise to the coercivity and remnance whereas the first gives rise to a superparamagnetic magnetization. Chantrell et al. (1980) solve the second term numerically and show that the presence of a size distribution "smears out" the transition from $(B_o)_c = 0$ to $(B_o)_c > 0$ as the temperature drops below the blocking temperature. It should be noted that they use a single value for the anisotropy constant of the particles whereas a distribution of anisotropies due to a distribution of elongations should be considered.

(ii) Freezing in an Applied Field

If the solidification temperature is above the blocking temperature then a random arrangement of easy axes is obtained. If, however, the fluid solidifies below the

blocking temperature then partial alignment of easy axes results. The case of complete alignment of easy axes was used by Chantrell as above. For fully aligned Stoner-Wohlfarth systems

$$(B_0)_c = (D_w - D_l) M_{ff}^\infty \qquad (2\cdot46a)$$

$$M^r = M_{ff}^\infty \qquad (2\cdot46b)$$

Systems which have a preferred orientation are said to have texture and these systems are considered more fully in Chapter 5. In general, the effect of freezing in a field is to increase the coercivity and remanence.

2.5.4 The Effect of Interactions

An ideal magnetic fluid consists of a spatially random arrangement of single magnetic dipoles. When these are sufficiently close, they interact via their dipole fields. The interaction problem is thus a classical many-body problem and cannot be solved explicitly. The most common approach to the problem has been to represent the interactions with an effective magnetic field at each particle due to all the others. (See Wohlfarth 1955, Kneller 1969). This ignores local fluctuations in the interaction energy due to particle size and shape distributions and aggregation. It should be borne in mind that even dilute magnetic fluids may contain particle clusters and hence not be free of interaction effects.

More recently, 2-dimensional computer models of magnetic fluids have been constructed and magnetization

processes studied using Monte Carlo methods (Menear et al. 1984, Bradbury et al. 1986). Analytical methods based on partition functions have also been applied (Chantrell and Wohlfarth 1983, Menear and Bradbury 1985). These techniques have been applied to explain the Curie-Weiss behaviour of magnetic fluids as observed by Soffge and Schmidbauer (1981) and O'Grady et al. (1983), O'Grady (1982). The initial susceptibility of magnetic fluids as a function of temperature is given by

$$ K_i = \frac{C}{(T - T_0)} \qquad (2 \cdot 47) $$

where T_0 is known as the ordering temperature and is explained by particle interactions. For weakly interacting systems (i.e. $\epsilon_v \ll 1$) such as those in this study, Menear and Bradbury (1985) show that

$$ T_0 \simeq \frac{M_b^{\infty 2} \pi d^3}{72 k} \left(4 \epsilon_v \right)^{\frac{2}{3}} \left(1 + \frac{2 \delta}{d} \right)^{-1} \qquad (2 \cdot 48) $$

where δ is the surfactant layer thickness and d is particle diameter. Chantrell and Wohlfarth (1983) also obtain this expression.

The Monte-Carlo calculations of Bradbury et al. (1984) revealed that the magnetization of a magnetic fluid is enhanced by weak interactions, i.e. its susceptibility is increased. They point out that this affects the derivation of particle size data from magnetization curves, as discussed in Chapter 4. The effect is mainly on the deduced spread of particle size. Menear and Bradbury (1985) point

out that the presence of interactions destroys the B_o/T superposition. They also show that superposition as a function of $b = m_p B_o/kT$ for different median diameters is lost. In the high field limit they find that the magnetization curve is affected only by an extra term in $1/b^2$ and so the interactions play minor role in this limit.

2.6 Previous Hydrocarbon - Metallic Systems

2.6.1 Introduction

The preparation of metal particle/hydrocarbon carrier magnetic fluids began in 1966 with the preparation of cobalt systems. These were studied occasionally between then and 1976 since when extensive investigations have been carried out. Thomas (1966) claimed that iron and nickel systems had been prepared but the first report of an iron system appeared in 1979 and the first nickel system in 1983. Iron and nickel systems have been investigated during this study in which the first mixed-metal systems are also reported.

2.6.2 Cobalt Systems

Thomas (1966) prepared Co in toluene systems using polymers with molecular weights of about 10^4 as dispersants obtaining particle sizes of 2-30nm with f.c.c. structure. Significant chaining was observed as was hysteresis for "dried" fluids. Hess and Parker (1966) extended this work by examining a range of polymer dispersants. It should be noted that these authors were not trying to produce magnetic

fluids but permanent magnet materials and so the polymers
they found most suitable were those that allowed chaining.
Hess and Parker found that particle size was strongly
dependent on the dispersant. High molecular weight polymers
(~ 100,000) with polar groups every 100 to 200 backbone
atoms were most suitable for their purposes.

McTague (1969) also prepared cobalt fluids by this
method for viscosity measurements (2.4.2). After
centrifuging he produced suspensions stable in the
gravitational field for over a year. Particle sizes were
5.5 to 12nm and concentrations ~ 10^{21} particles m^{-3} (ϵ_v ~
0.01%). Chantrell (1977) prepared cobalt fluids using
polymer dispersants achieving saturation magnetizations of
1.5 $JT^{-1}kg^{-1}$ but gravitational settling within 40 minutes.
Chantrell notes a discrepancy of ~ 3nm between magnetically
derived and electron microscopically derived median particle
sizes. He also achieved greater gravitational stability by
adding a commercial surfactant, Sarkosyl, to his systems,
although his attempts at preparing a fluid using this
surfactant on its own, were not successful. Papirer (1977)
studied the reaction mechanism of carbonyl decomposition by
observing the evolution of CO_2 as a function of time. A
surfactant, sodium di-2-ethyl methyl sulphosuccinate,
replaced the polymer and his results showed that the
surfactant aided carbonyl decomposition. O'Grady (1982)
studied a variety of surfactants for preparing Co fluids in
toluene and established the use of anionic surfactants such

as Sarkosyl or Manoxol-OT for preparing stable fluids. He found Gaussian size distributions, Curie-Weiss behaviour and time-dependent magnetization.

Davis and Llewellyn (1979a,b) observed birefringence and Faraday rotation in cobalt systems. Logarithmic time dependence of the isothermal remanent magnetisation in frozen fluids was found by O'Grady et al. (1981) and Cayless et al. (1983). The latter also noted non-logarithmic dependence for a cobalt system frozen in a small field which was attributed to either a bimodal anistropy distribution in the fluid (possibly due to chaining) or to the blocking diameter after a large time, t, becoming greater than was its value on freezing thus changing the weighting function for the magnetization from a non-Langevin to a Langevin function and so changing the gradient of the decay. These authors also noted non-logarithmic decay for a sample frozen in zero field and subsequently magnetized before reducing the field to zero. Chantrell et al. (1983) also observed this effect on Co systems and explain it by noting that the decay is due to a very small fraction of the particles. Cebula et al. (1981, 1983) carried out small angle neutron scattering experiments on cobalt systems and found the magnetic size to be smaller than the physical size. They also confirmed the electron microscope physical size and found a surfactant layer thickness of ~ 2.8nm in agreement with the length of their surfactant molecules. Chantrell et al. (1982) studied the effect of dilution on the stability

of cobalt fluids and found that dilution with pure carrier liquid resulted in aggregates of $\sim 10^6$ particles with radius $\sim 1\mu m$ forming and settling out. Dilution with carrier/surfactant solutions did not result in sedimentation indicating that a dynamic equilibrium exists between surfactant on particle surfaces and that in solution. Paige et al. (1984) measured torque hysteresis, finding anisotropy constants of $2.4 \times 10^5 J/m^3$ and rotational hysteresis of $\sim$ 0.7 which indicates that simple coherent or chain-of-spheres/fanning reversal mechanisms are not taking place. Hoon et al. (1983) took torque curves on frozen cobalt systems at 77K and obtained an anisotropy constant of $2 \times 10^5 Jm^{-3}$. These figures are in agreement with those deduced by O'Grady (1982). O'Grady et al. (1984) observed exchange anisotropy in frozen systems but found the exchange anisotropy constant to be a factor of $\frac{1}{4}$ too small and attribute this to the effect of the surfactant. The texture of Co systems was investigated by O'Grady et al. (1985) who found remanence was affected most strongly by irreversible particles while the slope of the approach to remanence after saturation gave the texture of reversible particles.

The above is a selection and is not meant to be exhaustive. Cobalt systems have been used to study fine particle effects and so have been investigated extensively. In contrast, Fe and Ni systems have hardly been studied at all.

2.6.3 Iron Systems

The first reported Fe fluid was that of Griffiths et al. (1979) who decomposed $Fe(CO)_5$ in polymer/solvent solutions. Particle sizes of 1.5 to 2.0 nm with narrow distributions (all particles within $\pm$ 20% of the median size) were obtained. They emphasize the difficulty of obtaining metallic iron if air is present during preparation. Rapid loss of magnetization was observed on exposure to air. They observed disordered small particles which became crystalline with disordered centres as they grew. The pre-oxidation magnetization of the particles was found to be 40-60% of that of bulk iron, indicating that surface interactions, e.g. spin pinning (Berkowitz et al. 1975), have a large effect on iron systems. They found that an oxidation layer of γ-Fe_2O_3 formed with a limiting thickness of ~ 2.8nm. Systems which contained Cl (from the solvent) formed β-Fe OOH in the presence of water (60% relative humidity air). The magnetization of these systems reached equilibrium after $\sim$ 150hrs exposure to air. Initial saturation magnetizations of 1.5-$2.2JT^{-1}kg^{-1}$ were obtained. Smith and Wychick (1980) studied the mechanism of particle formation in these systems. They conclude that in the absence of polymers the $Fe(CO)_5$ forms $Fe_2(CO)_9$ and then decomposes to Fe at the glass vessel surface. In the presence of the polymer, butadienyl, butadienyl-iron tricarbonyl residues form on the polymer chains. These act

as nucleation sites for particle growth which occurs by $Fe(CO)_5$ reacting with the particle surface.

Kilner et al. (1984) report the preparation of Fe systems from $Fe_2(CO)_9$ and this is discussed herein. Ayoub et al. (1985) report Mossbauer studies on iron fluids prepared from iron carbonyl (presumably $Fe(CO)_5$) in a decalin/sarkosyl solution. They obtained 6.5nm particles, 0.8% volume fraction, and $\sigma_{ff}^{\infty} = 14JT^{-1}kg^{-1}$. They find evidence for FeO at the particle surface. Fe systems are considered further in this work.

2.6.4 Nickel Systems

There is only one report, as yet, of Ni fluids in the literature, Hoon et al. (1983). These were prepared at Durham from $Ni(CO)_4$ and $(\pi - C_5H_5)_2Ni$. In the former case the decomposition was achieved by UV iradiation. Particle sizes were $\sim 5nm$ and in the UV fluid a large number of triangular particles were observed by electron microscopy. The lattice parameter was found to be 3.52Å (bulk Ni $a_o = 3.5\text{Å}$). Saturation magnetizations were $\sim 0.1JT^{-1}kg^{-1}$. The extreme toxicity of the precursor materials restricts the preparation of Ni systems. Again these are considered further in this study.

2.7 Intermetallic Systems

The saturation magnetization, magnetocrystalline anisotropy and Curie temperature for binary alloys of Fe, Ni and Co are shown in Figure 2.7. From this it can be seen
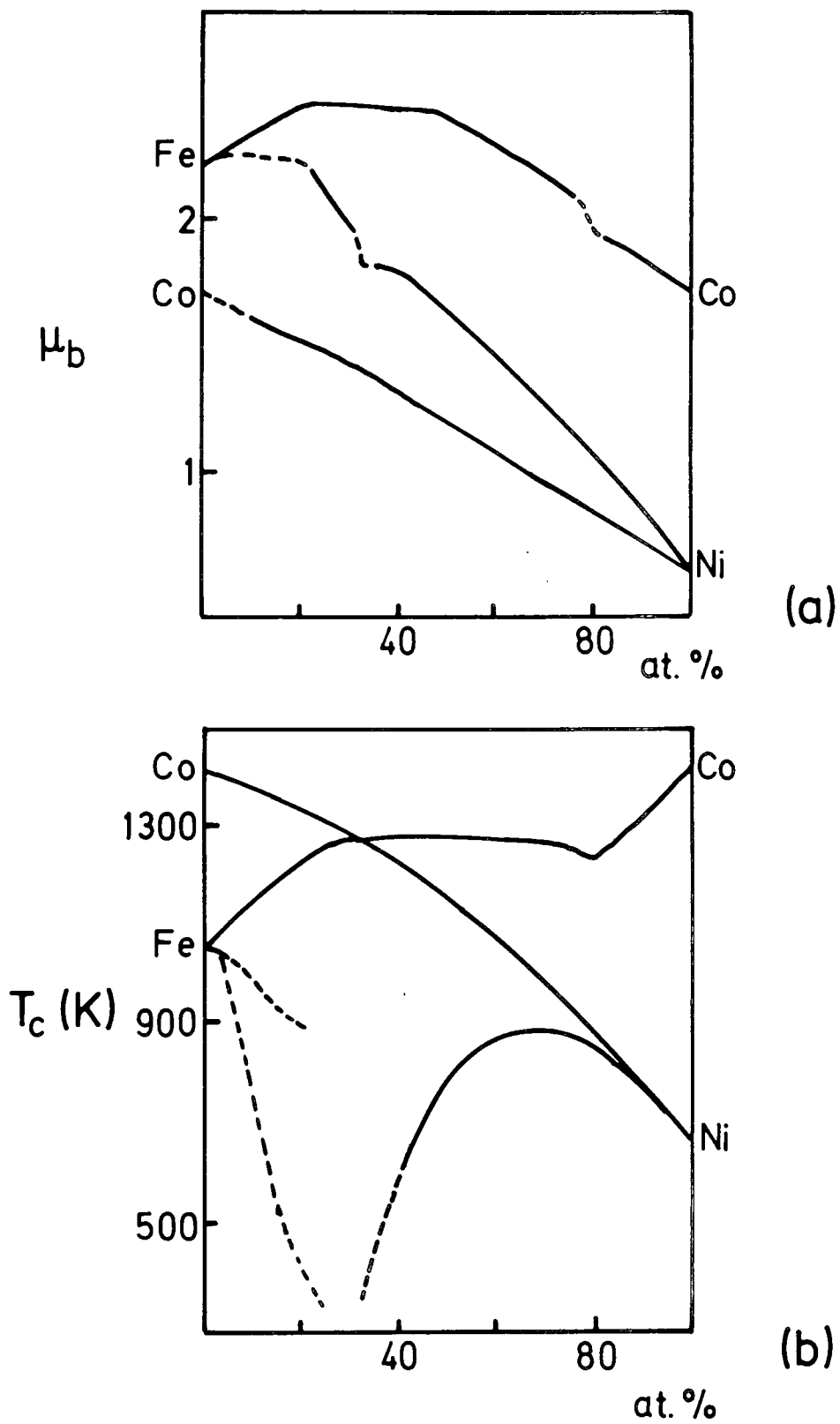
FIGURE 2.7
Intrinsic magnetic properties of binary alloys of Fe,Co & Ni.

(a) Magnetisation
(b) Curie temperature.
(c) First anisotropy constant.

Fe-Co

Fe-Ni
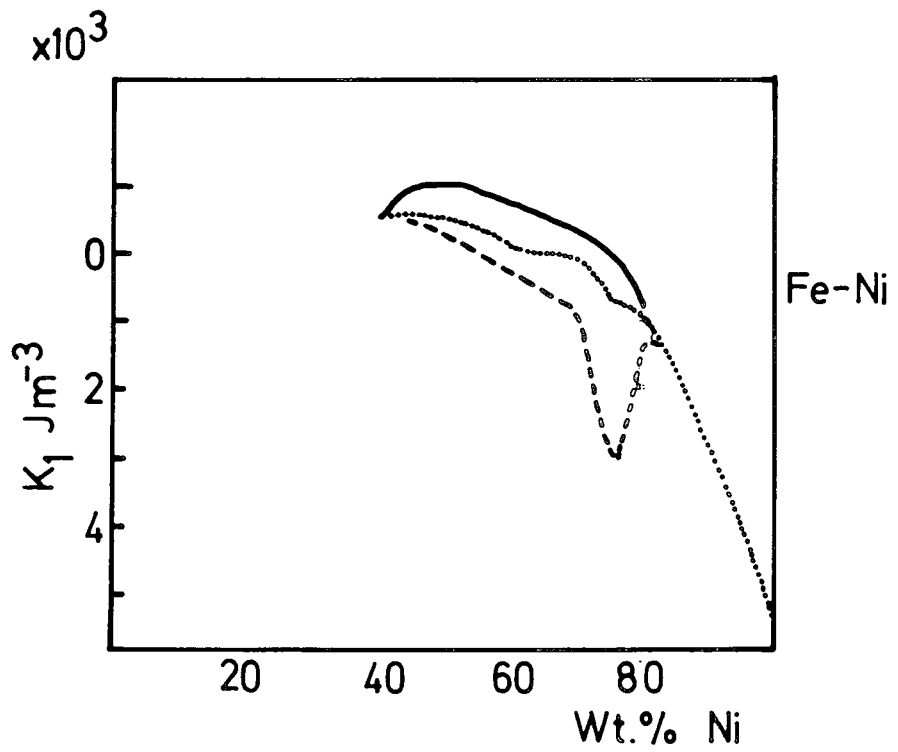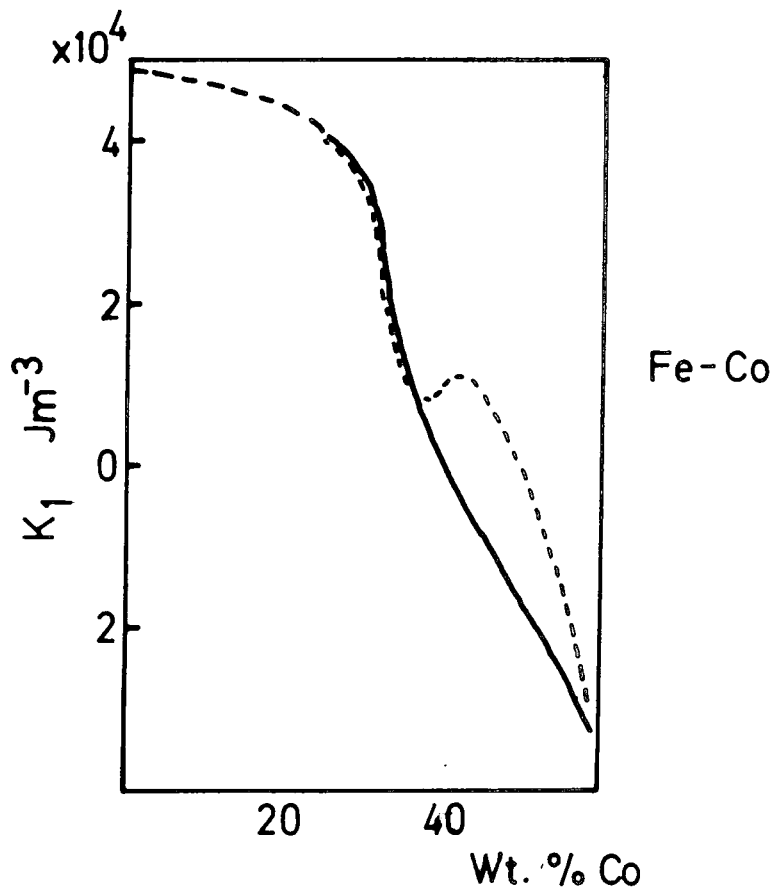
----- Ordered phases

(c)
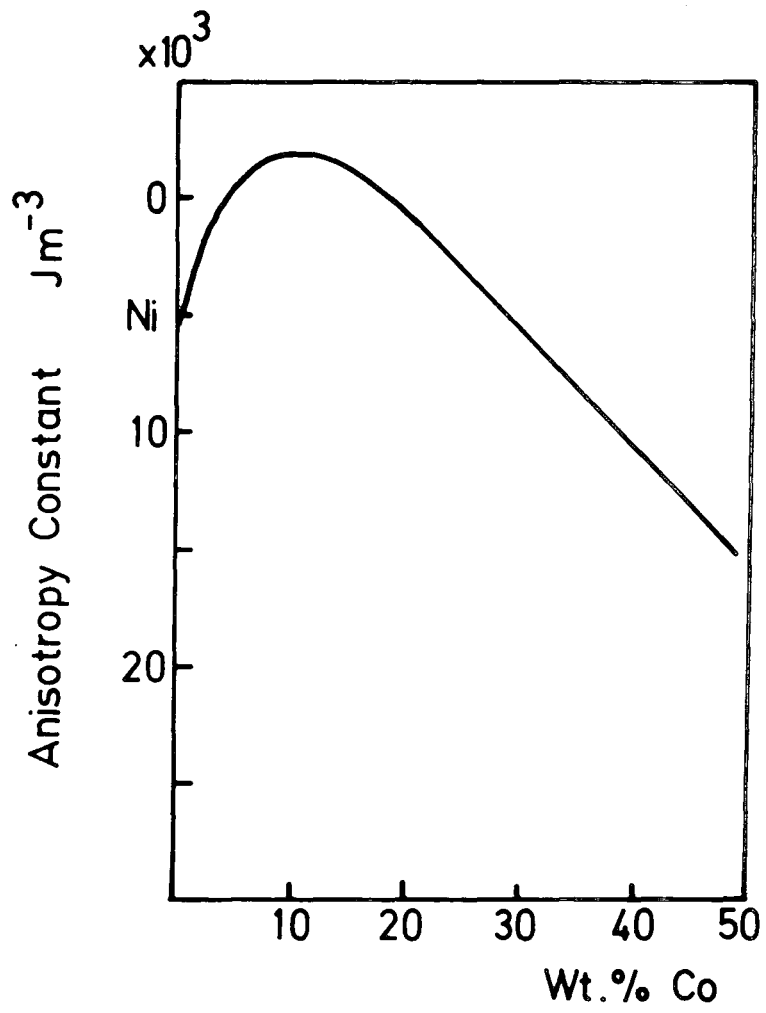
Ni-Co

2.7 (c)

that the ability to prepare 'alloy' systems would provide the means to control the intrinsic magnetic properties of magnetic fluids. For example, a primary reason for preparing metallic systems is to increase the magnetization of fluids. The FeCo alloys have a saturation magnetization greater than that of iron for $0 < wt\%Co < 60$. Fe systems are more prone to oxidation than Co or Ni systems and thus adding Ni or Co to Fe should reduce its rate of oxidation without decreasing the magnetization catastrophically. FeNi alloys exist with zero magnetocrystalline anisotropy which would allow studies of pure shape anisotropy. Control of the Curie temperature is particularly desirable as many applications (e.g. energy conversion) are dependent upon it. Alloy NiFe particles were prepared by Shepherd and Popplewell (1971) for this reason using techniques originally aimed at permanent magnet preparation (see Section 2.2.2).

Organometallic compounds offer excellent possibilities for preparing particles with different compositions including ternary or quatenary alloys. Elements such as Cr may be added to reduce oxidation whilst a particularly exciting possibility is the FeRh system which is antiferromagnetic at room temperature becoming ferromagnetic with a very sharp transition at $\sim 350K$. This would allow studies of interacting systems where the interactions could be "switched" on and off. The preparation of intermetallic systems was therefore the primary motivation for the present

study during which the first intermetallic systems of FeCo and FeNi were reported.

CHAPTER THREE

EXPERIMENTAL TECHNIQUES

3.1   The Vibrating Sample Magnetometer

The principal investigative tool in this study was the Durham vibrating sample magnetometer (V.S.M.). This instrument was designed and built in this laboratory by Drs. S.R. Hoon and S.N.M. Willcock and has been described by them in great detail (Hoon (1980) Willcock (1985), Hoon and Willcock (1986)). Consequently, only a broad outline of the system is given here highlighting those aspects most relevant to this study.

3.1.1.   Principal of Operation and System Outline

A V.S.M. detects the magnetic induction in the vicinity of the sample. The sample is vibrated between detection coils in a variable strength, uniform magnetic field. The magnetic moment of the sample gives rise to a magnetic flux which threads the detection coils. Vibrating the sample causes the flux through the coils to change and so induces an e.m.f. across the detection coils in accordance with Lenz's law. This e.m.f. is proportional to the moment of the sample and to the amplitude and frequency of vibration. The vibrator mechanism also provides an a.c. signal at the vibrational frequency allowing a phase sensitive detector (p.s.d.) to be used for signal detection. Calibration is by

means of a standard sample, in this study Ni.

(a)   <u>Measurements up to 1.2T</u>

Figure 3.1 shows the principal components of the Durham
V.S.M. as used in the 1.2T electromagnet. Sample vibration
is achieved by means of an electric motor and crank
mechanism. Mechanical noise is minimized by the 180° double
throw arrangement of the crank assembly. Accurate balancing
of the weights of the sample rod and counterweight
assemblies ensures no work is done against gravity so
permitting smooth running. The vibrating head mechanism is
isolated from the rest of the system by a pneumatic seating.
The reference signal is provided by an Alcomax permanent
magnet mounted on the motor shaft adjacent to a single
pancake pick-up coil.

The sample rod is of borosilicate glass and is located
centrally in the cryostat by a perforated polytetra-
fluoroethylene (P.T.F.E.) bush, the cryostat itself being
mounted centrally on the magnet axis. The cryostat used was
an Oxford Instruments type CF1200 gas flow cryostat with
separate exchange gas filled sample space. The detection
coils are mounted on the pole tips of an 8 inch Newport
Instruments Type D air cooled electromagnet. The geometry
of the detection coils is that due to Mallinson (1966)
consisting of two vertical pairs of pancake coils mounted
parallel to the faces of the pole tips.

The V.S.M. was fully automated as described by Willcock
(1986). Figure 3.2 shows the principal elements of the data

Counterweight

Reference Magnet

Crankshaft

Motor

Reference Coil

Conrods

Isolating Diaphragm

Couplings

Cryostat

Sample Rod

Bush

Pole Tip

Sample

Magnet Coil

Detection Coils
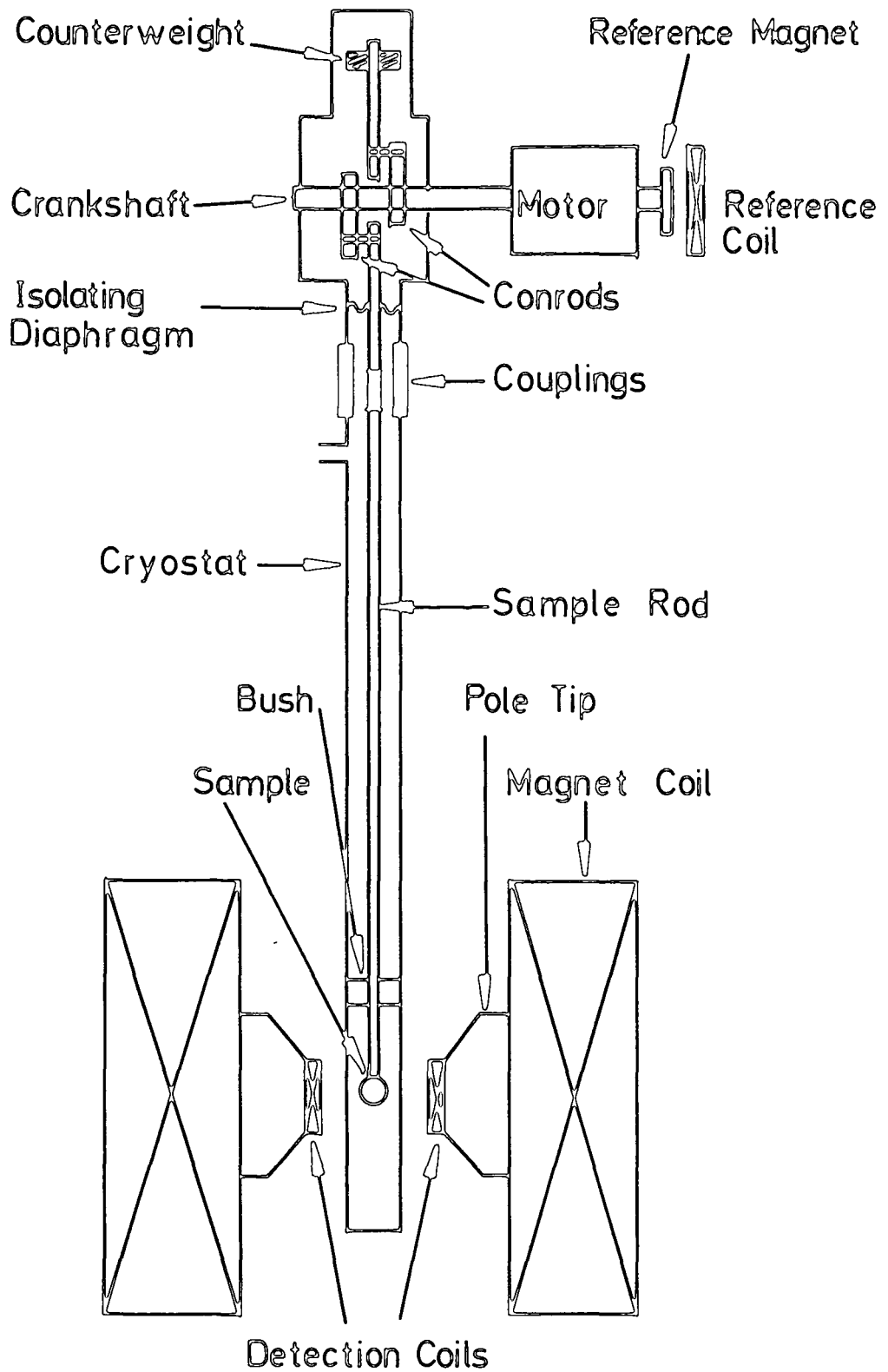
FIGURE 3.1
The principal elements of the Durham
V.S.M.
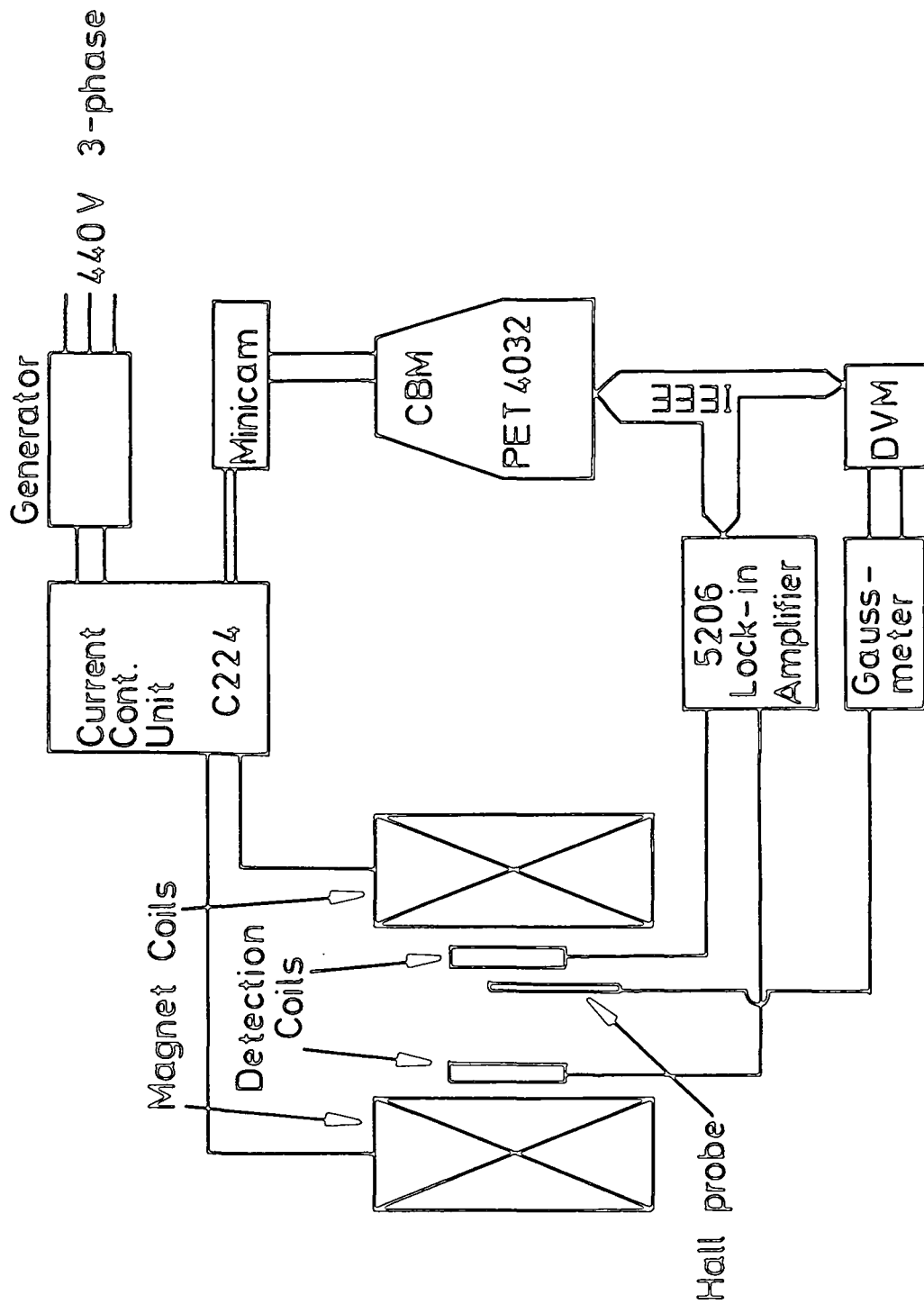
FIGURE 3.2
The data acquisition/control system
for the VSM.

acquisition/control system. Data acquisition was via a Brookdeal 5206 lock-in amplifier (a p.s.d.) operating in common mode rejection (A-B mode) to detect the signal from the two pairs A,B of detection coils and a Hall-effect Bell 640 Gaussmeter connected to a Fluke 8860A digital voltmeter to detect magnetic field. The CBM PET 4032 microcomputer obtained data from these instruments via the IEEE 488 communications bus. The control system comprised the Newport C224 350V-30A control unit with three phase motor generator interfaced to the PET via a Bede Scientific Minicam interface system. The V.S.M. control software is documented by Willcock (1985), the author made only minor modifications to this according to his needs.

(b) <u>Measurements up to 13T.</u>

The vibrating mechanism was designed to also operate with a 13T Nb_3Sn/NiTi superconducting solenoid and was simply transferred onto this device in toto. The data acquisition system remained the same but the field was now ramped and recorded under manual control. The sample rod in this case was a 1.3m long cupro-nickel tube. Thermal expansion/contraction of this rod had to be allowed for and so careful saddling of the sample position was required before each magnetization measurement. A variable temperature insert allowed measurements between 4.2 and 300K. The detection coils for the solenoid were axial, two sets being available; one mounted within the solenoid in the liquid Helium space, the other inside the variable

temperature insert. The data recorded in this study was obtained using the inner coils which consisted of two pairs of series opposition coils and a split coil at the sample position. Hoon and Willcock (1986) describe these in detail.

Sample temperature was monitored using AuFe-Chromel thermocouple whilst magnetic field was measured using a Hall device mounted in the liquid Helium space on the solenoid axis. Magnetization measurements were always recorded with the magnet in persistent mode. The system was calibrated at every field/temperature point in order to avoid calibration errors due to magnetic images.

For a full account of the Durham V.S.M. the reader is referred to Hoon and Willcock (1986).

3.1.2 Signal Loss Due to Magnet Coil Movement (Electromagnet)

The very small moments of the authors samples ($\sim 10^{-5} JT^{-1}$ /0.01 emu at saturation) revealed the presence of a sudden loss of signal when the magnetic field in the 1.2T facility reached 0.6T. This effect was not observable for sample moments in excess of $10^{-2} JT^{-1}$. Figure 3.3 shows the effect where it can be seen that the loss was reversible with slight hysteresis and was identical in the two halves of the $M-B_o$ cycle. The decrease in signal magnitude from the detection coils was approximately 3.7 μV and was found to be independent of sample. It was eventually discovered that at 0.6T the massive magnet coils, which were not fixed but
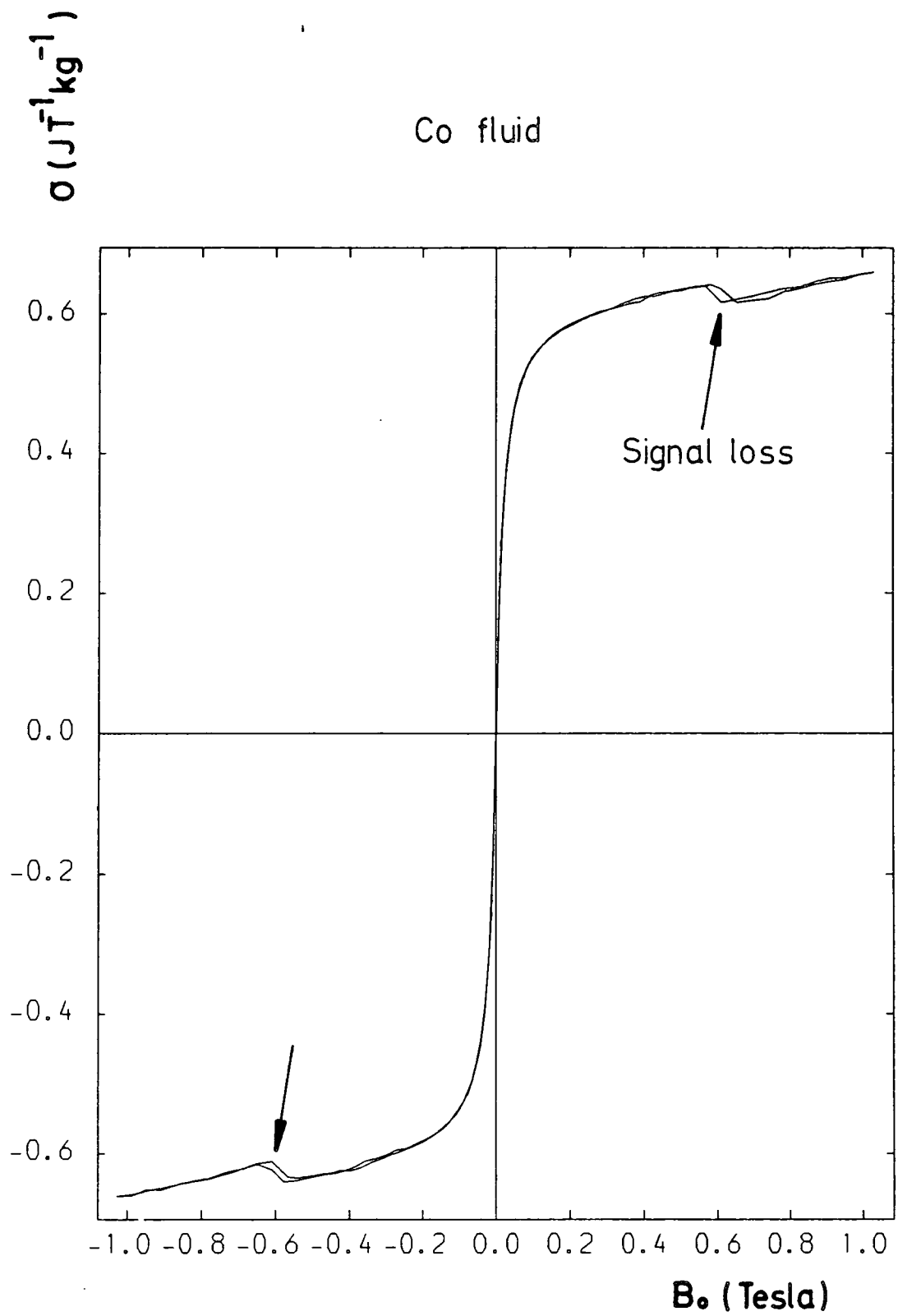
FIGURE 3.3
The effect of coil movement on a
typical magnetisation curve.

nested in grooves under their own weight, were tilting apart slightly as the magnetic attraction to the yoke overcame their weight. It is thought that as the coils were freed of a mechanical constraint by standing on one edge, their copper windings were permitted to ring microphonically with the 24Hz ripple in the magnetic field (which was due to the motor generator commutator slip frequency). This would suddenly induce an additional ripple to the magnetic field through the detection coils which were not perfectly balanced and so induce a voltage across them. The Mallinson geometry coils with their area perpendicular to the field are particularly susceptible to field ripple. The 24Hz frequency is sufficiently close to the 30Hz operating frequency of the V.S.M. for a proportion of the induced signal to be detected by the lock-in amplifier. As the magnetic field increased beyond 0.6T the tilting was limited by the supporting grooves, once again constraining the coils mechanically and so reducing the "humming" effect.

An estimate of the ripple field necessary to produce $3.7\,\mu V$ across the detection coils was obtained by applying an AC current at 30Hz through a pair of Helmholtz trim coils supplied on the magnet. It was found that a peak-peak ripple of $\sim 7\,\mu T$ would be sufficient. In order to estimate the winding movement necessary to produce this, the formula due to Zilstra (1967) for the field on the axis of thick coils was used,

$$B_i = \mu_o \tau r_i F_i \qquad\qquad (3 \cdot 1a)$$

$$F_1 = \tfrac{1}{2} \ln \left[\frac{\gamma + (\gamma^2 + \delta^2)^{\frac{1}{2}}}{1 + (1^2 + \delta^2)^{\frac{1}{2}}} \right] \qquad\qquad (3 \cdot 1b)$$

where $\gamma = r_2/r_1$, $\delta = z_o/r$ and r_1, r_2, z_o are defined in Figure 3.4. τ is the current density in the coils which at 0.6T is $4.96 \times 10^{-5} Am^{-2}$. By evaluating this for the known coil geometry and then inreasing z_o by 100μm it was found that field changes of $\sim$ 10μT could be obtained, more than sufficient to generate the voltage loss. Winding movement of this size is thought to be possible when "humming".

Solution of the problem was by fixing the coils by employing metal spacers between the coils and the yoke as shown in Figure 3.4. It is suggested that the coils be fixed permanently to facilitate sensitive measurements.

3.1.3 Signal Loss Due to Cryostat Eddy Currents

Figure 3.5 shows the signal obtained from the Ni reference sample as a function of temperature. As can be seen, a dramatic loss of signal $\sim$25% occurs below 60K. The source of this loss was determined to be the copper in the heat exchanger and radiation shield of the cryostat. The electrical conductivity of copper increases rapidly below 60K thus both increasing the eddy currents generated by the vibrating moment and reducing the skin depth so effectively increasing the shielding of the moment from the detection coils. As this was a design error by the manufacturers of the cryostat, it had to be tolerated during this study. Measurements below 60K therefore have a smaller signal to noise ratio and hence are noiser. In order to remove this
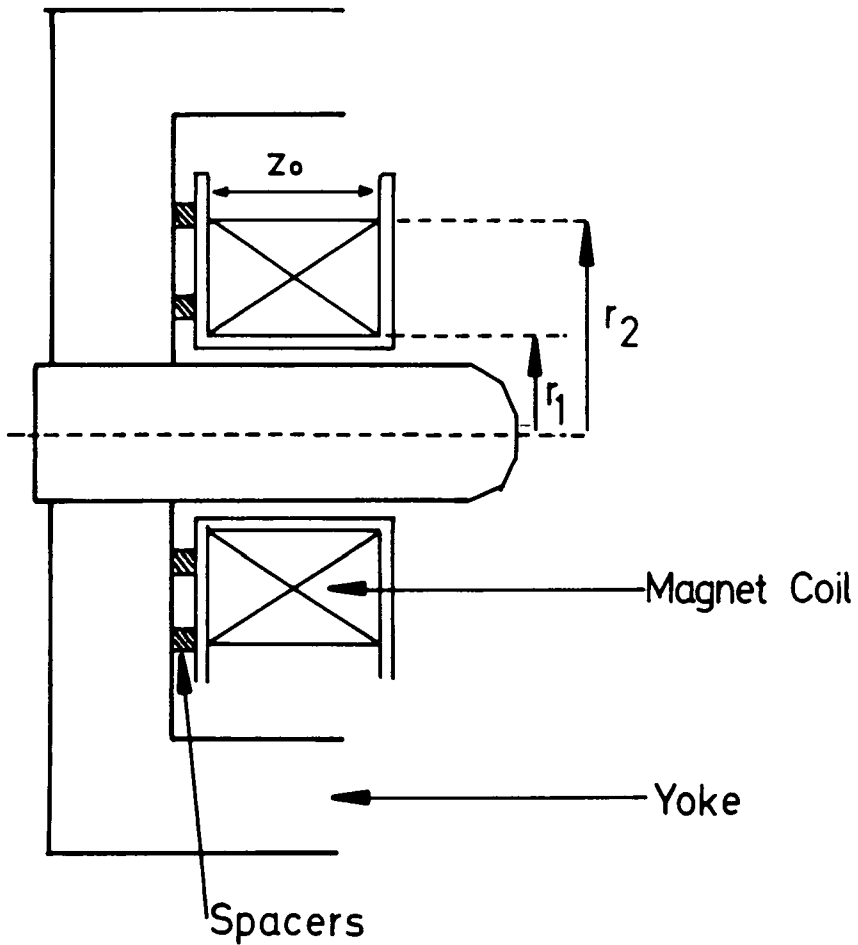
FIGURE 3.4
Part of the electromagnet showing symbols for eqn. 3.1 and the metal spacers used to eliminate coil movement.
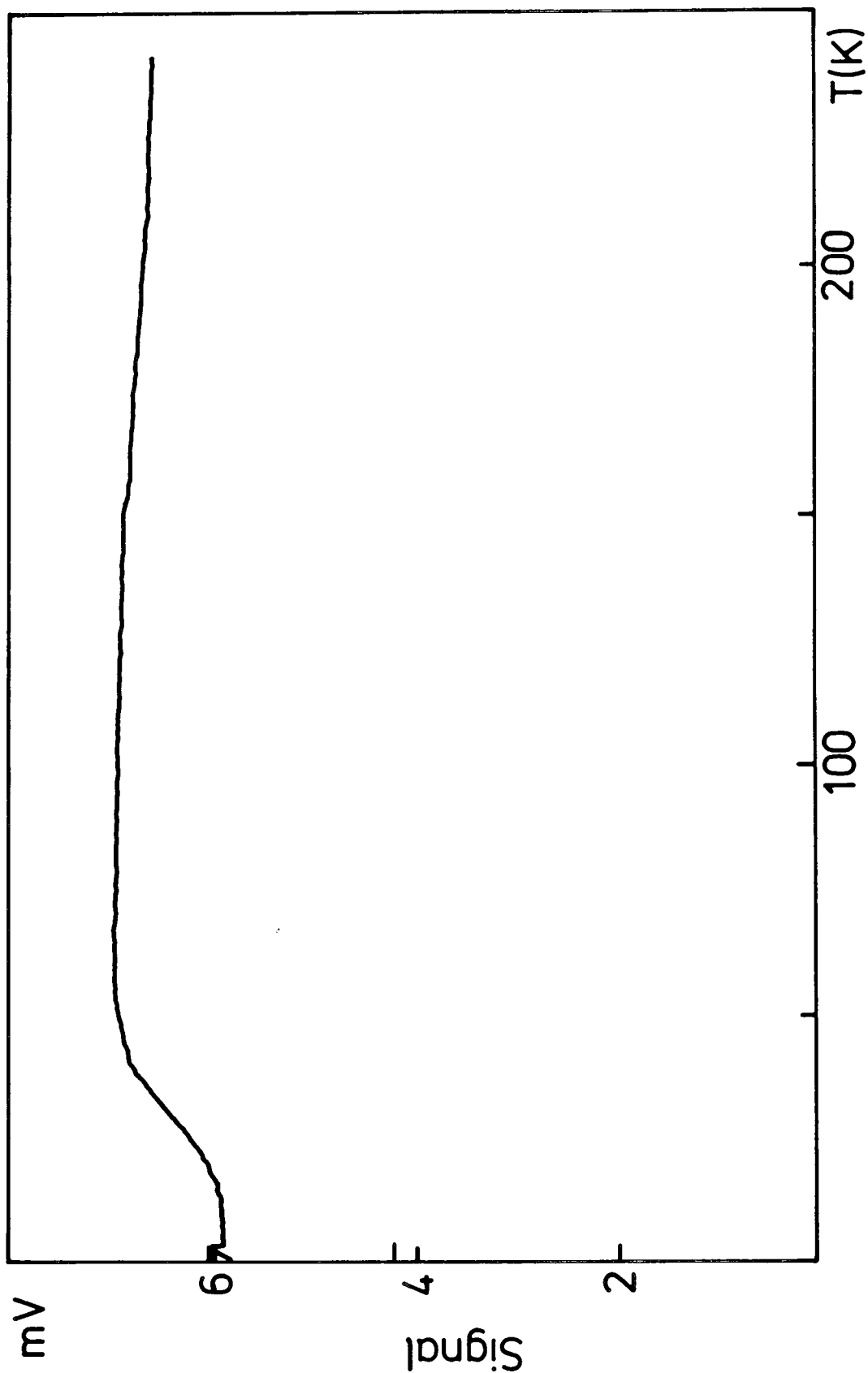
FIGURE 3.5
Signal loss at low temperature.
Signal output is from the lock
in amplifier for the Ni reference
crystal.

effect, the heat exchanger must be manufactured of a different material, e.g. brass or Beryllium-copper and the radiation shield must be slotted in a manner to reduce the eddy currents.

An additional source of noise in low temperature measurements was the vibration of the cryostat by the vacuum equipment attached to it. Unfortunatey it was found that the cryostat required continuous pumping in order to maintain its vacuum over the period of measurement. Again this had to be endured during this study.

3.1.4 Temperature Calibration of the Cryostat

A 0.07% Fe-Au/Chromel thermocouple attached to the heat exchanger enabled control of the sample space temperature by an Oxford Instruments 3120 controller. This was calibrated against a RhFe resistance thermometer supplied by Cryogenic Calibrations Ltd. which in turn had been calibrated against a National Physical Laboratory calibrated standard and was stated to be accurate to ± 0.01K. Figure 3.6 shows the "real" temperature obtained from this thermometer plotted against the displayed temperature on the 3120. A second 0.03% Fe-Au/Chromel thermocouple was calibrated simultaneously and then used later to calibrate the sample position temperature by placing it inside a sample sphere containing a representative fluid. Sample temperatures are taken as accurate to $\pm$ 0.5K.
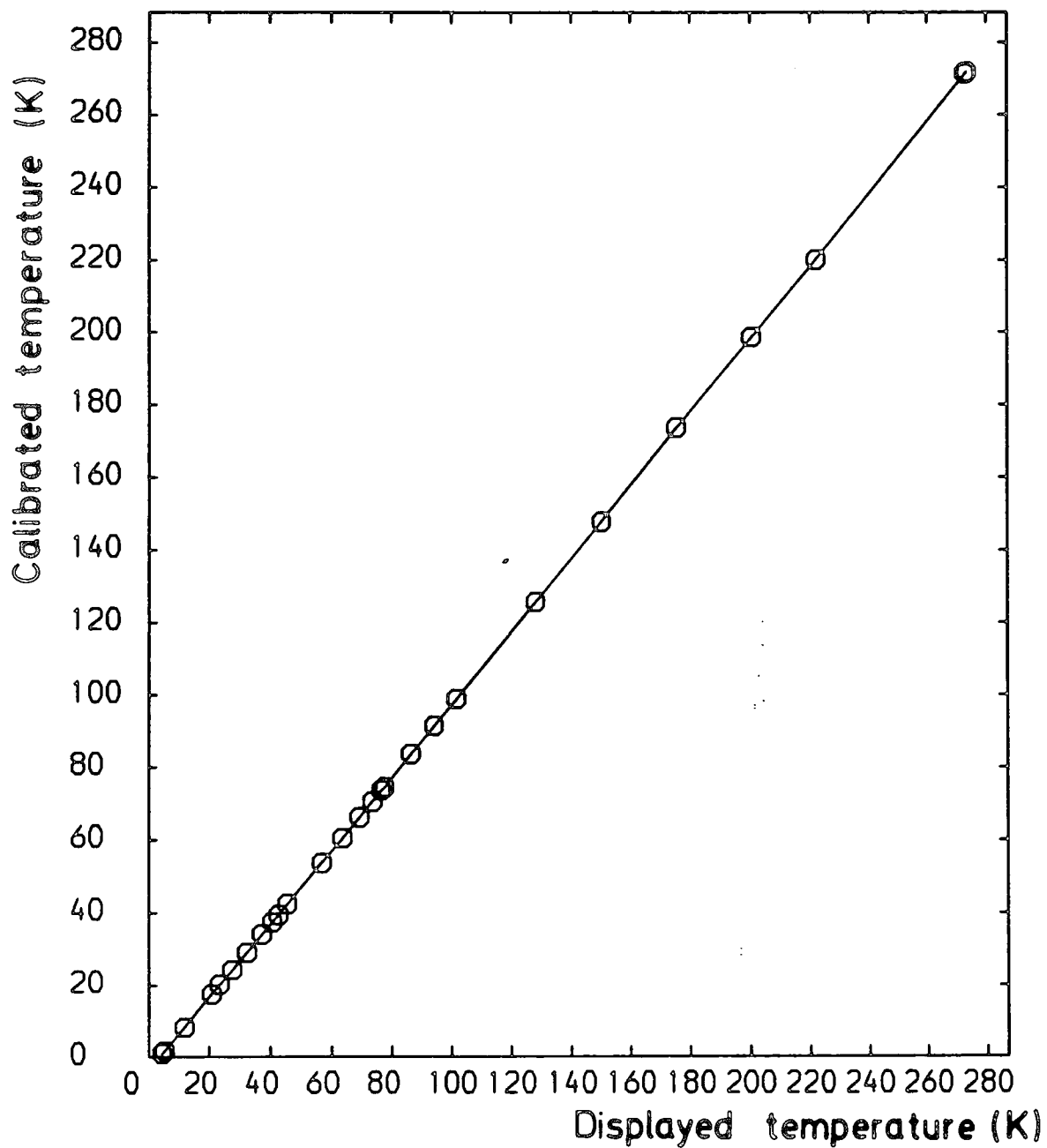
FIGURE 3.6
Calibrated temperature against
displayed temperature for the 3120.

3.1.5 Sample Details and Residual Signal

(a) Sample Details

Figure 3.7(a) shows the arrangement for attaching the sample to the downrod. The samples were contained in blown glass spheres of 6mm inside diameter ($\sim 110 \mu l$) which were sealed with an epoxy glue. These were held in a cylindrical cavity drilled into the bottom of the 20mm long cylindrical P.T.F.E. sample holder. P.T.F.E. tape was always wound over the glass sphere and round the holder to ensure the sample was held tightly. The top of the holder was drilled to push fit over the glass downrod. Glass was chosen as the material for the downrod rather than stainless steel or tufnal as it was both lighter and did not give a paramagnetic signal. For low temperature work it is essential that the P.T.F.E. holder fits over the downrod as then the contraction of the P.T.F.E. at low temperature holds it to the rod. Holders fitting into the bore of the rod become detached at low temperatures. A small hole drilled through the centre of the holder allowed gases inside the downrod to escape and be replaced with Helium exchange gas.

(b) Residual Signal

P.T.F.E. has a diamagnetic susceptibility and so the contribution of the holder to the total signal must be subtracted from sample data. Automation of the V.S.M. made

Epoxy Glue

Spherical sample
volume ~115μl

—Borosilicate glass rod

—Push fit P.T.F.E. sample holder

—P.T.F.E. tape

(a)

5.8mm   1.8mm
                    1.7mm

Ni reference crystal

(b)
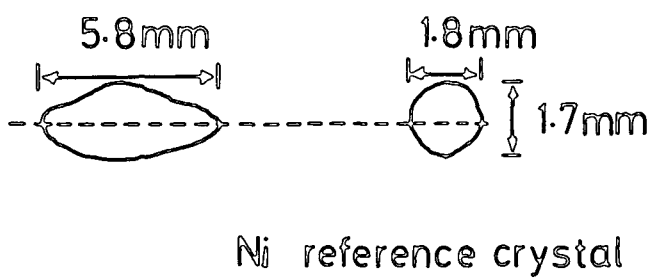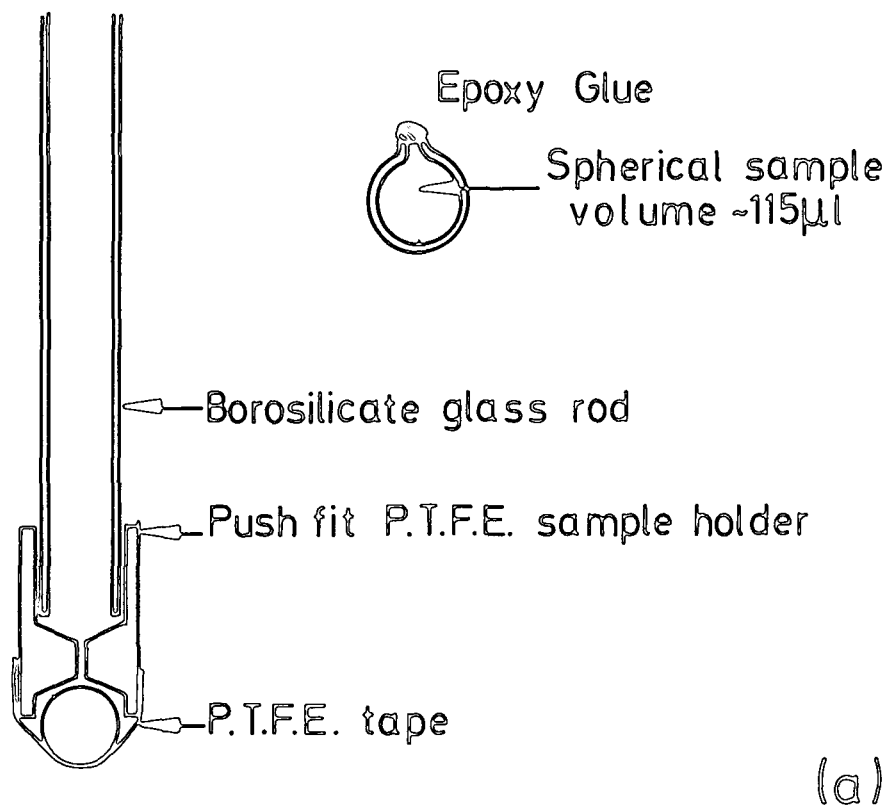
FIGURE 3.7
(a) Glass sample sphere and means
     of attachment to vibrating rod.
(b) Ni reference crystal dimensions.

this a simple process performed by software. Residual runs were taken with an empty, sealed glass sphere whenever a series of sample runs were taken. Straight lines were least-squares fitted to these and then incorporated into the analysis software for subtraction from the sample data. Figure 3.8 shows residual runs at various temperatures for a particular holder. It will be noticed that the residual signal is offset from (0,0). By successively removing the cryostat, sample holder, downrod and finally the entire vibrating head, it was found that this offset was inherent in the supply current and/or the environment. It amounted to $\sim$ 0.65 $\pm$ 0.25 V in zero field, the large variation presumed to be due to environment and the basic contribution to supply ripple. The "no head" experiment also revealed that a small diamagnetic signal was also present amounting to $\sim$ 0.8 $\pm$ 0.4 V at 1 Tesla and this is thought to be due to the 6μT field ripple due to the generator. This places a limit on the precision of any one magnetization measurement equivalent to $\pm$ 0.003 $JT^{-1}kg^{-1}$ for a 0.1g sample.

3.1.6 Calibration Details

Calibration was by means of a single crystal of Ni measured along its <111> axis. Figure 3.7(b) shows the dimensions of this crystal which yield a demagnetizing factor, D = $0.12\mu_0$ assuming an equivalent ellipsoid. In order to obtain an internal field of 1.0T it is therefore necessary to apply a field of 1.074T. In practice the author always calibrated at 1.1T. A standard has to be
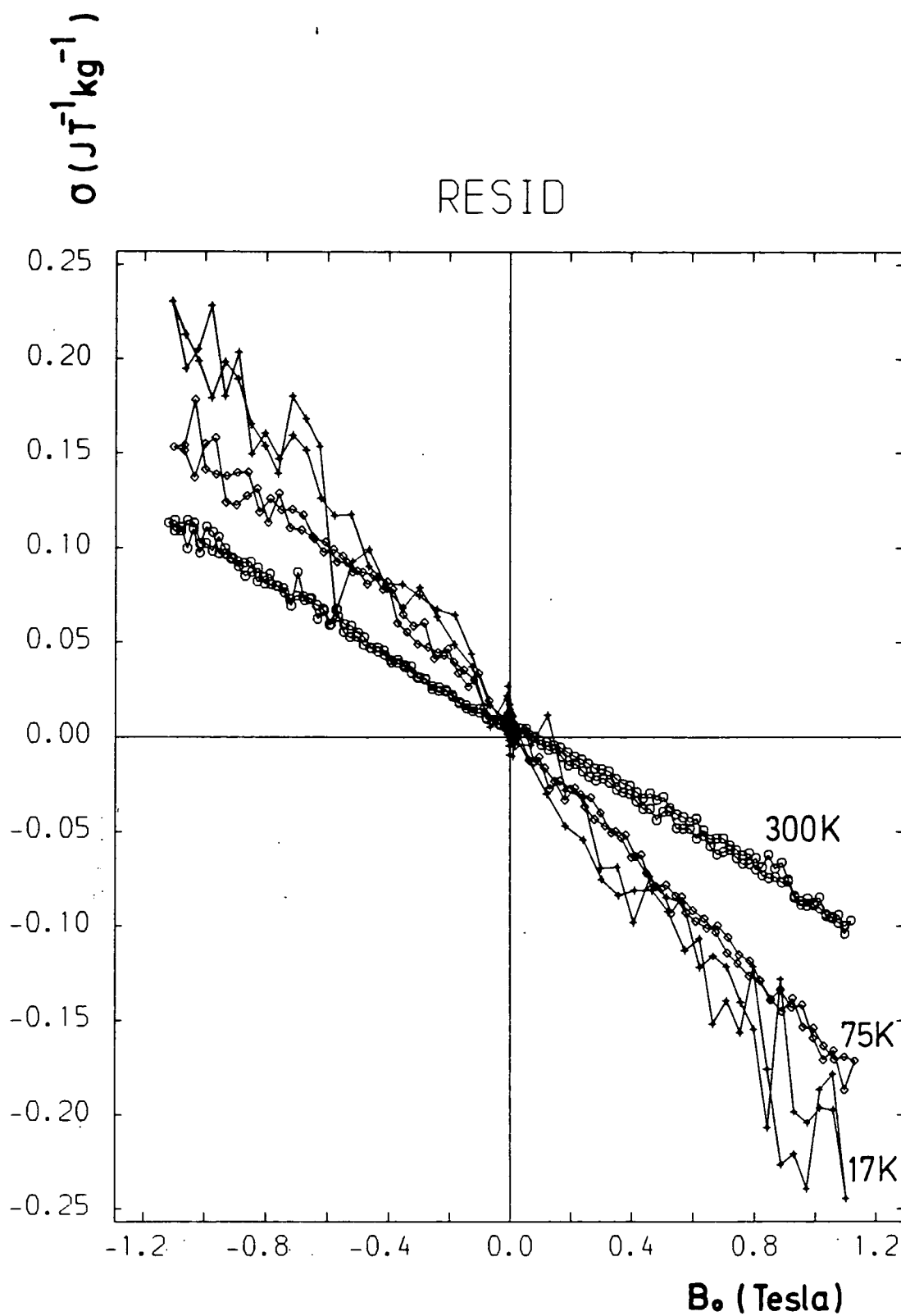
FIGURE 3.8
Residual signal on V.S.M. due to
sample holder at various temperatures.

chosen for the magnetization of Ni and after examination of

the literature (e.g. Pauthenet (1982)) the author has taken

the magnetization of Ni to be defined by:

$$\sigma(B_o = 1, T) = \sigma_o (1 - a_{32} T^{\frac{3}{2}} - a_{52} T^{\frac{5}{2}}) \qquad (3 \cdot 2)$$

where $\quad \sigma_o = 58.624 \ JT^{-1}kg^{-1}$

$\qquad a_{32} = 6.64 \times 10^{-6}$

$\qquad a_{52} = 1.85 \times 10^{-8}$

Calibration of the V.S.M. was carried out after every

sample run.

3.2 Colloidal Stability Apparatus ('Sedometer')

In order to assess the stabilizing quality of various

surfactants in the gravitational field, apparatus designed

to measure the concentration profile of magnetic fluids was

constructed. This instrument, termed a "sedometer"

(sedimentation meter) was similar in design to that of

Peterson et al. (1974) but employed an A-C inductance bridge

for signal detection, comparable to that of Rabinovici and

Badescu (1977), rather than a resonant frequency circuit.

Figure 3.9 shows the principal elements of the sedometer. A

4-phase unipolar stepper motor (SIGMA type 9904 112 27001)

drove a 2mm pitch lead screw which was held in bearings and

supported vertically in an aluminium housing. A matched nut

coupled the lead screw to a travelling table guided by two

stainless steel rods. The table had two collet clamps into

Detection Coils

Sample Rods

Lead screw

Travelling Table

Stepper Motor
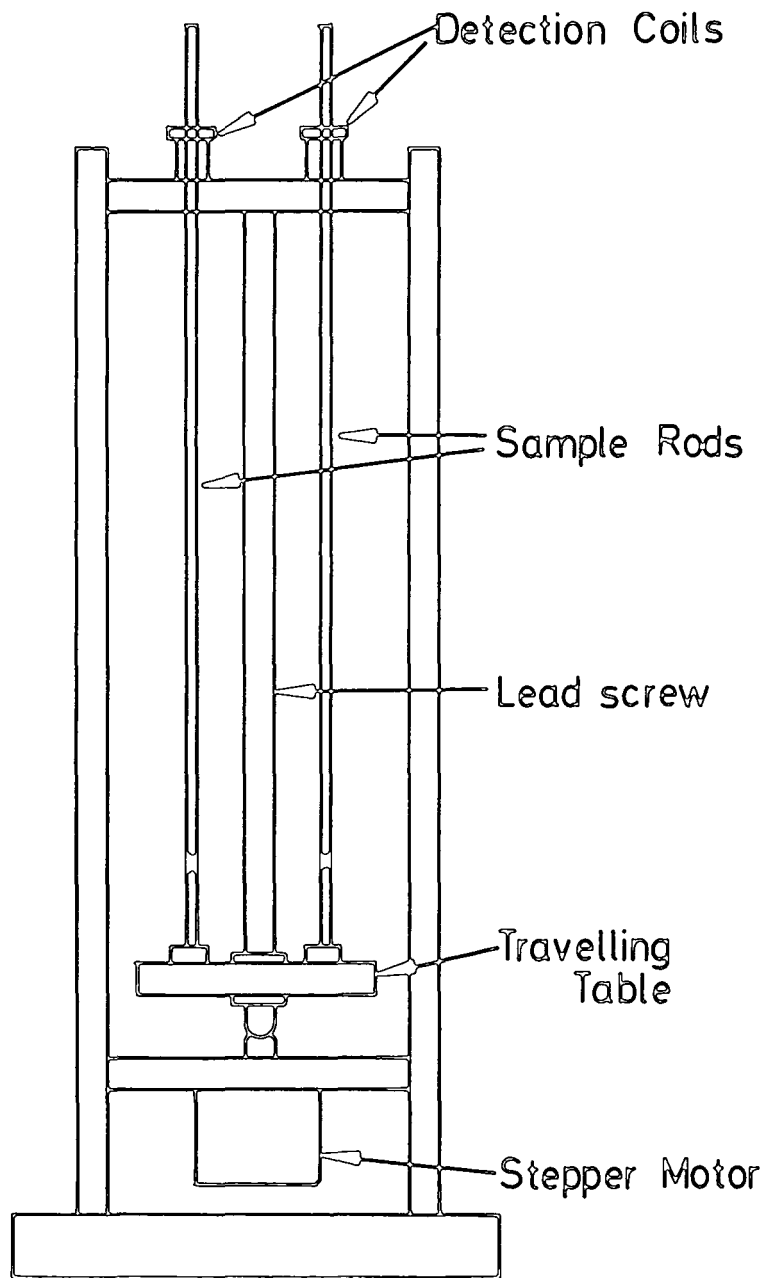
FIGURE 3.9
Schematic illustration of construct-
ion of colloidal stability apparatus.
("Sedometer")

which the 8mm O.D. glass sample rods were placed. These

passed through detection coils mounted on the top of the

aluminium housing. When the stepper motor was driven, the

travelling table scanned vertically allowing the entire

length of the column of magnetic fluid to pass through the

detection coils. The detection system and stepper motor

system were connected directly to the user port of a BBC

microcomputer which controlled the experiment and recorded

data onto magnetic disc. The detection system is outlined

briefly below. The control system, for which the author was

responsible, is described in more detail.

3.2.1 The Detection System

Figure 3.10 shows a block diagram of the complete

sedometer. A Feedback sine-square oscillator SS0603

provided a 1kHz, 10V pk-pk a.c. signal which was coupled to

the inductance bridge via a microphone transformer. The AC

bridge comprised 4 pancake coils wound with 46 s.w.g.

enamelled copper wire to give inductions of $\sim$ 8mH on tufnel

formers and were $\sim$ 2mm thick, 9mm inside diameter and $\sim$ 24mm

outside diameter. These were mounted on the apparatus and

then balanced in situ by positioning ferrite cores in two of

the coils, the sample rods passing through the other two.

The sedometer was always run with an empty glass rod through

one of these and the sample containing rod through the other

thus minimizing the effect of the glass. The out of balance

signal developed across the bridge when magnetic material

was present in the sample coil was amplified by 40/60 dB
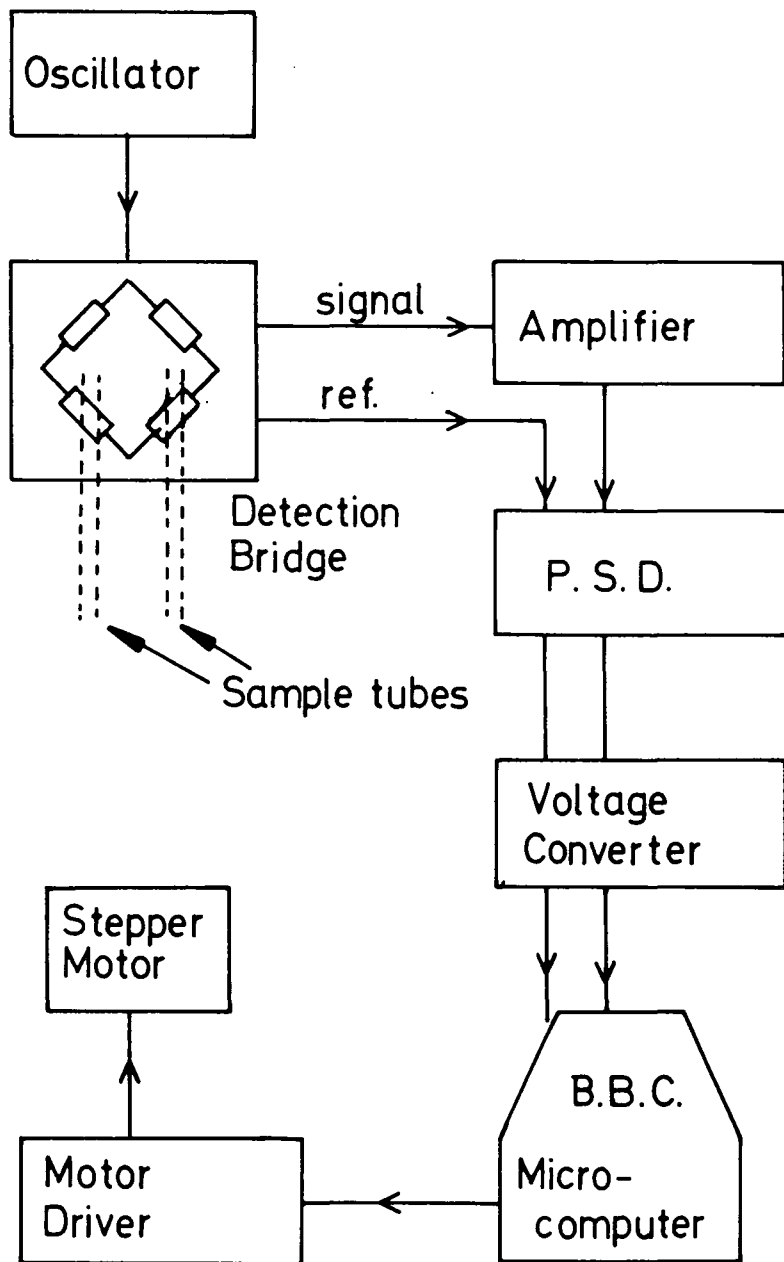
FIGURE 3.10
Block diagram showing sedometer
control/data acquisition system.

using a Brookdeal 432 High |Z| amplifier. This signal was then fed with a reference signal taken from the bridge input to a Brookdeal 402 lock-in-amplifier for signal detection. This provided a linearised ± 1V output proportional to the signal which had to be scaled to 0-1.8V in order to be accessible to the analogue-to-digital converter ('ADC' a μPD7002) on the BBC microcomputer. This was achieved using 741 amplifier circuitry designed by Dr. S.R. Hoon and shown in Appendix A. The reference signal was also scaled and fed into the BBC microcomputer. The voltages detected were stored onto magnetic disc and simultaneously displayed graphically on the computer. They were processed later by a second program after completion of the experiment the "raw" data thus always being preserved. The voltage across the bridge in the absence of the glass tubes was also recorded and then subtracted during data processing which also corrected for drift during the experiment assuming the drift to be linearly dependent on time. The software for this instrument is given in Appendix A.

3.2.2 Scanning Control

The user port of the BBC microcomputer is port B of a 6522 Versatile Interface Adaptor (VIA). It therefore provides 8 TTL logic lines which may be used as input or output. This chip also allows the generation of square wave pulses output on bit 7 of port B through a counter/latch under software control. These were used to drive the stepper motor driver circuit shown in Figure 3.11. Two
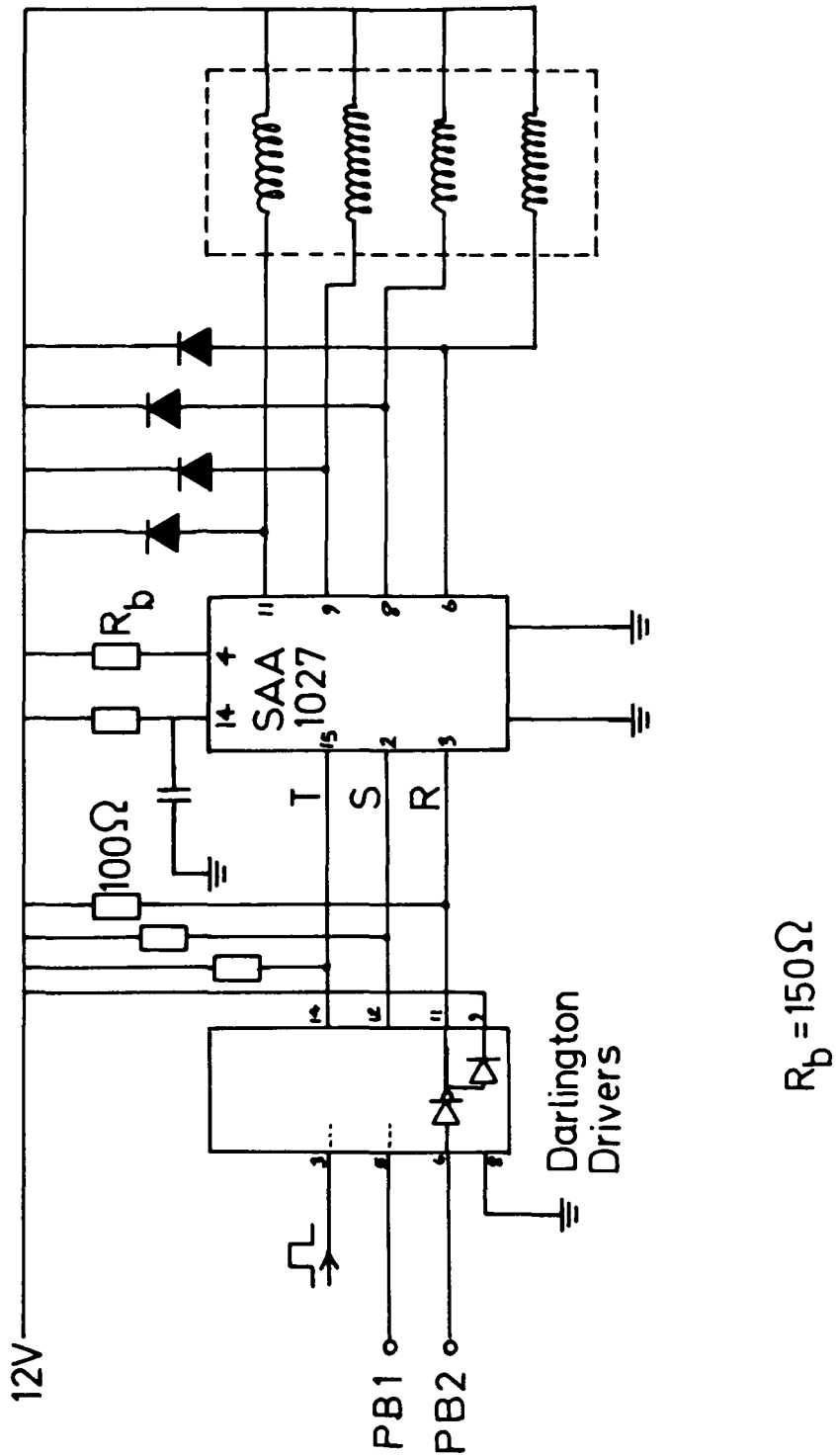
FIGURE 3.11
Circuitry used to drive the stepper motor from the BBC microcomputer.

other inputs were provided to this circuitry from the user
port, one to reset the driver chip (SAA 1027) and the other
to determine the direction of rotation. The 5V outputs from
the BBC were converted to the 12V required by the SAA 1027
using integrated Darlington Drivers. The 5 and 12V were
supplied by a standard RS components power supply unit (RS
591 253).

Two limit switches were placed on the aluminium housing
to detect and halt the motion of the travelling table at the
extremes of its travel. These were connected to the BBC via
the logic circuitry shown in Figure 3.12. Pulses from the
BBC always reached the 3-input AND gate which required both
of the other two inputs to be high (logic 1) in order to
transmit the pulses to the stepper motor circuitry. These
two inputs arise from the XOR gates through inverters and so
require the XOR outputs to be low (logic 0) to transmit
pulses. This is the case when neither or both of XOR inputs
are high. The two inputs to each XOR gate are from a limit
switch and the BBC user port. The limit switches normally
ground their input and the BBC output is always low unless
held high by software. The stepper motor may then receive
pulses until either limit switch is opened by the travelling
table. This causes one input to the XOR gate to go high and
immediately prevents pulses from passing through the AND
gate. The software may then reverse stepper motor direction
and then override the limit switch by setting the other XOR
input high, once again allowing stepper motor movement.
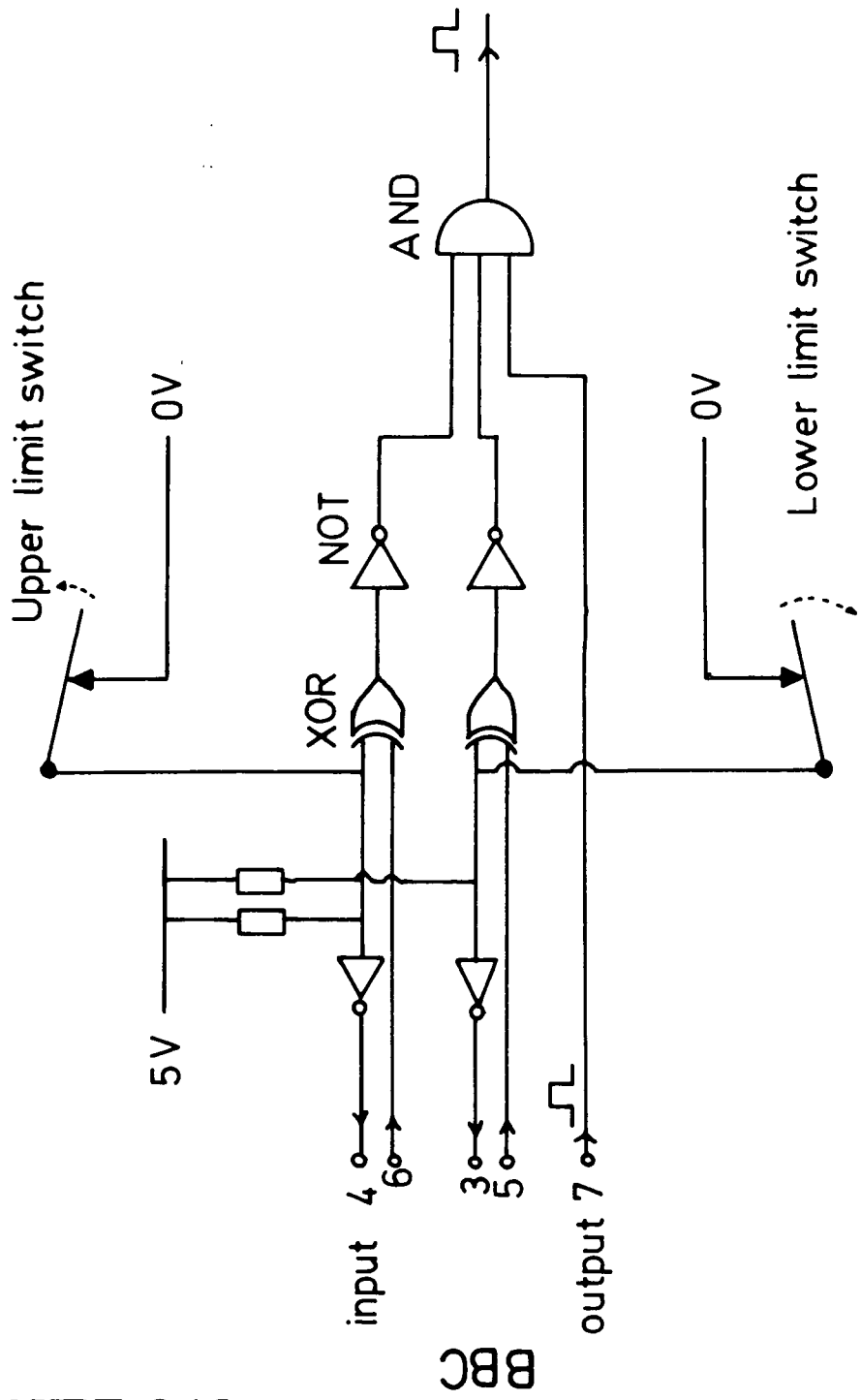
FIGURE 3.12
Logic circuitry for controlling the
sedometer from the BBC microcom-
puter.

When the limit switch closes again the motor will again be stopped as the XOR inputs are again different. On detecting this the software drops its XOR input low and motion may be resumed in the initial logic state. This process allows the table to be positioned at either end of its travel to within the tolerance of the limit switches, taken as $\pm$ 0.1mm. As the stepper motor is driven directly by the microcomputer, any computer crash will immediately halt its motions. Details of the software are given in Appendix A.

As described above, the instrument generated a signal of ~ 0.07V for a 2 $JT^{-1}kg^{-1}$ fluid. During this work, however, it was found that the stability of the balance of the bridge was not good and it is currently being replaced with a universal bridge type circuit.

3.3   The Image Size Analyser

The properties of magnetic fluids are strongly dependent on their particle size distributions. Physical particle sizes are observed using shadow electron microscopy and in order to obtain reliable data from micrograph prints, a large number of particle images (> 500) must be measured. This would be extremely slow and very prone to error if performed manually and so an automated image size analyser designed by Dr. S.R. Hoon was constructed during this study. This instrument is simple and quick to operate; the micrograph is printed onto translucent lightweight document paper, placed on the working surface onto to which a light spot is projected from below and the light spot is made to

coincide with the image diameter by means of a hand wheel
connected to an iris. A footpedal is then depressed which
causes the microcomputer to read the spot size and to
activate the marker pen mechanism which marks the image to
avoid multiple counting. A full description of the
instrument is given by Hoon et al. (1985), a shorter outline
is presented here.

3.3.1 Optical Design and Construction

Figure 3.13 shows the optical design and construction
of the instrument. A 100W tungsten lamp (L) powered by a
D.C. supply illuminates the iris (I) which forms the object
for the optical system. The D.C. supply is used in
preference to an A.C. supply as the periodicity of the
latter would be detectable which would require temporal
averaging of the output and so increase the data acquisition
time. A fibre optic cable coupled to a p-i-n diode (D_1)
samples the light intensity incident upon the iris allowing
the output from the large area photodiode (D_2) to be scaled
in the event of fluctuations in illumination. An optically
flat glass slide (m_1) with its plane at 45° to the optical
axis (ab) acts as a partially reflecting mirror and splits
the light beam. This enables the iris diameter to be
determined optoelectronically by the large area photodiode
(D_2) onto which the slide reflects the iris image. The area
of this diode $(100mm^2)$ always exceeds the cross-section of
the iris image and so its output is linearly proportional to
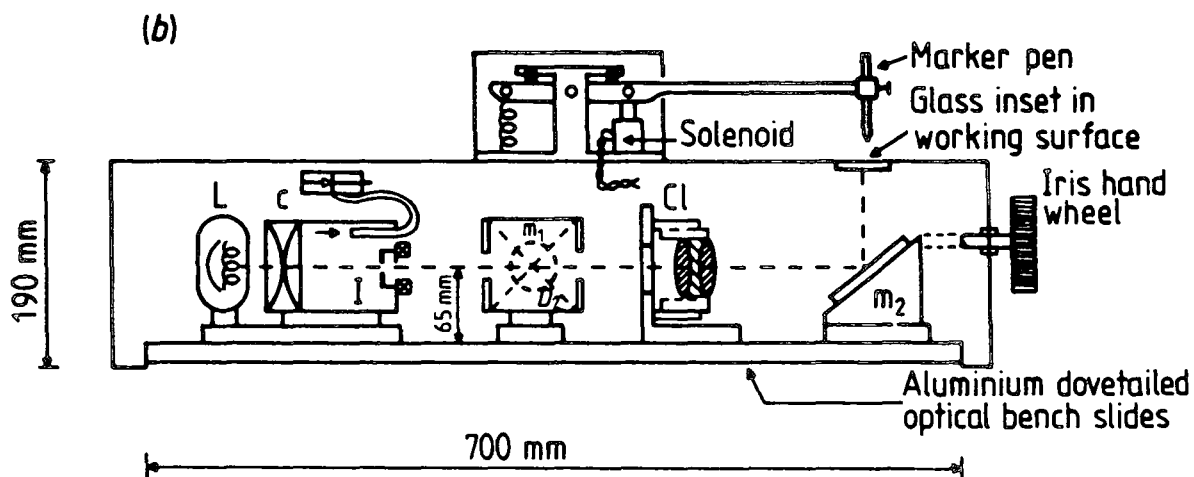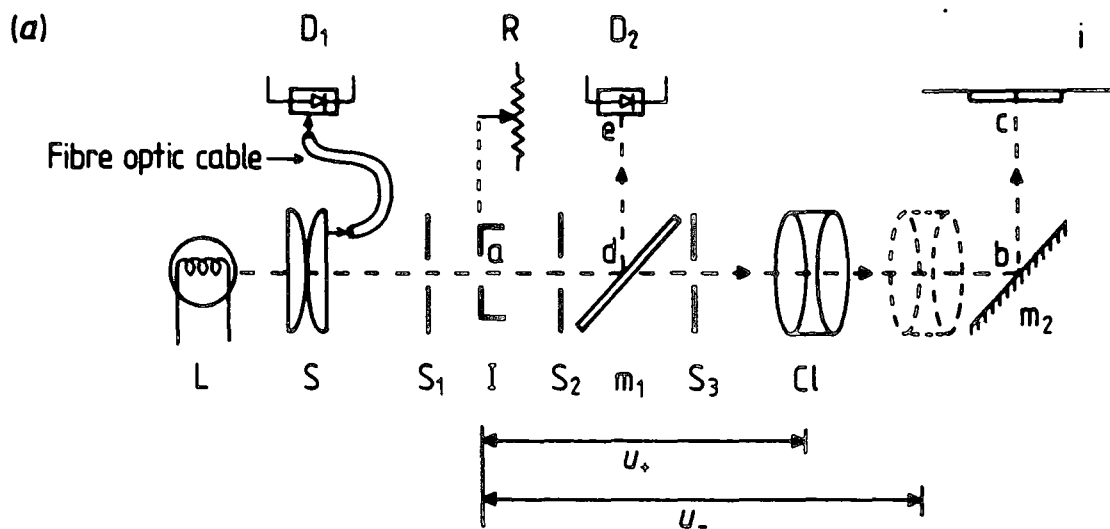
FIGURE 3.13
(a) Optical design and
(b) construction of the image size
analyser.

the image spot size. This device also eliminates mechanical backlash which was found to be present when a potentiometer attached to the iris drive mechanism was used to determine iris diameter. Figure 3.14 illustrates this and also displays the linearity of the photodiode method. The mirror (m_2) is positioned so that the image plane (i) falls just above the glass window (c) inset into the working surface. The compound lens (Cl) may be placed at either of two positions which satisfy the conjugate focii condition thus providing two magnification ranges. As used in this study, a magnification of 0.68 provided image diameters of 0.8 - 8.2mm on the working surface which were suitable for analysing < 10nm particles magnified a total of X 800,000 on the prints. The marker pen is operated by a solenoid attached to a lever and is pulled down towards the surface when the solenoid is activated.

The reproducible error in the optoelectric determination of spot diameter is $\pm$ 0.05mm. The operator error, however, is $\pm$ 0.1mm (naked eye) or $\pm$ 0.05 mm with a x10 eye-piece. The error is therefore limited by the operator. The voltage outputs from the photodiode and p-i-n diode are interfaced to a microcomputer which also senses the depressions of the footpedal and activates the marker pen. This interfacing is described below as it is the work of the author.

3.3.2 Interfacing Details

The two output voltages one proportional to image area,
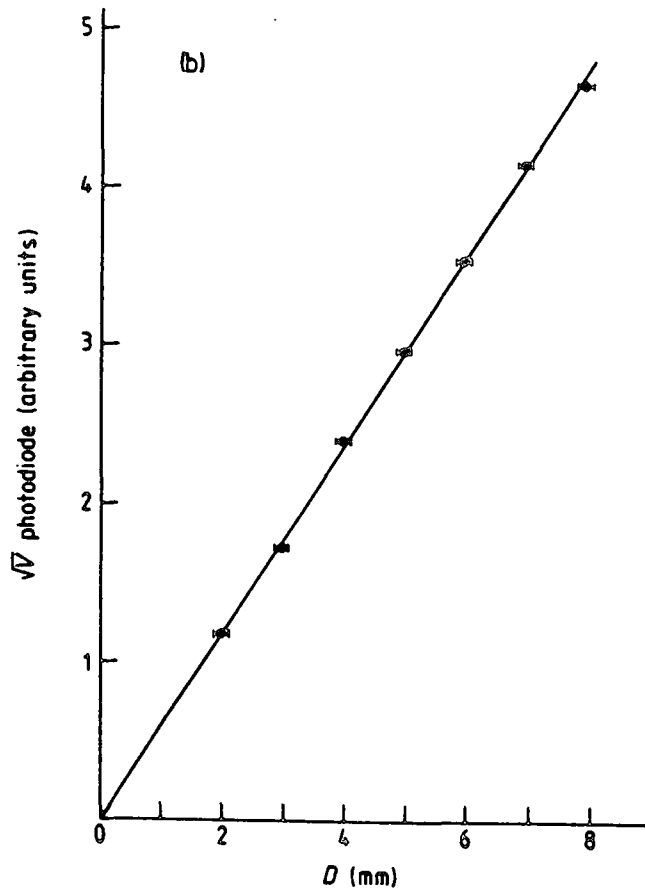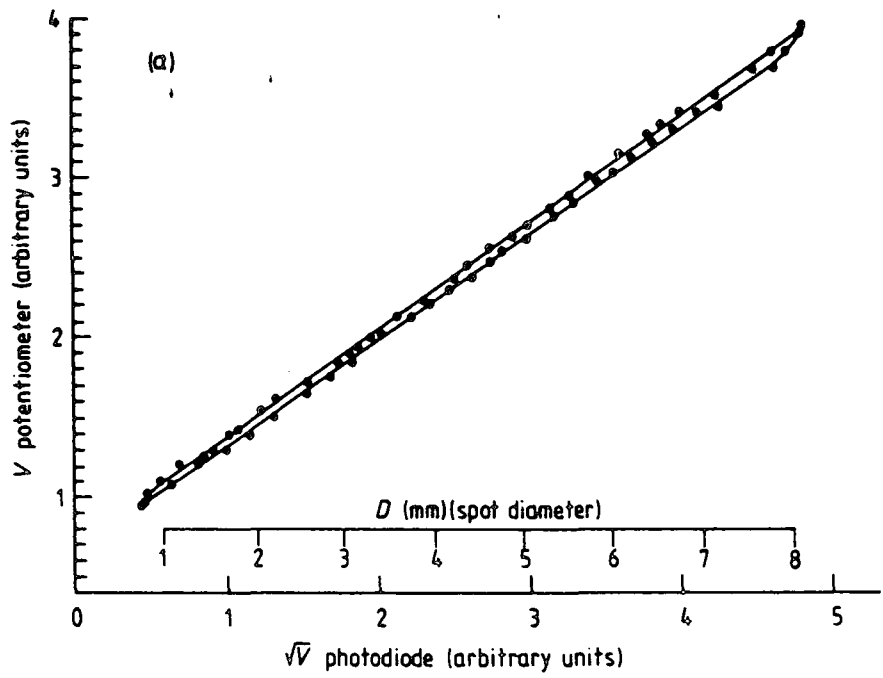
FIGURE 3.14
(a) Mechanical backlash in the iris
   drive mechanism for spot deter-
   mination.
(b) Linearity of the photodiode
   system.

the other to iris illumination must be scaled to be
compatible to the particular ADC of the microcomputer (in
this case 0 - 1.8V as for the sedometer see Section 3.2).
This was achieved in a manner similar to that used for the
sedometer and shown in Appendix A. Detection of the
footpedal and activation of the marker pen required an input
and an output line to the microcomputer. These were
provided by the BBC user port, bit 1 being used as an input
and connected to the footpedal mechanism. When this was
depressed, this bit was sent high which was interpreted by
the software as the signal to read in data. The ADC was
read using a predefined BBC Basic routine (ADVAL), each
voltage being read ten times and the average stored in
computer memory. When this was complete, bit 0, which was
set as an output was set high which activated the marker pen
mechanism. The ADC readings were held in memory (RAM) to
allow inadvertant pressings of the footpedal to be
corrected. After all the images had been analysed, the
voltages were stored onto magnetic disc without any
processing. This preserves the "raw" data without the
limitations of binning and allows maximum flexibility in the
subsequent analysis.

Calibration of the instrument is required and the
control program was written so that this had to be done
before data collection could proceed. A clear perspex
plate with three holes drilled and reamed to 3, 5 and 7mm is
used for calibration. The light spot is set equal to each

of these in turn and the average of 20 readings stored for each along with its diameter in the image data file. A calibration constant was then obtained from

$$CK = -\sum_{j=1}^{3} \frac{\pi d_j^2}{4} \left(\frac{V_i}{V_d} \right) \qquad (3\cdot3)$$

where V_i is the voltage from the intensity diode, V_d the voltage from the large area photodiode and d_j the diameters of the calibration holes. Full listings of the control and analysis software may be found in Appendix B. Since being commissioned this instrument has proved extremely successful and is now an invaluable tool in magnetic fluid research at Durham.

3.4   Electron Microscopy

3.4.1   Shadow Electron Micrographs

Shadow electron micrographs were taken on a Philips TEM 400 electron microscope. Experience found that the sharpest pictures of magnetic fluid particles were obtained at an operating voltage of 80kV, a magnification of 220 000 x using the middle aperture and an exposure time of 5-10s. Carbon-formvar supported on 200 mesh copper grids coated on only one side with magnetic fluid produced the best results. Enlargement of the negatives was by about 3x on printing for the image analyser.

Catalase crystals (supplied by Agar Aids Ltd., Essex) with lattice spacings of 8.75nm and 6.85nm were used to calibrate the microscope magnification. At a nominal 220000x only the larger of these spacings could be observed and

from them it was found that the true magnification of the microscope was 201 867x, an error of -8.2%. This introduces a correction of +8.9% to particle diameters calculated using the displayed magnification. The particle sizes in this study have been corrected acordingly.

3.4.2 Transmission Electron Diffraction

Transmission electron diffraction micrographs were taken by Dr. G.J. Russell (Department of Engineering and Applied Sciences) on a Joel JEM 120 transmission electron microscope using typically 100 kV accelerating voltage and camera constants (λL) of 8cm$\overset{\circ}{A}$. Photographs were calibrated using thin films of A (a_O = 4.0496$\overset{\circ}{A}$) or Ag (a_O = 4.0862$\overset{\circ}{A}$) whose diffraction lines gave the camera constant from,

$$K = a_o \sqrt{\frac{D^2}{h^2 + k^2 + l^2}} \qquad (3 \cdot 4)$$

where D is the diameter of the rings on the printed micrograph (and hence includes print magnification) and h, k and l are the Miller indices of the lattice planes. K was always obtained as an average over all the diffraction lines available. The lattice spacings of the unknown material are then obtained as

$$d = \frac{K}{D_u} \qquad (3 \cdot 5)$$

where D_u is the diameter of the diffraction rings of the unknown material. If the error in measuring D is $\pm \Delta D$ then this becomes

$$d = \frac{K}{D} \mp \frac{K \Delta D}{D^2} \qquad (3 \cdot 6)$$

to first order. ΔD is taken to be 0.5mm for which the error in d is typicaly $\pm$ 0.01$\overset{o}{A}$. Some diffraction pictures were obtained from samples in a goniometer stage below the projector lens instead of the normal objective lens position to avoid the high magnetic field in the latter. They were not as clear, however, as the usual pictures and did not reveal any magnetic field effects.

3.5 Torque Measurements

Torque curves were taken on an automated torque magnetometer which employed a mutual inductance technique to measure angular displacement. This instrument has been described by Paige and Tanner (1982) and Paige (1983) and will not be discussed here. The only major modifications made to the instrument since the above reports were further automation, especially of the magnet rotation which permitted rotational hysteresis measurements to be made and in the case of very small torques (as for magnetic fluids) the use of a tantalum wire suspension instead of the triple leaf spring arrangement. The author is indebted to Dr. D.M. Paige for many of the torque measurements and to Mr. C.D.H. Williams for a calibration of the magnetometer. This was performed using a single layer coil of copper wire. Torque amplitude errors are taken as $\pm$ 2%.

3.6   Demagnetization Apparatus

Measurements of the texture of potted ('frozen' in fibreglass resin) magnetic fluids by initial susceptibility required demagnetization of the samples.   The samples were flat discs of fibreglass resin, impregnated with magnetic fluid, of 5mm diameter and 3mm thickness.   They were allowed to set in magnetic fields of various strengths applied parallel to the plane of the disc.   Figure 3.15 shows the apparatus used to demagnetise these samples.   The discs were rotated about the normal to their plane by an air turbine fabricated from 'Perspex' and supplied with compressed air. This turbine was placed at the centre of a water cooled solenoid supplied with 240V, 50Hz mains.   At 240V this solenoid developed an AC magnetic field of B_{rms} = 0.04T at its centre.   The voltage supply was reduced manually and finally switched off before the air turbine was stopped. This process was adopted in order to ensure maximum randomization of the particle moments.   Measurements on these samples are reported in Chapter 5.

3mm

B_0

5mm

(a) Sample

Sample

Air turbine

Solenoid
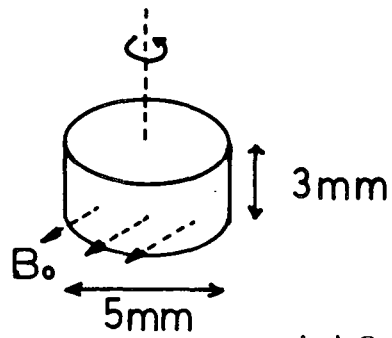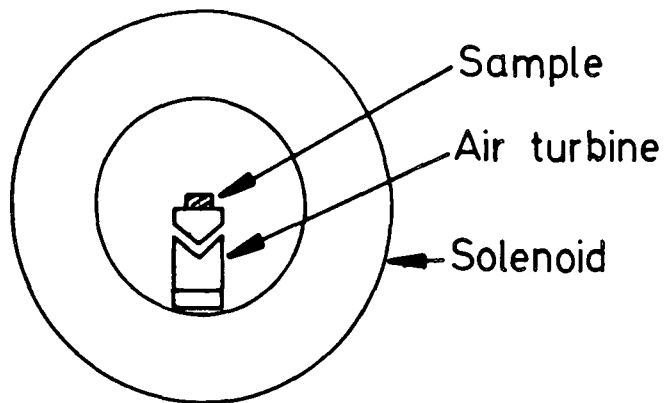
(b) Demagnetisation
Apparatus

FIGURE 3.15
Apparatus used to demagnetise disc
samples for initial susceptibility
measurements.

CHAPTER FOUR

PARTICLE SIZE DISTRIBUTIONS

4.1 Introduction

The preparation of magnetic fluids inevitably results in a distribution of particle volumes. The magnetic and physical properties of these fluids are strongly dependent upon the particle size distribution (p.s.d.). The magnetisation curve at room temperature, for example, will deviate from simple Langevin behaviour. The presence of a few large particles can precipitate aggregations via magnetostatic interactions and thus limit the colloidal stability of magnetic fluids. Optical properties, e.g. dichroism, or rheological properties, e.g. viscosity, are also strongly size dependent. If the p.s.d. is known then the behaviour of the magnetic fluid may be predicted. Usually, however, the p.s.d. is unknown and must be determined empirically. Knowledge of the p.s.d. is also desirable in order to assess the preparative routes used to make the fluids and is of particular interest for this reason in this study. The particle size distribution obtained will reflect the experiment used to obtain it. Measurements on viscosity or pulsed field dichroism/birefringence decay will result in hydrodynamic particle sizes which include the influence of the surfactant

coating and possible particle chaining. Measurements of magnetisation give <u>magnetic</u> sizes which exclude surfactant coating and any non-magnetic layers on the particle surface. Electron microscopy is the most direct method and the <u>physical</u> size obtained excludes surfactant but includes all the particle body. These measurement techniques are discussed further below.

4.2 Hydrodynamic Size

Rosensweig et al. (1969) noted that when viscosity was measured the sizes of the particles should include the thickness of the surfactant layer. Davies and Llewellyn (1979) measured the hydrodynamic size of the particles by using a pulsed field-birefringence decay technique. They obtained the particle size from the decay time using the expression

$$\frac{1}{\tau} = \left(\frac{9kT}{8\pi\eta r^3}\right)(2\ln 2 - 1) \qquad (4\cdot 1)$$

where r is the <u>mean</u> particle radius and η is the viscosity of the carrier liquid. For Co particles prepared by the method of Hess and Parker (1966) they obtained a particle diameter of 13.0nm. As electron microscopy revealed a particle size of 8.0nm, they concluded that the surfactant coating was 2.5nm thick. Hayes and Hwang (1977) measured dichroism decay using pulsed fields and obtained the particle size from the relaxation time according to

$$\frac{1}{\tau} = \frac{3kT}{2\pi\eta r^3} \qquad (4\cdot 2)$$

Examining a commercial magnetite system, they obtained
a particle diameter of 62.0nm whilst from electron
microscopy they obtained 28.0nm. They conclude that
aggregation/chaining is present in their fluids which is
consistent with the observations of Llewellyn (1983) and
Scholten (1980). O'Grady (1982) used the technique of
Davies and Llewellyn to examine cobalt particles prepared by
organometallic decomposition. This author also obtained
hydrodynamic sizes from viscosity measurements assuming the
Einstein relations (Equation 2.14) and relating the
hydrodynamic packing fraction derived from it to the
particle size by

$$\phi_H = n \ \frac{\pi \ d_H^3}{6} \hspace{3cm} (4 \cdot 3)$$

where n is the number of particles per unit volume and is
obtained from magnetic measurements. He obtains
birefringence diameters of between 20.5 and 26nm whilst
viscosity measurements give diameters from 14.3 to 20.5nm.
From electron microscopy, the physical size was about 5nm
and as the surfactant molecules (oleic acid) were 2nm in
length, the hydrodynamic size might have been expected to be
< 9nm. In the light of the later work by Llewellyn (1983)
it is seen to be likely that birefringence measurements
detect particle aggregates rather than single particles.
Viscosity measurements were also > 9nm and Weser and
Stierstadt (1985) point out that in a magnetic fluid there

PAGE 95

is usually excess surfactant present in the carrier liquid. They also consider the possibility of particles so small that they are not detected magnetically. Both of these contribute to the viscosity but are not accounted for in (4.3) which may explain why O'Grady over-estimates the hydrodynamic size with viscosity measurements.

It appears, therefore, that measurement of single particle hydrodynamic diameter is unreliable. Such measurements have not been attempted in this study.

4.3 Magnetic Particle Size

The magnetisation relation for a magnetic fluid containing a distribution of non-interacting moments, m, was given by equation (2.42);

$$M_{ff}(B_o) = M_{ff}^\infty \int_0^\infty f(m)\,dm\; L\left(\frac{mB_o}{kT}\right) \qquad (4\cdot4)$$

More generally one can write,

$$P(B_o) = \int_0^\infty f(m)\,dm\; G(m,K,B_o) \qquad (4\cdot5)$$

where P is a magnetic property, K is the anisotropy constant for the particles and G(m,K,Bo) is the relation between P and Bo for a single particle size. (Integrations over K should be included if there is a distribution of anisotropies although in practice an effective K for all particles is often assumed). For example, P could be the torque per unit volume (Chantrell et al. 1983) or the isothermal remanent magnetization (Chantrell et al. 1977).

The room temperature magnetization curve is considered here.

If f(x)dx is defined to be the fraction of the total volume with property $x \varepsilon (x, x+dx)$ then the magnetization curve is given by

$$M_{ff}(B_o) = M_{ff}^\infty \int_0^\infty f(x)dx\, L(x, B_o) \qquad (4 \cdot 6)$$

where x can be the particle moment, the particle volume, the particle diameter or the particle radius. Three aspects of this equation should be made clear; firstly, it is the distribution of magnetic moments which is measured and thus their distribution is fundamental, secondly, the preparative routes actually produce a distribution in particle volume and thirdly, that if the form of the distribution of a parameter, x, is assumed, then in general none of the other related parameters will have the same distribution. (For example, if the particle volumes are distributed acording to a normal distribution then the particle diameters, radii and moments will not have normal distributions). Thus, if a distribution is to be assumed in order to calculate the magnetization curve then it should be the moment distribution function. However, if the distribution of particle size is known from the preparative route, then it is the particle volume distribution which is known. The relationship between volume and moment is usually taken as

$$m_p = V_p\, M_b^\infty \qquad (4 \cdot 7)$$

This raises the question of whether the magnetisation retains its bulk value for particles of sizes down to 1nm.

This fundamental question has not yet been conclusively answered, for example Abeledo and Selwood (1961) claim that magnetization is size independent down to those sizes whilst Kohara et al. (1985) claim it decreases with decreasing size. Mossbauer data on thin films and fine particles, (Morrish and Haneda (1983)), on the other hand seems to indicate surface enhancement of magnetization which would increase magnetisation as size decreased. Whatever the fundamental effect may be, however, the influence of chemical oxidation and surfactant reactions on the surface of metallic particles will dominate and reduce the moments of the particles compared to (4.7). It is now common practice to assume the existence of magnetically "dead" layers on the surface of the particles in order to explain the difference between magnetic and physical sizes.

Equation (4.6) represents a linear integral equation (Fredholm integral) of the first kind in the unknown function $f(x)$. Even assuming $M(Bo)$ and $L(x,Bo)$ were known for every x and Bo, inversion of the integral to obtain an analytical solution for $f(x)$ may not be possible. In practice, only a limited number of values, $M_i = M(Bo=Bo_i)$, the experimental points, are available. Each of these has some uncertainty, δM_i, associated with them. This renders the problem (4.6) "ill-posed" in that no <u>unique</u> solution exists unless some other condition is imposed upon it. There have been two main approaches to this, either the form of the distribution $f(x)$ is decided a priori and its

parameters adjusted to obtain a best fit to the data, or an extreme condition such as maximising the entropy, is imposed. These are discussed below.

4.3.1 A priori Size Distribution

(a) Explicit Expressions

In possibly the first observation of superparamagnetic behaviour, Elmore (1938a,b) found deviation from a single volume Langevin magnetization curve. Selecting a normal (Gaussian) distribution function, he numerically integrated (4.6) until a least squares best fit had been obtained. This method has remained in use and indeed has been used by the author (see below). Bean and Jacobs (1956) pointed out that the method of magnetic granulometry, whereby particle sizes are obtained from the initial susceptibility and the approach to saturation could be applied to "frozen", intrinsically superparamagnetic systems as well as colloidal suspensions. The particle volumes are obtained from equations (1.24) assuming $m_p = v_p M_b^\infty$ as,

$$v_{lf} = 3 \frac{kT}{M_b^\infty} \cdot \frac{\kappa}{M_{ff}^\infty} \qquad (4 \cdot 8a)$$

$$v_{hf} = \frac{kT}{M_b^\infty} \cdot \frac{I^\circ}{M_{ff}^\infty} \qquad (4 \cdot 8b)$$

where κ is the initial susceptibility of the system, M_b^∞ is the saturation magnetisation of the bulk particle material, M_{ff}^∞ is the saturation magnetisation of the fine particle

system and I^O is the intercept on the $(1/B_0)$ axis of the limiting slope of an M vs $(1/B_0)$ plot as $(\frac{1}{B_0}) \to 0$, see figure 4.1. M_{ff}^{∞} is also obtained from this plot. Bean and Jacobs point out that these equations are for a single volume system and that if a size distribution is present then the low field value (4.8a) will favour larger particles whilst the high field value (4.8b) will be biased towards smaller particles. Becker (1957) assumed a rectangular distribution and using the above approach solved (4.6) to obtain

$$\overline{v} = 3 \frac{kT}{M_b^{\infty}} \cdot \frac{\kappa}{M_{ff}^{\infty}} \qquad (4 \cdot 9a)$$

$$\frac{\sigma}{\ln\left(\frac{2\overline{v}+\sigma}{2\overline{v}-\sigma}\right)} = \frac{kT}{M_b^{\infty}} \cdot I^O \qquad (4 \cdot 9b)$$

where $\overline{v}$ is the mean of the volume fraction distribution and 2σ its width (see Figure 4.1b). Kneller (1958) also assumed a rectangular distribution and obtained the same results. He does however, solve (4.6) analytically in this case to give

$$M_{ff}(B_0) = \frac{M_{ff}^{\infty}}{2b\alpha} \ln\left\{\frac{(1-b)\sinh(\alpha(1+b))}{(1+b)\sinh(\alpha(1-b))}\right\} \qquad (4 \cdot 10)$$

where $\alpha = mB_0/kT$ and $b = \sigma/v$, for the magnetisation curve. Asimow (1965) considers the general case of systems containing particles with anisotropy where the particles are frozen. He points out that use of the limiting slope on the M vs $1/B_0$ plot under these conditions can lead to serious errors as the approach to saturation can be very slow. This
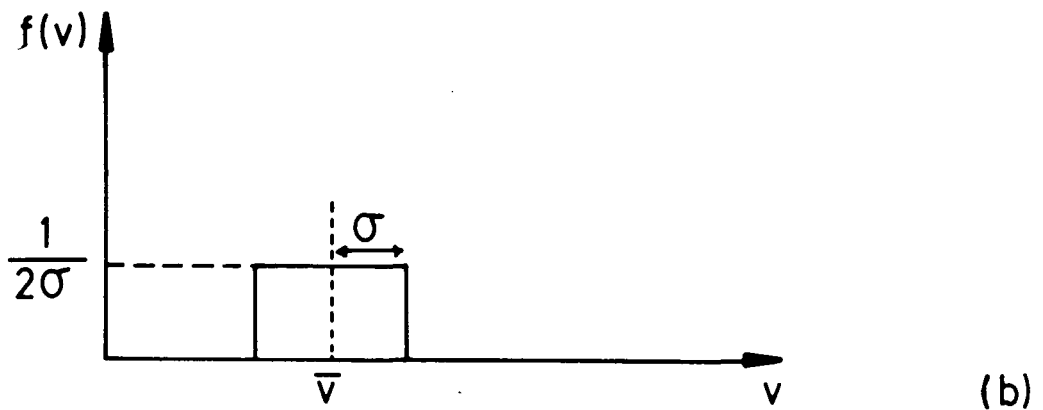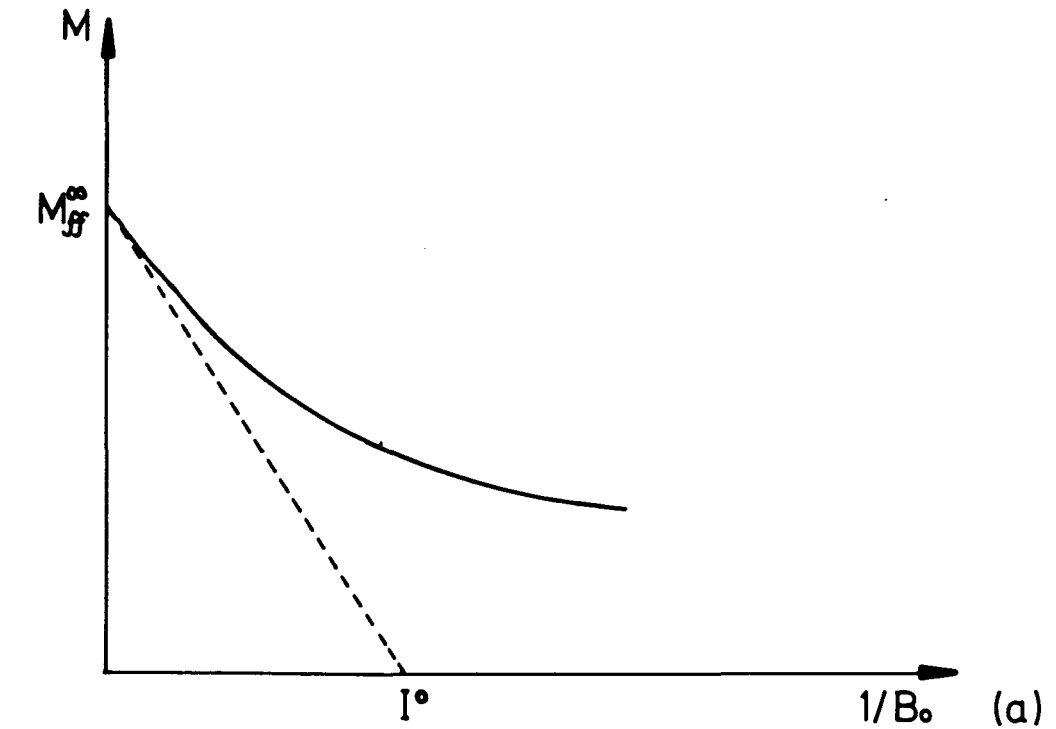
FIGURE 4.1
(a) Definition of symbols for magnetisation plotted against inverse field.(Eqn. 4.8)
(b) Rectangular distribution function of particle volumes. (Kneller 1958)

can also be the case for isotropic particles, colloidally suspended if they are very small (< 5.0nm) thus requiring higher fields for the magnetization curve. This has been studied herein and is reported below.

Chantrell (1978) assumes a lognormal distribution of particle diameters. Rewriting his results in terms of volume, results in

$$\overline{V}_{\frac{1}{2}} = \frac{kT}{M_t^\infty} \sqrt{\frac{3 \kappa I^0}{M_{ff}^\infty}} \qquad (4\cdot11a)$$

$$\sigma = \frac{1}{3}\sqrt{\ln\left(\frac{3\kappa}{I^0 M_{ff}^\infty}\right)} \qquad (4\cdot11b)$$

where $\overline{V}_{\frac{1}{2}}$ is the <u>median</u> particle volume and σ is a parameter of the <u>volume fraction</u> lognormal distribution. Appendix C describes the lognormal distribution and discusses how to convert from median volume fraction to mean number fraction values. A great deal of confusion arises when values from (4.11) above are compared with electron microscopy (EM) data. The values above are for a <u>volume fraction</u> distribution whereas EM data gives <u>number fraction</u> values. Thus $\overline{V}_{\frac{1}{2}}$ and σ must be converted to number fraction mean and standard deviation before making any comparisons. All of this can be avoided if the method of Cahn (1957) is applied.

Cahn, commenting on the work of Becker, pointed out that it is unnecessary to know the form of the distribution in order to calculate the number fraction mean and standard deviation. If n(v)dv is the number of particles per unit

volume of sample with volume $V \varepsilon (v,v+dv)$ then the packing fraction of the particles is given by

$$\varepsilon_v = \int_0^\infty v \, n(v) dv = \frac{M_{ff}^\infty}{M_b^\infty} \qquad (4 \cdot 12)$$

and the approach to saturation by

$$M(B_0 \longrightarrow \infty) = M_{ff}^\infty \left(1 - \frac{kT}{M_{ff}^\infty} \cdot \frac{1}{B_0} \int_0^\infty n(v) dv\right) \qquad (4 \cdot 13)$$

From the latter the number of particles per unit volume, N, may be obtained as

$$N = \frac{N_p}{V_{ff}} = \frac{M_{ff}^\infty}{kT} \cdot \frac{1}{I^\circ} \qquad (4 \cdot 14)$$

where Np is the total number of particles in the system. The mean particle volume, $\overline{v}$, is given by

$$\overline{v} = \frac{V_{ff}}{N_p} \int_0^\infty v \, n(v) \, dv = \frac{kT}{M_{ff}^\infty} \cdot I^\circ \cdot \frac{M_{ff}^\infty}{M_b^\infty}$$

$$= \frac{kT}{M_b^\infty} I^\circ \qquad (4 \cdot 15)$$

The standard deviation is obtained as

$$std \; dev. = \frac{kT}{M_b^\infty} I^\circ \sqrt{\frac{3\kappa}{M_b^\infty I^\circ} - 1} \qquad (4 \cdot 16)$$

these are, of course, identical to the equations obtained from the Chantrell and Becker analyses when converted to number fraction mean and standard deviation. Cahn also defines an expression for the root mean square volume;

$$(\overline{v^2})^{\frac{1}{2}} = \frac{kT}{M_b^\infty} \sqrt{\frac{3\kappa I^\circ}{M_{ff}^\infty}} \qquad (4 \cdot 17)$$

which is identical to the expression of Chantrell for the volume fraction median. This is a coincidental property of

the lognormal distribution which has

$$\overline{V}_n = (\overline{V^2})^{\frac{1}{2}}_v \tag{4.18}$$

where subscript n = number fraction, v = volume fraction.

From this survey of the particle size literature, it is

apparent that the method of Cahn has much to commend it.

Its values may be compared directly with EM values although

of course, it gives no indication of the form of the

distribution function.

(b) Numerical Integration

Equation (4.6) is susceptible to numerical integration

and the advent of powerful computing facilities makes this a

realistic method for determing p.s.d. This is an a priori

technique where for this study the lognormal and normal

distributions have been used. A program was written in

PASCAL and is listed in Appendix C. The integration method

used was a compound Simpson's rule (Davis and Rabinowitz

1984) which was fully tested on simpler functions before

being incorporated into the program. Care was taken to keep

numerical values in the integral to about ~ 100 by extracting

all exponents before programming. The limits of the

integral were chosen so that 99.8% of the distribution was

included. Approximations to the Langevin function, $L(x)$,

are required for very small or very large values of x and it

was found that for $x < 0.1$ the approximation $L(x) = x/3 -$

$x^3/45$ was satisfactory whereas for $x > 6$, $L(x) = 1-1/x$ was

appropriate and the error in either is less than 0.01%.

Minimization was a least squares type process using the

absolute difference between experimental and theoretical values. It was not found possible to automate this entirely as a unique minima does not exist. The operator can, however, easily recognize when the minima region has been reached. Some results from using this program are described below.

Before discussing the maximal constraint methods for obtaining p.s.d's, some comment on the choices of distribution functions used above is necessary.

4.3.2 Choice of Distribution Function

The major criticism of the a priori techniques is that they introduce unnecessary bias into the data. This is undeniably true, however, the reduction in effort obtained by so doing may be such that some bias is tolerable. Kneller (1969) claims that the magnetisation curve is insensitive to the exact form of the distribution. Whilst this would explain why various authors have obtained reasonable fits with normal, rectangular and lognormal distributions, it is not strictly true. This may be seen from Figure 4.2 which shows calculated curves for normal (solid line) and lognormal (circles) distributions using the program described above. It may be seen, however, that the difference is small and may well be less than the experimental errors in magnetisation measurement. As the real p.s.d. and preparation process are not independent, then it is reasonable that in choosing a distribution, the
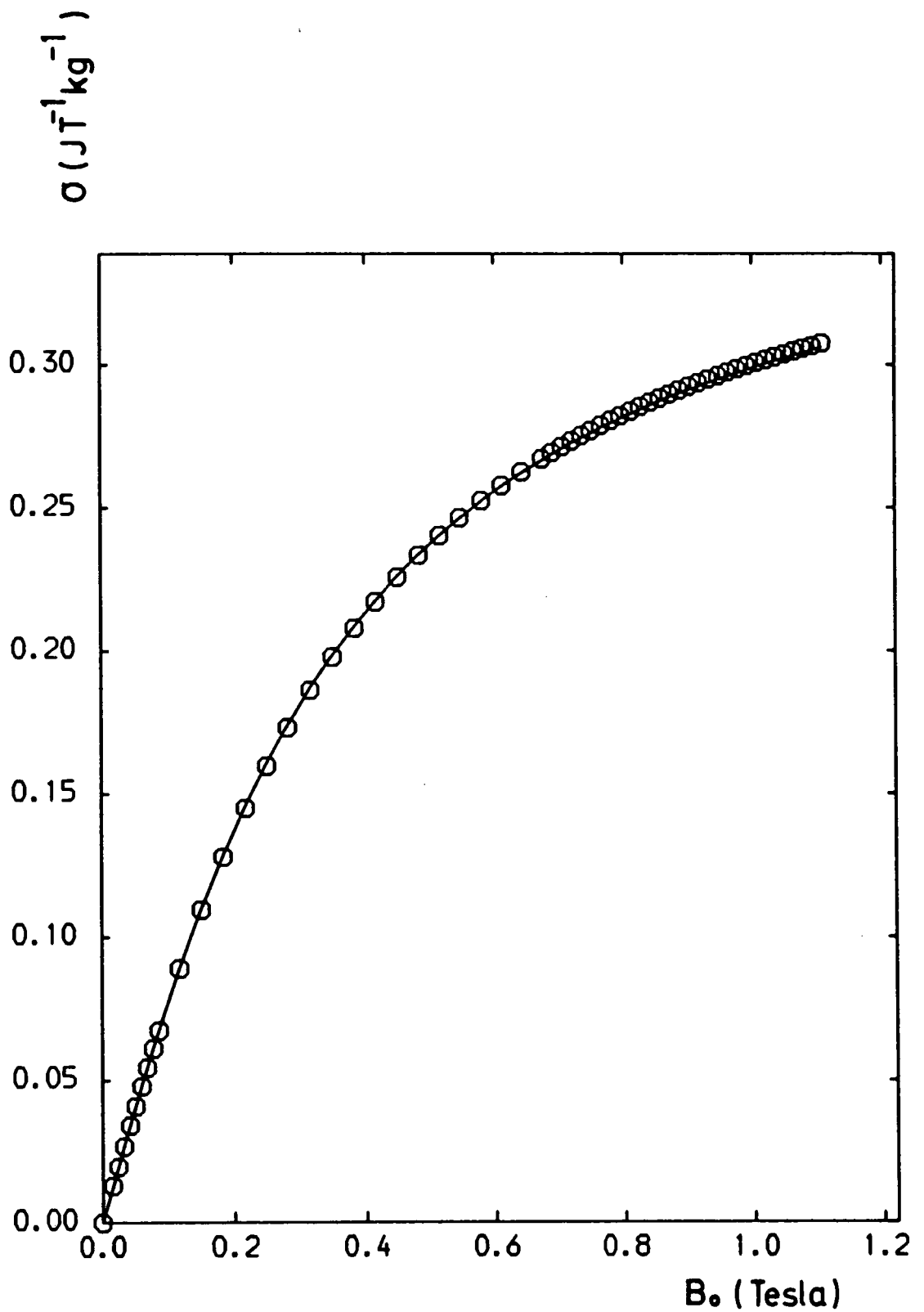
FIGURE 4.2
Calculated Langevin magnetisation curves assuming normal (solid line) and lognormal (circles) distributions of particle diameters.

physical process involved in forming the particles should

dictate the choice. Granqvist and Buhrman (1976a,b) discuss

this and state that for processes involving essentially

random atomic addition, the resulting distributions will be

normal, whereas if the process involves liquid-like

coalesence of particles already nucleated, then the

distribution will be lognormal. These authors also state

that the distribution width is predominantly a function of

the type of preparative route rather than the exact

conditions of a particular route, a conclusion which this

study would support. (See below). The lognormal

distribution is also appropriate to particles formed by

breaking larger particles into smaller areas which are a

random fraction of the original value. Thus commercial

fluids prepared by ball-milling follow a lognormal

distribution. The exact physical process involved in

particle formation during organometallic decomposition is

unknown but O'Grady and Bradbury (1983) have found that the

particle sizes are normally distributed. This would seem to

invalidate use of the lognormal distribution in analysing

these fluids. However, if the width of the distribution is

narrow, i.e. std. dev. < 1.0 say, then the difference

between normal and lognormal distributions is small as

illustrated in Figure 4.3. Under these conditions it is

unlikely to be possible to distinguish between them from

magnetic measurements unless the data is extremely precise.

    There are, however, other reasons why the lognormal
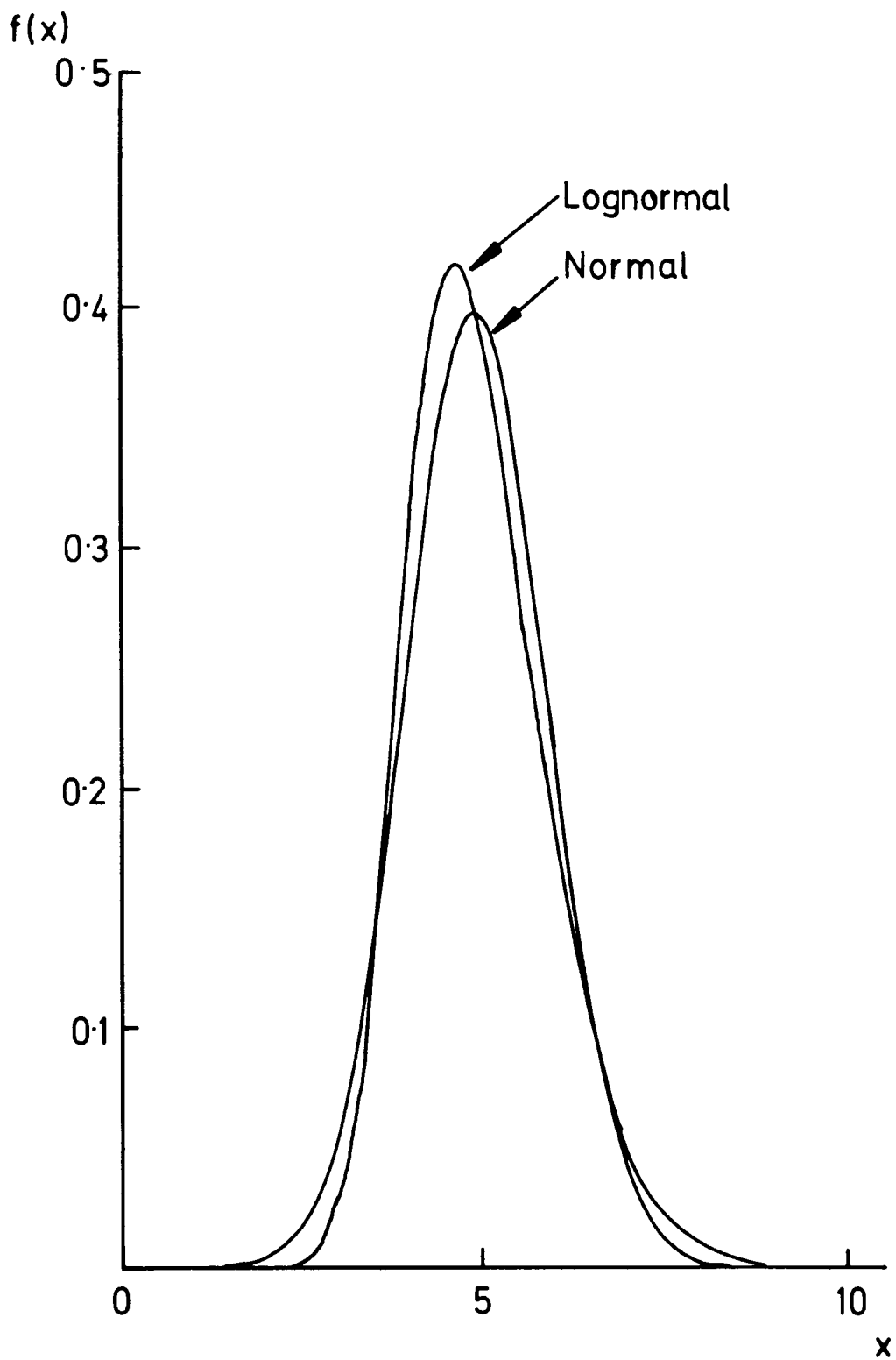
FIGURE 4.3
Comparison of normal and lognormal distribution functions each with a mean of 5.0 and standard deviation=1.0.

distribution is chosen: it is amenable to analytical
solution in equation (4.6) and it has the rare property that
if a random variable X is distributed according to the
lognormal distribution $\Lambda(\mu, \sigma^2)$ then the random variable cX^b
is also distributed lognormally according to $\Lambda(a+b\mu, b^2\sigma^2)$
where $c = e^a$. (See Appendix C). This latter property means
that if it is assumed that the particle volumes are
distributed lognormally then so are the particle moments,
particle diameters and particle radii. Therefore, the
assumption of one property's distribution gives those of all
the related properties. The fact that the lognormal
distribution allows analytical solution in many instances
for the magnetic equations involving particle sizes together
with the above rare property and the fact that it is not
very different to a normal distribution explains why its use
is almost universal in fine particle work.

4.3.3 External Constraint Methods

If the form of the distribution function is paramount,
then obviously the above technique cannot be applied. Two
approaches to obtaining the form of the distribution have
been published, Potton (1983), Potton et al. (1984) use a
maximum entropy external constraint whilst Weser and
Stierstadt (1985) use the regularization method.

(a) Maximum Entropy Technique

The additional criteria to be satisfied by the
probability distribution, p_i, in this case is that the

entropy

$$S = - \sum p_i \ln(p_i) \qquad (4 \cdot 19)$$

must be maximised. In addition, the noise of the data must

be considered and this is done using a single χ^2 statistic,

$$\chi^2 = \sum_{i=1}^{N} \frac{(M_i - D_i)}{\sigma_i} \qquad (4 \cdot 20)$$

where M_i are the noisy experimental points and D_i the data

obtained from the distribution function p_i. Each data point

should contribute ~ 1 to χ^2 and so a solution of (4.6) is

sought which maximises the entropy and has $\chi^2 = N$, the

number of data points. The starting distribution is taken

to be a uniform distribution over the range of particle

sizes to be considered. The resulting distribution is thus

largely free of bias, some inclination towards a uniform

distribution being the only bias present. This method does

not extract any information from the data which is not

present.

Potton et al. also consider the significance of the

solution. She points out that two restrictions are imposed

by the data, firstly the noise on the data (assumed

Gaussian) and secondly the finite number of data points

available. As a continuous distribution f(x) is sought from

(4.6) this last point places a serious limitation on the

solutions obtainable. Potton defines a quantity W which

measures the resolution of a solution, i.e. how close the

solution is to the "real" solution and also a measure, σ^2,

of the error introduced by the statistical noise on the data

points. She discovers that in general these cannot be minimized simultaneously, as the resolution is improved the statistical precision (error bars on the derived histogram) worsens and vice versa. This technique provides a means for establishing whether isolated secondary peaks in the distribution are significant or not.

This method has been applied to one of the fluids of this study together with various other techniques and the results are described below.

(b) Regularization Method

The above technique may be the best means for extracting p.s.d.s from magnetization curves however it does involve a great deal of computational effort. Weser and Stierstadt (1985b) have developed a discrete method based on the regularization technique which they claim requires less computational effort. These authors write the magnetisation of a fine particle system in terms of N magnetization fractions,

$$w_i = \left(\frac{n_i v_i}{V_{ff}} \right) M_b^{\infty} \qquad i = 1, N \qquad (4 \cdot 21)$$

where there are n_i particles with volume v_i. The magnetisation of the system is then

$$M_{ff}(B_o) = \sum_{i=1}^{N} w_i L \left(\frac{m_i B_o}{kT} \right) \qquad (4 \cdot 22)$$

and they fit this to the experimental data using least squares,

$$\sigma = \sum_{i=1}^{K} (M_t - M_e)^2 \qquad (4 \cdot 23)$$

where subscript t = theoretical, e = experimental and K is
the number of data points. The regularization technique
imposes another constraint on the data which they express as

$$\rho = \sum_{i=1}^{N} w_i^2 \qquad (4 \cdot 24)$$

where ρ must be as small as possible. This constraint
stabilizes solutions. Their external condition is then to
minimise σ' where

$$\sigma' = \sigma + \alpha \rho \qquad (4 \cdot 25)$$

where α is an adjustable parameter called the regularizing
parameter. Small values of this lead to accurately fitted
magnetization curves but wide size distributions. Large
values of α give smooth distributions but large errors in
the fitting. To select a value for α they note that the
quantity α/N must be comparable to the accuracy of the
measurements.

Weser and Stierstadt examine a magnetite fluid and
obtain a size distribution with α = 16, N = 10 which bears
some resemblance to a lognormal distribution. These authors
also include a mean demagnetizing field to account for
particle interactions.

Magnetic particle sizes may be obtained from either the
a priori or external methods. In order to assess their
worths for this study one fluid has been examined by four
techniques and the results are presented in 4.5 below.

4.4 Electron Microscopy

The means for obtaining electron micrographs and image size distributions from them is discussed in Chapter 3. It is worth noting here that the image size analyser has made it possible to count large numbers of particles, $\sim$ 1000-2000 and in addition to sample each fluid more than once by taking micrographs at different positions on the grid.

The most important feature of EM data is that it establishes directly the form of the diameter distribution function. This can then be used together with magnetic mean size and standard deviation to calculate magnetic properties. If it is desirable to use a different distribution from that found by EM analysis for calculation (e.g. lognormal), comparisons between the two will establish how reliable the calculations are. As the EM data is stored on computer disc, it is a very simple matter to compare various distributions with the EM histogram as is done in Chapter 6 and below.

4.5 Results

4.5.1 Form of the Distributions

Figure 4.4 shows a particle size distribution determined experimentally from electron micrographs. This was chosen at random and is representative of the data obtained for many samples. The sample was a NiFe-organometallic decomposition into sarkosyl/petroleum

N | NiFe6   mean = 6.96 nm   1583 pts.
std. dev. = 1.26
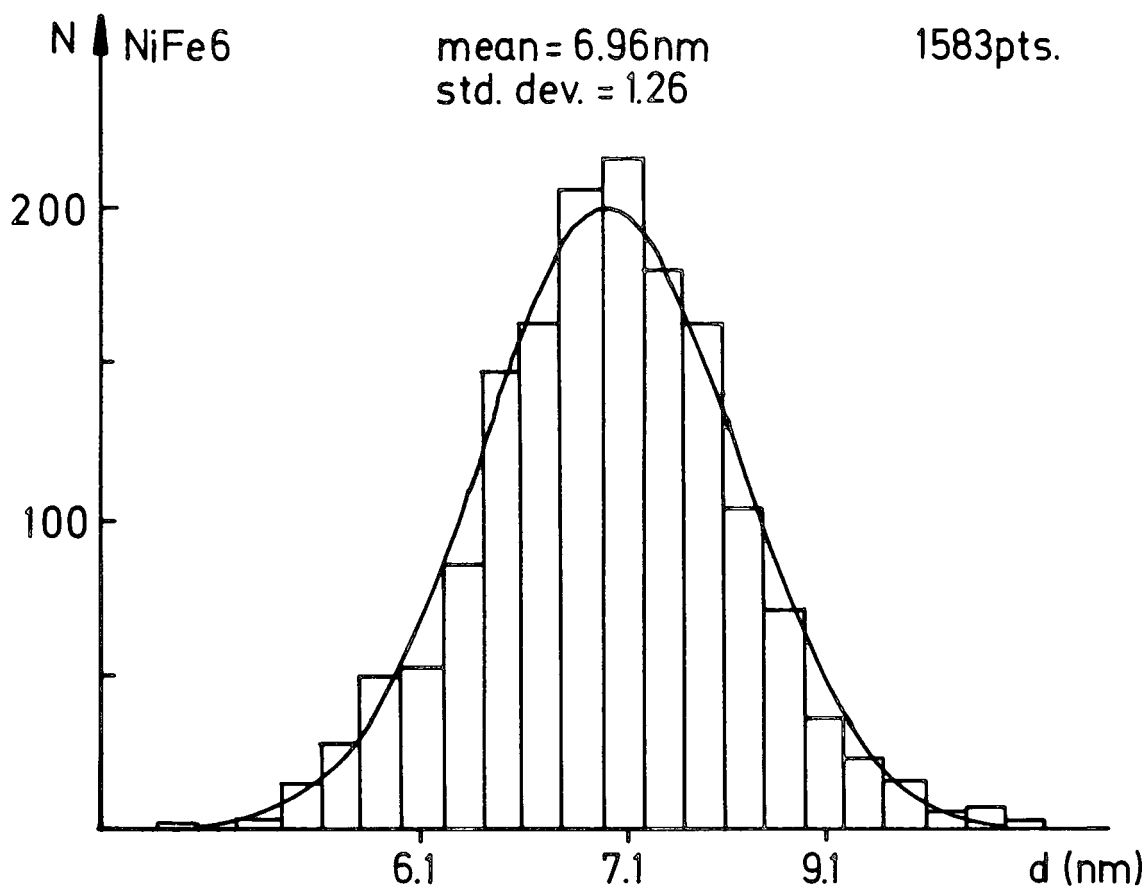
FIGURE 4.4
Histogram particle size distribution
obtained from electron microscopy. Solid
line represents a normal distribution
with the observed mean and standard
deviation.

ether. The sample mean and standard deviation are computed directly from the data points before they are placed into bins. For this sample $\bar{d}$ = 6.96nm and st. dev. = 1.26 and the bin width is 0.4nm. The solid line shows a normal distribution with these values normalised to the number of data points counted, viz. 1583. It can be seen that the normal distribution appears to give a good fit to the data. To quantify this a χ^2 test has been applied obtaining χ^2_{18} = 33.83 where the three bins at each extreme have been combined and the null hypothesis is that the data comes from a normal distribution. At the 5% significance level, $\chi^2_{0.05,18}$ = 28.869 which permits rejection of the hypothesis. At the 1% level $\chi^2_{0.01,18}$ = 34.805 and the hypothesis is just retained. On closer examination, however, it is seen that a large proportion of the χ^2 values originate from the bin at 10.7nm which contains 8 particle counts. If the data for d > 10.5nm is excluded then χ^2_{17} = 21.58 which at the 5% level where $\chi^2_{0.05,17}$ = 27.587 is then consistent with the population distribution being normal. If one particle count is removed from the bin at 10.7nm, then χ^2_{18} = 30.58 and the hypothesis stands, even at the 5% level. As it is quite possible that a double count may have occurred or that the extra count is virtually on the boundary of the bin, it seems reasonable to conclude that the sample is indeed drawn from a normal distribution. This conclusion is in accordance with the work of O'Grady (1982) and O'Grady and Bradbury (1983) who studied cobalt particles prepared by

organometallic decomposition. As the organometallic

molecules in a decomposition all contain the same number of

metal atoms this result suggests that it is discrete

addition of these units which is involved in particle

growth. This is in contrast to inert-gas evaporation where

Granqvist and Buhrman (1976a) found evidence for the

lognormal distribution and liquid-like coalescence just

above the liquid metal. It is consistent with their

observation that the form of the distribution depends on the

preparative route.

4.5.2 The range of Distribution Widths

Granqvist and Buhrman (1976a) also claim that the width

of the size distribution depends on the method of

preparation rather than the condition in any single

preparation. Narrow size distributions are desirable and it

has been claimed (Hess and Parker 1966) that the

organometallic route is successful in achieving this. This

is examined in Table 4.1 which tabulates data from 16

decompositions of various precursors in various

surfactant/carrier liquid combinations. All the

preparations have standard deviations between 0.84 and 1.92,

whilst 14 of the 16 have them between 1.0 and 1.5. This is

very similar to the data of Granqvist and Buhrman who found

standard deviations between 1.3 and 2.2 for their inert-gas

technique. The mean standard deviation ($\pm$ standard error)

is 1.27 $\pm$ 0.06 and the mean particle diameter is 7.59 $\pm$

TABLE 4.1

Preparation	Mean Particle Size (nm)	Standard Deviation	Material
NH18	6.65	1.17	Co
MK34	4.96	1.45	Fe
FeCo	5.24	1.29	FeCo
FeCo2	6.11	1.36	FeCo
FCD	6.80	1.14	FeCo
FCD2	8.03	1.08	FeCo
NiFe5S	8.17	1.04	Ni_3Fe
NiFe6S	6.96	1.26	Ni_3Fe
Co3FeD2	7.82	1.34	Co_3Fe
Co4.3	10.47	1.37	Co
Fe4S	7.98	1.92	Fe
Fe5S	7.38	1.31	Fe
FeCo4.13	6.58	0.84	FeCo
NiFe3S	7.16	1.25	Ni_3Fe
Fe4.24	10.33	1.06	Fe
Fe4.27	10.85	1.46	Fe

0.43 nm. These values have remarkably small spreads and indicate that the organometallic route has a tendency to produce normally distributed particle diameters with a mean of about 8nm and standard deviation of about 1.3. As this means that sixty eight per cent of the particles lie within a band of width 2.6nm whilst 99.7% (3σ) lie within a width of 7.6nm it seems reasonable to conclude that the organometallic route does result in narrow size distributions. Magnetite particles prepared by precipitation (i.e. also a condensation technique) tend to have standard deviations of > 2.0.

The one variable which was not changed a great deal, and on which the particle size distribution may be reasonably expected to be dependent is temperature. This varied between 120 °C - 200 °C for the preparations shown as it is determined by the decomposition temperature and boiling point of the carrier liquid. The choice of carrier liquid is additionally constrained by the requirement that the organometallic be soluble in it. There is some indication of a temperature effect on particle size for the FeCo system and this is reported in Chapter 6. In general terms, however, it may be said that the organometallic route leads to narrow widths of about 1.3. It is worth noting here that magnetic measurements will tend to find narrower distribution widths as the effect of "dead" layers will be to remove small particle data and reduce larger particle diameters. Granqvist and Buhrman (1976a) found that the

thickness of the oxide layer on Al particles was virtually independent of the particle diameter and this is thought likely to be the case for these particles too.

Table 4.2 shows particle size data taken from 5 micrographs of the same sample, taken at different grid positions. The mean diameter is 8.77 $\pm$ 0.46nm and the mean standard deviation is 0.92 $\pm$ 0.07. These standard errors are very similar to those above which suggests that they are mainly associated with the process of taking and analysing the micrographs. The value of counting many particles from more than one micrograph is illustrated here by the sample with mean diameter 10.44 which is much larger than the other four. In this work particle counts have usually been performed on 4-5 micrographs and the data combined to estimate particle size.

4.5.3 Comparison of Four Techniques

The techniques of electron microscopy, Chantrell/Cahn, Potton and numerical fitting have all been applied to one magnetic fluid. This was an iron fluid prepared by the decomposition of $Fe_2(CO)_9$ in Duomeen TDO/Toluene and is reported by Kilner et al. (1984).

(a) Electron Microscopy

Figure 4.5a shows the micrograph analysed. This was taken at 170000x, 80kV and then enlarged $\sim$x3 on printing before being analysed on the image size analyser. It can be seen that there appear to be two sets of particles, some

TABLE   4.2

Photograph Number	Mean (nm)	Standard Deviation
3709	8.92	0.87
3710	10.44	0.76
3711	8.54	1.16
3712	8.29	0.82
3713	7.67	0.98

FIGURE 4·5(a)
Electron micrograph – MK 34

FIG. 2
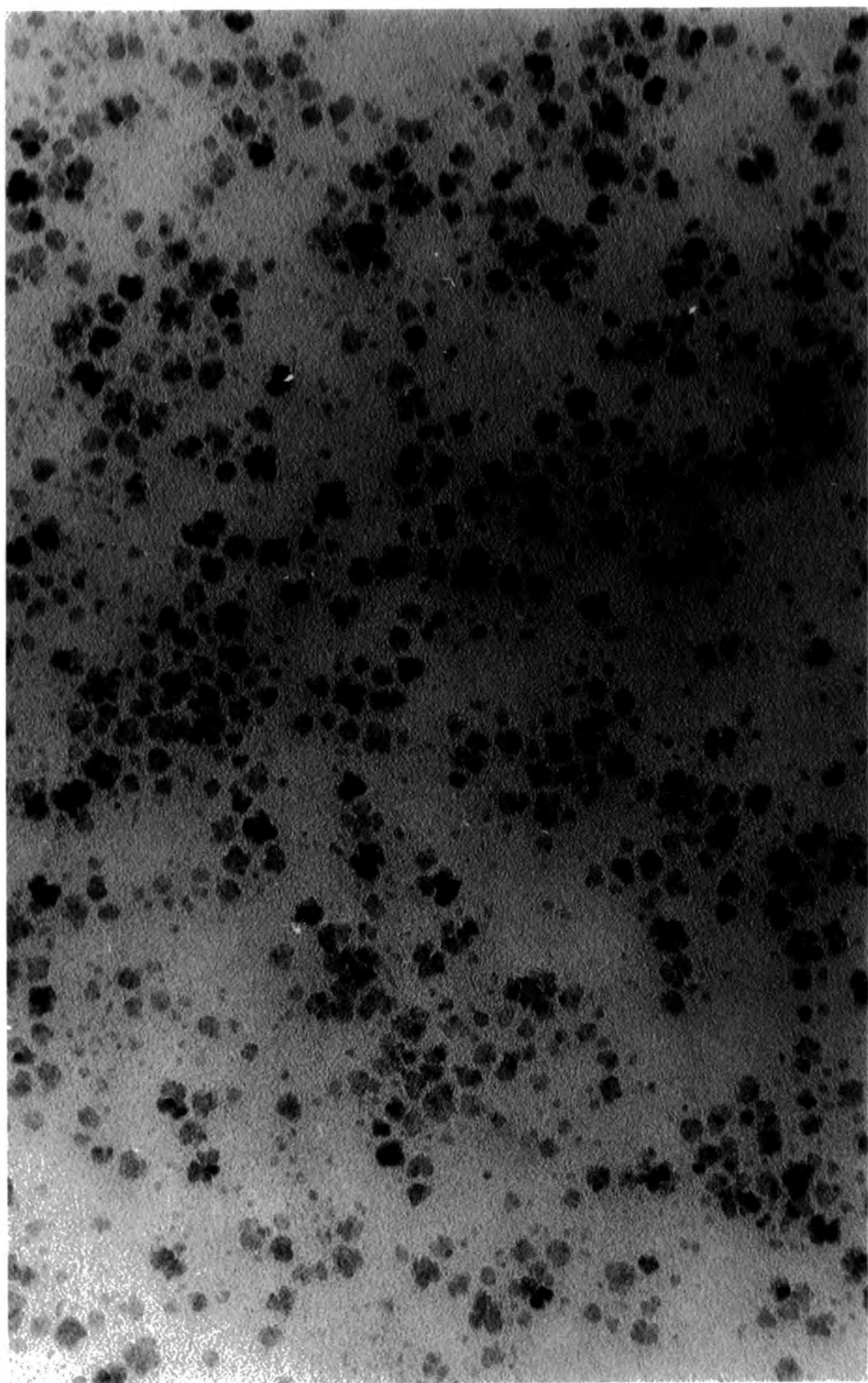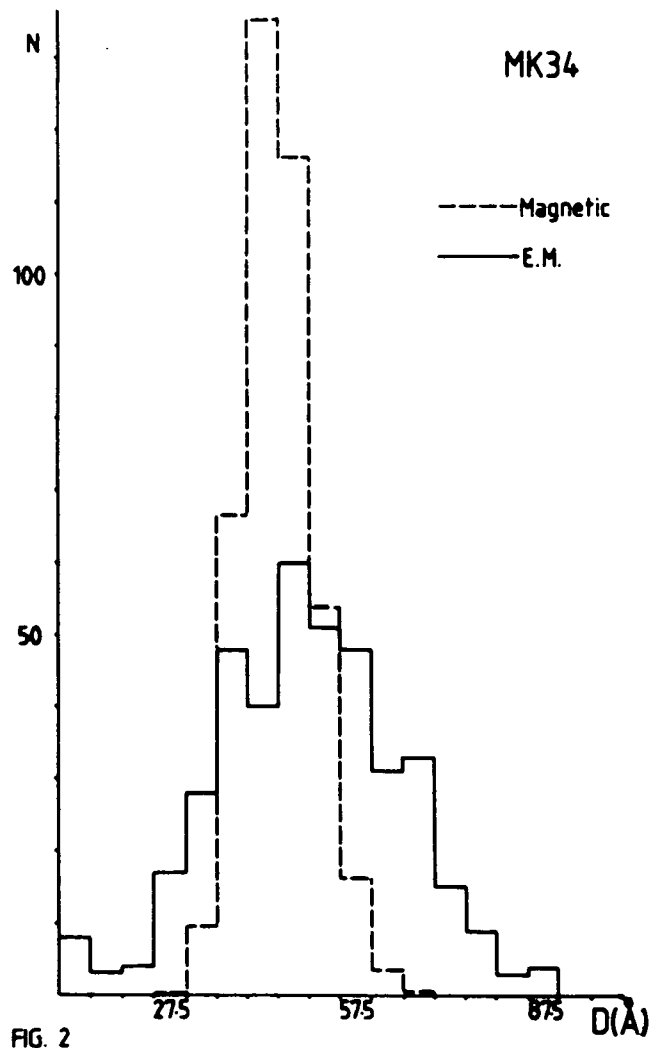
(b)

FIGURE 4.5
(a) Electron micrograph of fluid MK34 and
(b) particle size distribution determined
    from this using the image size analyser.

very small ∿2.0nm and some much larger ∿7.0nm. On inspection it was found that the larger particles were in fact clusters of the smaller. Figure 4.5b shows the histogram obtained (solid line). The mean diameter was found to be 4.96nm and the standard deviation = 1.45. If the clusters are treated as single particles a mean of 6.7nm is obtained.

(b) Method of Chantrell/Cahn

Figure 4.6a shows the magnetisation curve analysed (curve A) which was obtained at room temperature on the V.S.M. It should be noted that this curve extends up to 0.7T only (an experimental constraint at the time) but does appear to be well on the way to saturation. An inverse B_0 vs M plot finds saturation magnetisation to be 1.79 $JT^{-1}kg^{-1}$ and the volume fraction median is calculated to be 7.4nm. The large value of I^0, viz. 34.8, however, makes it impossible to calculate a value for the lognormal parameter σ or the standard deviation using Cahn's expression. This suggests that the curve is still some way from saturation. It can be seen from figure 4.1 that the effect on I^0 of an incorrect slope for the limiting magnetization is much greater than the effect on M_{ff}^{∞}. Applying the method of Cahn gives the mean number fraction volume as 84.3nm^3 equivalent to a diameter of 5.4nm. As I^0 is too large, this will be an overestimate. The lack of a value for lognormal parameter σ makes it impossible to calculate a number fraction mean from the volume fraction median, illustrating the usefulness of

M (J/T/KG)

A

B

B_0(TESLA)

(a)

PROBABILITY
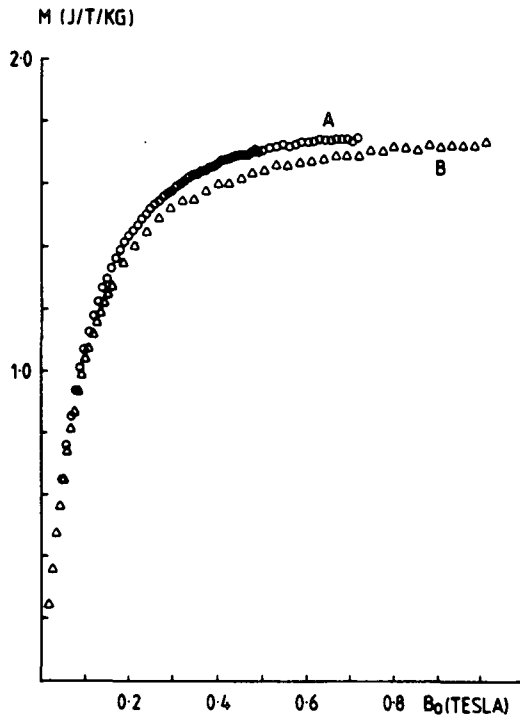
DIAMETER (Å)
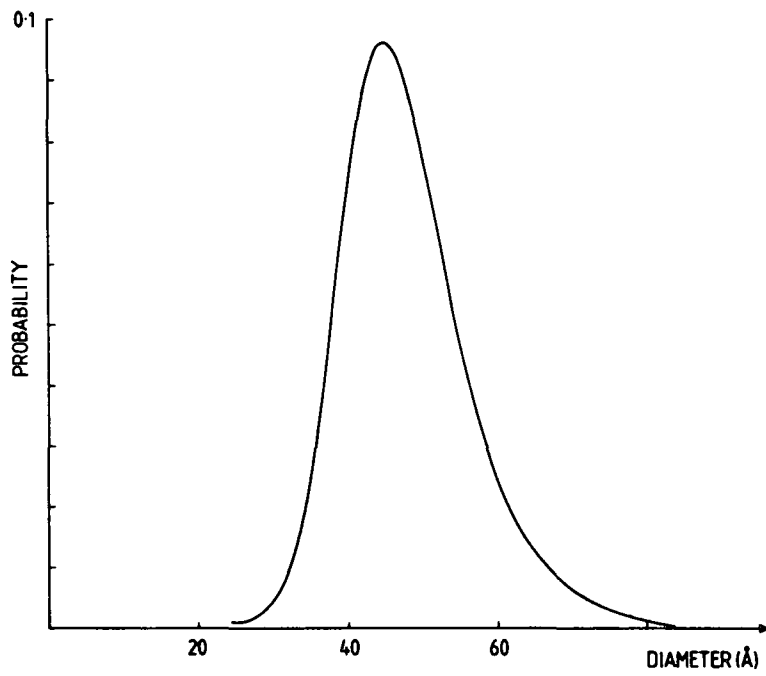
(b)

FIGURE 4.6
(a) Magnetisation curves of MK34 and
(b) particle size distribution derived
from curve A by Potton using the
maximum entropy technique.

Cahn's method. Bearing in mind that the mean size is an
overestimate and the saturation magnetisation an
underestimate the values obtained from the Chantrell/Cahn
methods retain meaning.

(c) Numerically Fitting

This was performed using the program described above
and listed in Appendix C. Fitting was to a lognormal
distribution and a best fit was obtained with a saturation
magnetization of 1.81 $JT^{-1}kg^{-1}$ a number fraction mean of
4.5nm and standard deviation of 0.55. For comparison with
the Chantrell technique, the volume fraction median was
4.7nm. The dashed line in Figure 4.5b shows the magnetic
distribution with these values normalized to the total EM
particle count.

(d) The Potton Technique

This was kindly performed by Dr. J. Potton at
Southampton University on the same magnetisation curve. The
resulting distribution is shown in Figure 4.6b which has a
number fraction mean of 4.78nm and a saturation
magnetization of 1.86 $JT^{-1}kg^{-1}$. Analysis of the significance
of the solution revealed that there is a severe lack of
information for particles < 2.0nm in diameter and for those
with d > 5.0nm. This observation also serves to highlight
why magnetically derived distributions from a priori
techniques tend to have smaller widths than those from EM
data.

(e) Discussion

Table 4.3 collects the data from all four methods. The agreement between the four is remarkable when it is recalled that the Chantrell/Cahn technique overestimates particle size. The physical size is, as it should be, larger than the magnetic sizes probably due to surfactant reaction at this stage, as oxidation of the sample was later observed to occur. It seems reasonable to conclude that any one of the methods may be used for particle size analysis as long as the same one is applied where comparisons are to be made. The three "magnetic" methods give consistent results for the saturation magnetisation as well, with the Potton technique probably giving the best value. A recommendation to use EM analysis together with Cahn analysis of magnetization curves seems thus to be acceptable.

4.5.4 On the lack of High Field Data

As can be seen above, the most serious drawback of the Cahn/Chantrell technique is the lack of high field or saturation data. To examine this problem, magnetization curves were taken on one sample up to 1.2T in the electromagnet and up to 6T in the superconducting solenoid. Figure 4.7 shows the 6T curve from which it can be seen that at 1.2T the sample had not yet saturated. Applying the Chantrell/Cahn method to the 1.2T data gives the saturation

TABLE 4.3

Technique	Mean diameter (nm)	Std. Deviation	Magnetisation $JT^{-1}kg^{-1}$
E.M.	4.96	1.45	–
Chantrell/Cahn	5.40	–	1.79
Numerical Fit	4.50	0.55	1.81
Potton	4.78	–	1.86
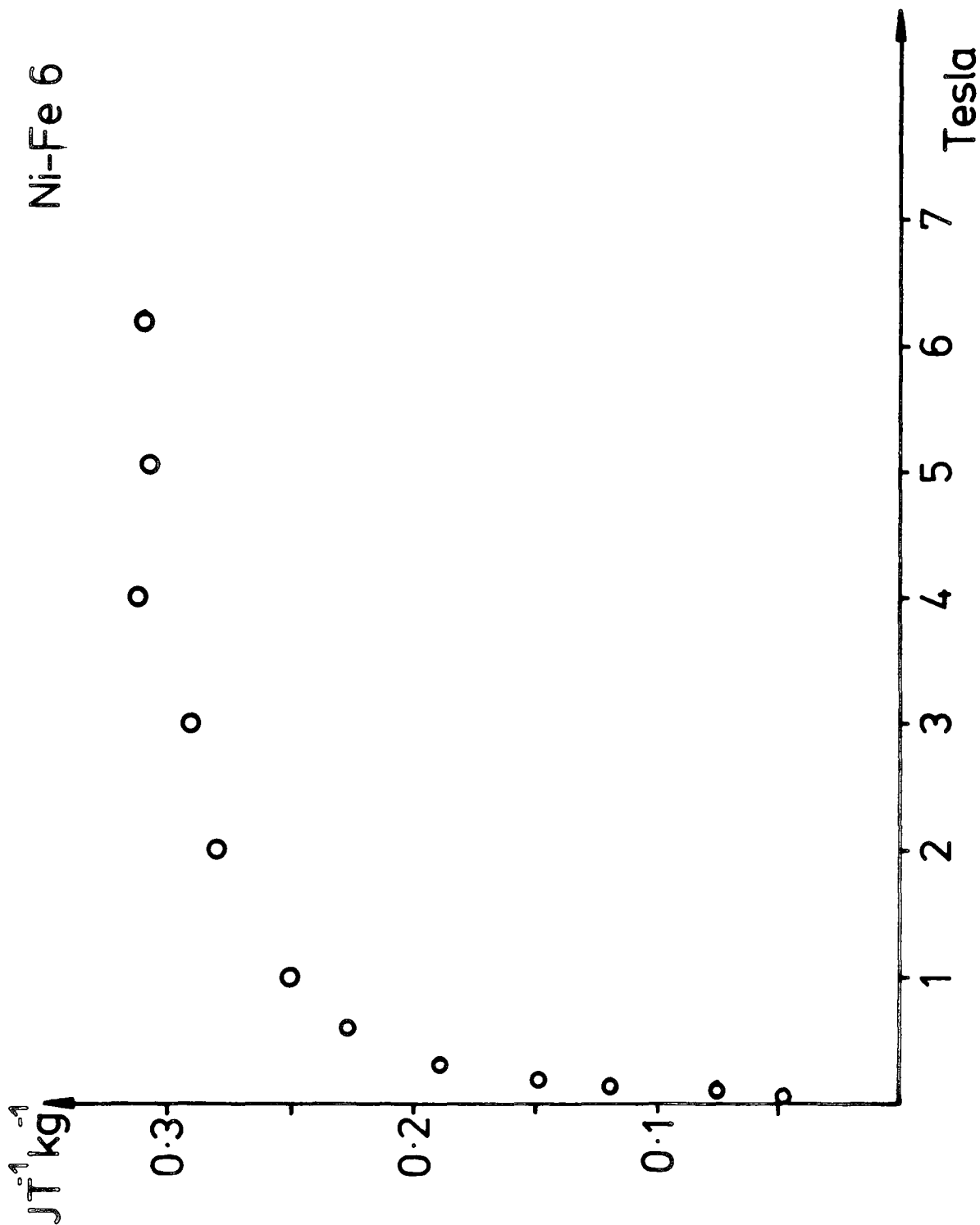
FIGURE 4.7
Magnetisation curve of fluid NiFe6 taken
in the superconducting solenoid, showing
lack of saturation at 1 Tesla.

magnetisation as 0.287 $JT^{-1}kg^{-1}$ and the number fraction mean as 3.7nm and standard deviation 0.98. The 6T data reveals saturation magnetisation of 0.348 $JT^{-1}kg^{-1}$, a mean number fraction diameter of 3.0nm and standard deviation of 1.1. Electron microscopy resulted in mean diameter of 7.0nm and standard deviation of 1.26. There is thus an increase of 11% in saturation magnetization, a decrease of 19% in mean diameter and an increase of 12% in standard deviation.

The magnitude of these errors will depend on the particle size as small particles approach saturation more slowly than large particles. The particles above are amongst the smallest (magnetically that is) examined in this work and so the errors above represent upper bounds. It must, therefore, always be remembered that data taken up to $\sim1.2T$ will overestimate particle size. This should be particularly borne in mind when "dead" layers are being discussed. Previous workers have probably underestimated the thickness of the "dead" layers, the sample above has a difference of 4.0nm in the magnetic (6T) and physical size which is much larger than those normally quoted.

The Chantrell equation for median size has been analysed to estimate the effect errors in the quantities κ, M_b^∞, M_{ff}^∞ and T have in particle diameter. For alloy particles such as those above, uncertainty in M_b^∞ ranks next after I^o and it was found that an error of $\pm$ 10% in this would result in an error of $\pm$ 0.2nm or $\pm$ 5% in median particle diameter. Thus I^o remains the most influential parameter and whenever

possible data should be taken to fields greater than 1.0T.

4.6 Conclusions

It seems reasonable to conclude that the methods of Cahn and electron microscopy, used together, provide a good characterisation of particle size distribution in magnetic fluids. The caveat to be borne in mind is that if the magnetic size is less than $\sim$ 10.0nm and data is taken only to 1.0T then the method of Cahn will be an overestimate of particle diameter and if possible higher fields should be used. Comparison of particles prepared by one technique, as in this study, remains valid as the error is approximately the same for all samples. The value of electron microscopy data is, however, underlined.

When the form of the distribution is required, then more involved techniques must be used and that of Potton has been found to be most suitable in analysing the magnetisation curves of magnetic fluids.

CHAPTER FIVE

TEXTURE STUDIES

5.1 Introduction

The texture of a system is usually described by an
orientation distribution function (Bunge 1982). In
polycrystalline metallurgical systems it is the
crystallographic orientation of the grains which is of
interest. In fine particle magnetic systems the magnetic
easy axes are important, in most cases fine particles
possess uniaxial anisotropy due to shape and the
distribution of this axis with respect to the applied field
influences the magnetic properties of the system. Stoner
and Wohlfarth (1948) first considered the influence of
texture on the magnetisation curve of assemblies of
'blocked' single domain particles. They considered the two
limiting cases of perfect and random alignment of easy axes
which correspond to delta and uniform distribution functions
respectively. In the first case the resulting magnetisation
curve is dependent upon the measuring direction and ranges
from a completely square hysteresis loop when measured
parallel to the alignment direction, to a straight line
through the origin which saturates abruptly when measured
perpendicular to it. For the randomly aligned system they
found a rounded hysteresis loop with a gradual approach to

saturation. In this case they obtain the following
expressions for the initial susceptibility, remanence and
coercivity:-

$$\kappa = \frac{1}{3}\varepsilon_v \frac{M_b^{\infty 2}}{K_{eff}} \qquad (5\cdot1)$$

$$M_{ff}^r = \frac{1}{2}\varepsilon_v M_b^{\infty} \qquad (5\cdot2)$$

$$(B_o)_c = 0\cdot479\,(B_o)_K \qquad (5\cdot3)$$

where $(B_o)_K = 2K/M_b^{\infty}$ and K_{eff} is the (first) effective
uniaxial anisotropy constant. This model applies to
'blocked' particles for which $kT \ll K_{eff}v_p$ and the applied
magnetic field is the only agent pulling the magnetisation
away from the easy axis. This will be the case for
particles of sufficient size, such as those found in
permanent magnet materials for which the model was
developed. In these materials it may be possible to
approach the two limiting textures but in general the
texture will lie somewhere between them. Szpunar and
Szpunar (1984) have extended this model by incorporating a
more general texture function which they express in terms of
a series of associated Legendre polynomials. They obtain
the initial susceptibility and remanence as

$$\kappa = \frac{1}{2}\varepsilon_v \frac{M_b^{\infty 2}}{K_{eff}}(0\cdot667 - 0\cdot422\,t_2) \qquad (5\cdot4)$$

$$M_{ff}^r = M_{ff}^{\infty}\sum_{l=0}^{L} t_l \gamma_l \qquad (5\cdot5)$$

where $\gamma_l = \frac{1}{2}\int_0^{\pi} P_l(\theta)\sin 2\theta d\theta$, θ is the angle between the

easy axis and applied field, $P_\ell(\theta)$ are associated Legendre polynomials and the t_ℓ are the texture coefficients. The texture coefficients characterise the orientation distribution function and in the case of random texture $t_2 = 0$ in (5.4) and the Stoner-Wohlfarth expression is recovered. Equations (5.4) and (5.5) permit the texture function to be obtained from magnetisation measurements. However their calculations revealed that when most of the particles are oriented within $\sim 20^\circ$ of the alignment direction the initial susceptibility is most strongly influenced but yields only one texture coefficient, while on the other hand the remanence provides a greater number of coefficients but is less strongly influenced by the texture.

These two models are only applicable to 'blocked' particles which, in the magnetic fluids considered herein, comprise only a small fraction of the system for temperatures above about 10K. In order to obtain the anisotropy constant of the particles, however, the texture of the sample must be taken into account, as it is the blocked particles which provide the information. The anisotropy constant is a fundamental property of magnetic fluids depending as it does on the magnetisation and shape of the particles. It will be determined by the preparative conditions (application of a magnetic field during particle formation can increase elongation) and composition of particles (the influence of "impurities" and crystal structures is mentioned below). In turn, the anisotropy may

determine the applications possible for the fluid, for example in magnetic printing. In order to obtain this constant magnetic measurements have been made on frozen or solidified fluids using torque or VSM magnetometers. Theories appropriate to superparamagnetic systems have been developed by Chantrell et al. (1983), O'Grady et al. (1980, 1985), Raikher (1983) and Hartmann and Mende (1984a,b,1985) and are discussed below together with results obtained during this study.

5.2   Textured Superparamagnetic Systems

In the liquid state, the anisotropy of the particles has no influence on the magnetisation of a fluid, as shown by Krueger (1979). A magnetic fluid containing a spread in particle sizes will, at an appropriate temperature, contain particles that are blocked (i.e. $v \gg v_c$), particles with sizes near the critical size ($v \sim v_c$) and particles which are intrinsically superparamagnetic ($v \ll v_c$). An 'abrupt transition' approximation has often been applied to magnetic fluids due to the exponential rate of change of volume with respect to measurement time. Chantrell et al. and Hartmann and Mende have, however, shown the importance of including the particles in the transition region when analysing texture sensitive properties. In the liquid state the easy axes of blocked or nearly blocked particles will be aligned with the applied field by their moments, whereas for the superparamagnetic particles there will be no correlation

between moment and easy axis orientation. In both cases thermal disruption of moment alignment occurs via Brownian or Néel relaxation respectively. If the fluid is frozen or polymerised in the presence of the applied field, however, then the partial alignment of easy axes will be preserved and the fluid textured.

This is a necessary condition for obtaining torque curves as Chantrell et al. (1983) have shown that randomly oriented easy axes (obtained by freezing in zero field) give rise to no net torque. Those particles which have relaxation times similar to the time of freezing are partially aligned in addition to those which are completely blocked ($\tau \gg \tau_f$, τ_f = freezing time) and make a significant contribution to the torque. Chantrell et al. and Hartmann and Mende obtain the alignment function for the assembly of fine particles from the partition function of the system. This is obtained in the normal manner, by summing the energy states available to the system as

$$ Z = \int_0^{2\pi} \int_0^{\pi} \int_0^{\pi} \exp(-q \sin^2\alpha + p \cos\beta) \sin\alpha \sin\beta \, d\alpha \, d\beta \, d\eta \qquad (5\cdot6) $$

where α is the angle between moment and easy axis, β is the angle between moment and field, $q = Kv_p/kT$, and $p = mB_o/kT$ and η is given in Figure 5.1. Following Hartmann and Mende this may be written

$$ Z = 8\pi^2 \, e^{-q} \, (q)^{-\frac{1}{2}} \, \phi \, (\sqrt{q}) \, p^{-1} \sinh(p) \qquad (5\cdot7) $$

where $\phi (\sqrt{q}) = \int_0^{\sqrt{q}} e^{x^2} \, dx$. The orientation distribution
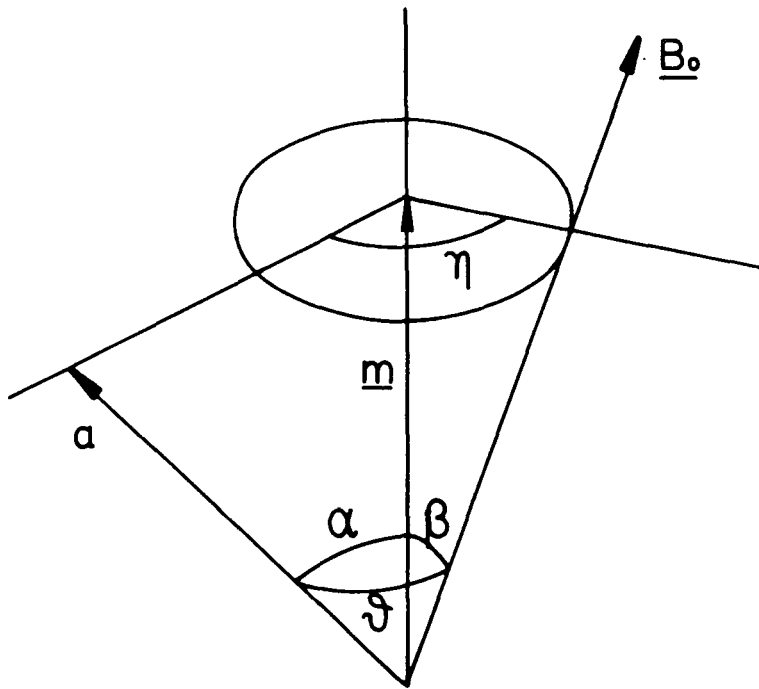
FIGURE 5.1
Definition of angles between easy axis (a),
moment (m) and appled field (Bo).

function of the easy axes would normally be described in terms of the distribution of θ, the angle between an axis and the measuring field, however it is the quantity $\cos^2\theta$ which enters the magnetostatic energy equation and thus the alignment function is given in terms of the average value of this quantity by

$$\langle \cos^2\theta \rangle = \int_0^{2\pi}\int_0^{\pi}\int_0^{\pi} (\cos^2\theta) \exp(-q\sin^2\alpha + p\cos\beta) \sin\alpha \sin\beta \, d\alpha \, d\beta \, d\eta \qquad (5\cdot8)$$

Again, following Hartmann and Mende, this may be written as

$$\langle \cos^2\theta \rangle = \frac{1}{3}\left\{ 1 + 2\xi(q)[1 - 3p'L(p)] \right\} \qquad (5\cdot9)$$

where

$$\xi(q) = \frac{3}{4q}\left(\frac{\sqrt{q}\, e^q}{\phi(\sqrt{q})} - 1 \right) - \frac{1}{2} \qquad (5\cdot10)$$

and $L(p)$ denotes the Langevin equation.

5.2.1 Torque Curves

The above result was first obtained by Chantrell et al. (1983) who used it to obtain an expression for the torque on a magnetic fluid,

$$\Gamma_H(\psi) = \frac{1}{2}\, \varepsilon_v K \sin2\psi \int_0^{\infty} [1 - 3\langle \cos^2\theta \rangle]\, f(y)\, dy \qquad (5\cdot11)$$

For values of $q > 1.5$ these authors found that the alignment function may be simplified and the torque expressed as

$$\Gamma_H(\psi) = \varepsilon_v K \sin2\psi \int_0^{\infty} \left(\frac{3}{P}L(p) - 1 + \frac{3}{2q} \right) f(y)\, dy \qquad (5\cdot12)$$

where f(y)dy is the particle size distribution in terms of reduced diameter $y = d/\bar{d}_x$. This expression may be evaluated numerically and has been used to obtain some of the anisotropy constants given below. If large freezing fields are available and extrapolation to infinite freezing field is possible (Hoon et al. 1983) then the anisotropy constant is given by

$$K = \frac{\Gamma_{pp}^{\infty\infty}}{2\varepsilon_v \, v_{ff}} + \frac{9kT_f}{\pi \, \bar{d}_x^3} \, e^{9\sigma^2/2} \qquad (5\cdot13)$$

where $\Gamma_{pp}^{\infty\infty}$ is the peak-peak limiting torque for infinite freezing field and measuring field (Nm), v_{ff} is the volume of the sample, T_f is the freezing temperature of the fluid and $\bar{d}_x$, σ are lognormal size distribution parameters.

5.2.2. Initial Magnetisation

Hartmann and Mende use the alignment function to obtain the initial magnetization of magnetic fluids which for perfectly aligned systems is given by

$$M_i(\theta) = M_{sf}^{\infty} \, p \left\{ \frac{1}{3} - \frac{1}{3} \xi(q) + \xi(q)\cos^2\theta \right\} \qquad (5\cdot14)$$

where θ is the angle between the alignment direction and the measuring directions. For partially aligned systems they obtain

$$M_i(\theta) = M_{sf}^{\infty} \, p_m \left\{ \frac{1}{3} + \xi(q_f) \xi(q_m) \, [1 - 3p_f^{-1} L(p_f)](\cos^2\theta - \frac{1}{3}) \right\} \qquad (5\cdot15)$$

where the subscript f refers to the values prevailing upon freezing and m those when measured. A very similar analysis had been given earlier by Raikher (1983) who demonstrated

the effect of texture on initial magnetisation by plotting

$\delta M_{\parallel,\perp} = M_{\parallel,\perp} - (M_\ell / M^\infty_{ff})$ against p for various p_ℓ ($\theta = 0^O : \parallel$,

$\theta = 90^O : \perp$ and 1 refers to the liquid state values).

These show (see Figure 5.2) that for $\underline{B}_M \parallel \underline{B}_f$ and

$|\underline{B}_M| < |\underline{B}_f|$ the magnetisation of the textured system is

greater than that for the untextured. When $|\underline{B}_M| = |\underline{B}_f|$ the

equilibrium state is repeated and the magnetisations are

equal whilst for $|\underline{B}_M| > |\underline{B}_f|$ the textured system has a

smaller magnetisation than the untextured. This result may

be thought of as the induced texture initially increasing

the magnetisation as some alignment is already present but

when $|\underline{B}_M| > |\underline{B}_f|$ the fixed anisotropy axes hinder further

alignment with the field. When measured perpendicular to

the alignment direction, the magnetisation is always smaller

at each $\underline{B}_f$ than that for the liquid state. Both Raikher and

Hartmann and Mende (1985) obtained good agreement between

theory and experiment for textured magnetite systems.

5.2.3   The Approach to Remanence

O'Grady et al. (1980, 1985) considered the approach to

remanence for cobalt particles dispersed in toluene. For a

random distribution of easy axes they found

$$M_{ff}(B_0) = M^\infty_{ff}\left[\frac{\overline{v}_b M^\infty_b}{3kT} B_0 \int_0^{y_c} y^3 f(y)dy + \frac{1}{2}\int_{y_c}^\infty f(y)dy \right.$$
$$\left. + \frac{2 B_0}{3(B_0)_k}\int_{y_c}^\infty f(y)dy\right] \qquad (5\cdot16)$$

where y is the reduced diameter and y_c is the critical
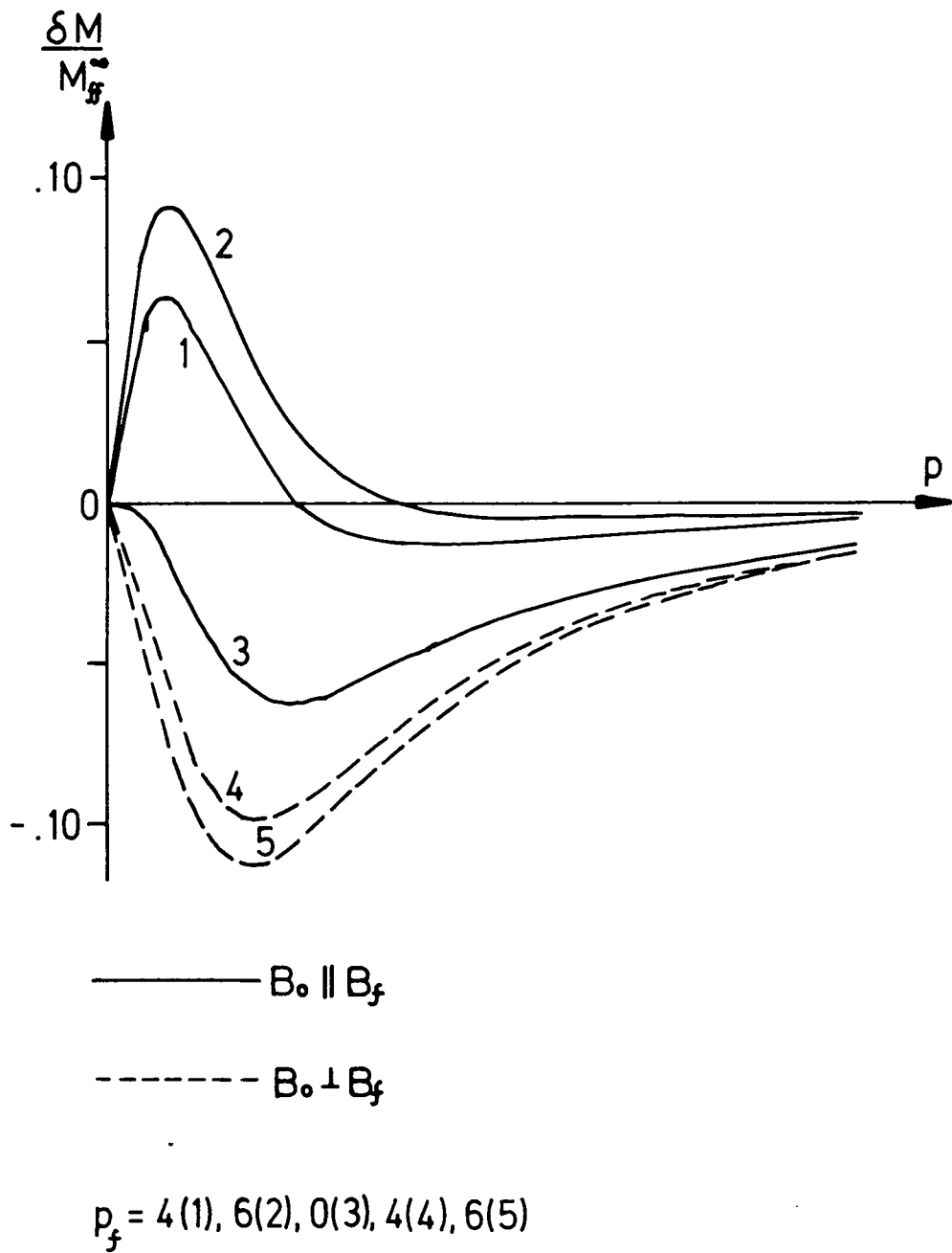
FIGURE 5.2
Reduced initial magnetisation, $\delta M = (M_{\parallel} - M_{\perp})/M_{f}^{\infty}$, as a function of applied field. (After Raikher 1983.)

diameter for blocking (abrupt transition model). The first
term represents the superparamagnetic fraction, the second
is the remanence and the third represents the blocked
particle's magnetisation. It may be noted here that the
properties of the lognormal distribution make it simple to
obtain the remanence from tabulated values of the area under
the standard normal distribution. The area under the
lognormal function, $\Lambda(\mu, \sigma^2)$

$$A = \int_{y_q}^{\infty} f(y) \, dy \qquad (5 \cdot 17)$$

is the same as that under the normal function, $N(0, 1)$

$$A = \int_{v_q}^{\infty} g(y) \, dy \qquad (5 \cdot 18)$$

where $v_q = \dfrac{1}{\sigma} \ln \left(\dfrac{y_q}{e^\mu} \right)$ and $\overline{d}_{\frac{1}{2}} = e^\mu$. If the remanence is known
then the blocking diameter d_c may be obtained by finding v_q.
Evaluating equation (5.16) it is found that the approach to
remanence is a straight line given by

$$\overline{M}_{ff}(B_o) = g B_o + \overline{M}_{ff}^r \qquad (5 \cdot 19)$$

where

$$g = \frac{\overline{v}_b \, M_b^\infty}{3kT} \, e^{\frac{9x^2}{2}} I(\alpha) + \frac{4 \overline{M}_{ff}^r}{3 (B_o)_K} \qquad (5 \cdot 20)$$

$$I(\alpha) = \frac{1}{\sqrt{2\pi}} \int_{-\infty}^{\alpha} \exp\left(-\frac{z^2}{2}\right) dz \qquad (5 \cdot 21a)$$

and

$$\alpha = \frac{1}{\sigma} \ln(y_c) - 3\sigma \qquad (5 \cdot 21b)$$

and $\bar{M} = M/M_{ff}^{\infty}$ is the reduced magnetisation. The anisotropy constant may thus be obtained from the gradient of the approach to remanence. For cobalt particles with $\bar{d}_{\frac{1}{2}} =$ 5.2nm, $\sigma = 0.2$ O'Grady et al. found $K = (1.6 \pm 0.5) \times 10^{-5}$ Jm^{-3} at 77K.

In a subsequent paper, (O'Grady et al. 1985) these authors consider the influence of partial alignment by using the alignment function described above. The magnetisation near remanence is then given by

$$M_{ff}(B_0) = M_{ff}^{\infty}\left[\frac{\bar{v}_{\frac{1}{2}}M_b^{\infty}}{3kT}B_0\int_0^{y_c} y^3 G(y)f(y)dy + \int_{y_c}^{\infty} \langle\cos\theta\rangle f(y)dy \right.$$

$$\left. + \frac{B_0}{(B_0)_K}\int_{y_c}^{\infty} \langle\sin^2\theta\rangle f(y)dy \right] \qquad (5\cdot 22)$$

where $G(y) = \langle\cos^2\theta\rangle + \frac{1}{2}(1-3\langle\cos^2\theta\rangle)\left[1 + \frac{1}{2q} + \frac{e^q}{q\,I(q)}\right]$. This may be simplified for the two cases of predominantly blocked and predominantly superparamagnetic systems. In the first case the remanence is given by

$$\bar{M}^r = 2\bar{M}^r(0) - \frac{kT_f}{\bar{v}_{\frac{1}{2}}M_b^{\infty}}I(\alpha)\left[\frac{1}{B_f} - \frac{1}{(B_0)_K}\right] \qquad (5\cdot 23)$$

where $\bar{M}^r(o)$ is the reduced remanence when the system is frozen in zero field. Evaluation of this expression for a cobalt magnetic fluid revealed that the effect of texture on remanence was not pronounced due to imperfect coupling between moment and easy axis.

For predominantly superparamagnetic systems, the

gradient of the approach to remanence becomes

$$g_T = 3g_R - \frac{2 T_f}{(B_o)_k T_m}\left\{ \frac{(B_o)_k}{B_f} -1 \div \frac{T_m}{T_f} \right\}(1-2\overline{M^r}(0)) \qquad (5\cdot24)$$

where g_R is the gradient in the case of randomly arranged easy axes. Measurement of the approach to remanence of a system frozen in zero field and then frozen in a large applied field may be used to obtain the anisotropy constant using equation (5.24).

5.3   Results

Room temperature measurements have been made on a magnetite fluid which was set in fibreglass (polyester) resin, samples being prepared in aligning fields of 0.4, 0.7, 1.0 and 1.4T. These were prepared in the shape of discs 3mm thick and 5mm in diameter and the setting temperature of the resin was measured to be 325K. Measurements at 77K have been made on frozen NiFe fine particles prepared by organometallic decomposition and described in Chapter 6.

5.3.1   Torque Measurements

(a)   Magnetite System

Figure 5.3 shows the torque curves obtained as a function of measuring field for the sample aligned in 1.0T and are representative of those obtained for the other three samples. It is evident that a θ component, due to side pull is present but as extrapolated torque amplitudes are used in
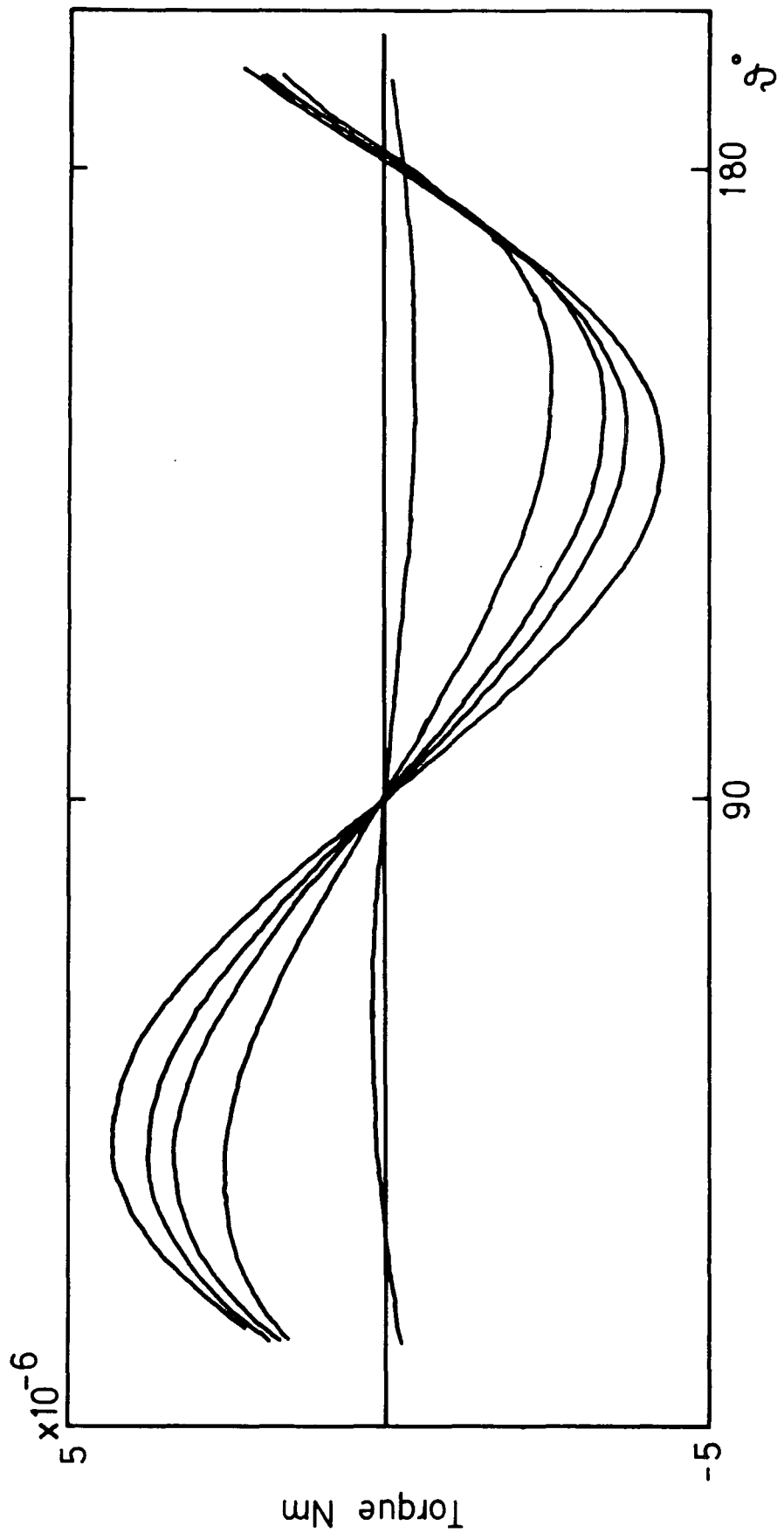
FIGURE 5.3
Torque curves obtained from magnetite/polyester
resin sample frozen in 1.0 Tesla in various
measuring fields. Room temperature measurement.

calculations this should not introduce large error. Figure 5.4 shows the peak-peak torque amplitude plotted against measuring field for all four samples from which it can be seen that all four appear to be approaching saturation at 0.7T. Figure 5.5 shows these values plotted against inverse field from which extrapolation to $(1/B_o) \rightarrow 0$ gives saturation values for pk - pk torque amplitude of the samples. These are shown in Table 5.1 and were used in equation (5.12) together with the values $\bar{d}_{\frac{1}{2}} = 8.23$nm, $\sigma = 0.43$ (otained from room temperature magnetisation curves) $T_f = 300$K, $v_{ff} = 5.9 \times 10^{-8}$m^3 and the volume fraction appropriate to each sample, to obtain values of K. These are given in Table 5.1 where it can be seen that the value for the 1.4T sample is in disagreement with the others and may be indicative of an error during its experiment. Rotational hysteresis was measured immediately after the torque curves and Figure 5.6 shows the result for the 0.4T sample. Again the 1.4T sample gave an inconsistent result confirming that some error, possibly in the attachment of the sample to the magnetometer, was present during its measurement. The 0.7T and 1.0T samples produced almost identical plots to the 0.4T sample. Figure 5.7 shows the rotational hysteresis data beyond the maximum plotted against inverse field. From this plot a value for $(B_o)_K$ may be obtained (Paige et al. 1984) and was found to be 0.233T. This gives the anisotropy constant as 5.6×10^4Jm^{-3} in good agreement with the torque curve values. An average value
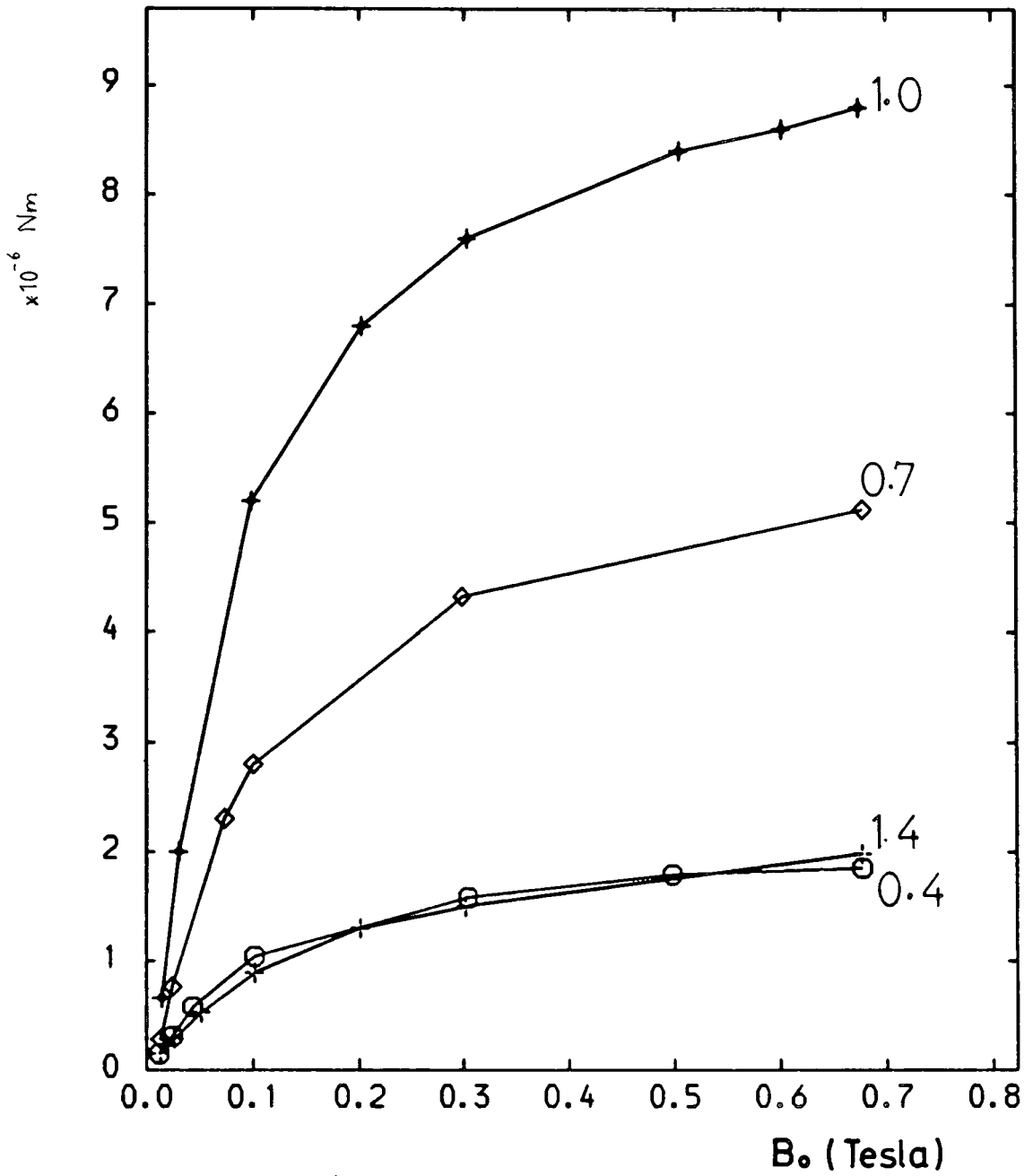
FIGURE 5.4
Peak-peak torque amplitude plotted against
measuring field for the magnetite samples
aligned in 0.4,0.7,1.0 and 1.4 Tesla.
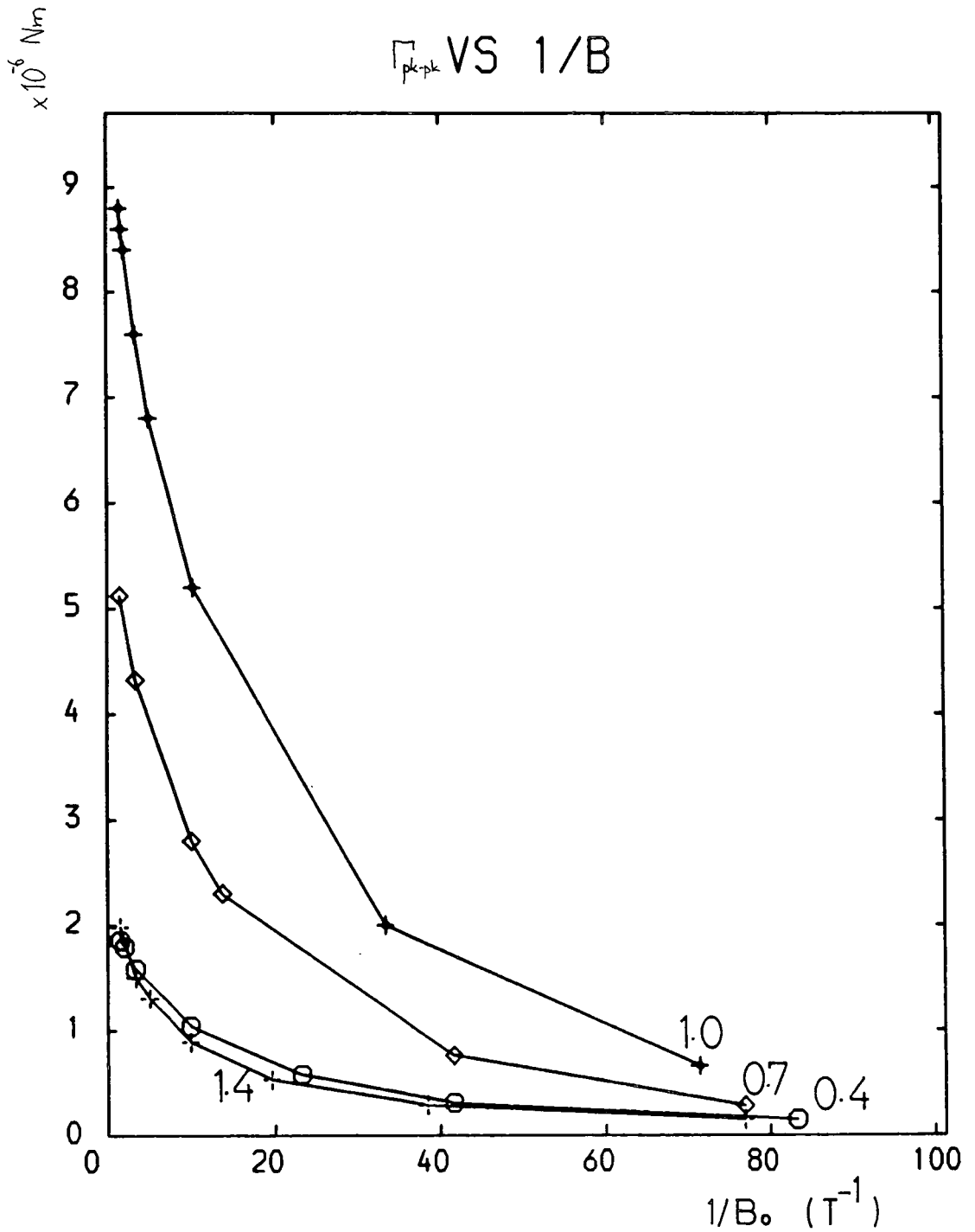
FIGURE 5.5

Peak-peak torque amplitude plotted against inverse measuring field to obtain saturation values of torque amplitude.

TABLE   5.1

Sample	Pk-pk Torque $(\times 10^{-6}$ Nm)	Anisotropy const. $(\times 10^{5}$ Jm^{-3})
0.4	2.10	5.8
0.7	5.75	5.9
1.0	9.80	6.1
1.4	2.37	5.0
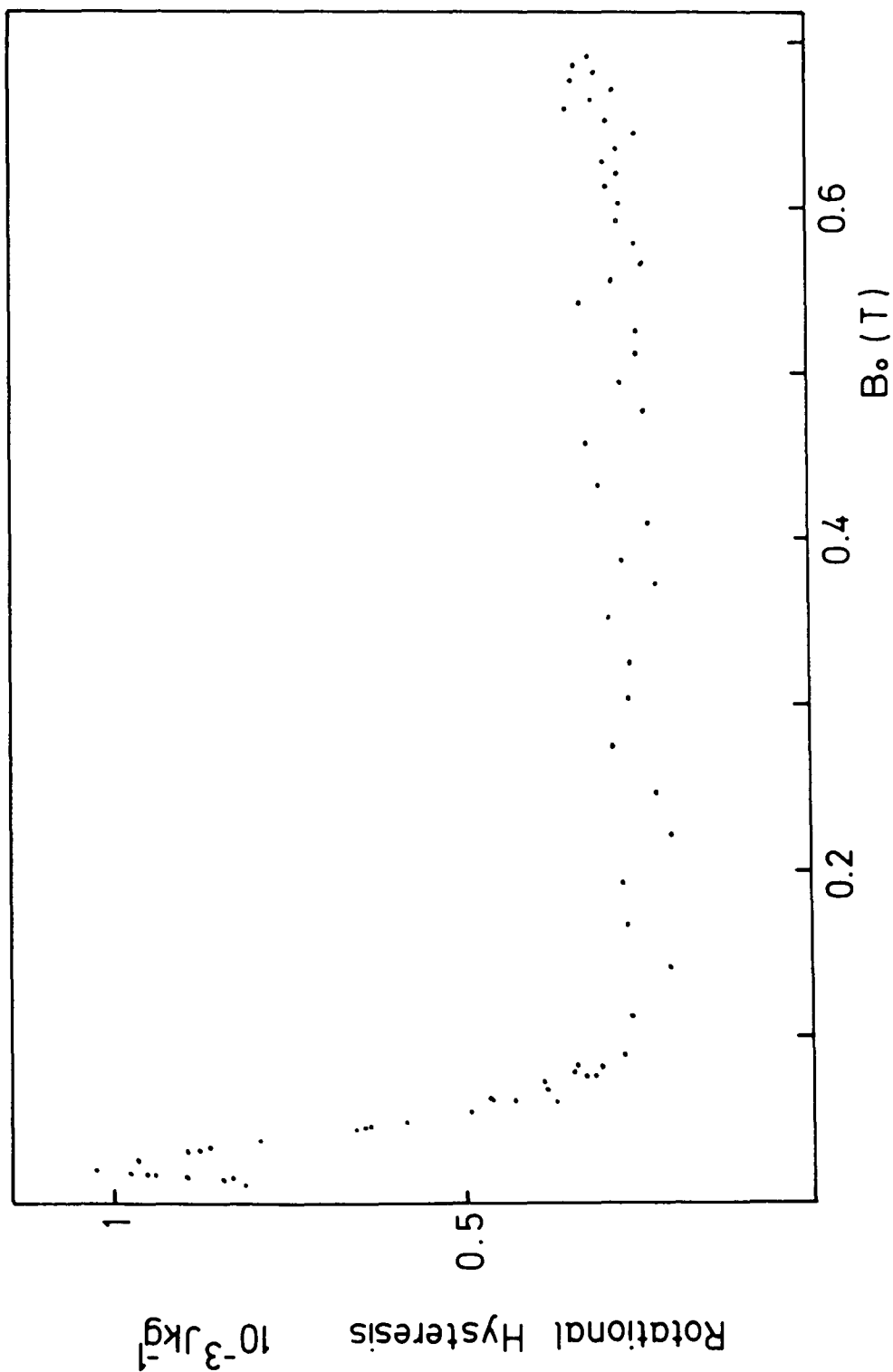
FIGURE 5.6
Rotational hysteresis of magnetite/polyester resin sample aligned in 0.4 Tesla. Room temperature measurement.
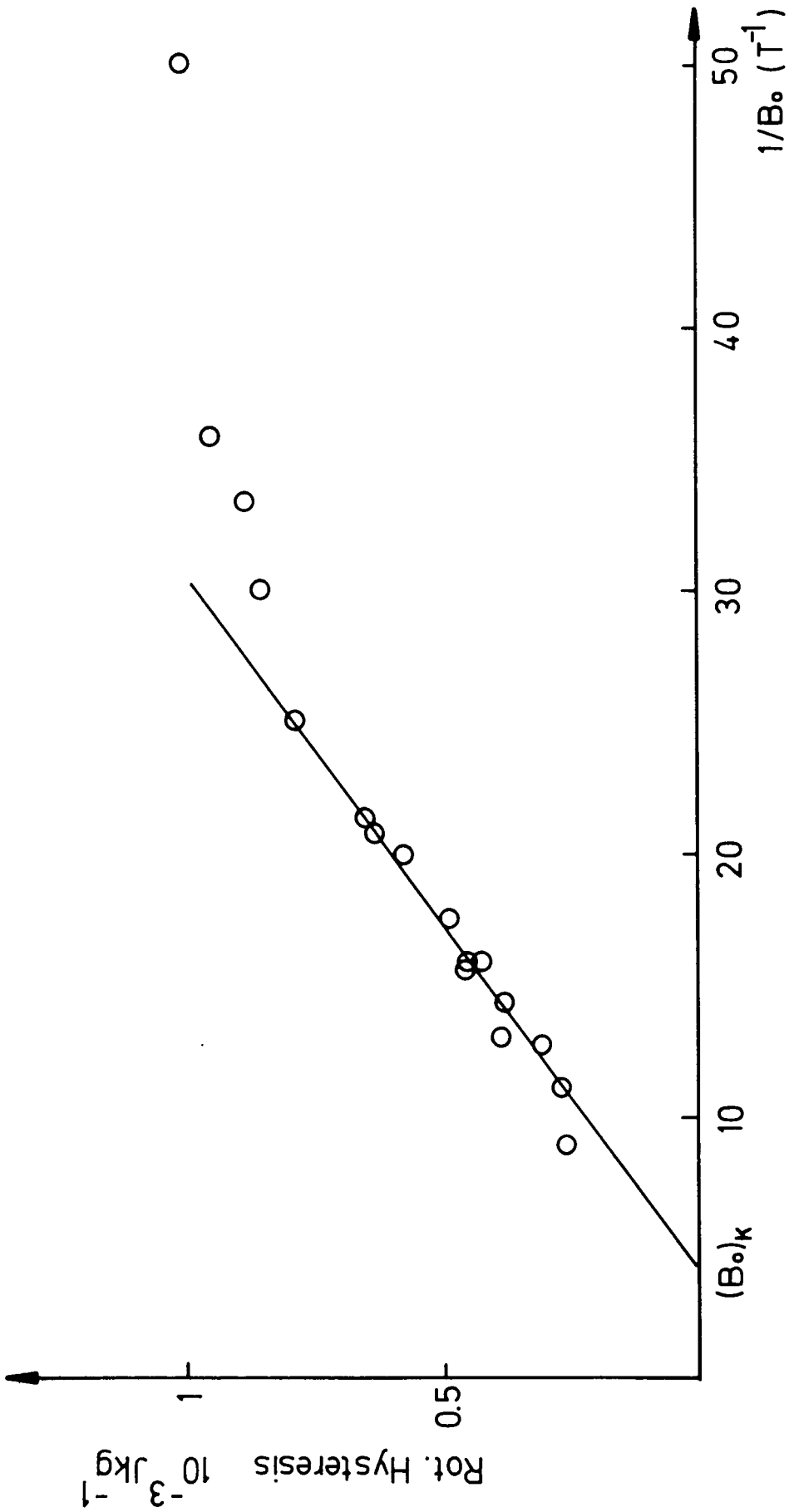
FIGURE 5.7
Rotational hysteresis plotted against inverse
measuring field to extract anisotropy field.
0.4 T magnetite/polyester sample.

for these samples (omitting the 1.4T) is found to be 5.85 x 10^4 Jm^{-3}. The error in this value arises from those in the particle size data as well as those in the torque measurements. The side pull will tend to be compensated for as the extrapolated pk - pk torques tend to be underestimates. The error is estimated as

$$K = (5.8 \pm 0.4) \times 10^4 \, Jm^{-3} \qquad (5.25)$$

This value is somewhat higher than that obtained by Hoon et al. (1983) for a similar magnetite system, 4.6 x 10^4 Jm^{-3}. Their value, however, was an underestimate as they did not use an extrapolated value for the saturation torque.

(b) Organometallic Ni₃Fe system

Measurements were made on the system NiFe4 detailed in Chapter 6 where the average composition of these particles is found to be Ni_3Fe. The fluid was frozen to 77K in freezing fields between 0.05 and 0.7T and measured in fields in the same range. The freezing point of the fluid is taken to be that of the carrier liquid, toluene, 251K. Figure 5.8 shows the torque curves obtained after freezing the sample in a 0.5T field and measured in increasing measuring fields. The unaxial nature of the curves is apparent with some slight side pull which was accounted for in the analysis. Figure 5.9 shows torque curves obtained for the fluid frozen in increasing fields all measured at 0.7T. From these the torque amplitude (½ pk-pk) was extracted and Figure 5.10 shows this plotted against measuring field for the 0.5T
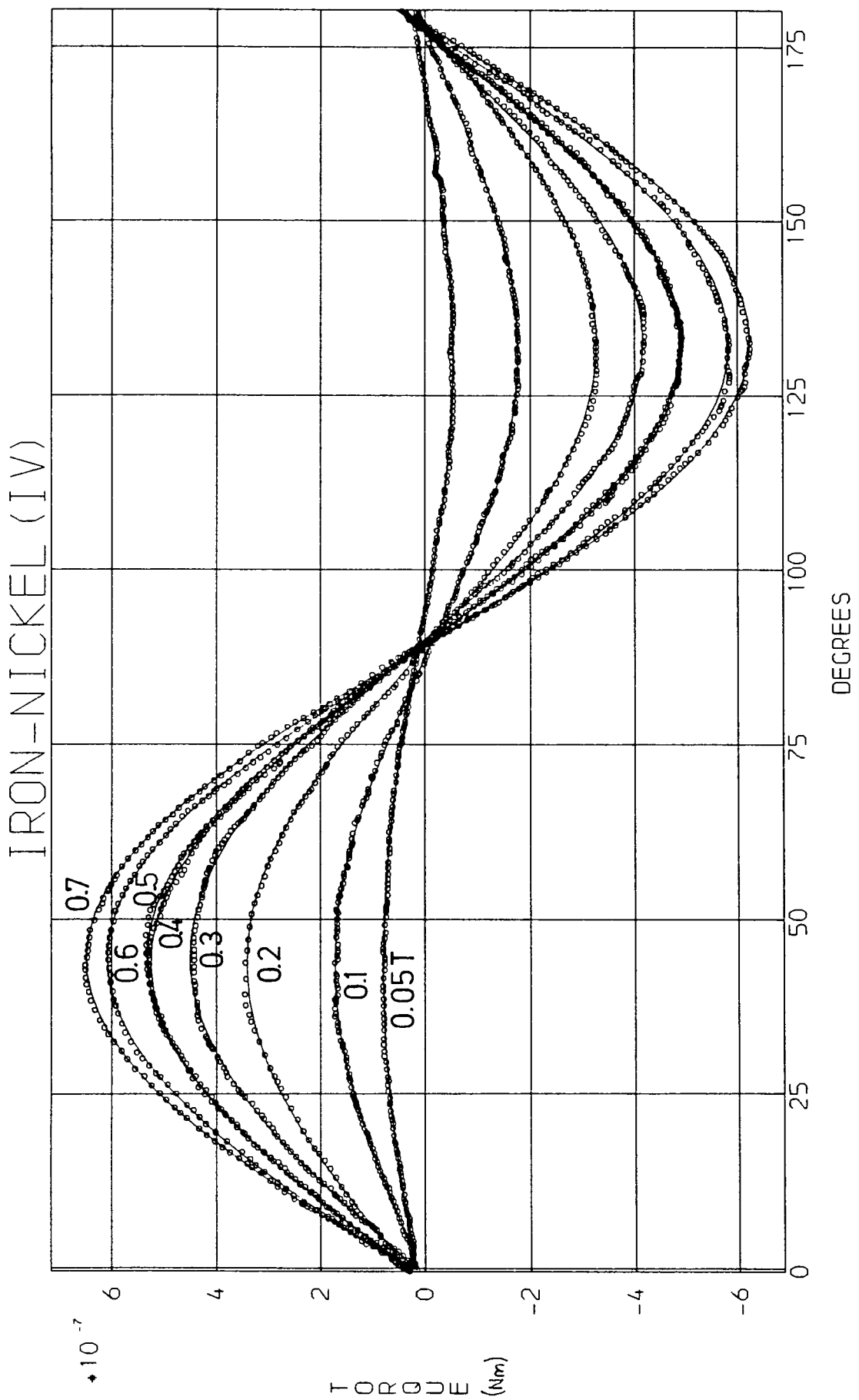
FIGURE 5.8
Torque curves for fluid NiFe4 frozen in 0.5T
measured at 77K in various measuring fields.
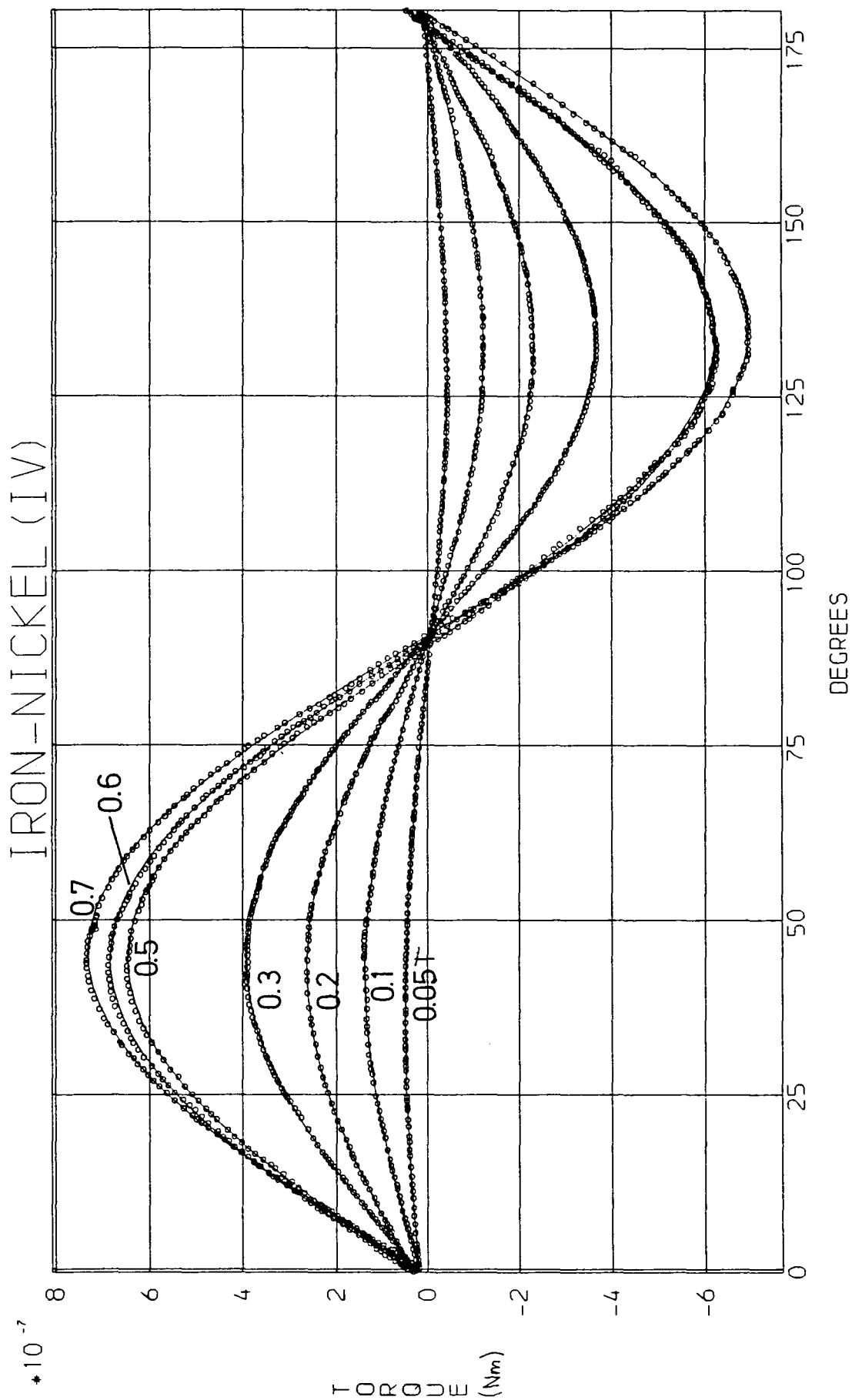
FIGURE 5.9
Torque curves for fluid NiFe4 frozen in
various fields and measured in 0.7T.
77K measurements.
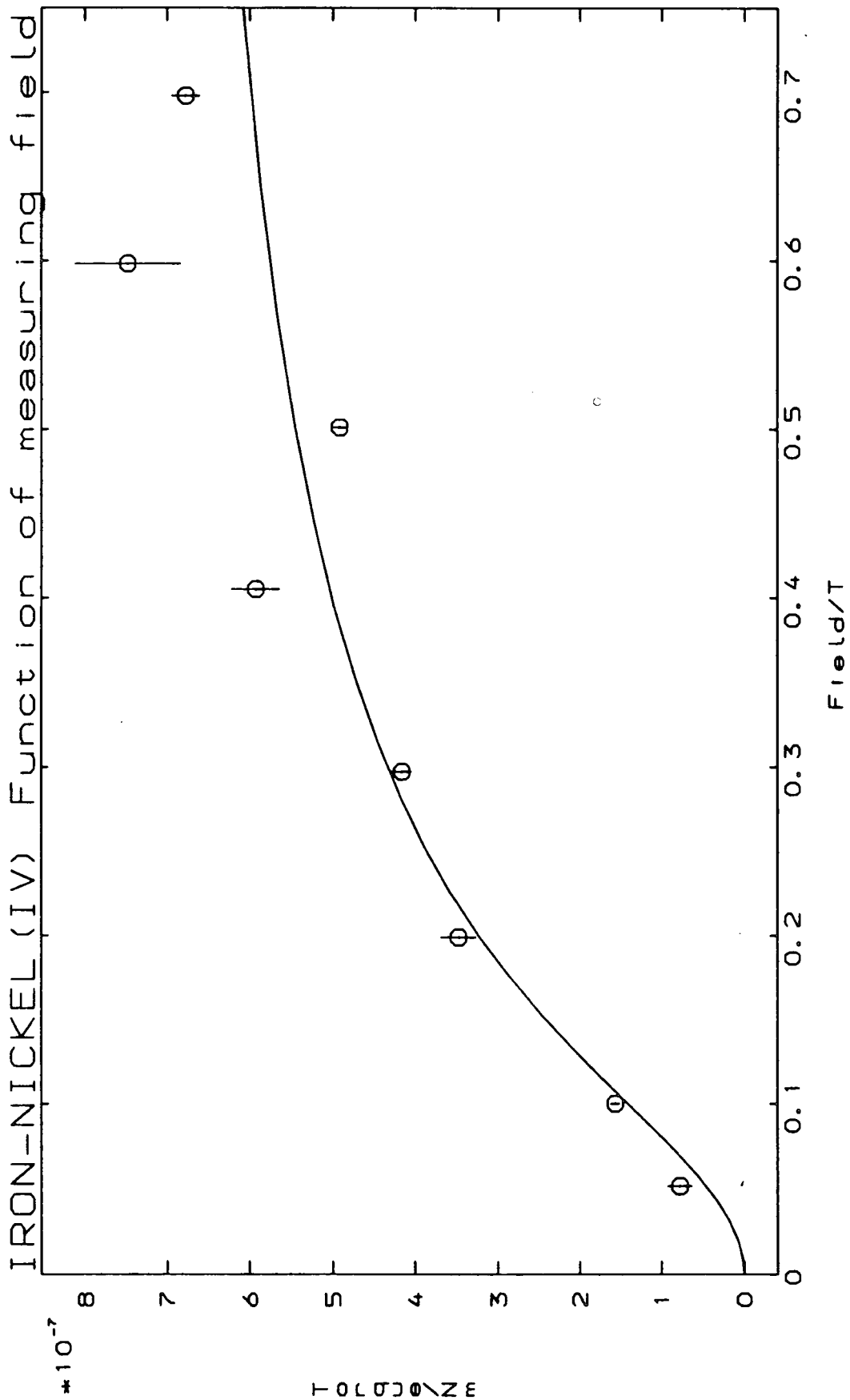
FIGURE 5.10
Torque amplitude plotted against measuring field for NiFe4.

freezing field where it can be seen that saturation is being
approached at 0.7T. Figure 5.11 shows the torque amplitude
plotted against freezing field from which a saturating
torque in 0.7T measuring field has been obtained as $|\Gamma| =$
$(0.99 \pm 0.20) \times 10^{-6}$ Nm. The particle size data from room
temperature magnetisation curves is $\bar{d}_{\frac{1}{2}} = 3.6$nm, $\sigma = 0.23$ and
$\varepsilon_v = 0.0004$. The volume of the samples (estimated using the
mass of Hg required to fill the sample space) was 1.7×10^{-7}
m^3 and inserting these values into equation (5.13) yields a
value for the anisotropy constant of $2.9 \times 10^5 Jm^{-3}$.

(c) Discussion

Table 5.2 lists some results for the anisotropy
constant of fine particle systems. This is usually ascribed
to shape, most often prolate ellipsoid elongation of the
particles. The degree of elongation required to produce
these K values may be calculated from the expressions

$$K = \frac{1}{2} M_b^{\infty^2} (D_w - D_\ell) \qquad (5\cdot26a)$$

$$(D_w - D_\ell) = \frac{\mu_0}{2} (1 - 3N_\ell) \qquad (5\cdot26b)$$

$$N_\ell = \frac{1}{a_r^2 - 1} \left\{ \frac{a_r}{\sqrt{a_r^2 - 1}} \ln(a + \sqrt{a_r^2 - 1}) - 1 \right\} \qquad (5\cdot26c)$$

where D are the demagnetisation factors and a_r is the aspect
ratio, l/w of the particle. Substituting the values shown
in Table 5.2 results in aspect ratios of ~ 2.7, 4.0 for
magnetite, ~ 1.5 for cobalt and $a_r \to \infty$ for the Ni_3Fe system.
Elongations of these magnitudes ought to be readily
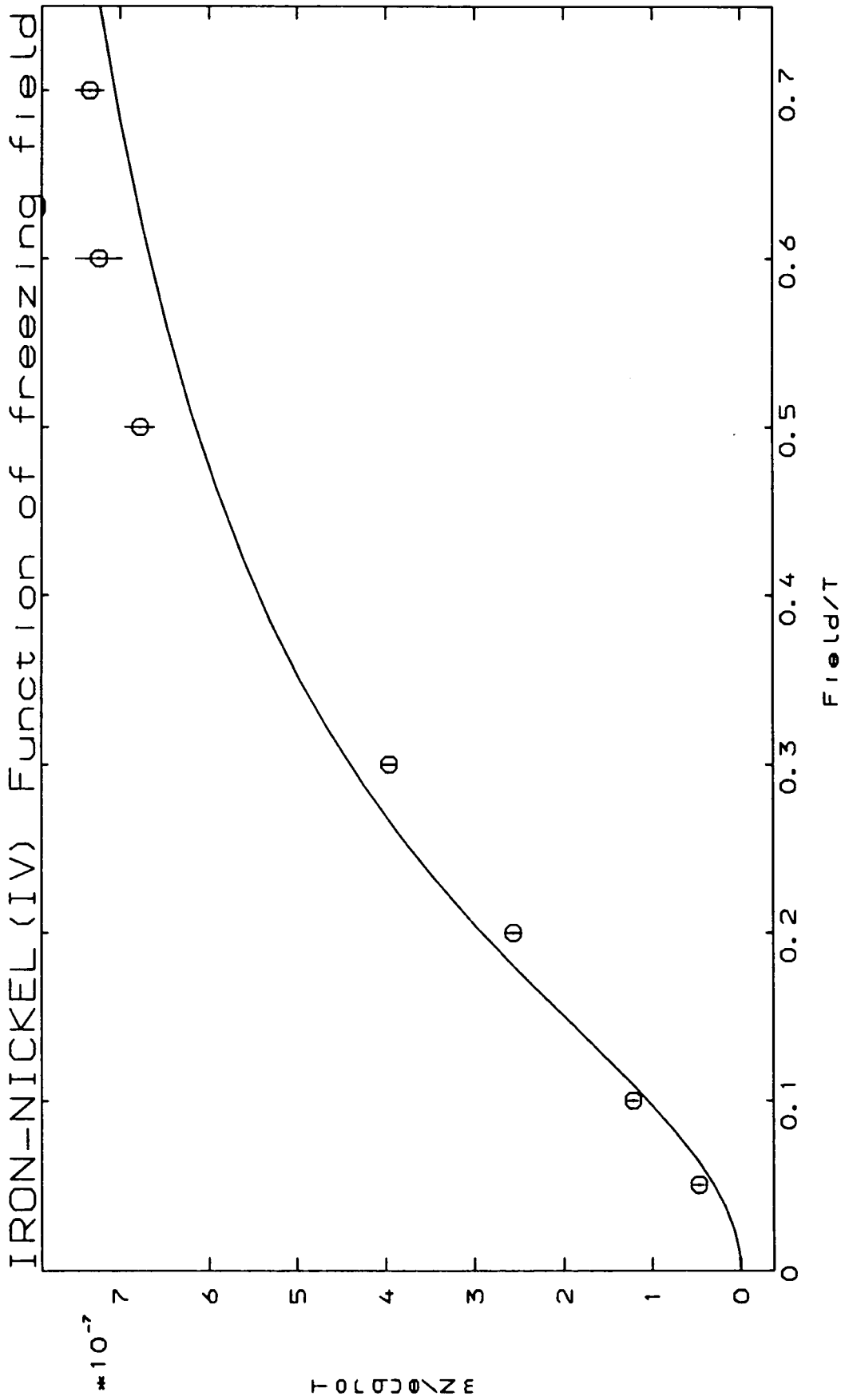
FIGURE 5.11
Torque amplitude plotted against freezing
field for NiFe4.

TABLE   5.2

Material	Authors	Anisotropy Const. $(\times 10^5 \, Jm^{-3})$
Fe_3O_4	Hoon et. al.(1983)	0.46
Fe_3O_4	This study	0.58
Co	Hoon et. al.(1983)	2.00
Co	O'Grady et. al. (1980)	1.90
Co	O'Grady et. al. (1984)	2.60
Ni_3Fe	This study (Torque)	2.90
Ni_3Fe	This study (Magn.)	1.15

observable in an electron micrograph whereas nearly spherical particles are usually encountered. This is sometimes attributed to the particle easy axis being aligned normally to the observation plane by the magnetic field of the microscope lens. However, for superparamagnetic particles being heated by an electron beam, this seems unlikely and some of the particles should be lying with their elongation axis parallel to the microscope grid. There remain, then the conclusions that either the K values are in gross error or that shape is not solely responsible for the uniaxial anisotropy of these particles. The fact that very similar values of K have been obtained by different authors using different techniques points to the latter conclusion.

There are various reasons why the anisotropy constant could be larger than expected, foremost being that the assumption of coherent rotation is not entirely correct. The particles are not perfect ellipsoids and they have large surface effects which must interfere with coherent rotation, for example exchange anisotropy in cobalt systems has been observed in this study. It may be noted that increasing the diameter in equation (5.13) would reduce the anisotropy constant and thus errors in particle size data would lead to incorrect K values. It has been shown in Chapter 4, however, that median diameters are overestimated and σ underestimated and so correct values would tend to increase the anisotropy constant. It is possible that

magnetocrystalline anisotropy contributes to shape anisotropy and that the magnetocrystalline anisotropy of the fine particles may be greater than that of the bulk material. The lattice parameter of fine particles is usually smaller than that of the bulk material which must affect the magnetocrystalline anisotropy. The inclusion of impurities may induce strain anisotropies and may also alter the crystal structure of the particles. Recent Mossbauer observations by van Wonterghem et al. (1985) and Williams (Priv. Comm. 1986) have shown that particles prepared by the decomposition of $Fe(CO)_5$ are composed of Fe/C and not α-Fe. The particles may thus have orthorhombic lattices which would tend to increase the magnetocrystalline anisotropy. In cobalt systems hexagonal particles have been observed in this study (Chapter 6) and some may be present in all cobalt systems prepared via the organometallic route. It is evident that further investigation of this problem is required, in particular new techniques for obtaining the anisotropy constant.

5.3.2 Magnetisation Measurements

(a) Magnetite System

The initial magnetisation of three aligned magnetite samples, prepared in the same manner as those used in the torque study and aligned in fields of 0.4, 0.7 and 1.4T, were measured using the VSM. Each sample was demagnetised in the manner described in Chapter 3 before measurement. The results were obtained by rotating the magnet, a control

experiment in which the sample was rotated and not the magnet yielded the same results. Figures 5.12, 5.13 and 5.14 show the initial magnetisation measured at 0°, 45° and 90° to the alignment direction for the 0.4, 0.7 and 1.4T samples respectively. The effect of texture on initial magnetisation is clearly demonstrated, the magnetisation rising most quickly when measured parallel to the alignment direction and least quickly when measured perpendicular to it, increasing texture leads to an increased difference between the two. Initial susceptibility has been calculated from the first two points of each curve and full room temperature magnetisation curves used to obtain saturation magnetisation and particle size distribution. Table 5.3 shows the data where $\bar{\chi} = \chi / \sigma_{ff}^{\infty}$ is the reduced initial susceptibility.

Equation (5.15) may be written for the susceptibility in terms of two components, one due to the superparamagnetic component, the other to textured particles,

$$\overline{\chi} = \overline{\chi}_{spm} + \overline{\chi}_{text} \qquad (5.27a)$$

where

$$\overline{\chi}_{spm} = \frac{1}{3}\left(\frac{\overline{v_i}\, M_b^{\,ool}}{kT}\right) e^{\frac{9\sigma^2}{2}} \qquad (5.27b)$$

$$\overline{\chi}_{text} = 3\,\overline{\chi}_{spm}\, \xi(q_f)\,\xi(q_m)\,(1-3p_f^{-1}L(p_f))(\cos^2\theta - \tfrac{1}{3}) \qquad (5.27c)$$

where the factor $e^{9\sigma^2/2}$ has been obtained by integrating over the particle size distribution. It is included in (5.27c) as a first approximation to integrating this term

PAGE 136
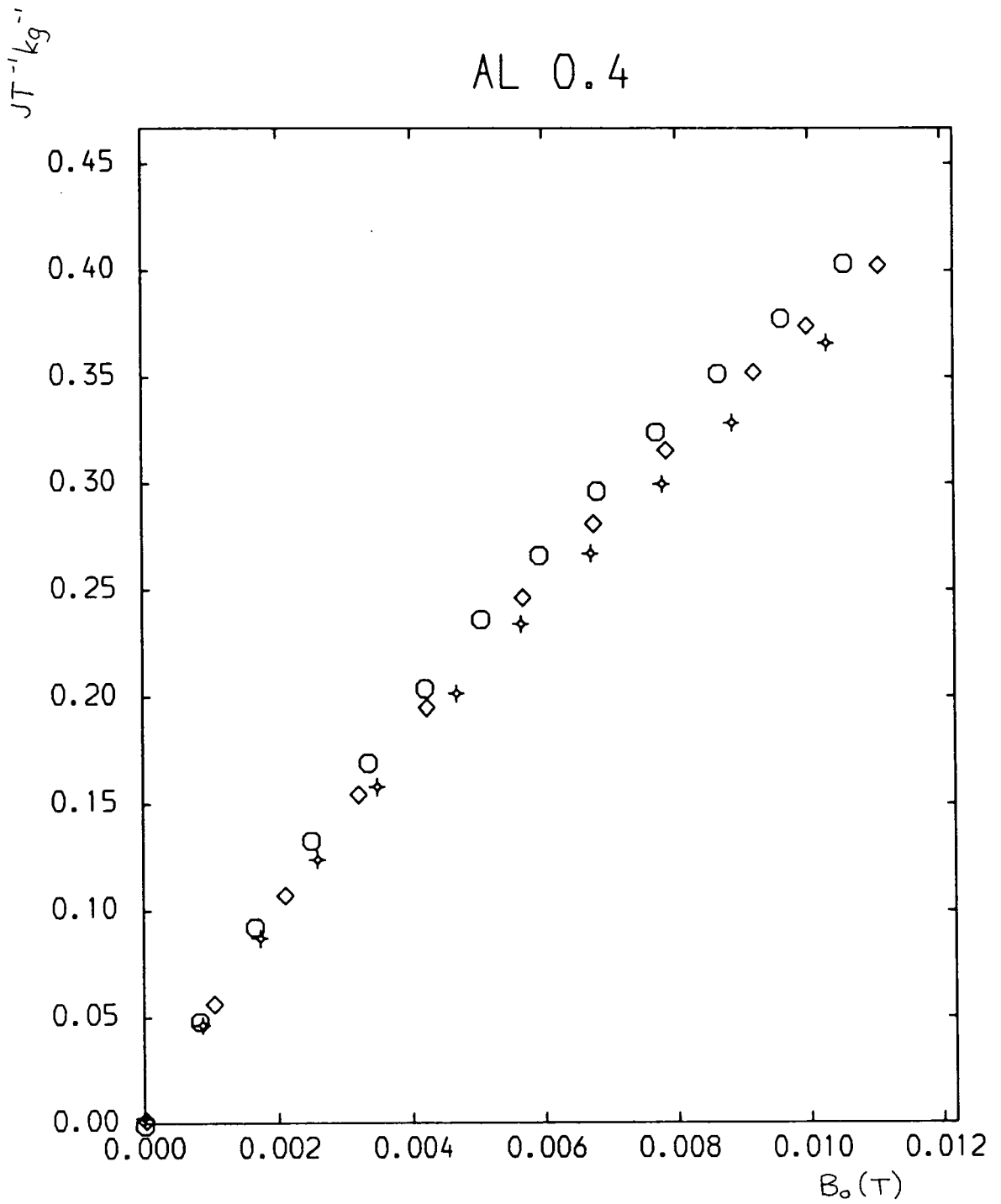
FIGURE 5.12
Initial magnetisation for magnetite/poly-
ester resin sample aligned in 0.4T.
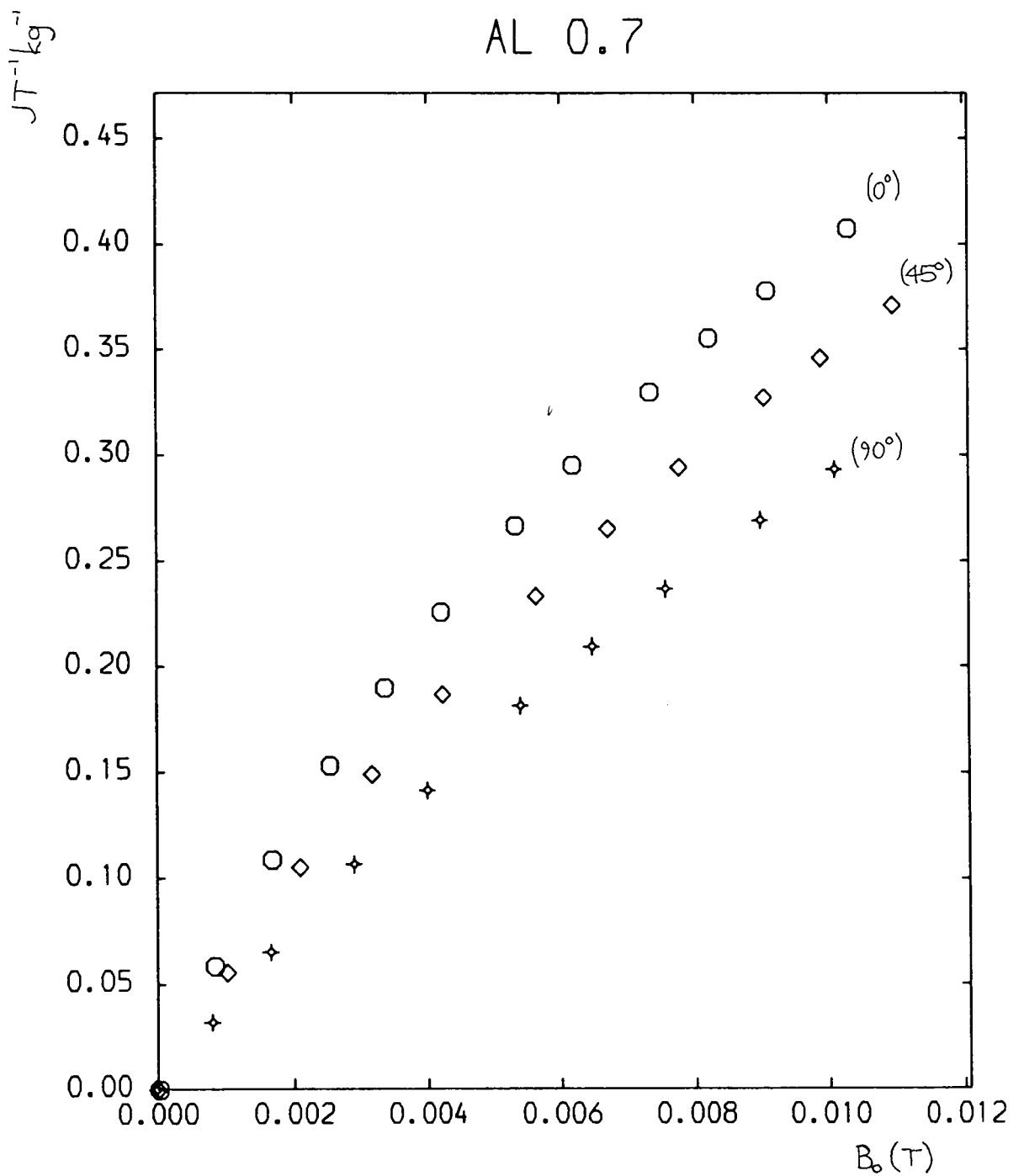
FIGURE 5.13
Initial magnetisation for magnetite/poly-
ester resin sample aligned in 0.7T.
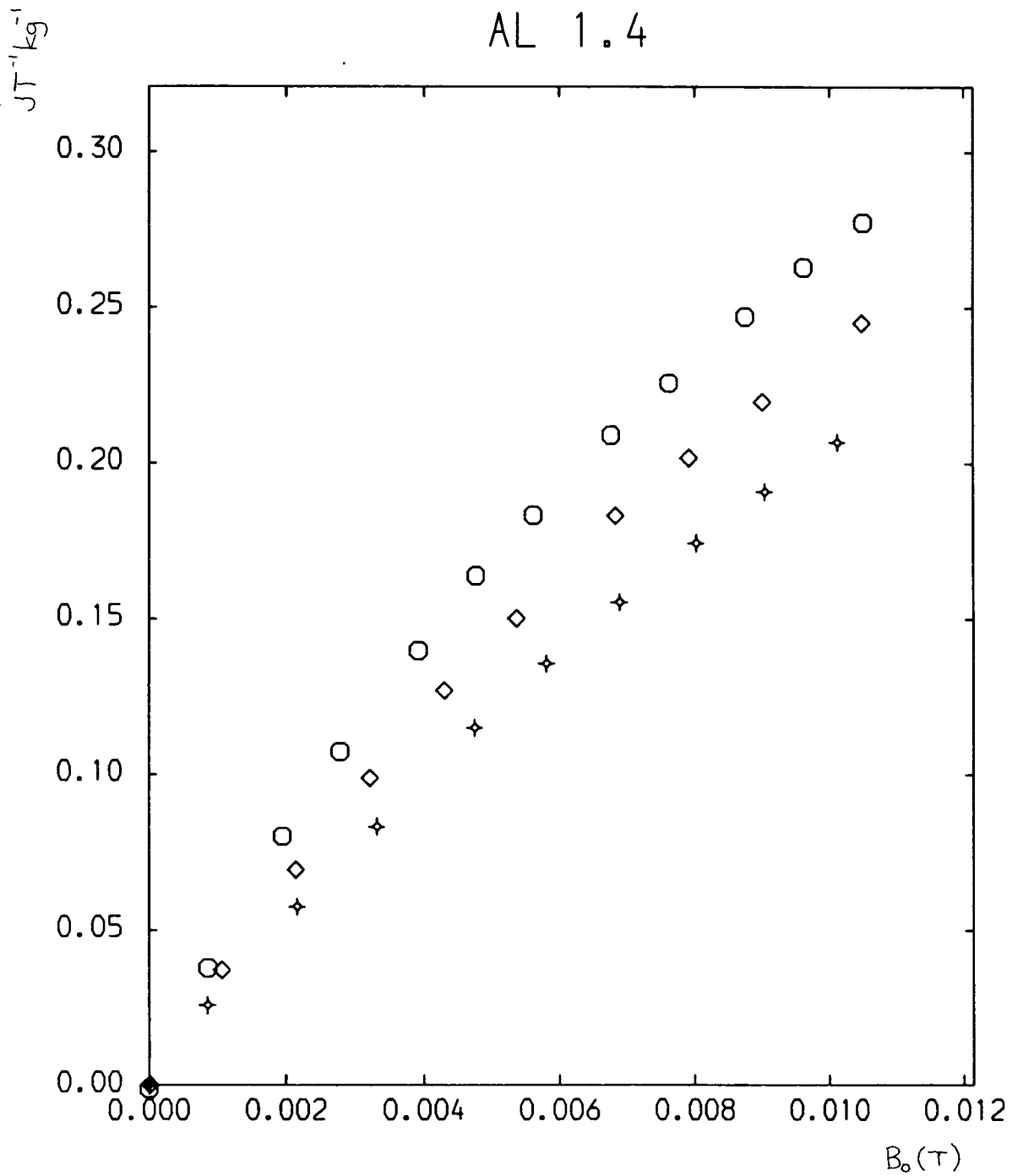
FIGURE 5.14
Initial magnetisation for magnetite/poly-
ester resin sample aligned in 1.4T.

TABLE 5.3

	$\chi_{\parallel}$	χ_{45}	$\chi_{\perp}$	σ^{∞}_{ff} $JT^{-1}kg^{-1}$	ρ_{ff} kgm^{-3}	ε_m	ε_v $\times 10^{-3}$	$\overline{\chi}_{\parallel}$	$\overline{\chi}_{45}$	$\overline{\chi}_{\perp}$
0.4	54.5	53.77	50.52	1.84	1125	0.018	3.86	29.62	29.22	27.46
0.7	69.2	54.05	39.70	1.72	1098	0.016	3.36	40.23	31.42	23.08
1.4	45.57	35.42	30.27	1.19	1138	0.012	2.50	38.29	29.76	25.44

Magnetic data for aligned magnetite

over the particle size distribution. The particle size

distribution has a large effect on the initial

susceptibility and so this factor must be included. Values

for $\bar{X}_{spm}$ may be obtained for each sample using

$$\bar{X}_{spm} = \frac{1}{3} \left(4\bar{X}_{45} - \bar{X}_{\parallel} \right) \qquad (5 \cdot 28a)$$

$$\bar{X}_{spm} = \frac{1}{3} \left(\bar{X}_{\parallel} + 2\bar{X}_{\perp} \right) \qquad (5 \cdot 28b)$$

where $\parallel$ and $\perp$ refer to $\theta = 0°$, $90°$ respectively in (5.27)c.

The values obtained are:-

$$
\begin{array}{llll}
0.4 & : & 29.09 & \text{and} & 28.18 \\
0.7 & : & 28.48 & \text{and} & 28.80 \\
1.4 & : & 26.92 & \text{and} & 29.72 \\
\end{array}
$$

which give an average value of 28.53 ± 0.40. A theoretical

value is obtained from equation (5. 7b) using $\bar{d}_{\frac{1}{2}} = 8.23$nm,

$\sigma = 0.43$, T = 292K which results in 26.47. The agreement is

very good especially when it is noted that the calculated

value is very sensitive to σ, for example $\sigma = 0.45$ would

lead to a value of 28.66.

An estimate of the blocked volume fraction may be made

using the relationship between the normal and lognormal

distributions described in Section 5.2.3. Assuming K = 5.8

x 10^4Jm^{-3}, τ = 600s and T_f = 325K gives a value of 15.9nm

for the critical diameter which corresponds to a fraction of

0.069 of the total particle volume being blocked. Thus when

the resin polymerises only $\sim$ 7% of the particle volume, that due to the largest particles, will be textured. Table 5.4 shows the experimentally determined texture component in the initial susceptibility. This has been obtained by subtracting the superparamagnetic contribution obtained above from the total susceptibility. Theoretical values are also shown which have been calculated using equation (5.27a). As can be seen, only the 0.7T sample exhibits any agreement with the theoretical calculation. The other two samples have values which are much lower than expected which is almost certainly due to polymerisation having begun before the samples were properly inserted into the aligning field. The change in viscosity of the resin is fairly rapid and as the resin/magnetic fluid mixture had to be mixed prior to being placed in a mould some delay was inevitable. For the 0.7T sample the experimental values $\overline{X}_{45}/\overline{X}_{\parallel} = 0.247$ and $\overline{X}_{\perp}/\overline{X}_{\parallel} = -0.467$ are in good agreement with the theoretical values of 0.25 and -0.50 respectively. Values of the texture factor,

$$\xi(q_f)\xi(q_m)\left(1-3\rho_f^{-1}L(\rho_f)\right) \qquad (5.29)$$

have been obtained for the 0.7T sample from $\overline{X}_{11}, \overline{X}_{45}$ and $\overline{X}_{\perp}$ as 0.205, 0.203 and 0.191 which average 0.200. By setting $q_f = q_m$ and using T = 300K as an average between setting and measurement temperatures enables an estimate of K to be made from equation (5.29) using the experimental value of 0.2. This is found to be $4.7 \times 10^4 \mathrm{Jm}^{-3}$ which is

TABLE 5.4

The texture component in the susceptibility

	$\overline{X}$ 0°	$\overline{X}$ 45°	$\overline{X}$ 90°
EXPERIMENTAL			
0.4:	1.09	0.69	−1.07
0.7:	11.70	2.89	−5.45
1.4:	9.76	1.23	−3.09
THEORETICAL			
0.4:	13.64	3.41	−6.82
0.7:	15.24	3.81	−7.62
1.4:	16.38	4.10	−8.19

smaller than that given by torque measurements but is very similar to that obtained by Hoon et al. (1983). This is a fairly crude approximation, however, and the torque data is considered more reliable.

(b)   Organometallic Ni$_3$Fe System

Figure 5.15 shows the hysteresis loop obtained at $\sim$8K for the NiFe6 system. This was frozen in an applied field of 1T, however as the carrier liquid froze at $\sim$ 240K and the magnetic particle size is small, $\bar{d}_{\frac{1}{2}}$ = 4.4nm, σ = 0.34 and estimating K $\sim$ 10^5Jm^{-3}, less than 0.5% of the particle volume will be blocked on freezing. Further support for this was obtained when no hysteresis was observed for this system frozen to 77K in an applied field of 1.0T. It is therefore assumed that the easy axes are randomly oriented.

The hysteresis loop is characterised by a remanence of 0.1JT^{-1}kg^{-1}, a coercivity of 0.013T and gradient through remanence of 7.45. For a randomly aligned system the analysis of O'Grady et al. (1980) may be applied. The remanence may be used to estimate a value for d$_c$ and hence K as described in 5.2.3. A value of $\sim$ 1.1 x 10^5Jm^{-3} is obtained. Equation (5.20) was used to estimate K from the approach to remanence and resulted in $\sim$ 1.15 x 10^5Jm^{-3}. The coercivity may be used to make an order of magnitude estimate for K using the formula given by Kneller (1969) for $(B_o)c/(B_o)_K$ assuming coherent rotation and this yields K $\sim$ 10^5Jm^{-3}.
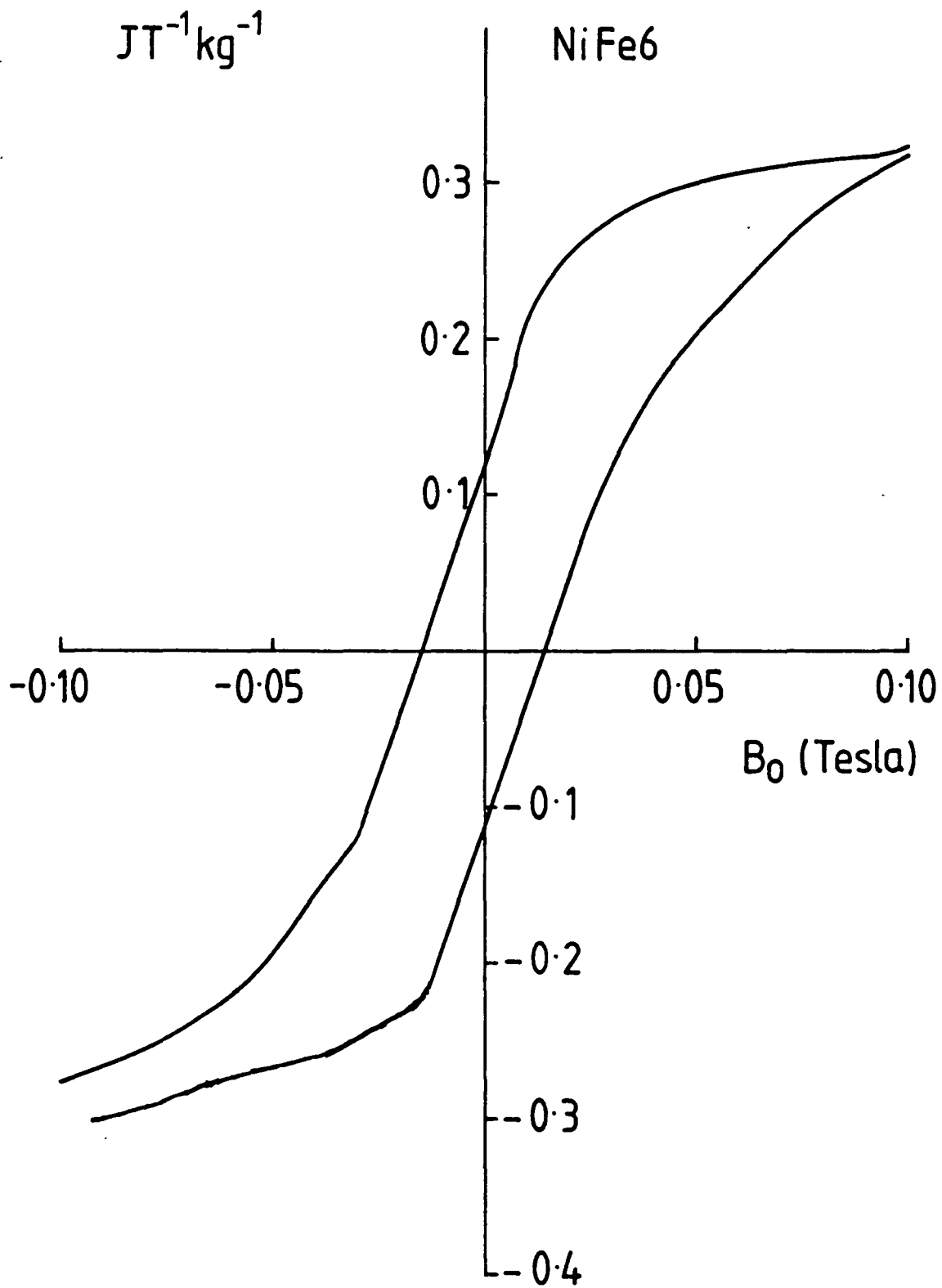
FIGURE 5.15
Hysteresis loop for fluid NiFe6 measured at
8 K.

(c) Discussion

The magnetisation data has yielded lower values for the anisotropy constant than the torque data in both cases. For the metallic system the measurements were made on different fluids, however the difference in their preparation was only in the carrier liquid and heating temperature. This is not expected to affect particle elongation sufficiently to explain the difference in anisotropy constants obtained.

The differences are felt to be due to the experimental method. The torque magnetometer had been carefully calibrated by Mr. C.D.H. Williams prior to the NiFe measurements making it unlikely that the torque values have large errors. The magnetisation data is subject to polymerisation problems in the magnetite case and to low temperature problems (see Chapter 3) in the NiFe case. It is therefore felt that the torque data is more reliable, especially as the initial susceptibility data is more sensitive to particle size distribution than the torque data. In all cases, however, the anisotropy constant would require particle elongations in excess of 1.5 which are not observed. This suggests that factors other than shape play an important role and highlights the need for more data and further work on this problem.

CHAPTER SIX

NEW MAGNETIC FLUIDS

6.1 Introduction

The principal aim of the present study was to investigate the properties of new magnetic fluids prepared via the organometallic route and in particular mixed metal systems. The preparation of single metal systems was first investigated in order to test the applicability of the cyclopentadienyl-carbonyl compounds to magnetic fluid preparations. Once this was achieved the mixed metal systems, which had to be prepared from cyclopentadienyl-carbonyl compounds, were investigated. Mixed metal systems containing Fe and Co and Fe and Ni were successfully prepared during this study.

6.2 Single Metal Systems

Prior to the work reported herein and a previous publication from the Durham group, Hoon et al (1983), metallic hydrocarbon based magnetic fluids had been prepared only from the simple carbonyls $Co_2(CO)_8$ and $Fe(CO)_5$. The work of Hoon et al. (1983) extended the range of precursors to another carbonyl, $Ni(CO)_4$ and to the non-carbonyl organometallic, $(\pi-C_5H_5)_2Ni$. During this study the spectrum of successful precursors has been further extended, the results for single metal systems are presented below.

6.2.1 Preparative Details

Iron systems have been successfully prepared from $Fe_2(CO)_9$, $Fe_3(CO)_{12}$ and $[(\pi\text{-}C_5H_5)Fe(CO)_2]_2$, cobalt systems have resulted from the simultaneous decomposition of $Fe_3(CO)_{12}$ and $Co_2(CO)_8$ and nickel systems have been obtained using $[(\pi\text{-}C_5H_5)Ni(CO)_2]_2$ and $(\pi\text{-}C_5H_5)_2Ni$. The $Fe_2(CO)_9$ and $Fe_3(CO)_{12}$ are both crystalline solids and therefore much easier to handle than $Fe(CO)_5$ which is a liquid at room temperature. The addition of the cyclopentadiene ligand, $(\pi\text{-}C_5H_5)$, to carbonyl complexes results in compounds which are crystalline and have greater stability than the simple carbonyls. They tend, therefore, to require higher temperatures for decomposition to occur and in order to achieve this a metal heating bath (Woods metal) and higher boiling point carrier liquids, such as 1-methyl-napthalene were used. The nickel complex is particularly useful as $Ni(CO)_4$ is a very toxic, very volatile liquid and is therefore difficult to handle whereas the cyclopentadienyl-carbonyl complex is a solid and may be handled in the normal laboratory. It also decomposes more readily than $(\pi\text{-}C_5H_5)_2Ni$ which is also a crystalline solid. Nickel fluids are not easy to prepare, however, as the cyclopentadienyl-carbonyl compound has to be prepared from $Ni(CO)_4$. They tend to have very large particle sizes and often no colloidal stability, a full investigation of surfactants appropriate to nickel is required.

The simultaneous decomposition of iron and cobalt

carbonyls surprisingly resulted in an h.c.p. cobalt system.
This has not proved repeatable and another h.c.p. system was
obtained from $Co_2(CO)_8$ alone although the same surfactant
was used in both cases. The loss of iron is discussed
further in Section 6.2. The preparative conditions for the
fluids discussed in this section are summarised in Table
6.1.

6.2.2 Particle Composition, Structure and Size

(a) Transmission Electron Diffraction

The Fe fluid MK34 gave only two lines which may have
been b.c.c., however the results of Griffiths et al. (1979)
on similar sized "Fe" particles suggests that these
particles may be largely disordered. The recent Mössbauer
study of van Wonterghem et al. (1985), who found that the
decomposition of $Fe(CO)_5$ did not result in α-Fe but in
amorphous iron-carbide particles with 5-10 at % carbon,
lends support to this argument. When these authors annealed
their particles at 523K in a stream of hydrogen the
particles became α-Fe. Griffiths et al. obtained α-Fe for
particle sizes of the order 16nm. It has been impossible to
obtain more than one or two diffraction lines from all our
Fe fluids which may indicate that they are indeed largely
amorphous. The van Wonterghem result has been confirmed for
Durham fluids prepared from $Fe(CO)_5$ by Dr. J. Williams of
Sheffield University (priv. comm.).

The Fe + Co and Co(2) systems both gave electron

TABLE 6·1

Fluid Designation	Starting Material	Carrier Liquid	Surfactant	Mass of Precursor (g)	Mass of Surf. (g)	Volume Carrier cm^3	Bath Temp.°C	Heating Time hrs
MK34	$Fe_2(CO)_9$	Toluene	Duomeen TDO	3·5	0·69	10	130	3
FS2	$[(\pi-C_5H_5)Fe(CO)_2]$	1-m-n	Sarkosyl	1·5482	0·6221	15	220	5
FS4	$Fe_3(CO)_{12}$	1-m-n	Sarkosyl	1·5069	0·7288	15	195	3
Fe+Co	$Fe_3(CO)_{12}/$ $Co_2(CO)_8$	Toluene	Solsperse 3000	1·0 1·0	0·4	30	140	3
Co(1)	"	"	"	0·991 1·067	0·7	40	140	3
Co(2)	$Co_2(CO)_8$	"	"	1·0	0·7	40	140	3
Co(3)	$Co_2(CO)_8$	"	Manoxol OT	1·0	0·3477	40	140	3
Ni1M	$[(\pi-C_5H_5)Ni(CO)_2]_2$	Pet. Eth.	Manoxol OT	0·2407	0·2137	3	200	0·25
Ni2M	"	1-m-n	"	0·6285	0·4850	15	160	3
NiS53	$(\pi-C_5H_5)_2Ni$	2-m-n	"	1·51	1·0	15	160	2

1,2-m-n = 1,2 methyl napthalene   Pet. Eth. = Petroleum Ether (200-260°C)

diffraction patterns containing the characteristic triplet grouping of reflections due to hexagonal close packed cobalt. The fluid Co(1), which was a repeat preparation of the Fe + Co system, gave diffuse lines of the f.c.c. phase which is normally observed for fine particle cobalt. It has not, therefore, been possible to repeat the preparation of hexagonal cobalt which may be due to the difficulty in recreating the precise experimental conditions. The energy difference between the two phases is believed to be small (Szpunar, B. 1985) and may be sensitive to the exact conditions prevailing.

The nickel systems have been found to be f.c.c. nickel with results very similar to those of Hoon et al. (1983).

(b) <u>EXAFS</u>

Extended X-ray Absorbtion Fine Structure spectra were obtained on the laboratory scale instrument in the University of Durham Industrial Research Laboratories. Figure 6.1 shows that obtained for Fe fluid 4.41 which is typical of the spectra obtained for Fe fluids. Figure 6.2 shows the spectrum resulting from an 8 micron thick Fe foil and it can be seen the Fe fluid spectrum does not correspond with this. The large initial peak in fluid spectrum indicates that most of the Fe is not in the zero valence state. Precautions had been taken to ensure that the fluid did not oxidise before this experiment and the fluid spectrum does not correspond with any iron-oxide spectrum obtained on this instrument. It is thought that this may be
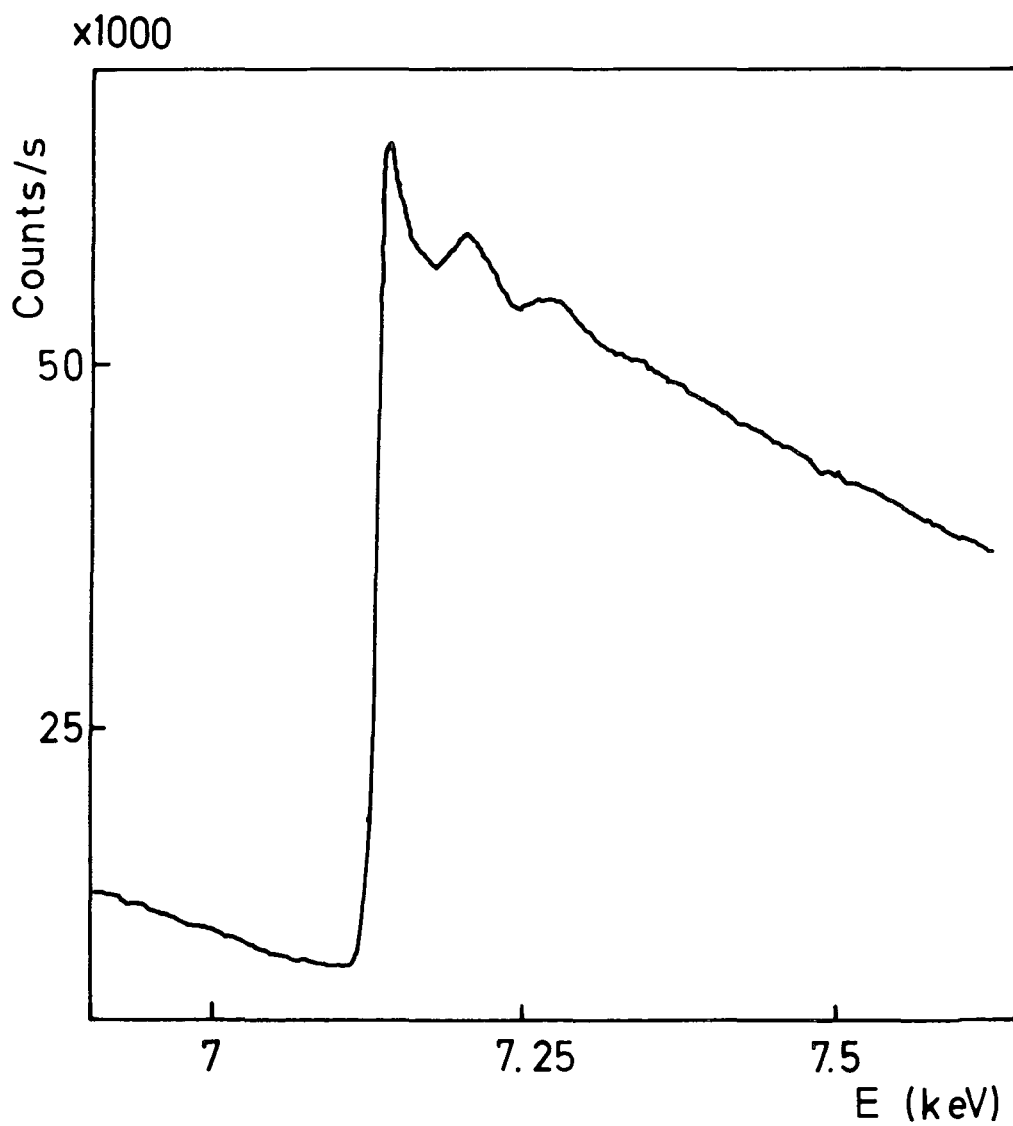
FIGURE 6.1
Absorption EXAFS spectrum for a typical Fe
system (Fe4.41) showing large initial peak.
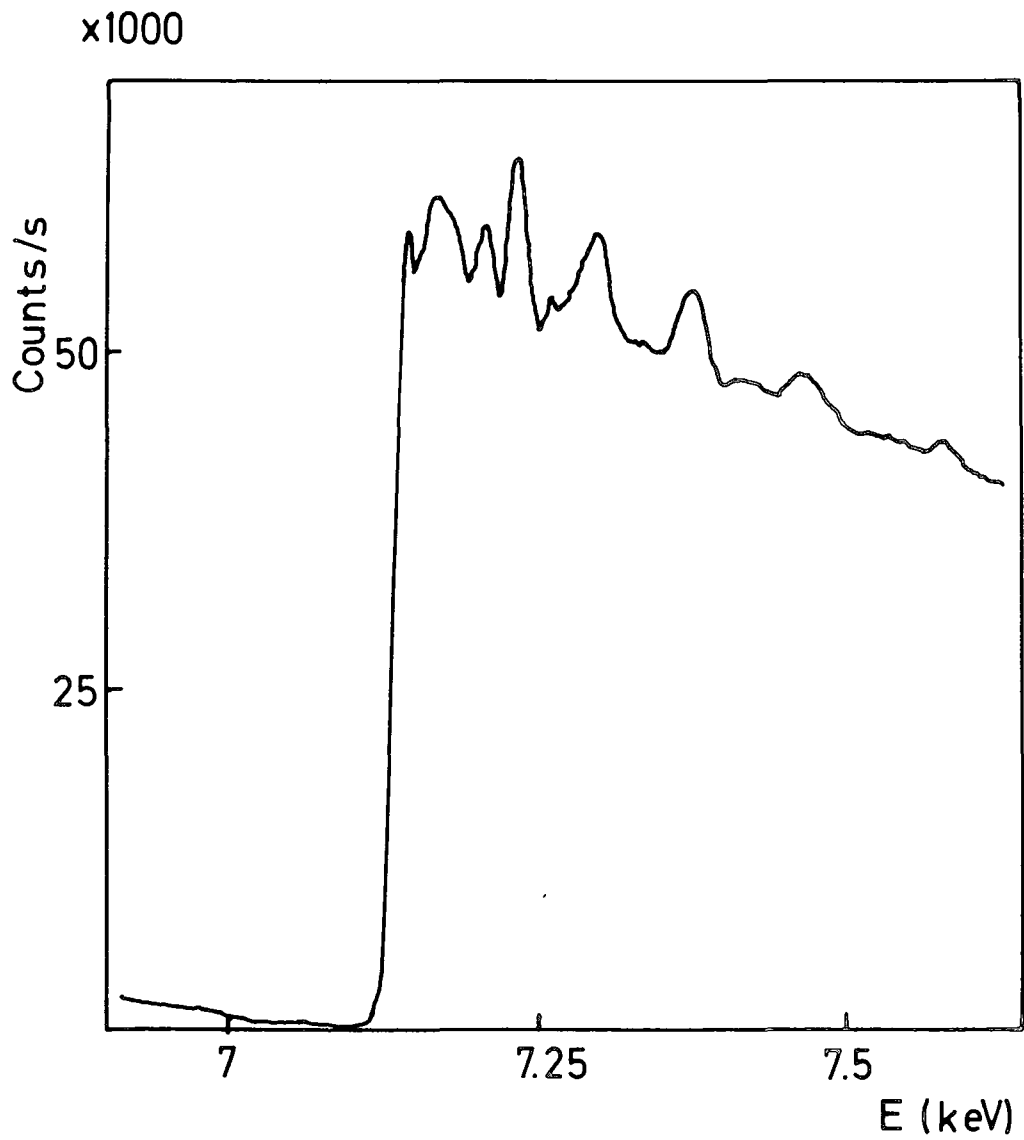
FIGURE 6.2
Absorption EXAFS spectrum for an 8nm Fe foil
showing bulk characteristics.

further evidence of iron-carbide formation and further investigation is under way. Cobalt fluids were also examined and were found to contain metallic cobalt whose oxidation could be recorded on this instrument.

(c)   Shadow Electron Microscopy

The fluids MK34 and Fe5S (an identical preparation to Fe4S) were examined at magnifications of 170 000x and 220 000x respectively and the micrograph prints examined on the image size analyser (Chapter 3). The results are shown in Figure 6.3. The histogram for the MK34 system is that obtained by counting the small particles making up the aggregates. The particle size data for this system has been fully discussed in Chapter 4. The result for Fe5S is very typical of the organometallic decomposition route with a mean diameter of 7.4nm and standard deviation of 1.3.

6.2.3   Room Temperature Magnetisation Curves

Figure 6.4 shows the room temperature magnetisation curves recorded on the V.S.M. for the systems MK34 and FS2, whilst Figure 6.5 shows those for FS2 and FS4. The saturation magnetisations of MK34, FS2 and FS4 were 1.86, 0.36 and $\sim$ 0.16 $JT^{-1}kg^{-1}$ repectively which correspond to mass fractions of 0.85%, 0.17% and $\sim$ 0.07%. These may be compared with the initial metal mass fractions in the starting solutions which were 1.18%, 2.8% and 2.86%. The ratio of surfactant to precursor mass was 0.2, 0.4 and 0.5 in each case. Preparation MK34 is thus the most efficient in magnetic terms and this may be due to
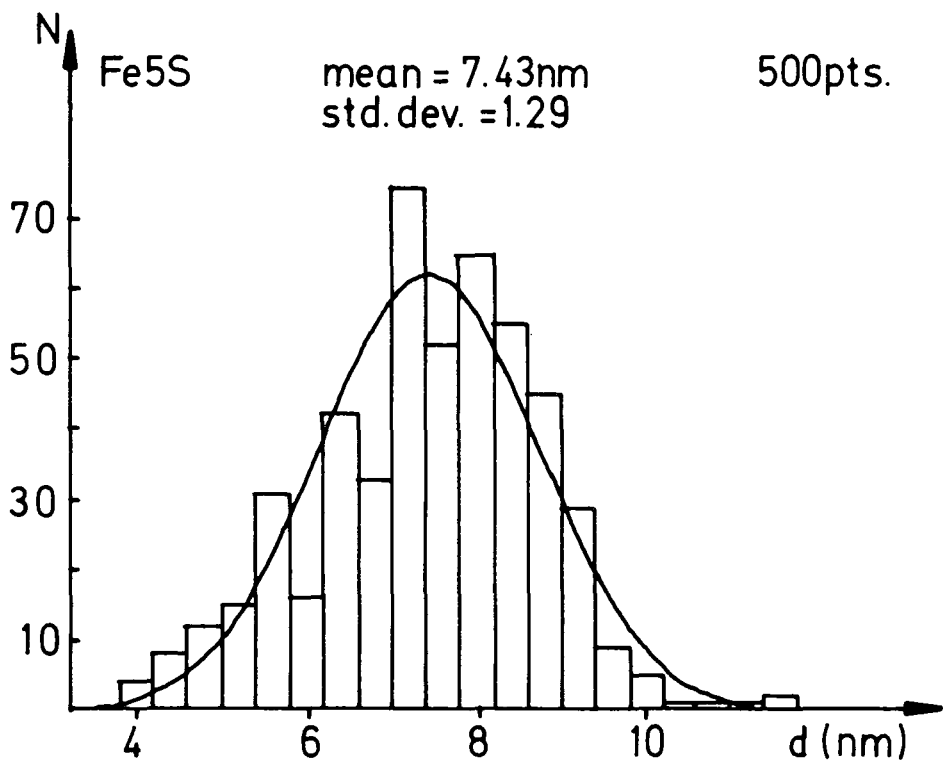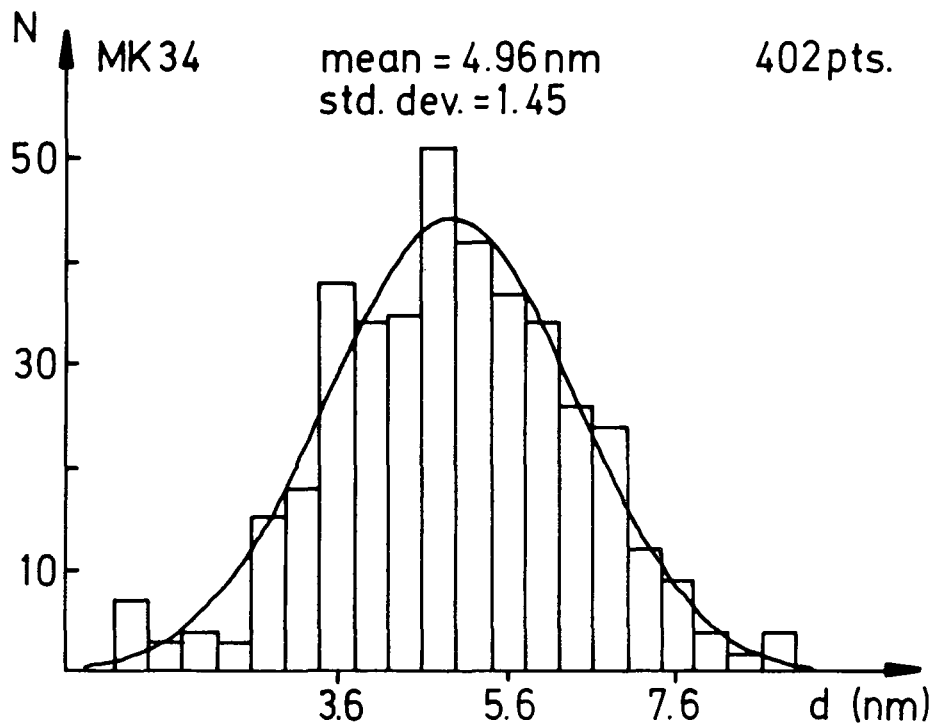
FIGURE 6.3
Particle size distributions obtained from electron micrographs using the image size analyser for Fe fluids MK34 and Fe5S. Solid line represents a normal distribution with the experimental mean and standard deviation.
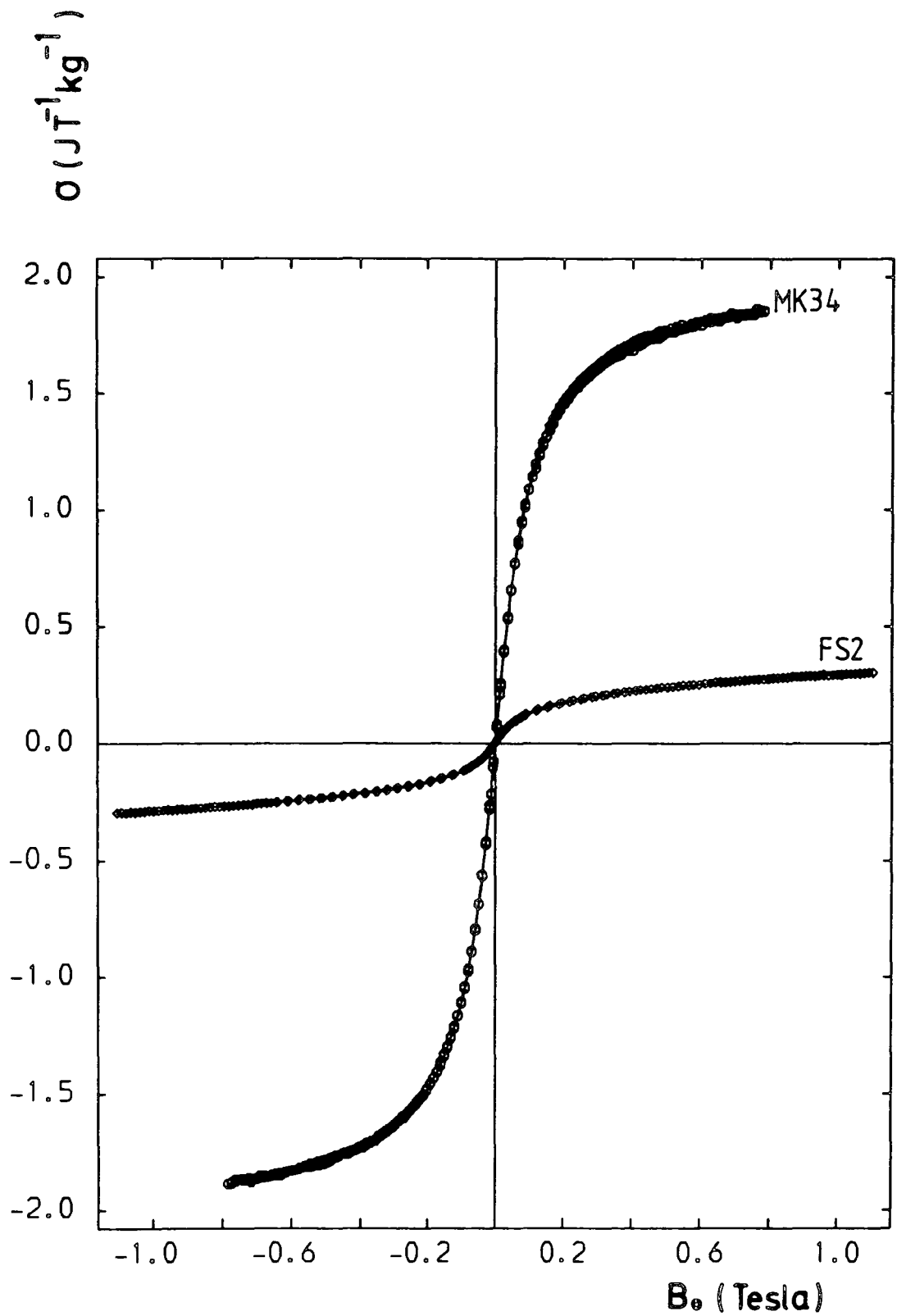
FIGURE 6.4
Room temperature magnetisation curves for the Fe fluids MK34 and FS2.
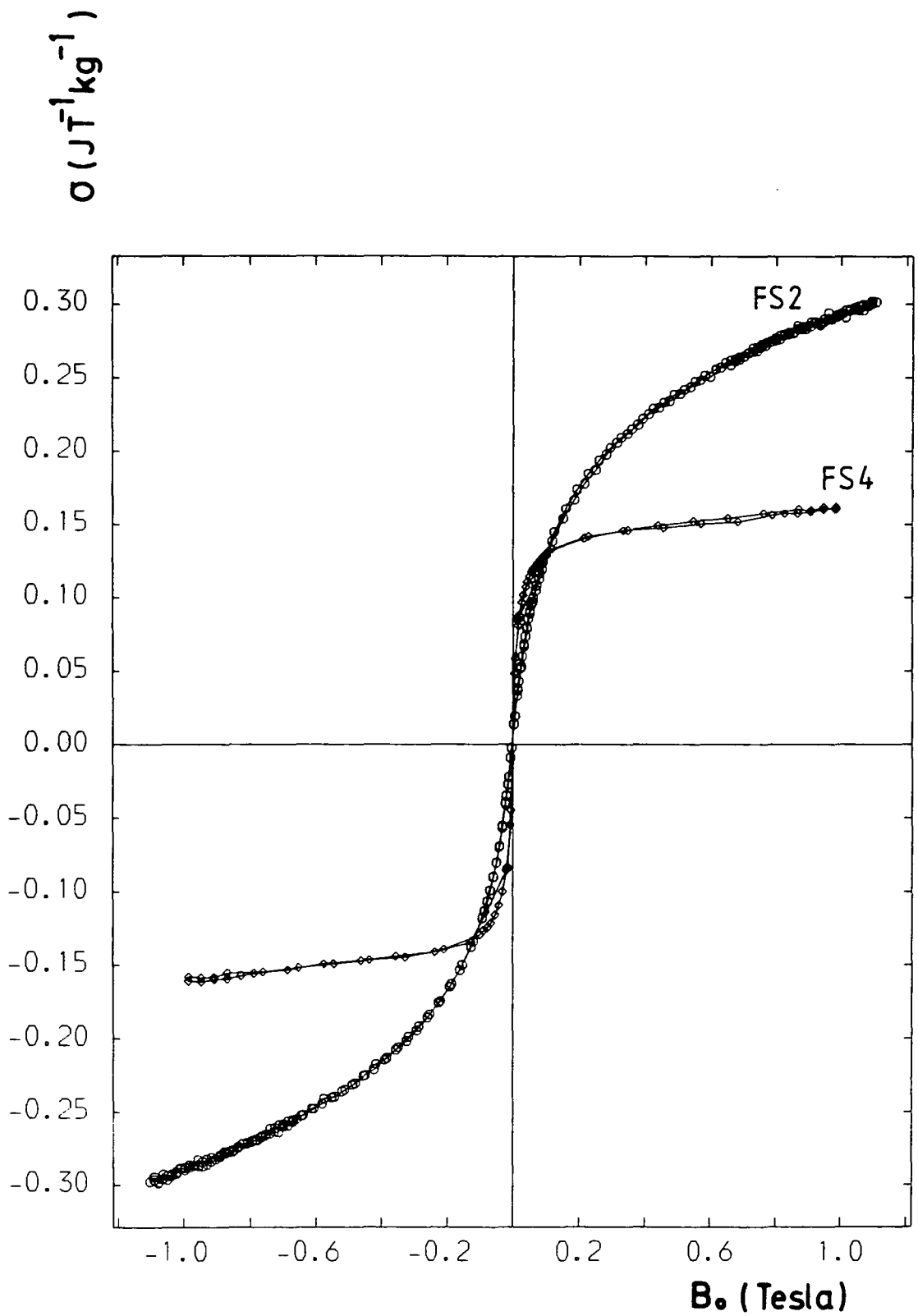
FIGURE 6.5
Room temperature magnetisation curves for the
Fe fluids FS2 and FS4.

surfactant/precursor ratio being lowest for this system. In

the fluids FS2 and FS4, over 90% (by mass) of the original

Fe atoms do not appear to contribute to the magnetisation and

this may be because they form complexes with the surfactants

before forming particles and there then being insufficient

Fe in these two systems to form particles. Of course, if

they are composed primarily of amorphous iron-carbides, then

the above magnetic mass fractions will be gross

underestimates. The influence of surfactant and heating

temperature may also explain the difference between MK34 and

these two systems.

The magnetisation curves of the four cobalt systems are

shown in Figures 6.6 and 6.7. These had saturation

magnetisations in the range 0.7 - 1.3 $JT^{-1}kg^{-1}$ which

correspond to mass fractions of 0.4 to 0.8% which compare

with the original solution values for Co of 0.9 to 1.2%.

Again a large proportion of the metal atoms have not been

incorporated into the magnetic state (i.e. exchange coupled

spins), though not as large as for iron systems and this may

be due to magnetically "dead" layers existing at the surface

as well as to surfactant-metal complex formation. The

magnetisation curve of Co(3) rises more slowly than those of

the other three which is due to the much smaller magnetic

diameter in this system, $\bar{d}_{\frac{1}{2}}$ ∿ 4nm as opposed to ∿ 7nm in the

other three. This may be due to the surfactant used in this

preparation, Manoxol-OT, as the other three were all

prepared using Solsperse-3000 and resulted in similar sizes.
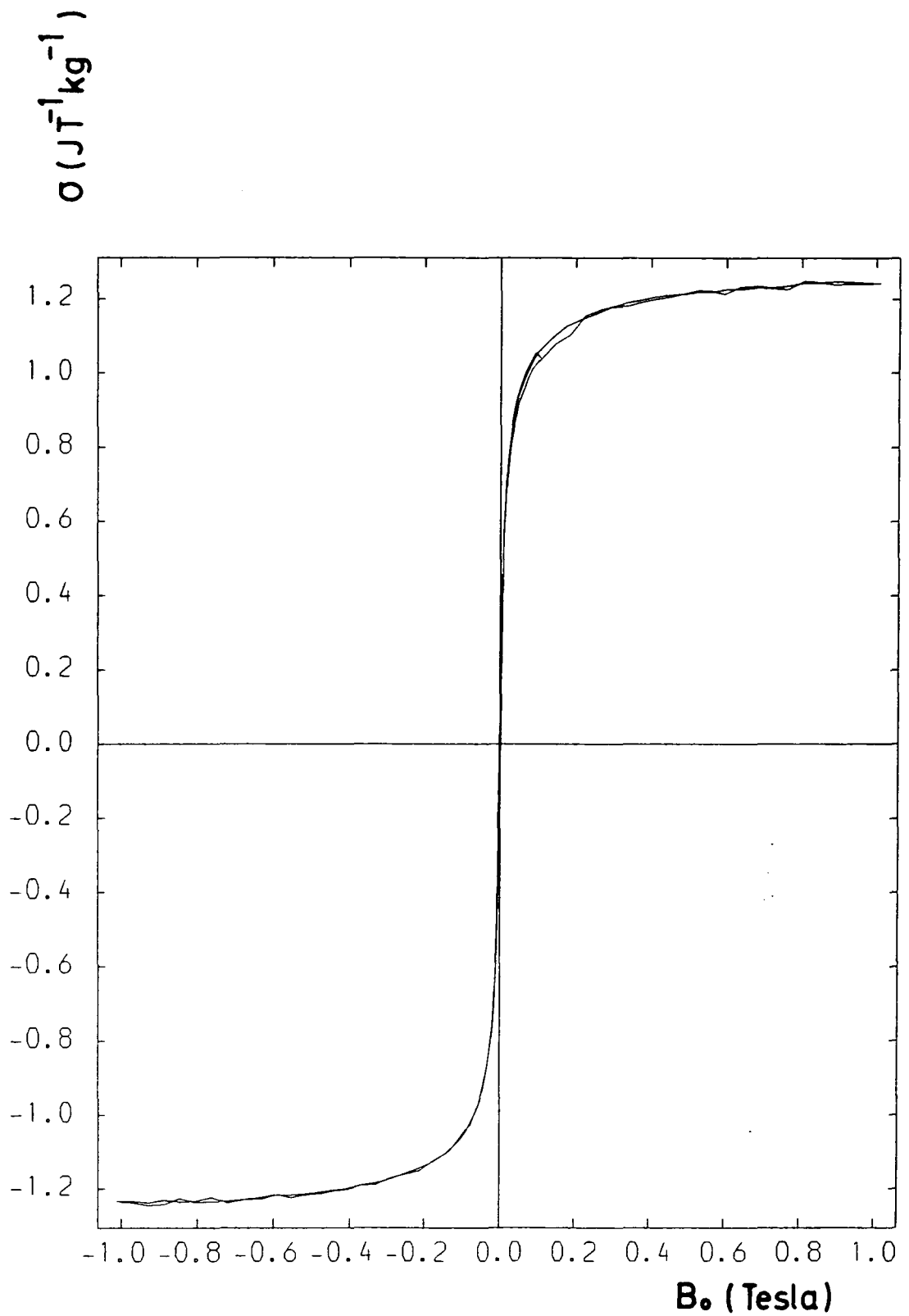
FIGURE 6.6
Room temperature magnetisation curve for the
Co fluid Fe+Co.
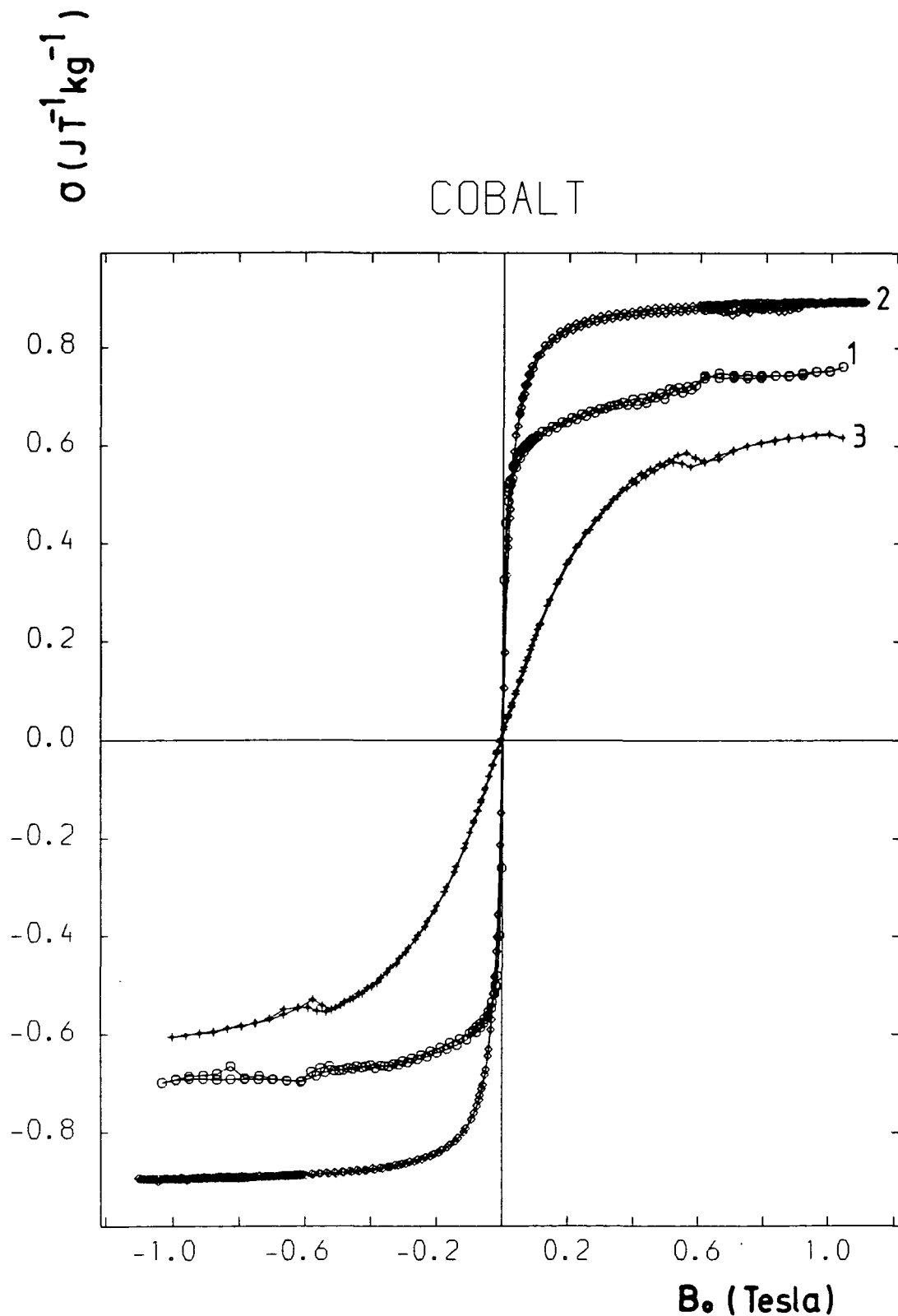
FIGURE 6.7
Room temperature magnetisation curves for the
Co fluids Co(1),Co(2) and Co(3). The "glitch"
at 0.6T is discussed in Chapter 3.

The magnetic data for all the single metal systems is presented in Table 6.2.

The room temperature curves for the nickel systems are shown in Figures 6.8 and 6.9. Saturation magnetisations of 0.05, 0.2 and 0.4 $JT^{-1}kg^{-1}$ were obtained for Ni1M, Ni2M and NiS53 respectively. These represent mass fractions of 0.09, 0.4 and 0.7% compared to 2.3, 1.3 and 2.7% in the starting solutions. Once again at least 75% of the metal atoms do not become "magnetic". Magnetic particle sizes could not be obtained for these systems as the gradient of approach to saturation could not be determined. They are believed to exceed 10.0nm as in all cases the rise to saturation is extremely rapid and settling out was observed in the system NiS53. The carrier for this fluid was 2-methyl-napthalene which melts at $35^{O}C$ and is thus solid at room temperature. A sample was heated and then left to cool in the presence of a magnetic field whereupon it was found that the nickel content had settled to the bottom of the container. This fraction had a greenish tint indicating the presence of nickel oxide. It has not proved possible to obtain small nickel particles using the precursors and surfactants listed in Table 6.1.

6.2.4 Stability to Oxidation

The room temperature magnetisation curves of MK34 0, 5, 9 and 11 months after preparation are shown in Figure 6.10. Examining the magnetisation at 0.1, 0.5 and 0.7T reveals that after 5 months the magnetisation had decreased by an

TABLE 6.2
Single metal systems magnetic data

Fluid	Magneti- sation $JT^{-1}kg^{-1}$	Mass fraction %	Vol. Fraction median (nm)	Lognormal parameter (σ)
MK34	1.86	0.85	5.4	-
FS2	0.36	0.17	3.5	0.38
FS4	0.16	0.07	5.8	0.50
Fe+Co	1.26	0.77	8.3	0.35
Co(1)	0.75	0.46	7.7	0.50
Co(2)	0.91	0.56	7.5	0.29
Co(3)	0.69	0.43	3.7	0.10
Ni1M	0.05	0.09	-	-
Ni2M	0.20	0.40	-	-
NiS53	0.40	0.70	12.4	-
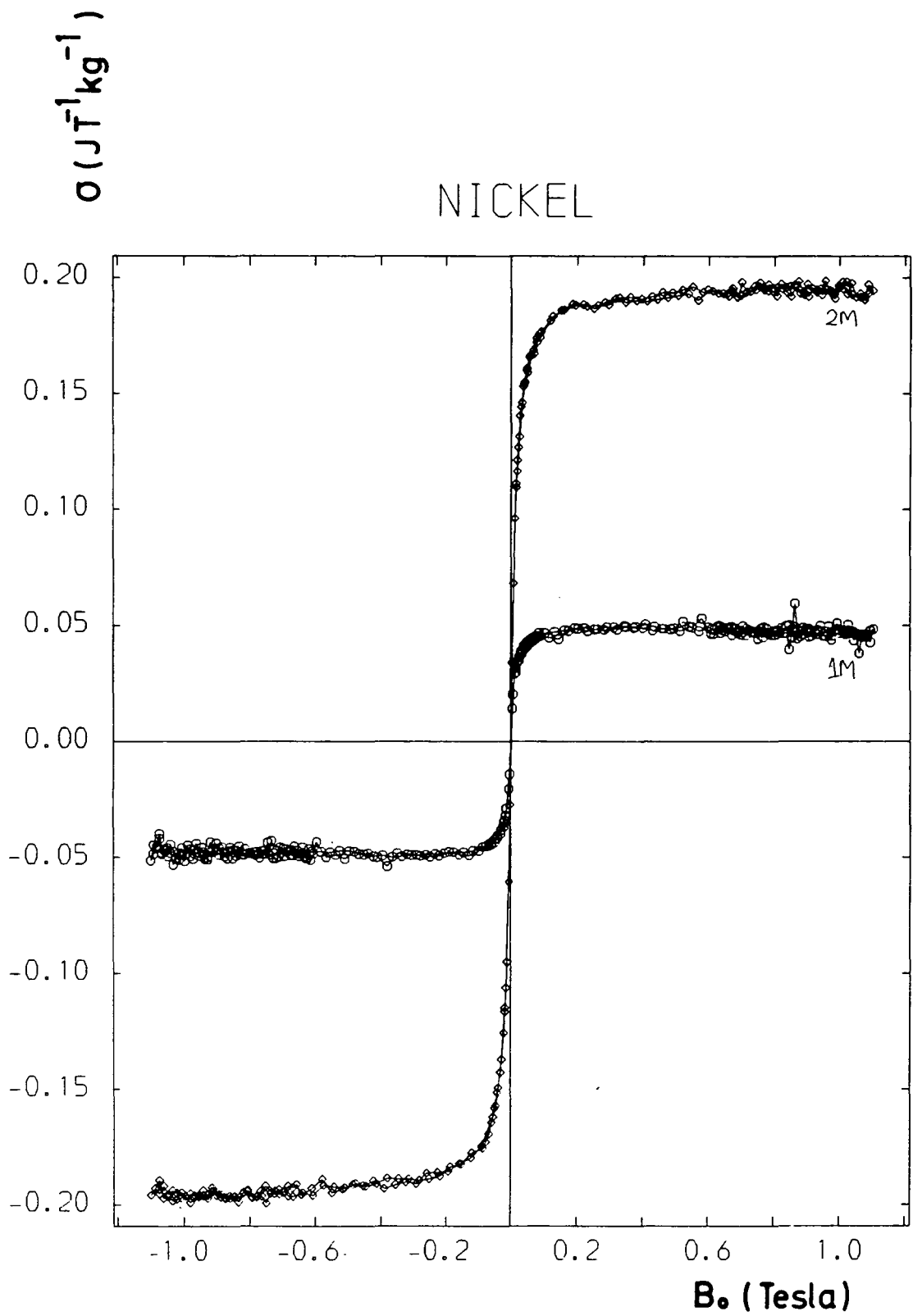
FIGURE 6.8
Room temperature magnetisation curves for the
Ni fluids Ni1M and Ni2M.
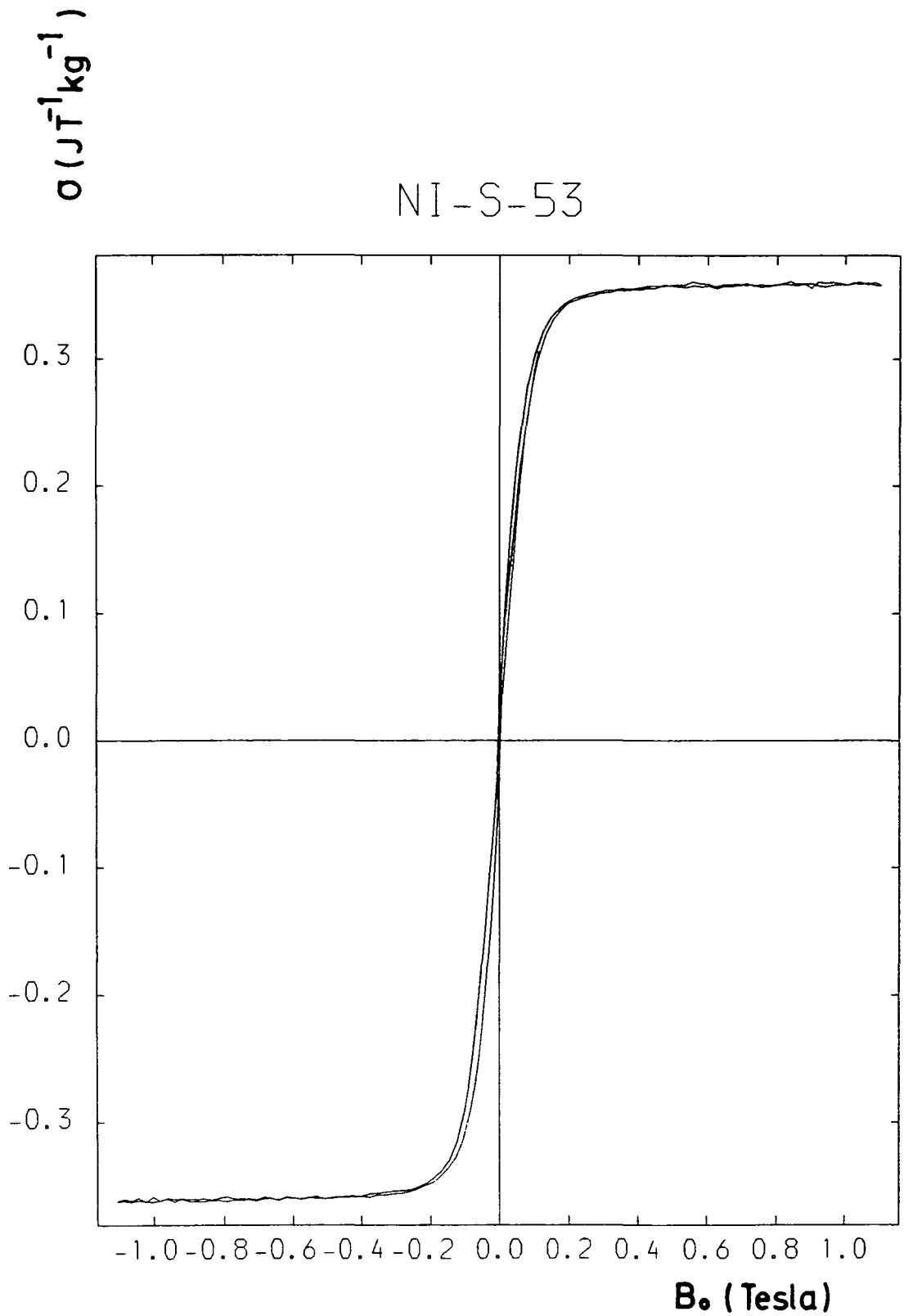
FIGURE 6.9
Room temperature magnetisation curve for the
"fluid" NiS53 which is solid at RT.
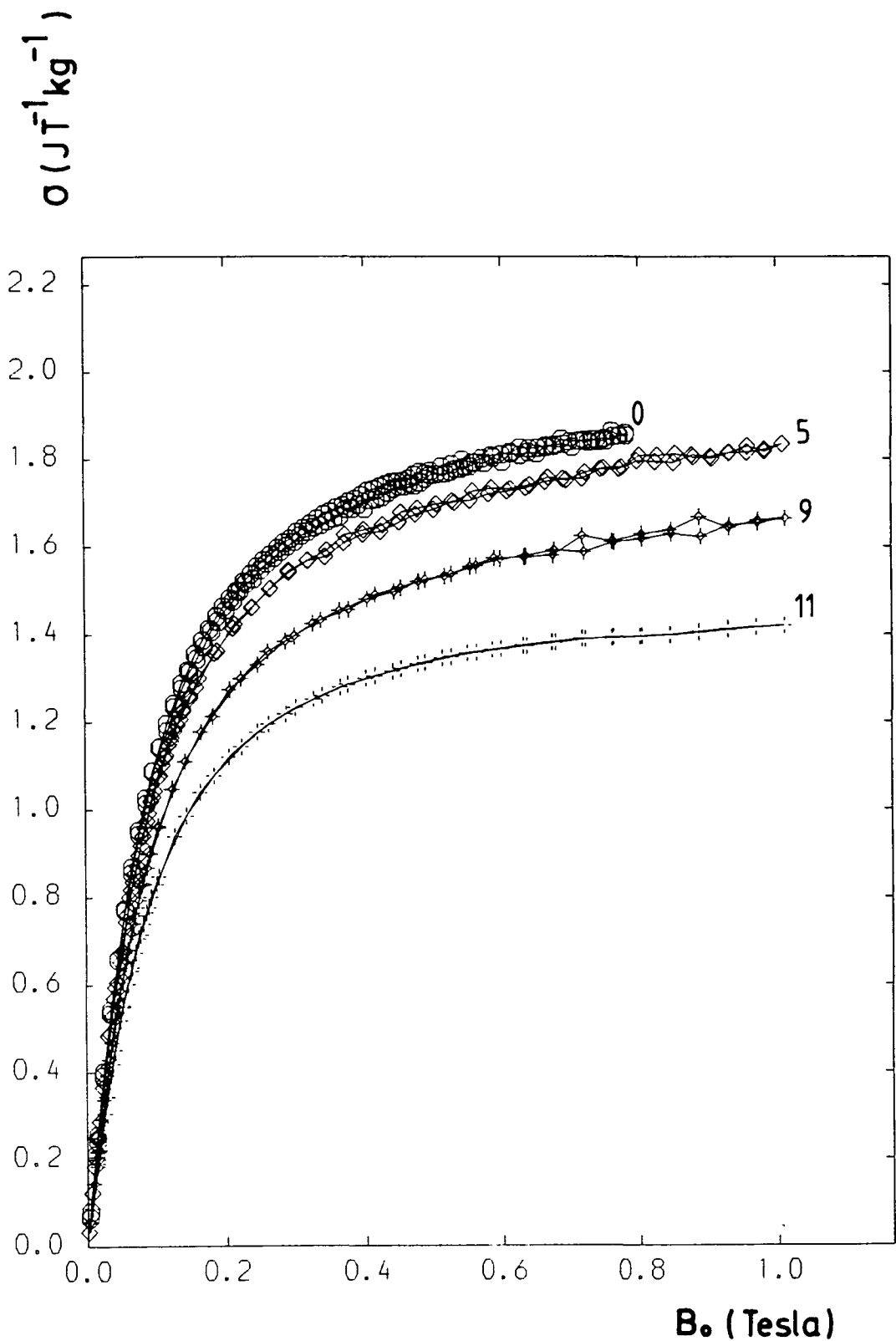
FIGURE 6.10
Oxidation of the Fe fluid MK34 as recorded by room temperature magnetisation curves. Measurements were made 0,5,9 and 11 months after preparation.

average of 4-5%, after 9 months by ∿14% and after 11 months

by 21%. This represents a loss of about 0.05 $JT^{-1} kg^{-1}$ per

month for this fluid and is remarkably slow in comparison to

other systems (see Section 6.3.4). The reason for this is

unknown, the same surfactant was found to offer less

protection against oxidation to the FeCo systems reported in

section 6.2. The oxidation study of this fluid excludes the

initial rapid loss of magnetisation which occurs within

hours of exposure to atmosphere reported by Griffiths et al.

(1979). Oxidation is slowed considerably by storing the

fluids at low temperatures, the magnetisation of MK34

decreased by only 7% over 11 months when stored at $-3^{O}C$.

The oxidation of the Ni2M system was examined over a

period of days, the initial and 14th day magnetisation

curves are presented in Figure 6.11. No observable loss in

magnetisation could be detected 1, 4 or 6 days after

preparation. After 14 days the magnetisation had decreased

by 15%. This is a slower decrease than that observed for

the Ni-Fe system 3 reported in 6.2.4 but this is probably

due to the much larger particle size for this system

reducing the proportion of surface atoms.

6.2.5 Low Temperature Magnetisation

The magnetisation curve of Fe system FS4 at 77K is

shown in Figure 6.12 where it can be seen that no hysteresis

developed. This implies that at this temperature the

majority of the particles are below the critical diameter

for "blocking". As the median magnetic particle diameter
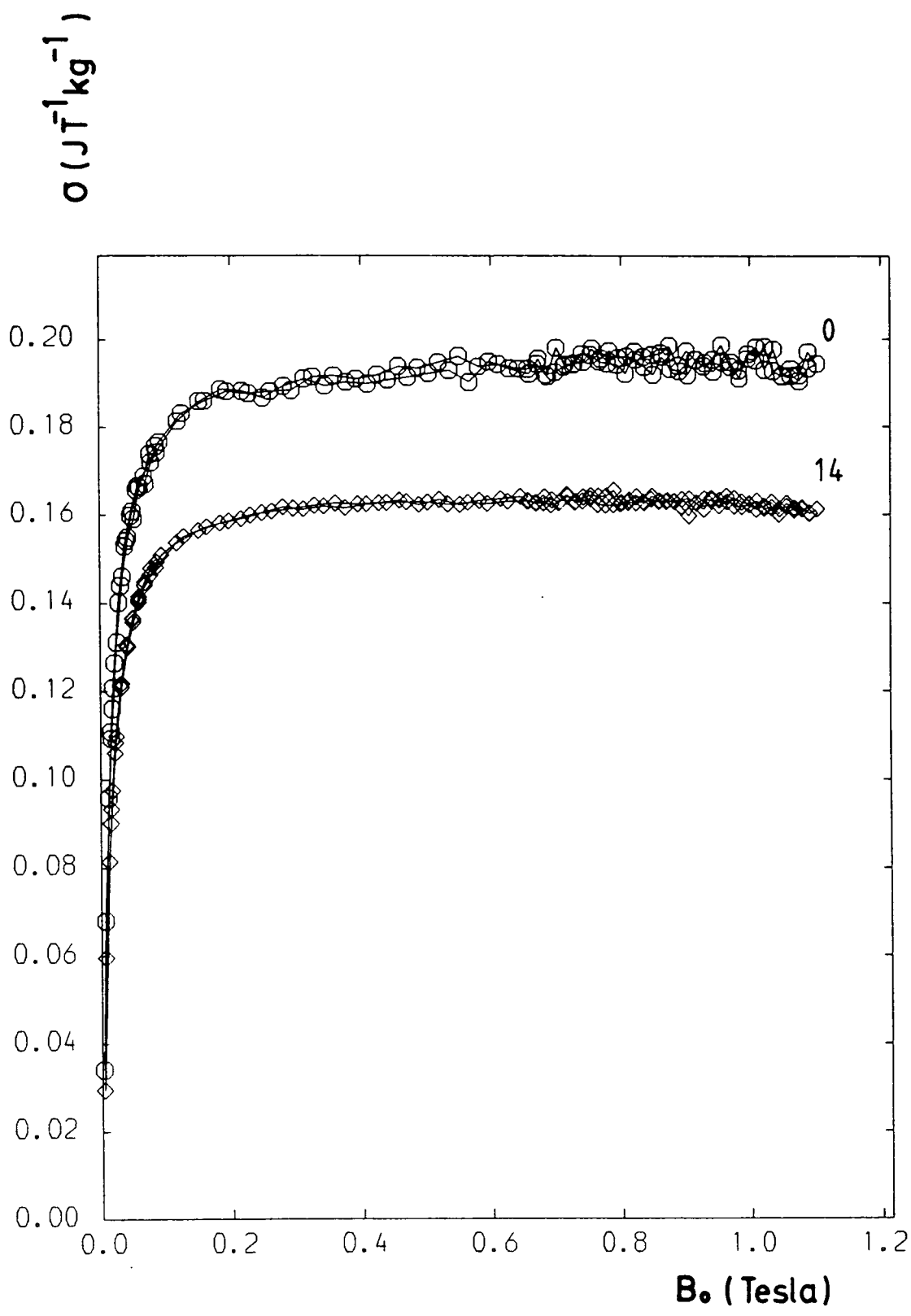
FIGURE 6.11
Magnetisation curves (RT) of Ni2M 0 and 14
days after preparation.
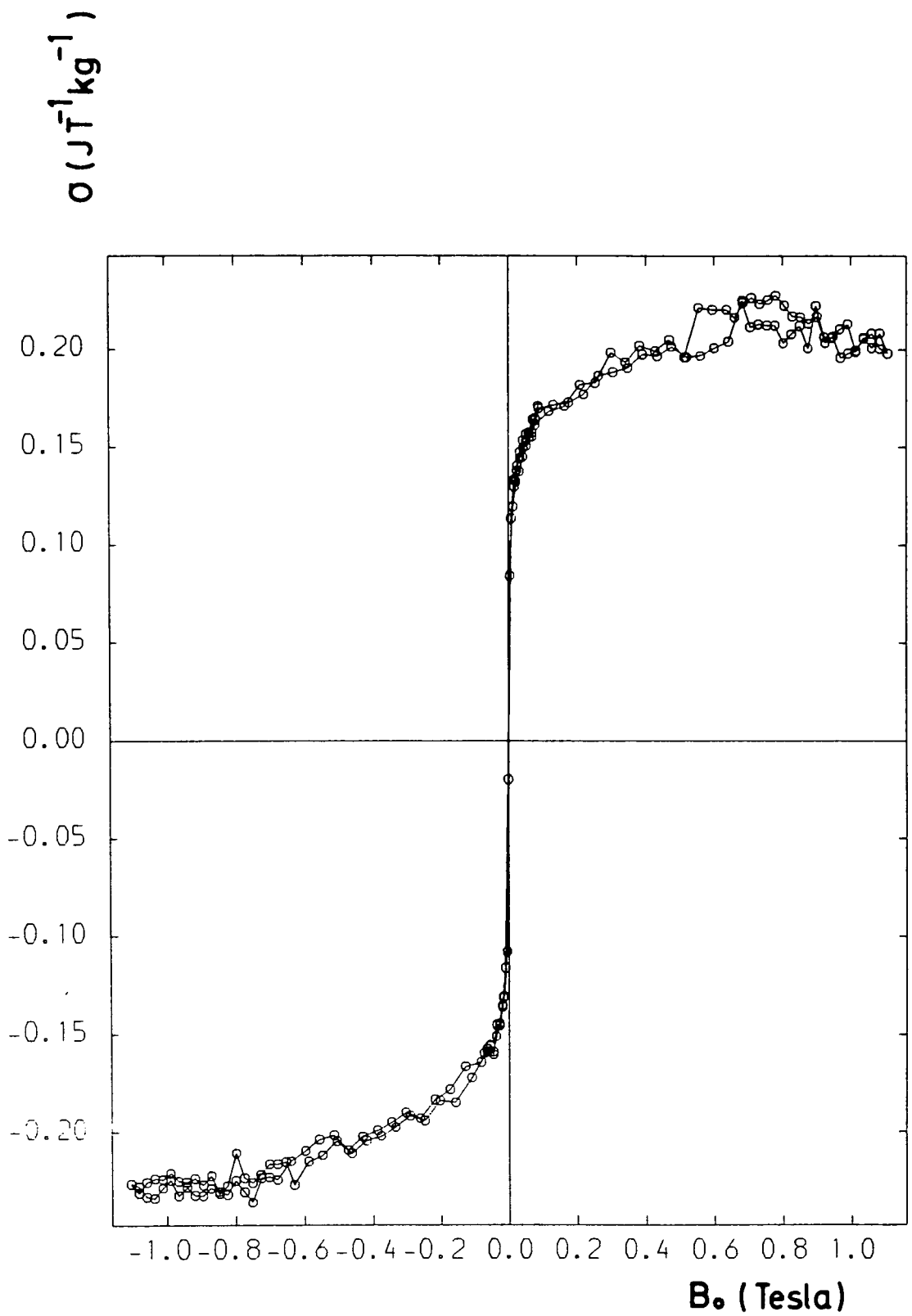
FIGURE 6.12
Magnetisation curves of Fe system FS4 at 77K showing lack of hysteresis.

for this system is 5.8nm it can be assumed that d_c > 5.8nm
which implies an upper limit for the anisotropy constant
K < 2.6 x 10^5 Jm^{-3}. By comparison, Figure 6.13 shows the
magnetisation curve of an Fe in mercury system prepared by
electrodeposition (Chapter 2) which has median magnetic
diameters of ∿ 7nm. This developed a coercivity of 0.022T
and a remanence of 0.01 $JT^{-1}kg^{-1}$ at 77K implying that most
of the particles are above the critical diameter at this
temperature, i.e. d_c < 7nm and thus K < 1.5 x 10^5 Jm^{-3}.
(Coherent rotation is assumed).

At liquid helium temperatures, however, the FS4
particles are blocked and the hysteresis loop is shown in
Figure 6.14. This has a coercivity of 0.058T and a
remanence of 0.054 $JT^{-1}kg^{-1}$. If the saturation
magnetisation of this system is taken to be 0.19 $JT^{-1}kg^{-1}$,
then by means of the method given in Section 5.2.3 the
remanence gives the critical diameter at this temperature as
5.3nm. This gives an estimate for the anisotropy constant
of K = 0.5 x 10^5 Jm^{-3}. The saturation magnetisation cannot
be estimated from this loop as a strong paramagnetic
component can be seen to be present. This is thought to be
due to paramagnetic iron compounds in the fluid, which may
explain what occurs to the iron "lost" ferromagnetically.

The magnetisation curves of fluids Co(1) and Co(2) at
77K are shown in Figures 6.15 and 6.16. Both were recorded
after oxidation had occurred but neither shows any shifting
of the hysteresis loop due to exchange anisotropy. The
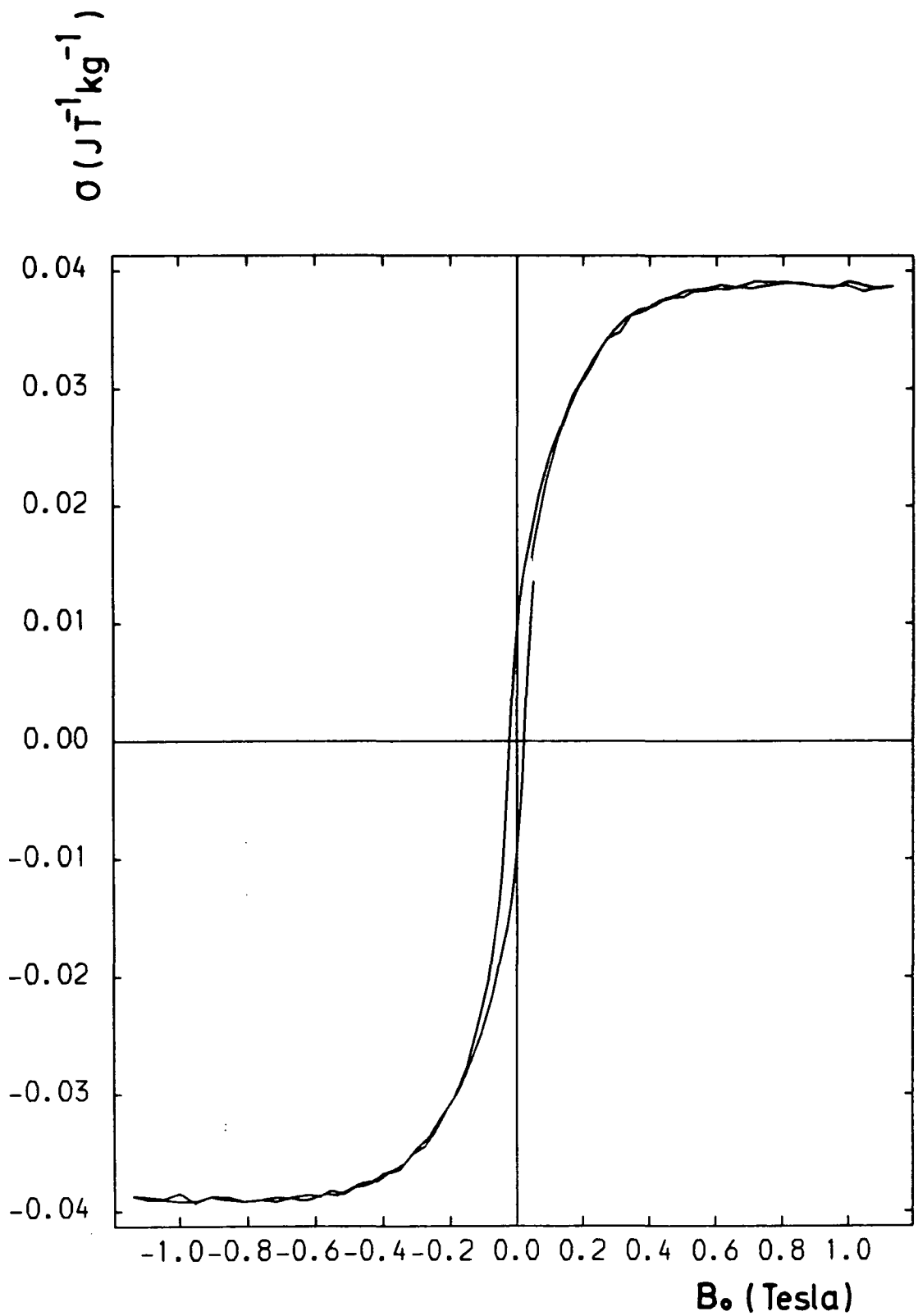
FIGURE 6.13
Magnetisation curve at 77K of an Fe in mecury
fluid showing hysteresis due to large particles.
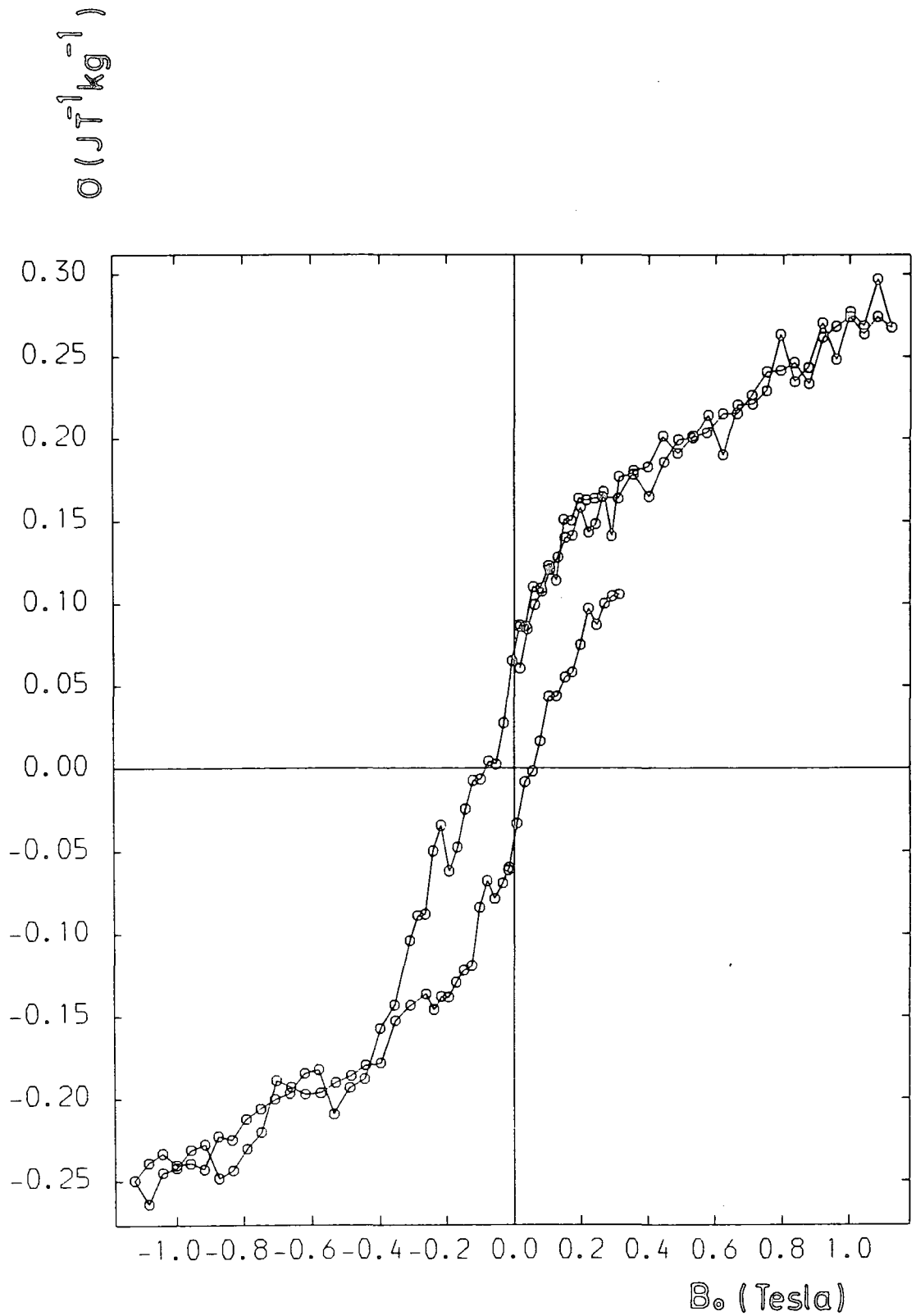
FIGURE 6.14
Hysteresis loop of Fe system FS4 at liquid helium temperature.
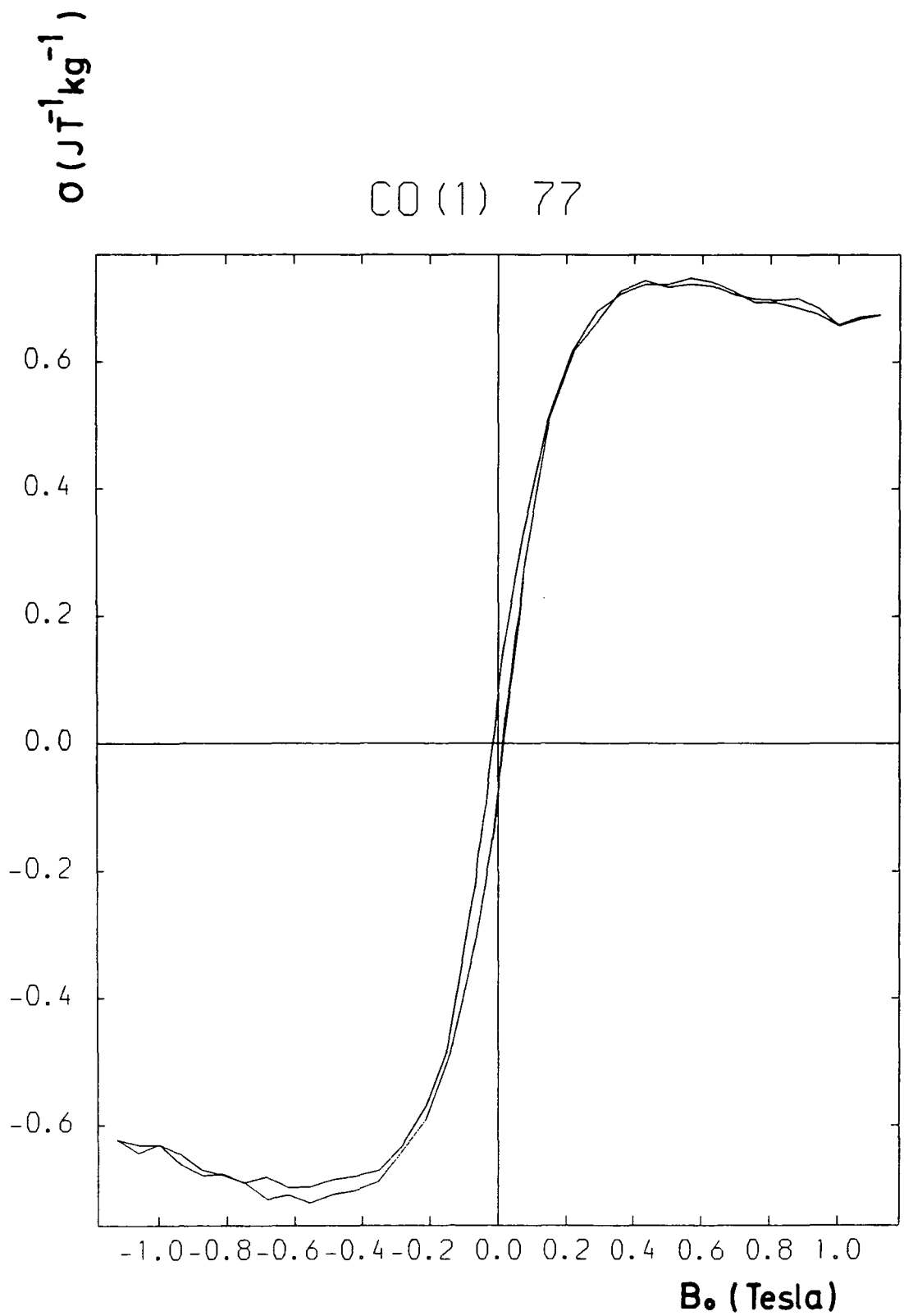
FIGURE 6.15
77K magnetisation curve for Co system Co(1).
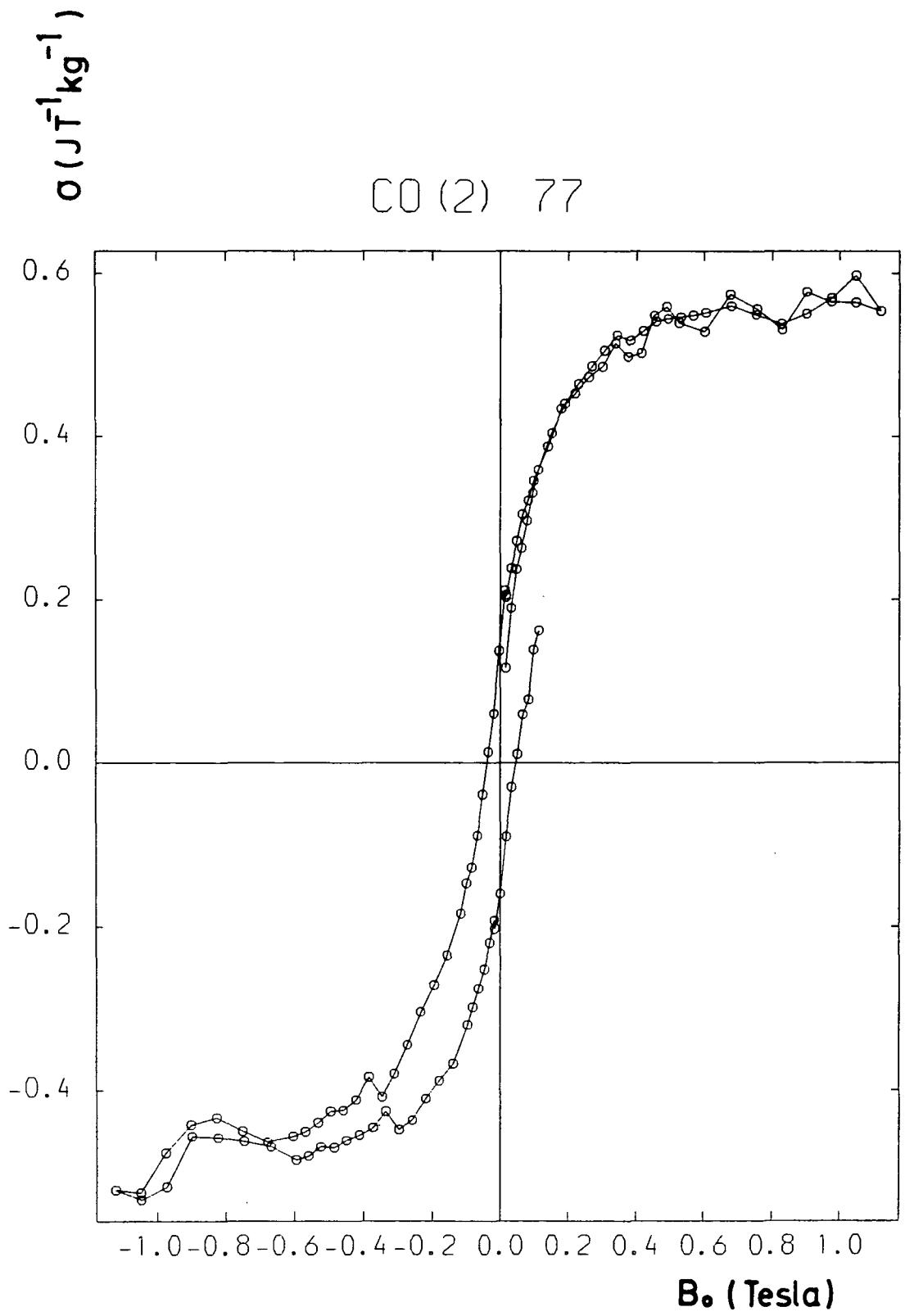
FIGURE 6.16
77K hysteresis loop of Co system Co(2).

coercivity and remanence of fluid Co(2) were 0.045T and 0.135 $JT^{-1}kg^{-1}$ whilst those of fluid Co(1) were 0.017T and 0.076 $JT^{-1}kg^{-1}$. The values for Co(2) are greater than those of Co(1) even though the particle sizes are similar and this may be due to Co(2) being hexagonal whilst Co(1) is f.c.c. Again using the analysis of Section 5.2.3, estimates of the anisotropy constants of these systems are obtained as 1.1 x $10^5 Jm^{-3}$ for Co(2) and 0.3 x $10^5 Jm^{-3}$ for Co(1). Fluid Co(1) also has a much broader size distribution which tends to increase the fraction of blocked particles at any given temperature. These estimates of the anisotropy constant are somewhat crude but it is clear that fluid Co(2) has a much higher anisotropy than that of fluid Co(1) and this may be linked to its h.c.p. structure.

Figure 6.17 shows the magnetisation loop obtained for fluid Co(2) at $\sim$ 8K. The sample had been exposed to atmosphere for a year and may be safely assumed to have partially oxidised. It can be seen that the hysteresis loop is shifted leftwards along the field axis and this is ascribed to exchange anisotropy. The coercivities are 0.193 and -0.447T and the remanences are 0.58 and -0.34 $JT^{-1}kg^{-1}$ and once more there appears to be a paramagnetic component at very low temperatures. Estimates of the anisotropy constant are not made from this data as coherent rotation is almost certainly not taking place.

Figure 6.18 shows the hysteresis loop obtained from the
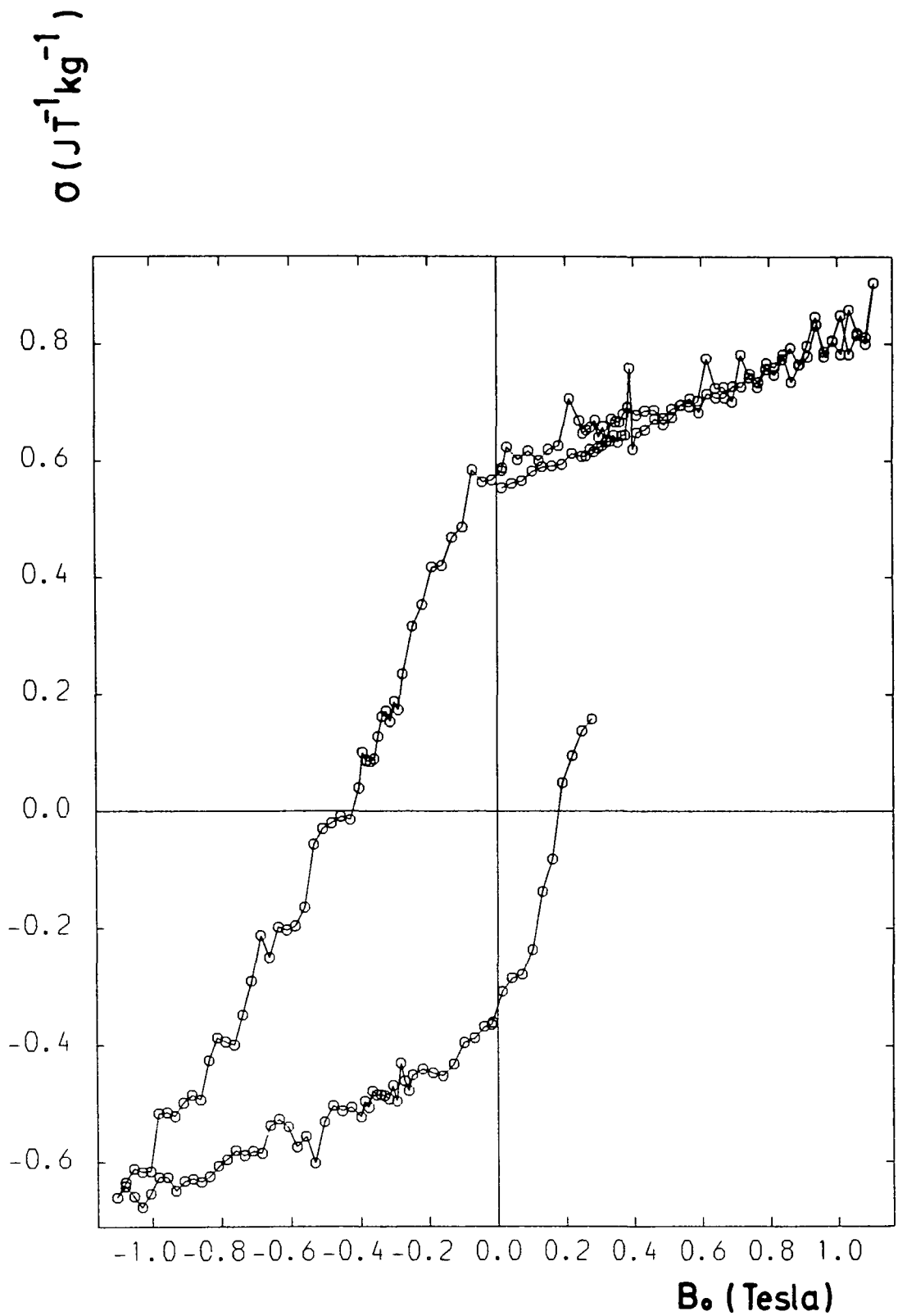
FIGURE 6.17
Shifted hysteresis loop of Co system Co(2) at
8K due to exchange anisotropy.
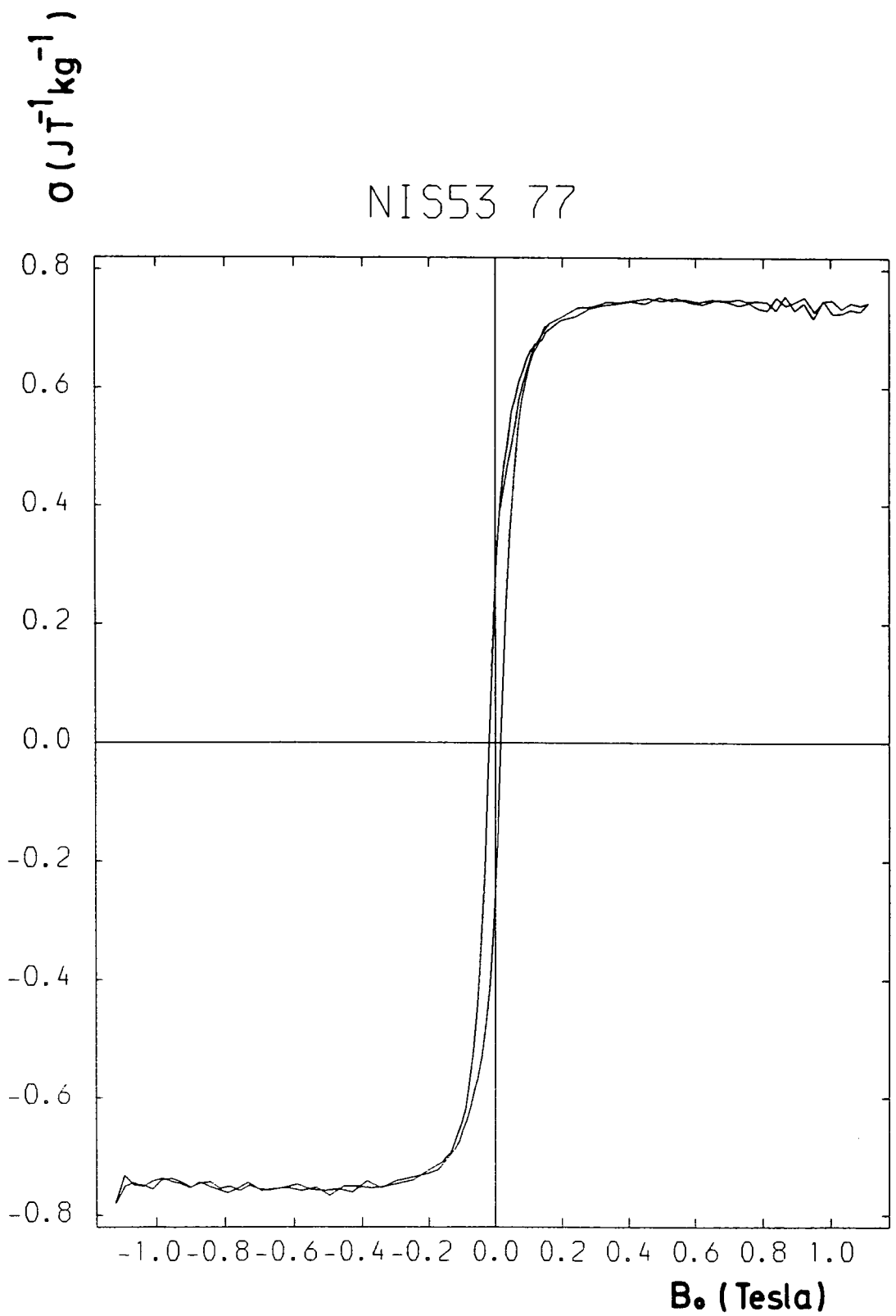
FIGURE 6.18
Hysteresis loop of NiS53 at 77K.

system NiS53 at 77K. The coercivity and remanence are 0.021T and 0.27 $JT^{-1}kg^{-1}$ respectively. The anisotropy constant is estimated as $K \sim 1 \times 10^5$ Jm^{-3}. Once again this a value incompatible with shape anisotropy.

6.2.6 Rotational Hysteresis

Fluid Co(3) was set in polyester resin and the rotational hysteresis examined at room temperature. Figure 6.19 shows the result of a 3-day experiment. The anisotropy field has been calculated from an inverse field plot as 0.28 $\pm$ 0.03T which corresponds to an anisotropy constant of (2.1 $\pm$ 0.3) $\times 10^5$ Jm^{-3}. This value is somewhat larger than that obtained from magnetisation measurements for Co(1) but as discussed in Chapter 5 is considered more reliable.

The nickel system NiS53 was examined at 77K in a much shorter experiment and the result is shown in Figure 6.20. This yielded a value of (0.43 $\pm$ 0.2) T for the anisotropy field corresponding to an anisotropy constant of (1.5 $\pm$ 0.5) $\times 10^5$ Jm^{-3}. No rotational hysteresis was observed on this system at room temperature.

6.2.7 Discussion

The preparation of single metal fine particle systems from new organometallics, particularly cyclopentadienyl carbonyl complexes, has proved successful. α-Fe may have been observed in one instance but it is thought that in most cases the iron in the particles is not in the zero valence state. Hexagonal cobalt does occur but the factors controlling its preparation have not yet been discovered.
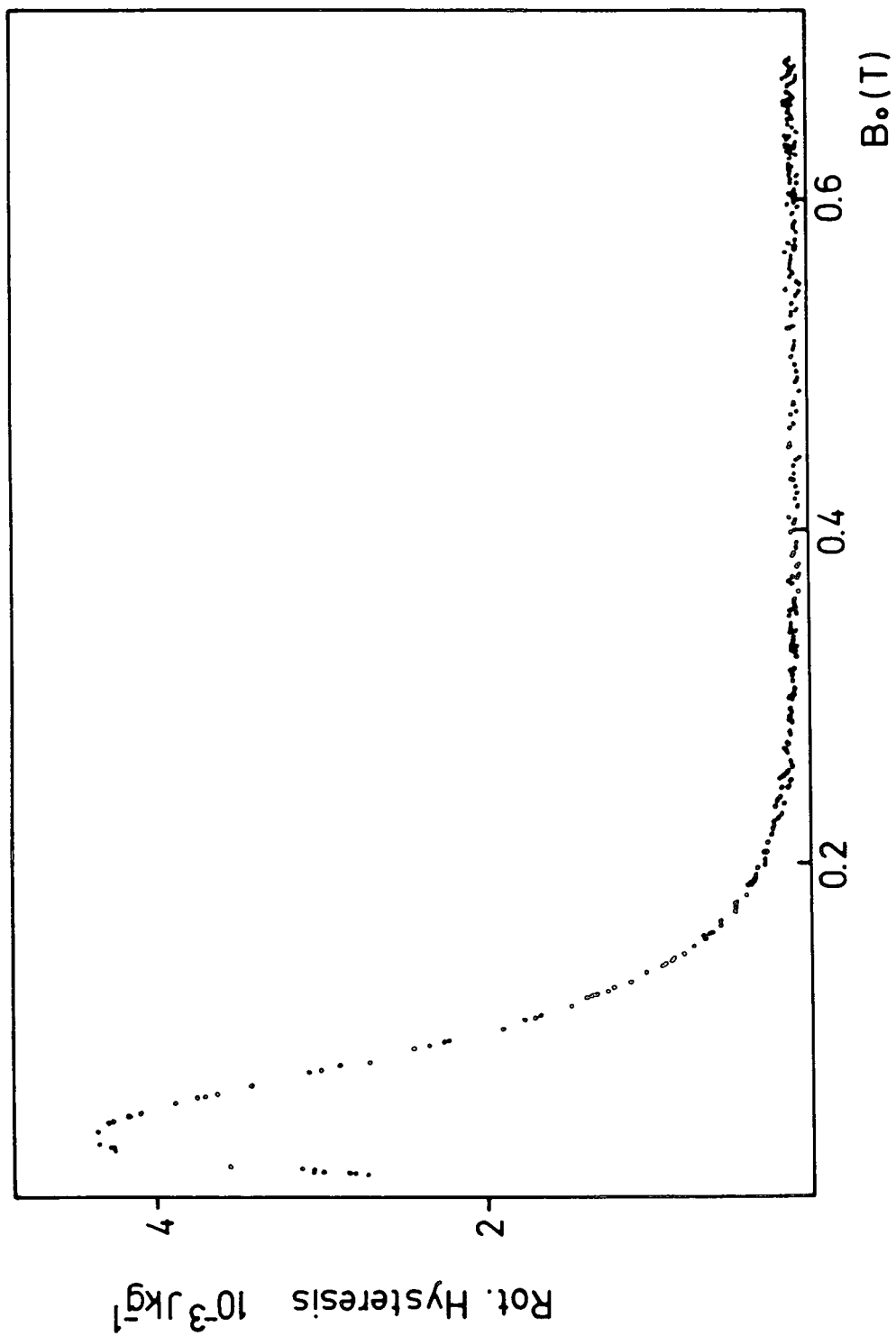
FIGURE 6.19
Rotational hysteresis of Co system Co(3) set
in polyester resin. Room temperature measure-
ment.
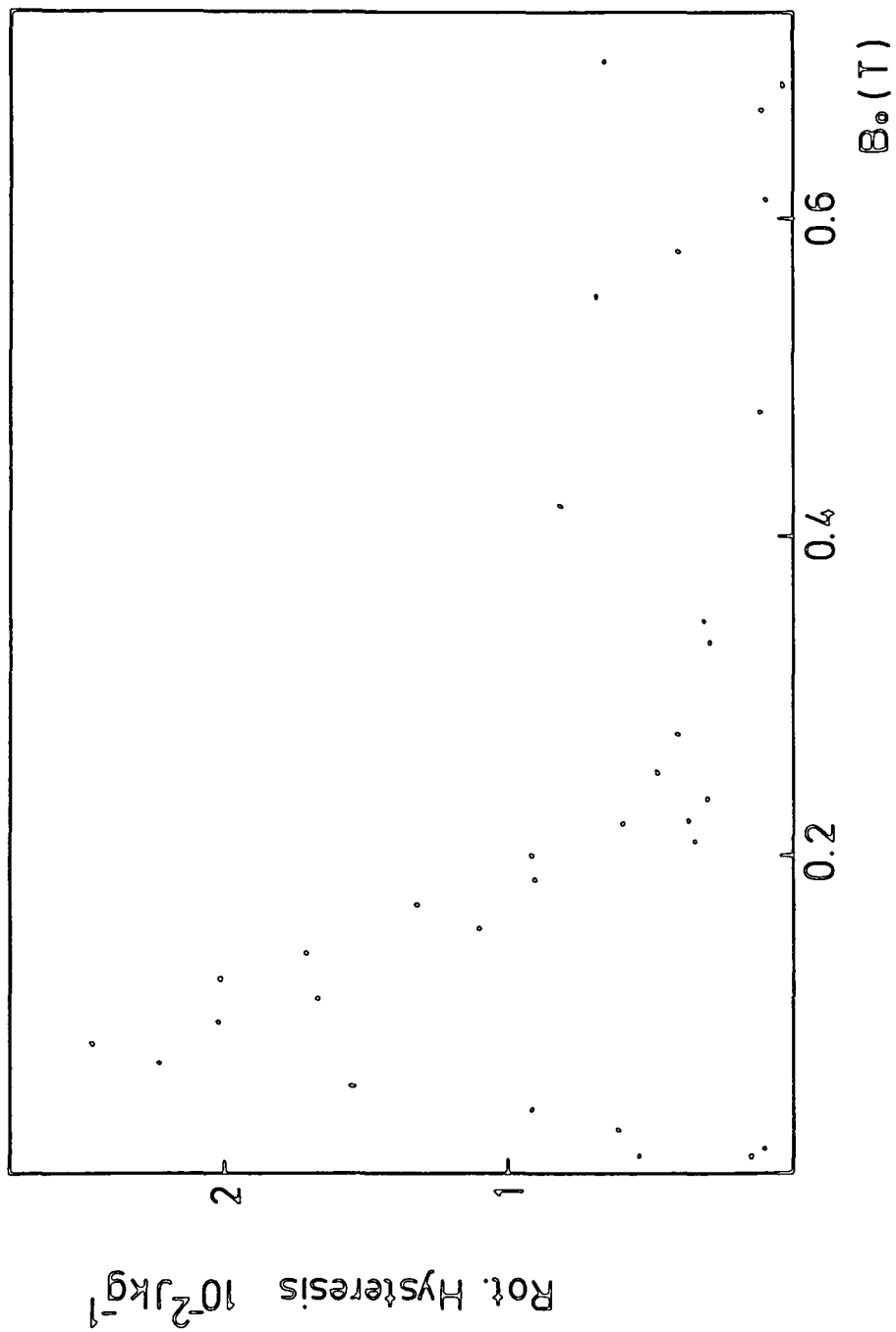
FIGURE 6.20
Rotational hysteresis of Ni system NiS53 at
77K.

Nickel fluids are difficult to prepare but use of the cyclopentadienyl carbonyl complex makes it somewhat easier. Apart from nickel systems the particle size distributions obtained are very similar to each other and those obtained previously. For all three metals a loss of about 80% of the metal atoms is observed magnetically and it is thought that this is largely attributable to the formation of surfactant-metal complexes and non-magnetic surface layers. The anisotropy of all the systems is incompatible with pure shape anisotropy.

6.3 Mixed Metal Systems

In this section the preparation and properties of the first hydrocarbon based mixed-metal ("alloy") magnetic fluids are reported. Some of this work has already been published (Lambrick et al. 1985, 1986).

6.3.1 Preparative Details

The primary objective of this study was to prepare magnetic fluids containing particles of mixed-metal composition. In order to achieve this, the decomposition of heteronuclear organometallic precursors containing metal-metal bonds was found to be necessary. Attempts involving the simultaneous decomposition of Fe and Co carbonyls proved unsuccessful in producing alloy particles. Iron-cobalt particles were successfully prepared using $[(\pi-C_5H_5)Fe(CO)_2$ $Co(CO)_4]$ and $H FeCo_3(CO)_{12}$ as precursors whilst Ni-Fe fluids were obtained from the trinuclear cluster $[(\pi-C_5H_5)_2Ni_2$

Fe(CO)$_5$]. Figure 6.21 shows the structure of the latter,
illustrating the metal-metal bonds. The preparation of
these compounds together with full details of the fluid
preparations are given by Mason (1986), the general
technique is described in Chapter 2. Some of the
preparation details for the Fe-Co systems are shown in Table
6.3 and for the Ni-Fe systems in Table 6.4. The major
differences in the preparations of the two systems are the
surfactants employed and the heating bath temperature.

6.3.2 Electron Microscopy

(a) Diffraction

The electron diffraction patterns obtained from the
fluids FeCo1A and NiFe4 are shown in Figures 6.22 and 6.23.
Table 6.5 lists the d-spacings obtained from these patterns.
The ratios of the lines were clearly b.c.c. for the Fe-Co
and f.c.c. for the Ni-Fe. However when simply indexed as
such, lattice parameters of 3.8Å and 5.8Å were obtained.
These values are incompatible with any Fe, Co or Fe-Co
structure in the first instance, or any Fe, Ni, or Ni-Fe in
the second. Fe-Co alloys possess an ordered structure in
the region 1:1 Fe:Co with the b.c.c. lattice composed of
two interpenetrating simple cubic lattices, one of Fe atoms
the other of Co, as shown in Figure 6.24. This superlattice
structure will give rise to extra reflections in the
diffraction pattern from the (100), (111), (210) etc.
planes. When these extra reflections are incorporated into
the indexing of the pattern a lattice parameter of 2.67Å is

TABLE 6.3
FeCo preparative details

Fluid	Surfactant	Mass of precursor (g)	Mass of surfactant (g)	Vol. toluene cm^3	Oil Bath Temp. C	Heating time hrs.
1A	Solsperse 3000	3.1	3.0	20	130	3
2	Solsperse 3000	1.4973	1.4962	10	130	2
D	Duomeen-TDO	1.4067	0.6984	10	130	2
D2	Duomeen-TDO	1.0012	1.0427	10	140	2
DT	Duomeen-T	0.9654	0.9962	10	130	2
Co$_3$Fe(1)	Sarkosyl-O	0.8578	0.5060	10	140	1
Co$_3$FeD2	Duomeen-TDO	0.8169	0.5856	10	140	1

Fluid	Surfactant	Carrier	Mass of Complex (g)	Mass of Surf. (g)	Vol. Carrier liquid (cm^3)	Metal Bath Temp. °C	Heating Time hrs
3	Manoxol OT	1-M-N	0.7018	0.4542	10	170	3
4	Sarkosyl O	1-M-N	0.6027	0.3654	10	170-180	3.5
5	Sarkosyl O	1-M-N	0.4482	0.4152	15	200-205	5.5
6	Sarkosyl O	Pet.E	0.5683	0.4212	10	200-210	3

1-M-N = 1-methyl-napthalene, Pet.E. = Petroluem Ether (200-260)

Manoxol OT = Dioctyl sulphosuccinate, sodium salt

Sarkosyl O = N-methyl-N-(1-oxo)-9-octadecenyl glycine

TABLE 6.4
NiFe preparative details
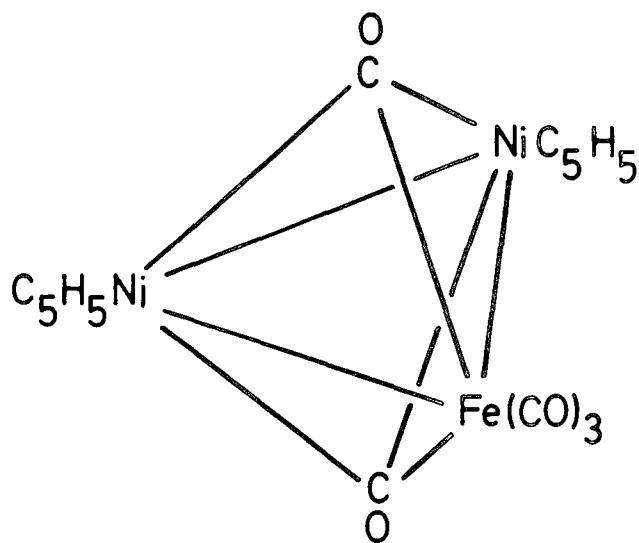
FIGURE 6.21
Probable structure of the organometallic precursor $(\pi\text{-}C_5H_5)_2Ni_2Fe(CO)_5$.

FIGURE 6·22
FeCo1A   Diffraction image
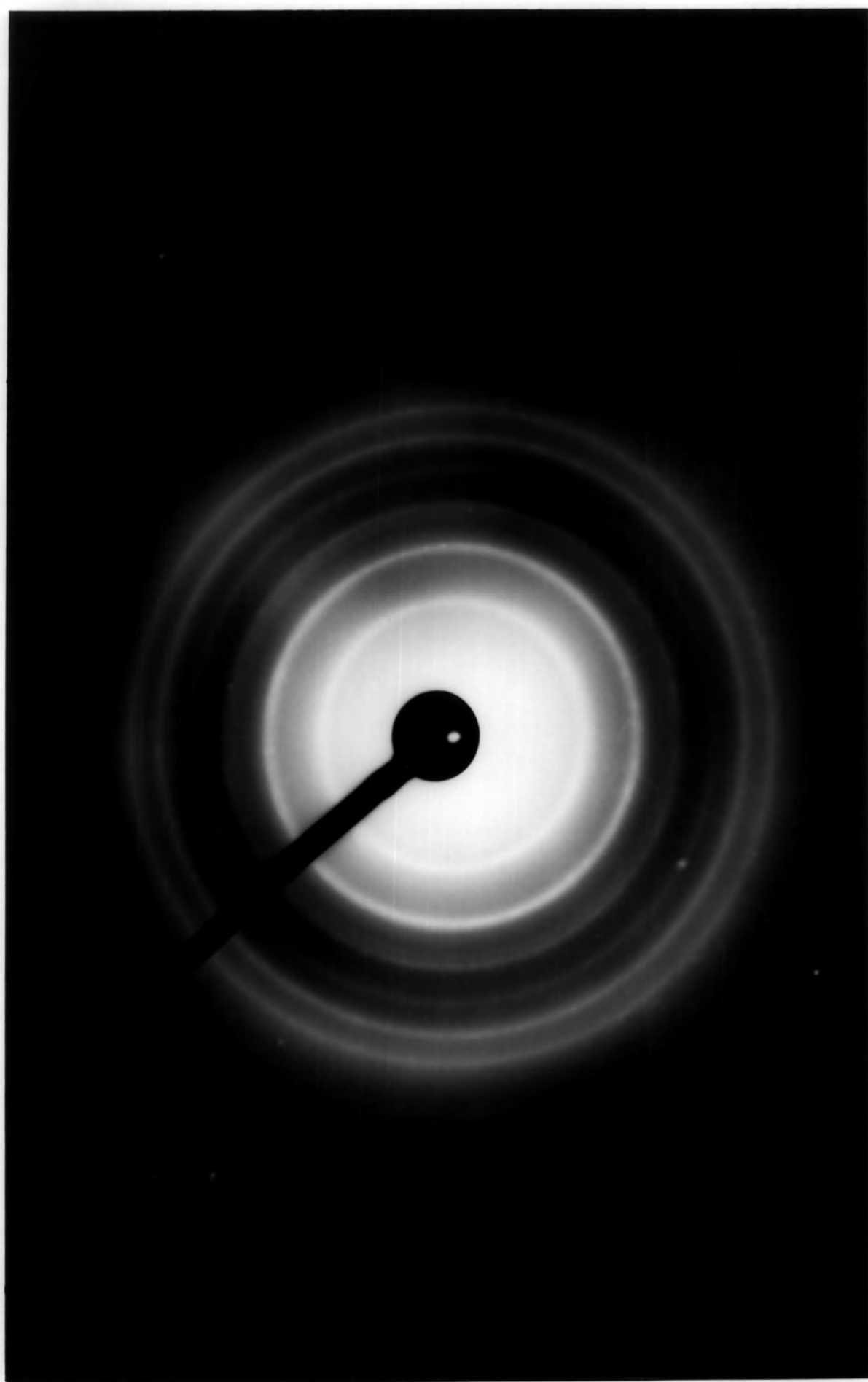
FIGURE 6·23
NiFe4 Diffraction image
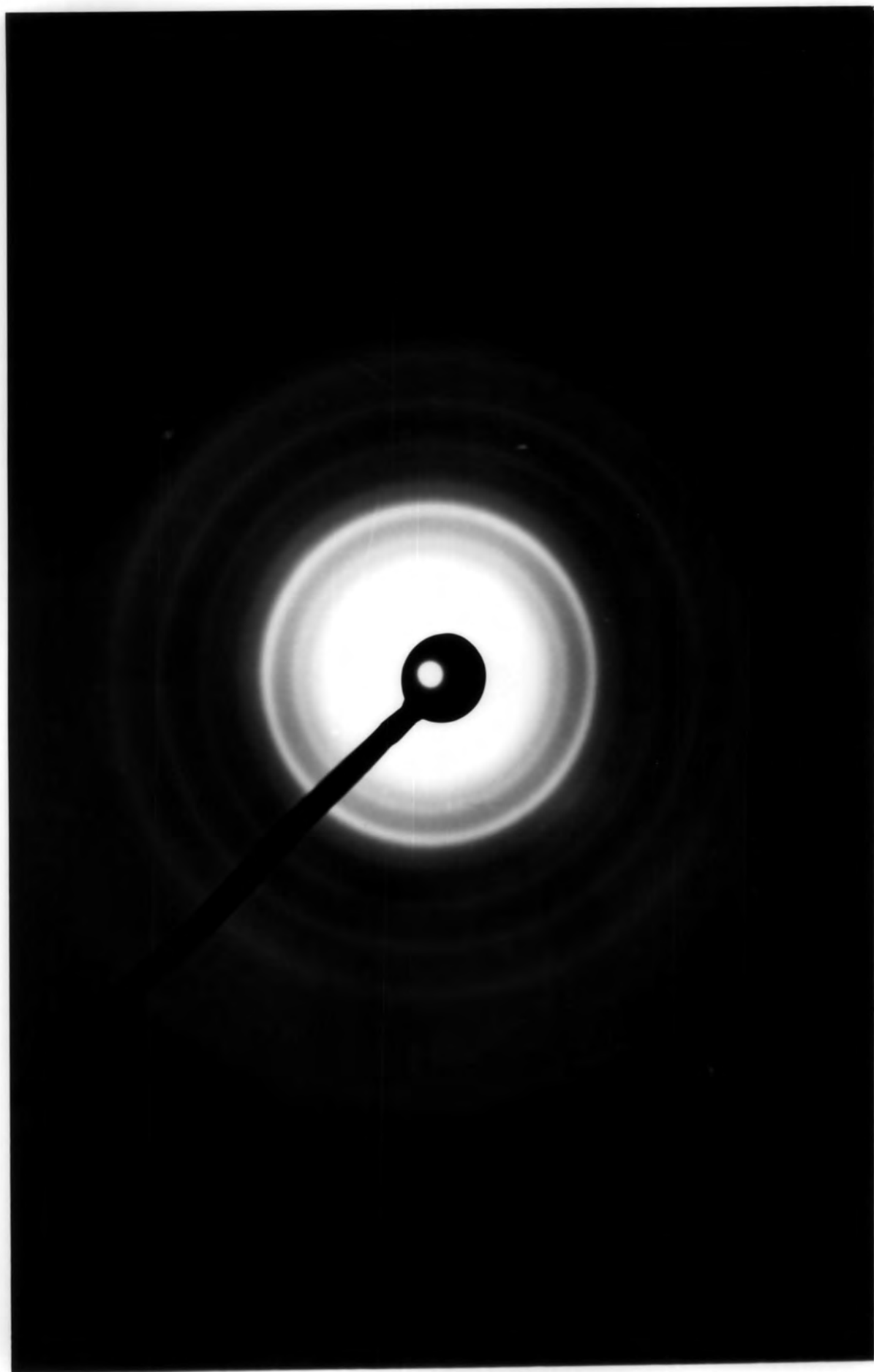
NiFe4

d (Å)	(hkl)	a_0
2.525	(110)	3.571
2.069	(111)	3.584
1.775	(200)	3.550
1.609	(210)	3.598
1.483	(211)	3.633
1.257	(220)	3.550
1.071	(311)	3.552

3.577 Å   Lit. value = 3.5523

FeCo1A

d (Å)	(hkl)	a_0
2.63	(100)	2.63
1.91	(110)	2.70
1.55	(111)	2.68
1.34	(200)	2.68
1.20	(210)	2.68
1.10	(211)	2.69
0.93	(220)	2.63
0.89	(300)(211)	2.67
0.84	(310)	2.66
0.80	(311)	2.65

2.67 Å   Lit. value = 2.857

TABLE 6.5
NiFe and FeCo
d-spacings from electron diffraction
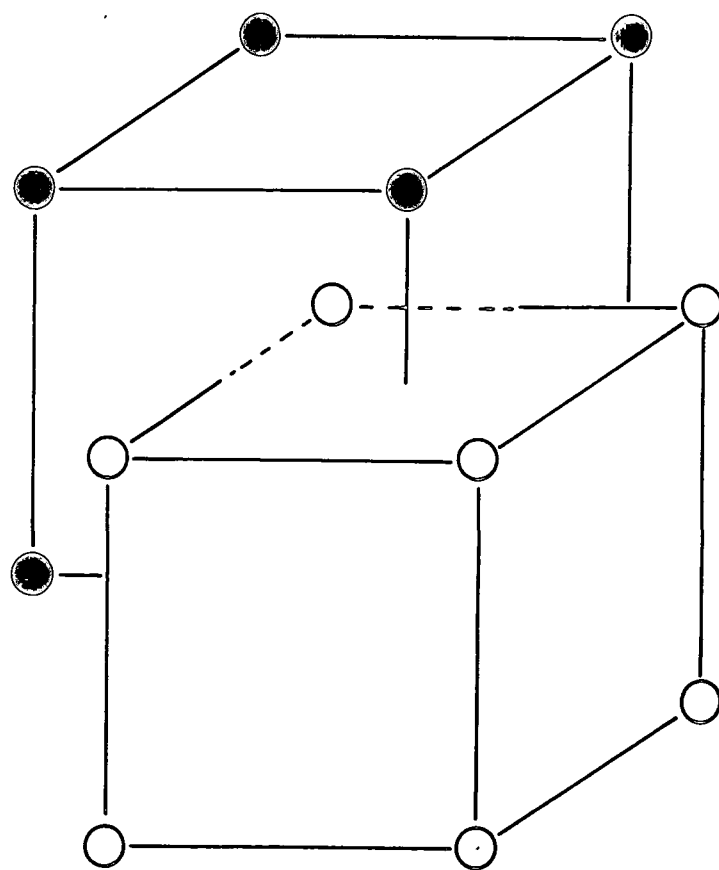
O Fe
● Co

FIGURE 6.24
Superlattice structure of the ordered 1:1 Fe:Co alloy.

obtained. This is now within experimental error of the
literature value of 2.85Å for the Fe-Co superlattice.
Similarly, the Ni-Fe alloys possess a superlattice structure
of type $L\ell_2$ (Cu_3Au) in the region Ni_3Fe with a lattice
parameter of 3.55Å. Assuming this superlattice for the
NiFe4 pattern results in a lattice parameter of 3.58Å, again
within experimental error of the literature value. In some
recent work on the preparation of fine particles by the
radiation induced reduction of metal ions in solution,
Marignier et al. (1985) have also observed a tendency to
superlattice formation in Cu-Pd systems. An ordered
structure represents a state of lower potential energy than
a disordered structure (Bragg and Williams 1934) but in bulk
alloy systems the time required to reach equilibrium can be
days, requiring slow annealing. In fine particle systems
the growth temperature is lower but the growth process is
probably atomic addition which might make it possible for
ordered structures to develop from nucleation. Order sets
in at compositions near to the stoichiometric ratios and
thus the existence of superlattice reflections does not
guarantee these ratios. The fine particles are very likely
to have a distribution of compositions with a large number
in the region of the superlattice ratios.

It will be noticed that the Ni_3Fe particles have been
obtained from a Ni_2Fe precursor. The loss of iron is
thought to be due to its greater reactivity leading to the
formation of oxides, surfactant complexes or volatile

Fe-carbonyl compounds before the iron can be incorporated into the particles. When cobalt particles are prepared by the evaporation of cobalt atoms into toluene/sarkosyl solutions, the cobalt atoms are initially incorporated into $Co(Sarkosyl)_2$ complexes before particle formation begins (P.D. Hooker, P.L. Timms, priv. comm.). A similar process may occur in organometallic decompositions with the iron reacting preferentially to the cobalt in the mixed-metal case. $Fe(CO)_5$ is a liquid at room temperature and thus if it is formed during the decomposition of the Ni-Fe precursor then it may be lost to the reactions.

The average composition of the Fe-Co and Ni-Fe systems are assumed to be close to the stoichiometric superlattice ratios but biased towards the Fe deficient side. The bulk magnetisation of FeCo is taken as 1 898 820 $JT^{-1}m^{-3}$ (231 $JT^{-1}kg^{-1}$) and that of Ni_3Fe 983 100 $JT^{-1}m^{-3}$ (116 $JT^{-2}kg^{-1}$).

(b)   Shadow Electron Microscopy

Shadow electron micrographs were taken at a magnification of 220 000x and were analysed using the automated image size analyser (Chapter 3). The diameter distributions for the Fe-Co fluids 1A, 2, D and D2 are shown in Figure 6.25 and that for the Ni-Fe fluid 6 in Figure 6.26. Mean particle diameters in the range 5-9 nm have been obtained with narrow distributions in all cases. Although confined to a small interval, the mean particle diameter is sensitive to experimental conditions as illustrated by the Fe-Co fluids D and D2. The only significant difference in
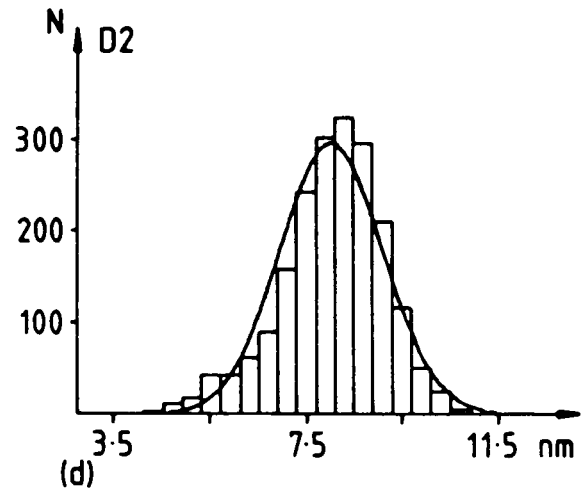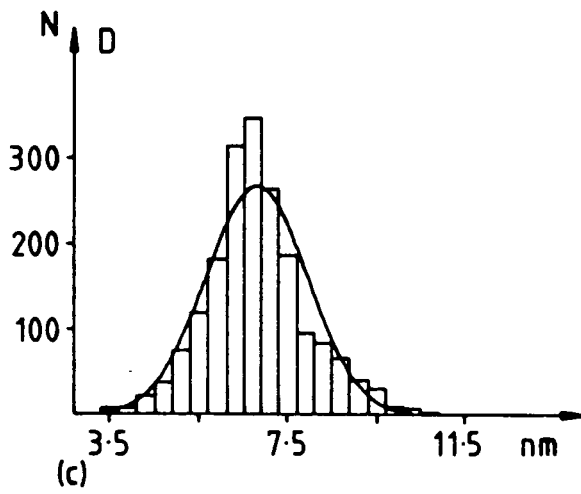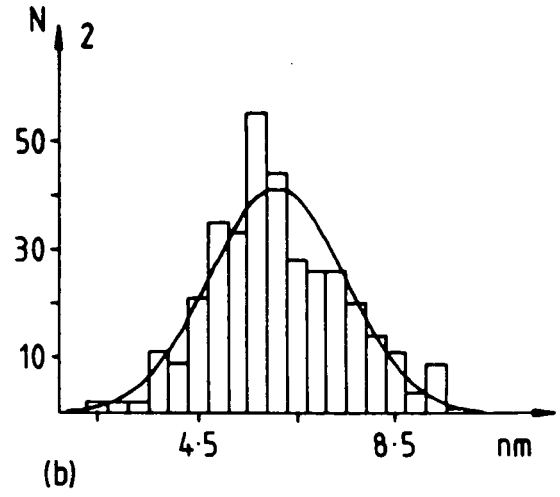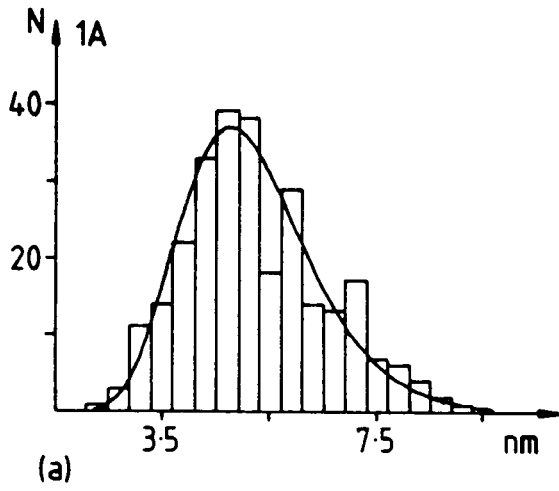
FIGURE 6.25
Diameter distributions obtained from electron micrographs for the Fe-Co systems 1A,2,D and D2.
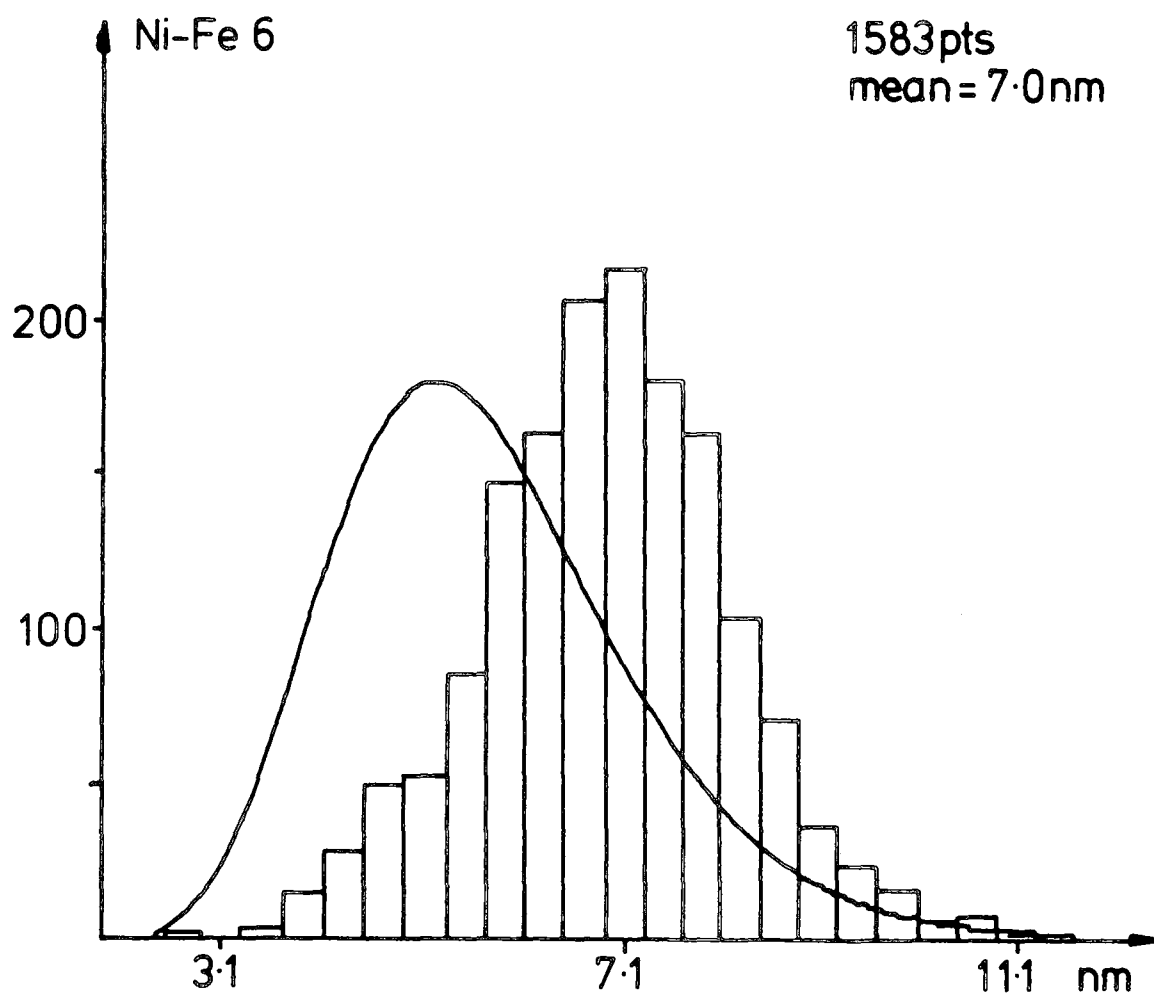
FIGURE 6.26
Diameter distribution obtained from electron microscopy for the system NiFe6.

their preparations was the amount of surfactant relative to precursor molecule, D2 having approximately $\frac{1}{2}$ that of D and the mean diameter of D2 is 1.2nm larger than that of D. Particle size data is discussed fully in Chapter 4. The particle sizes from electron microscopy for all the Fe-Co and Ni-Fe systems are given in Tables 6.6 and 6.7 together with the magnetic sizes.

(c) <u>EDX data</u>

The $Co_3Fe(1)$ fluid was examined using the HB5 electron microscope at the University of Glasgow under the supervision of Dr. J. Chapman. This microscope was fitted with a Link Instruments energy dispersive X-ray analyser which enabled the composition of the particles to be determined. The high magnification of the instrument meant that individual particles could be examined. Figure 6.27 shows the counts obtained from Fe and Co atoms. It can be seen that two elemental ratios were obtained, for well dispersed, isolated single particles a ratio of 3:1 Co:Fe is obtained which is identical to that in the precursor molecule. Where the particles were in clusters, possibly due to a high concentration of surfactant material the ratio is 8:1 Co:Fe. This deficit of iron is consistent with the Ni_3Fe diffraction result and the higher Co concentration in the clusters with the Co-surfactant complex formation discussed above. The EDX results point towards the formation of volatile Fe-compounds during decomposition as a source of iron loss. These results clearly show that
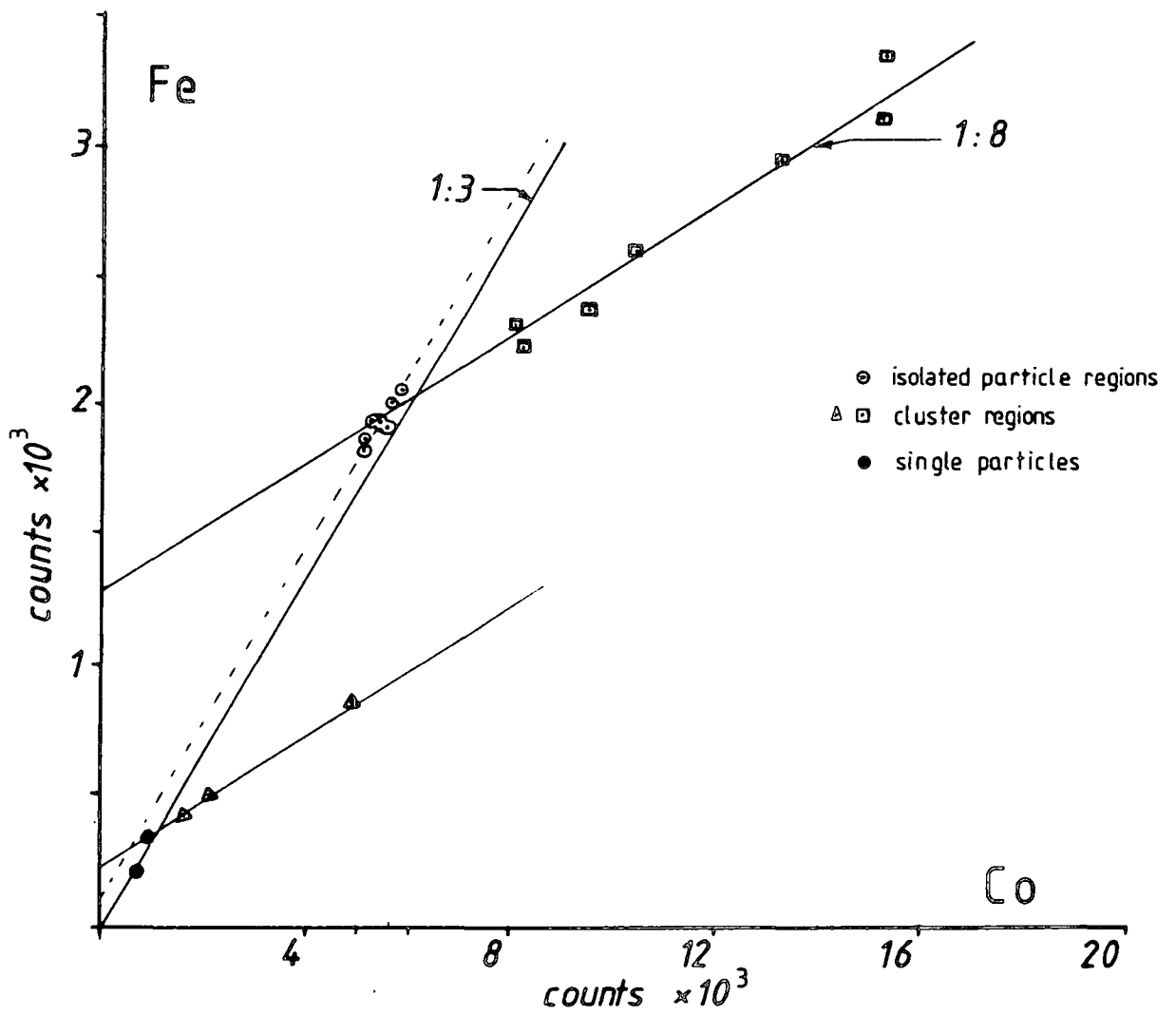
FIGURE 6.27
The composition of particles in the fluid
$Co_3 Fe(1)$ as revealed by EDX analysis.

mixed-metal particles have been formed from hetero-nuclear organometallic precursor molecules.

6.3.3 Room Temperature Magnetisation

The room temperature magnetisation curves obtained on the V.S.M. from the Fe-Co fluids are shown in Figures 6.28 and 6.29 and those from the Ni-Fe systems in Figure 6.30. They are all superparamagnetic, the very different shapes of the curves for NiFe3 and NiFe4 reflects the large difference (3.1nm) in particle diameter for these fluids. Saturation magnetisations were obtained from inverse field plots, where least squares fitting was used on points above $B_o = 0.7T$ and the line extrapolated to $(1/B_o) = 0$. Values of between 0.3 and 3.0 $JT^{-1}kg^{-1}$ (3-30G) were obtained for the Fe-Co systems, 5.91 $JT^{-1}kg^{-1}$ for the Co_3Fe D2 system and 0.2 - 0.06 for Ni-Fe. The mass fraction of metal atoms in the original solution was $\sim$ 0.05 for the Ni-Fe systems whilst the magnetic mass fraction in the final fluid was $\sim$ 0.003, i.e. a factor of 10-20 smaller. A 70-90% loss of metal atoms was also found in Fe-Co systems and is typical. This may be partly explained by surface effects as up to 40% of the atoms in an 8nm diameter particle may be considered surface atoms (first two layers). If these make no contribution to the magnetic moment of the particle then 40% of the particle mass will not be detected by the magnetisation measurement. There remains, however, a large loss of metal atoms which may again be explained in terms of surfactant-metal complexes forming in the solution or the
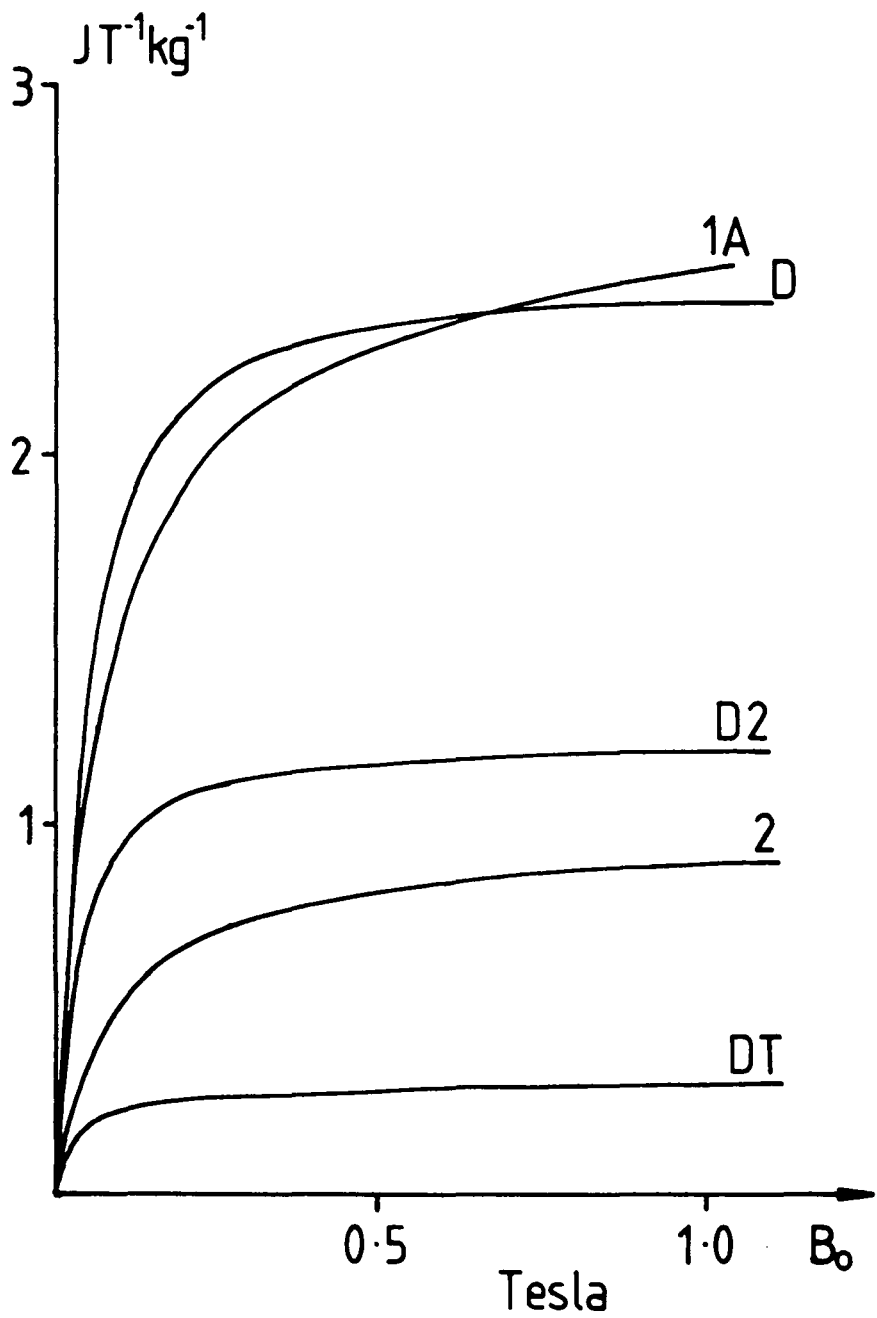
FIGURE 6.28
Room temperature magnetisation curves for the Fe-Co fluids 1A,2,D,D2 and DT.
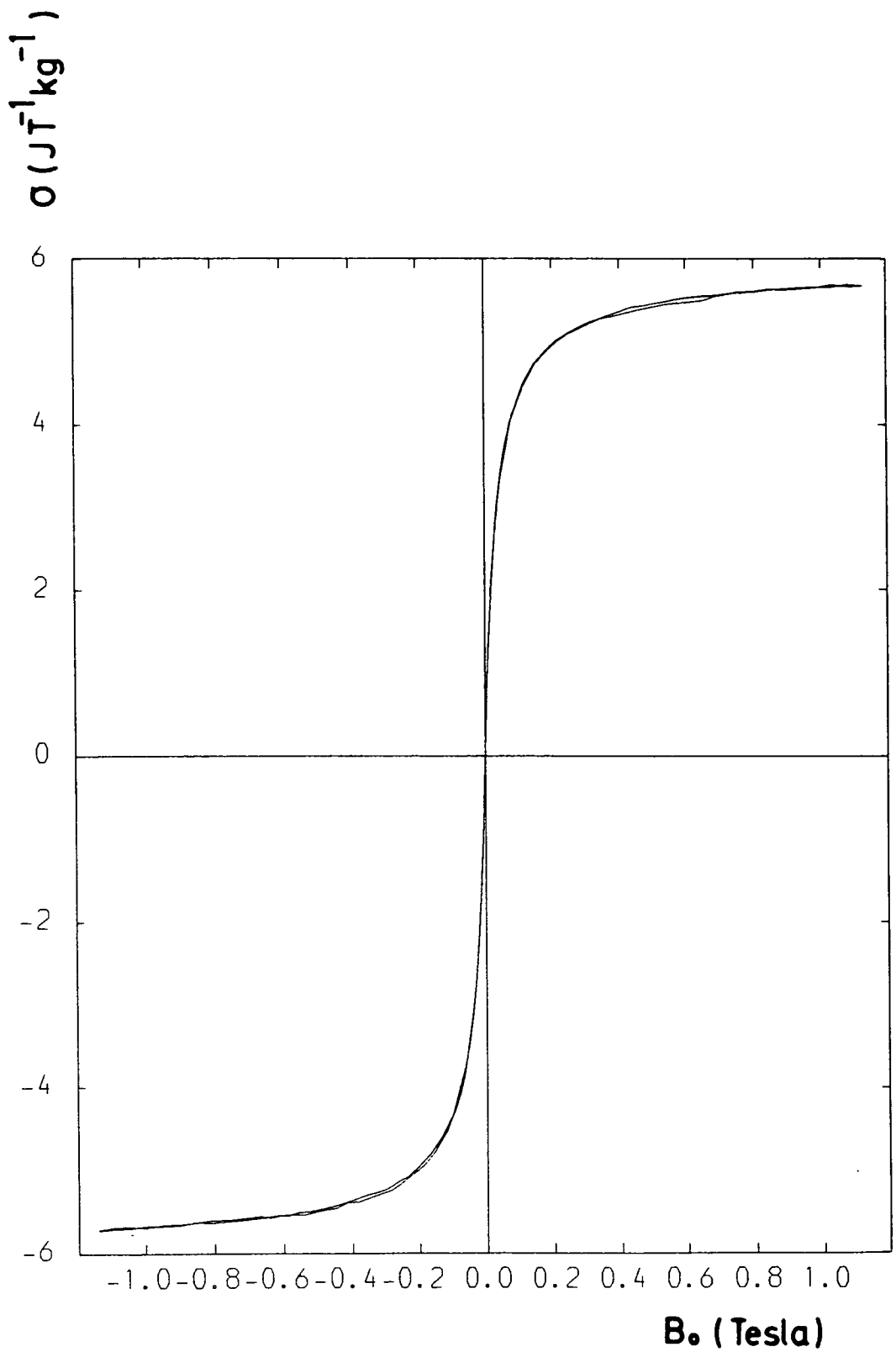
FIGURE 6.29
Room temperature magnetisation curve for
the Fe-Co system Co$_3$FeD2.
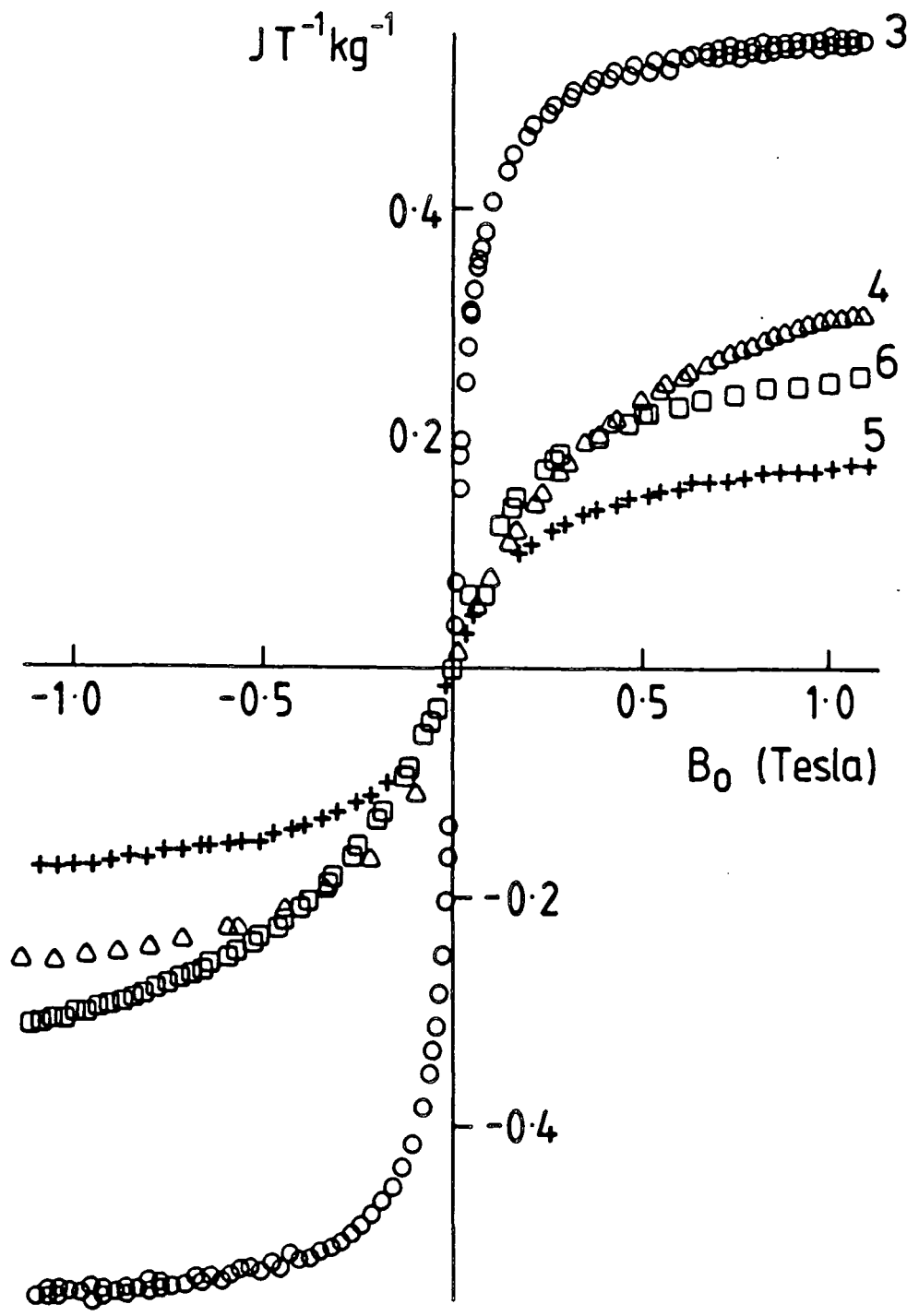
FIGURE 6.30
Room temperature magnetisation curves for the Ni-Fe systems 3,4,5 and 6.

loss of volatile Fe carbonyl complexes as mentioned previously.

The system Co_3FeD2 had an original solution mass fraction of 3.3% and a magnetic mass fraction of 2.9% assuming the particles are 3:1 Co:Fe and have a bulk magnetisation of 202.2 $JT^{-1}kg^{-1}$. This result is somewhat anomalous and is akin to that for the Fe system MK34. In both cases the surfactant Duomeen-TDO had been employed with precursor to surfactant mass ratio >2. This however, was also the case for the fluid FeCoD which did not have an efficient "magnetic conversion". The much higher cobalt content is thought to be partly responsible for this result. The V.S.M. sample of this fluid was sealed within a nitrogen atmosphere whereas the FeCo and NiFe systems were exposed to atmosphere upon sealing and this is thought to contribute to the improved magnetic mass fraction. The EDX result on the other Co_3Fe fluid confirms the loss of Fe however.

The magnetic particle sizes have been obtained as described in Chapter 4 and are displayed together with the other magnetic data in Tables 6.6 and 6.7. Also shown are the particle sizes obtained from electron microscopy. As can be seen the discrepancy between these diameters is typically 2-4nm, that is the magnetic diameter can be less than half the electron microscopy diameter. One reason for this may be that the assumed value for the bulk magnetisation is too high which would lead to smaller

TABLE 6.6
FeCo Magnetic Data

	Magnetic data					TEM data	
Fluid	Magneti-sation	Mass fraction	Vol. fract. median	Lognormal parameter	No. fract. mean	Physical mean	Std. Dev.
	$JT^{-1}kg^{-1}$	%	(nm)	(σ)	(nm)	(nm)	
1A	2.80	1.20	4.3	0.32	3.3	5.2	1.29
2	0.98	0.40	4.2	0.29	3.4	6.1	1.36
D	2.52	1.10	4.9	0.30	3.9	6.8	0.81
D2	1.25	0.50	5.2	0.30	4.2	8.0	1.08
DT	0.34	0.15	4.5	0.41	3.0	–	–
Co_3FeD2	5.91	2.90	5.8	0.34	4.3	7.8	1.34

TABLE 6.7
NiFe Magnetic Data

	Magnetic data					TEM data	
Fluid	Magneti-sation	Mass fraction	Vol. fract. median	Lognormal parameter	No. fract. mean	Physical mean	Std. Dev.
	$JT^{-1}kg^{-1}$	%	(nm)	(σ)	(nm)	(nm)	
3	0.572	0.054	6.7	0.36	4.8	–	–
4	0.386	0.036	3.6	0.23	3.2	7.2	1.25
5	0.224	0.020	3.9	0.36	2.8	8.2	1.04
6	0.287	0.027	4.4	0.26	3.7	7.0	1.26
6(6T)	0.318	0.029	4.0	0.34	3.0	7.0	1.26

diameters being calculated from the magnetic data. (See equation 4.25). This would tend to be counter-balanced, however, by the lack of high field data described in Chapter 4, Section 4.5.4, and illustrated by NiFe fluid 6 in Table 6.7. The large difference therefore remains and must be ascribed to surface effects, most likely to be oxidation or reaction with surfactant leading to a non-magnetic layer on the surface of the particles. In the light of the Mössbauer result for Fe particles (Section 6.1) the possibility of incorporation of C atoms into other metallic particles must be permitted which could severely reduce the value of the magnetisation of the particles which would make the magnetic diameters obtained above underestimates and thus explain the magnitude of the difference.

The small magnetic particle size of the NiFe fluids suggests that at 1.2T they had not yet reached saturation. Fluid 6 was therefore examined at room temperature in the superconducting solenoid, the resulting magnetisation curve is shown in Figure 4.7 where it can be seen that at 1.2T the fluid had not reached saturation. The 6T curve results in an 11% increase in the saturation magnetisation value and a decrease in mean magnetic diameter as described in Chapter 4.

6.3.4 Stability

(a) Gravitational

This was examined for the Fe-Co fluids 2 and D2 which had similar particle sizes and densities. The concentration

profiles were measured using the sedometer with 20cm columns of fluid. The final profiles measured after 49 hrs and 101 hrs for 2 and D2 respectively are shown in Figure 6.31. The profile for D2 had remained unchanged over this period whereas the profile for 2 had gradually changed from uniformity. The partial settling out of fluid 2 may be evidence the the surfactant Duomeen-TDO (Akzo-Chemie) may be more successful in stabilizing against the gravitational field than Solsperse 3000 (ICI). However, fluid 2 did have a larger size distribution and thus a higher proportion of large particles which may have aggregated and then settled out. This fluid could be redispersed by shaking.

(b)   To Oxidation

Room temperature magnetisation curves were measured over a period of days for the Ni-Fe system NiFe3 and over months for the Fe-Co systems 1A, 2, D and D2. The NiFe3, FeCo1A, 2 and D samples were stored at room temperature in atmosphere over the experiment whilst the FeCoD2 sample was stored at $8^{O}C$. The decay in saturation magnetisation for NiFe3 is shown in Figure 6.32 and for the Fe-Co systems in Figure 6.33. The NiFe3 data shows that the rate of oxidation is initially very rapid and then much slower. The data points may be reasonably represented by

$\sigma(t) = \sigma(o)(k_1 - k_2 \ell nt)$ (with $k_1 = 0.926$, and $k_2 = -0.04$) as would be expected for an oxide layer growing logarithmically with time on the surface. The decay in magnetisation over the first 8 days was 39% but then over the next 11 days
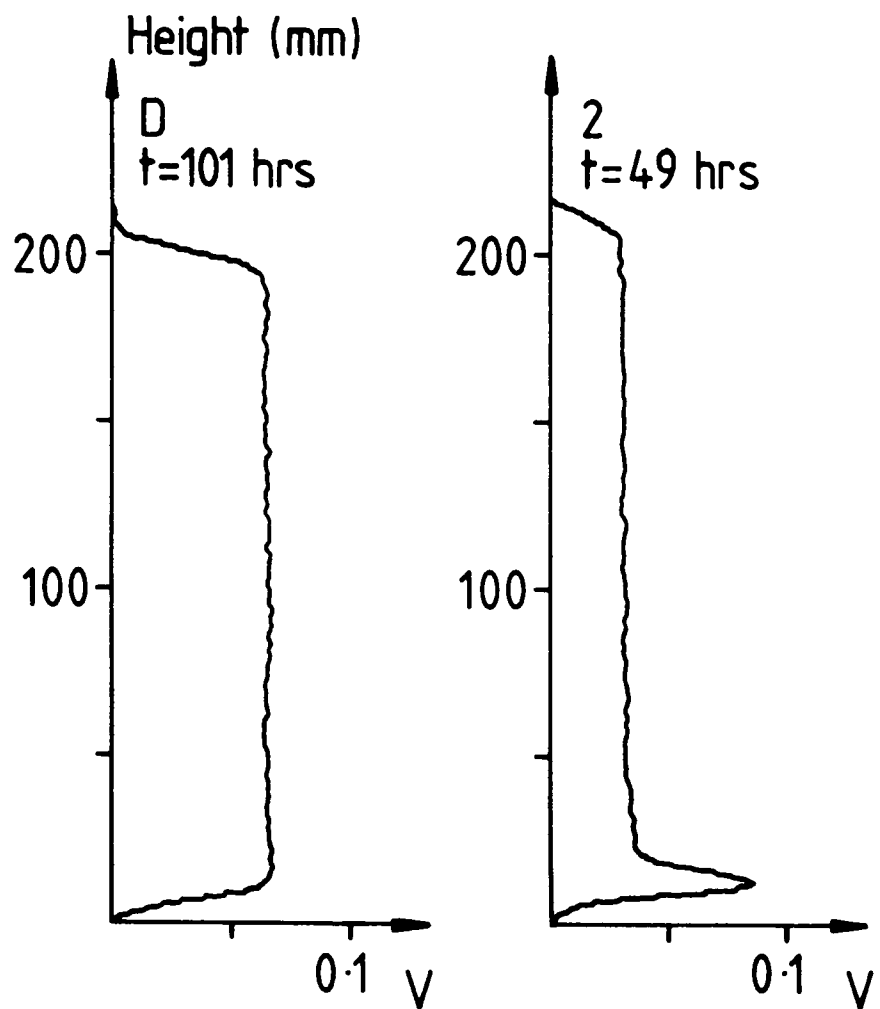
FIGURE 6.31
Magnetic profiles measured in the sedometer of the Fe-Co systems D and 2 after standing for 101 and 49 hrs respectively.
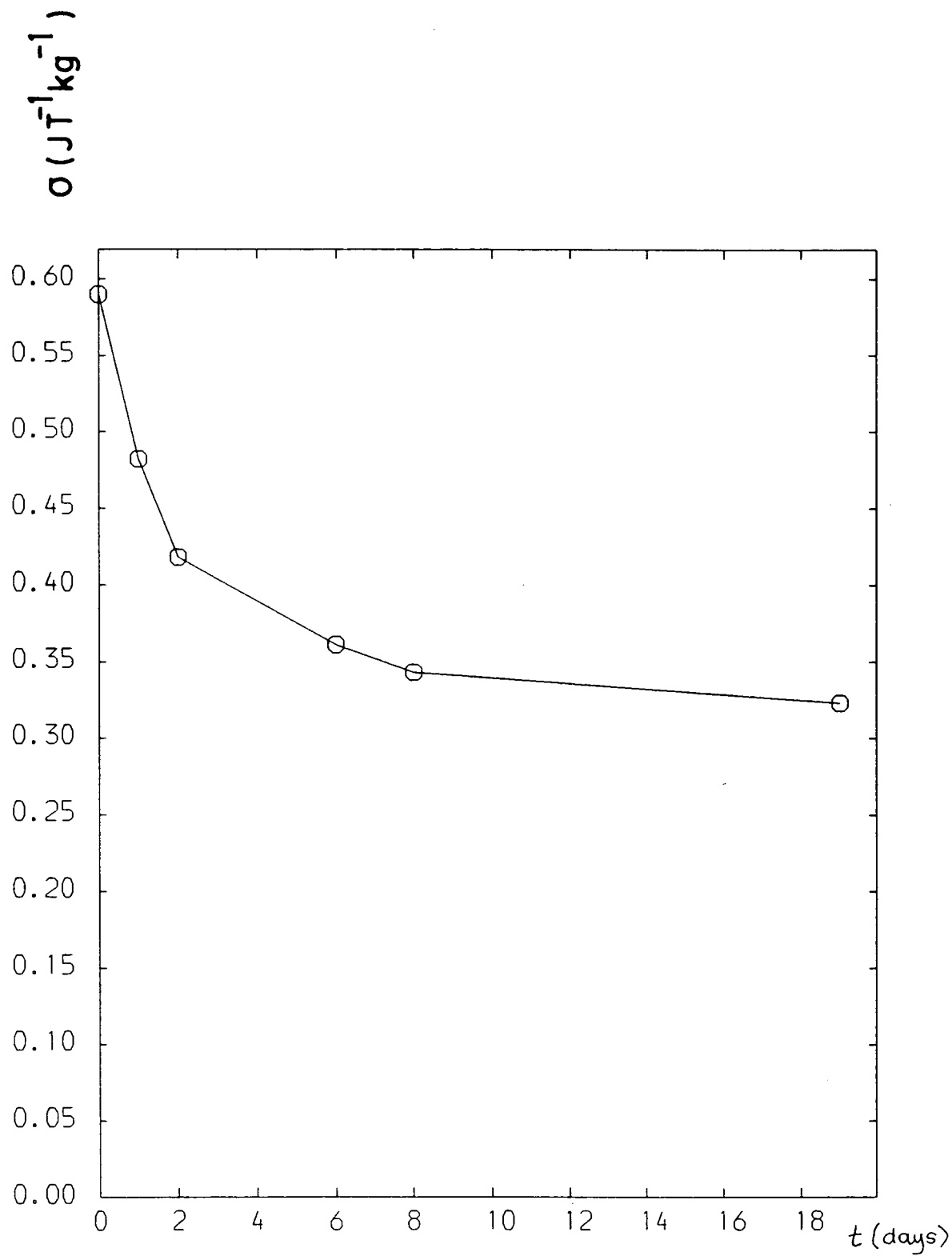
FIGURE 6.32
Decay in magnetisation of the NiFe3 system
on exposure to atmosphere.
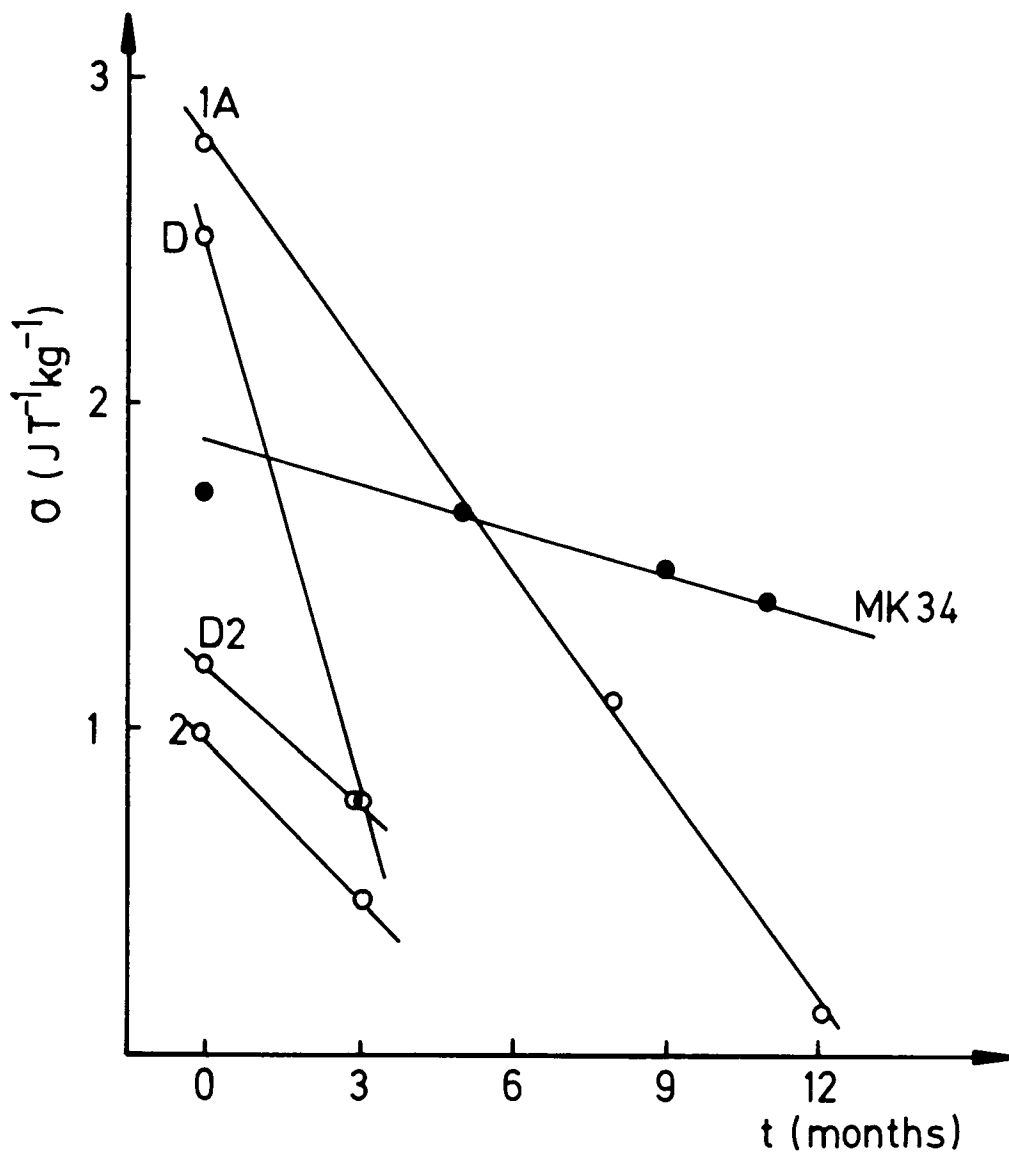
FIGURE 6.33
Loss of magnetisation on exposure to atmosphere for the Fe–Co systems 1A,D,2 at RT and D2 at 8 C. Also shown is the loss experienced by the Fe system MK34.

further decay was only 5%. The rate of decay after the first 6 days is about -0.09 $JT^{-1}kg^{-1}$ per month assuming it is linear. The Fe-Co data reveals that oxidation, although slow, continues over a period of months, the fluids eventually becoming non-magnetic (in the sense of having no superparamagnetic response) which took just over 12 months in the case of fluid FeCo1A. The rate of decay for fluids 1A, 2 and D is -0.22, -0.16 and -0.58 $JT^{-1}kg^{-1}$ per month respectively. These fluids decay more rapidly than the Ni-Fe system which is probably due to the relatively higher Fe concentration in their particles. The rate of decay for FeCo1A and FeCo2 is very similar which may be attributable to the fact that they were prepared using the same surfactant. FeCoD oxidised much more rapidly than 1A or 2 which may be evidence that Duomeen-TDO offers less protection to oxidation than Solsperse 3000. The oxidation of the Duomeen-TDO fluid D2 was slowed to about the same rate as that of the Solsperse fluids by storage at $8^{O}C$.

The initially rapid rate of oxidation may be explained by the formation of an oxide coating on the particle surface which affects only $\sim$ 2 layers of atoms ($\sim$ 40%) and then acts to protect the core from further oxidation. Oxidation would then require the passage of metal ions through this layer which would grow and slow further oxidation. For small particle sizes, however, this would be a linear process as the core would be almost completely oxidised by the first oxidation layer forming. Although the oxidation slows, it

remains relentless and no fluid has survived for longer than
$\sim$ 18 months in atmosphere.

6.3.5 Low Temperature Magnetisation

The magnetisation curve of fluid FeCoD2 at 77K is shown
in Figure 6.34. This sample had been stored at room
temperature in a sealed glass bulb for two months prior to
the measurements. Inevitably, air had entered the bulb
before sealing and thus some oxidation had occurred. The
saturation magnetisation at 77K was found to be $\sim$ 0.9 $JT^{-1}kg^{-1}$
compared with the original room temperature value of 1.25
$JT^{-1}kg^{-1}$. In a one month period another sample of this
fluid was found to have lost 9% of its magnetisation under
the same conditions. The striking feature of this curve,
however, is the absence of hysteresis. This fluid had a
median particle diameter of 4.5nm and thus it is reasonable
to assume that at 77K the critical diameter for intrinsic
superparamagnetism is > 4.5nm which implies that the
anisotropy constant K < 5.6 x $10^5 Jm^{-3}$. This is once more
too large a value to be explained simply by shape
anisotropy.

The magnetisation curves of NiFe4 and NiFe6 at room
temperature and at 77K are shown in figures 6.35 and 6.36
respectively. The low temperature curves have much higher
magnetisations than the room temperature curves, increases
of 85% and 72% for NiFe4 at 0.7 and 1.0T and 56% and 48% for
NiFe6 at these field values.

The expected increase may be estimated from the
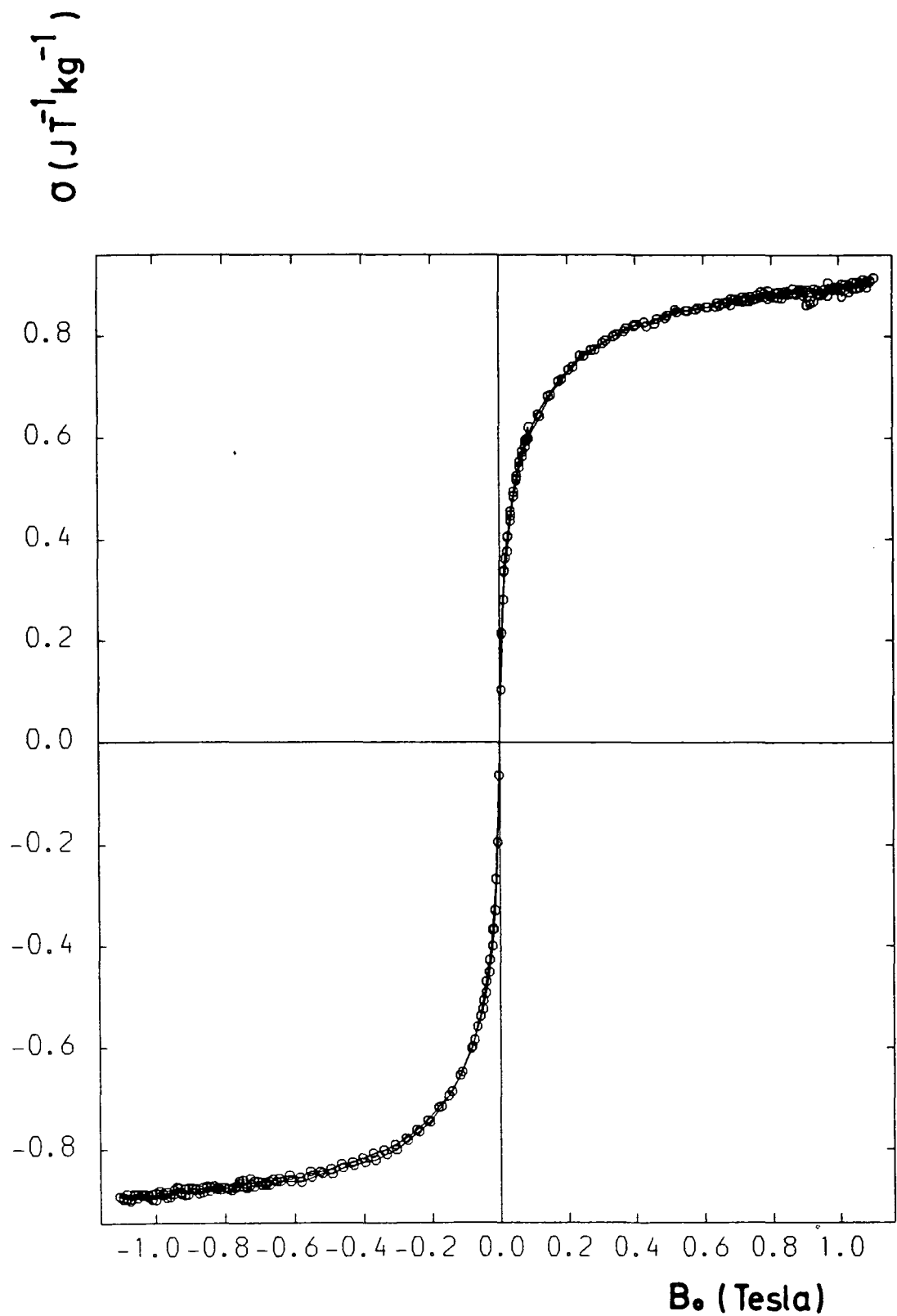
FIGURE 6.34
Magnetisation curve recorded on the system
FeCoD at 77K showing no hysteresis.

$\sigma\,(\mathrm{J\,T^{-1}\,kg^{-1}})$

NIFE4

77K

RT

B_o (Tesla)
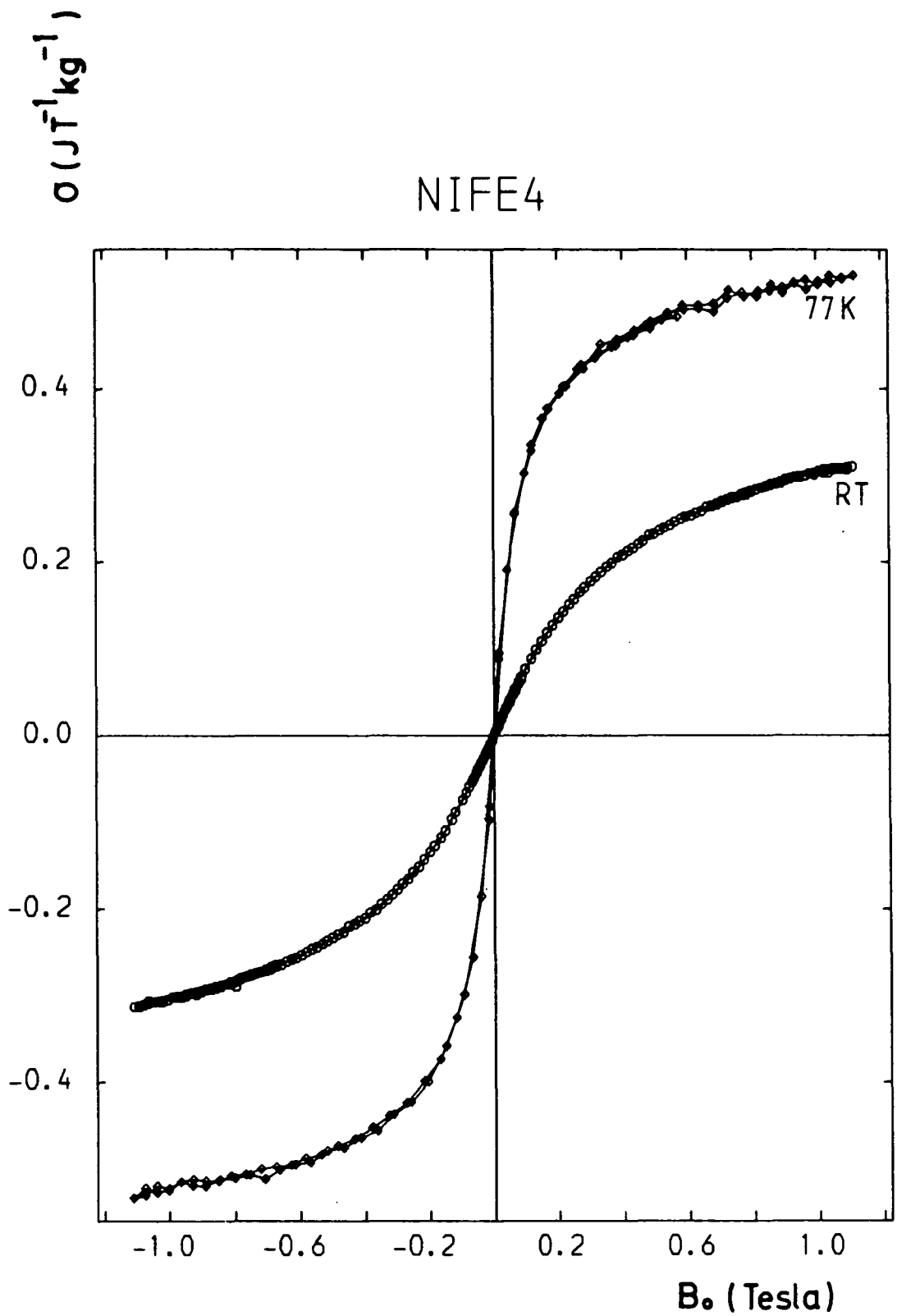
FIGURE 6.35
Room temperature and 77K measurements of the magnetisation of Ni-Fe system 4.
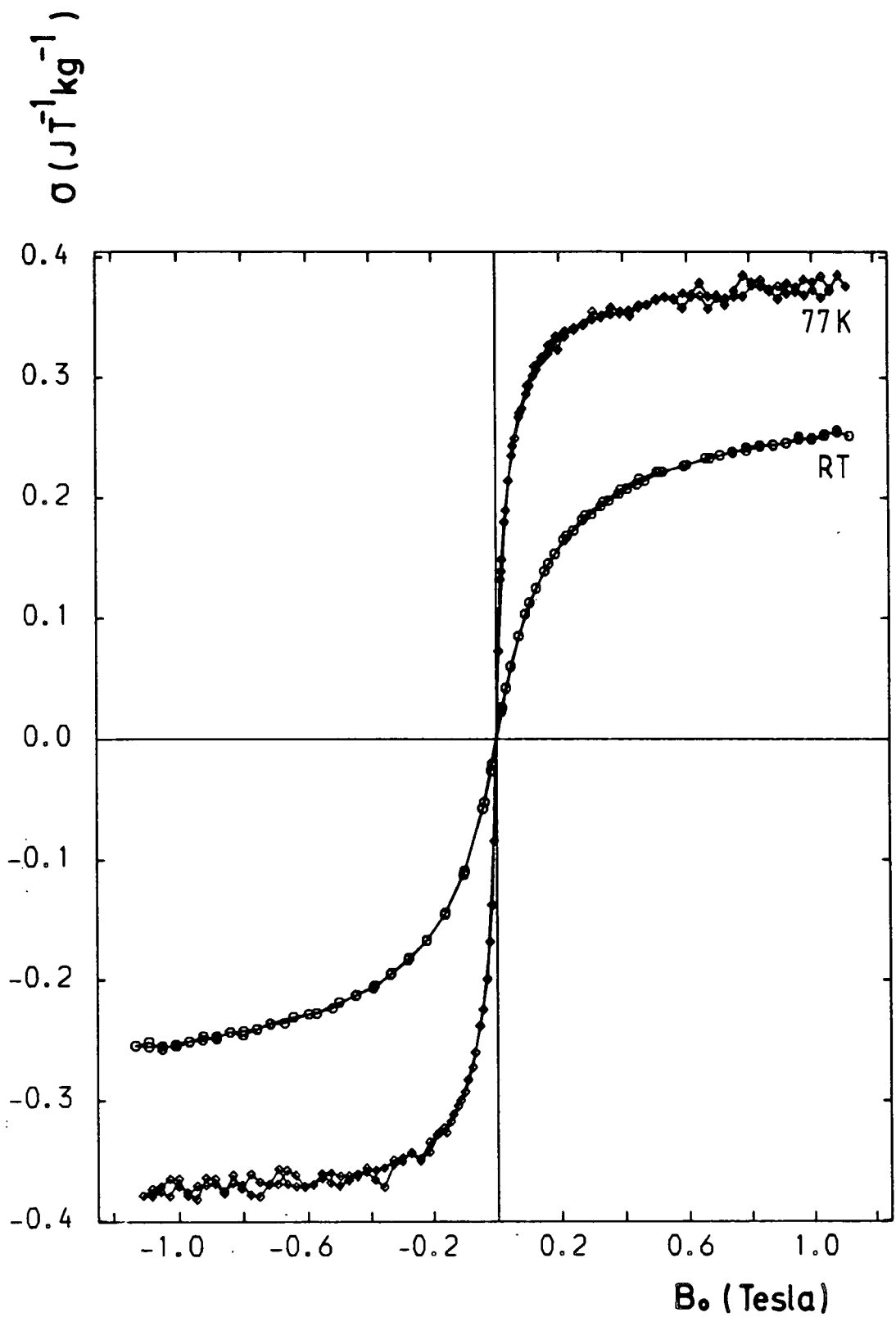
FIGURE 6.36
Room temperature and 77K measurements of the
magnetisation of Ni-Fe system 6.

Langevin function weighted by the particle size distribution. If the values for the particle sizes obtained from room temperature 1.2T curves are inserted, values of 24% and 15% at 0.7 and 1.0T are obtained for the fluid NiFe4. For NiFe6 values of 15 and 10% are obtained for these field values, however when the particle size data obtained from the 6T measurements are used they become 22 and 16%. The NiFe4 room temperature magnetisation curve approaches saturation even more slowly than the NiFe6 curve and thus one would expect the estimated particle size for NiFe4 to be an even greater over-estimate. Decreasing the bulk magnetisation, i.e. increasing the nickel content, would also raise the theoretical increases still further and the experimental values can be obtained. However, it should be recalled that approximately 80% of the original metal atoms have not been incorporated into metallic paticles and may be present in the form of paramagnetic or ferrimagnetic compounds. If so, their contribution would increase approximately fourfold on decreasing the temperature from 300 to 77K.

Evidence for the existence of a paramagnetic constituent in the fluid is provided by the magnetisation loop of fluid NiFe6 at ∿8K. This has already been discussed in Chapter 5 with regard to the anisotropy constant, but in Figure 6.37 the entire curve is displayed. The paramagnetic component can be seen above 0.1T. Estimation of this component proved impossible due to the
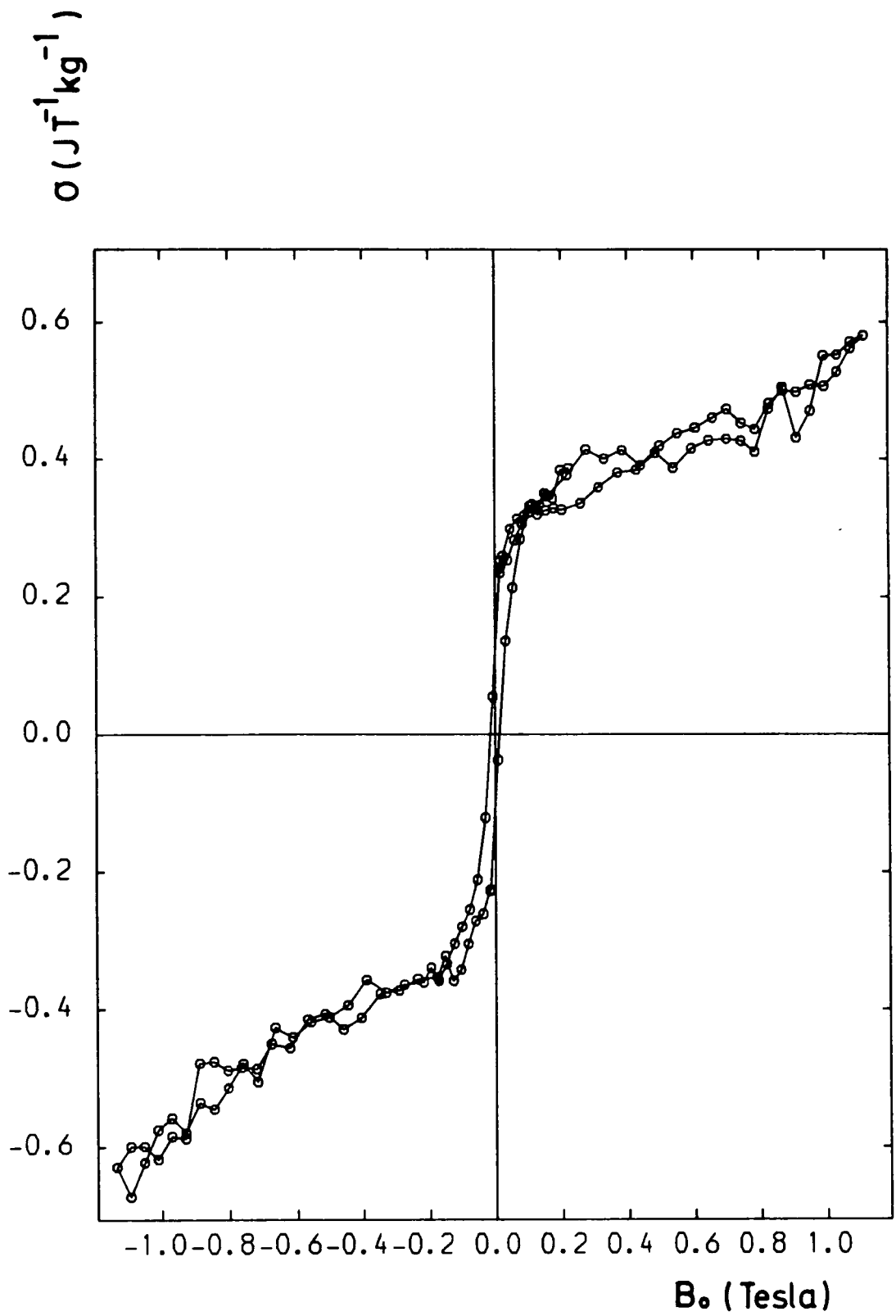
FIGURE 6.37
Magnetisation curve of Ni-Fe system 6 recorded
at 8K.

noise on the run and on the residual run.

6.3.6 Discussion

From the electron diffraction and EDX data it is clear
that "alloy" particles have been prepared from mixed-metal
organometallic precursors. As outlined in Chapter 4, small
particle sizes and narrow distributions have been obtained.
The large discrepancy between physical and magnetic sizes
may be attributable to magnetically "dead" layers on the
particle surfaces due to oxidation, reaction with surfactant
or more fundamental effects such as spin pinning. However,
the calculation of the magnetic particle size requires
knowledge of the magnetisation of the particles and together
with the low temperature data this raises the question of
the exact composition of the particles. It seems unlikely
in the light of the above data and the recent results of van
Wonterghem et al. (1985) that the "alloy" particles are
uniformly composed of FeCo of Ni_3Fe. It remains possible
that a large proportion of the particles are amorphous *or*
that very small particles may not make any contribution to
the magnetisation of the fluid. The effects of these
possibilities on the intrinsic magnetic properties such as
Curie temperature remain unknown and may alter the above
analyses considerably.

CHAPTER SEVEN

CONCLUSIONS AND FURTHER WORK

7.1 Conclusions

The aim of this study was to investigate the properties of new hydrocarbon based magnetic fluids prepared by the decomposition of organometallic compounds. The data reported in sections 6.2 and 6.3 has shown that the use of cyclopentadienyl-carbonyl complexes is successful in preparing magnetic fluids. Iron, cobalt and nickel fluids have been routinely prepared and investigated during the course of this study. The yield of "magnetic" metal atoms has been found to be extremely low at about 20 to 40% in most cases. It is particularly low for iron fluids and this may be explained by the formation of iron-carbides rather than α-Fe and the loss of volatile iron complexes during decomposition. The low yield may also be explained by the existence of magnetically "dead" layers on the surfaces of the particles and by the formation of metal-surfactant complexes which remain in solution. The existence of a paramagnetic component to the magnetisation of these systems at low temperature is an indication that   paramagnetic complexes may be present.

Iron particles in the b.c.c. phase have not been conclusively observed and the EXAFS data has shown that in

most cases the iron is not in the zero valence state.
Cobalt particles with hexagonal structure have been prepared
but it has not been possible to repeat their preparation.
Nickel systems have invariably been found in the f.c.c.
phase with the one extra line reported previously by Hoon
et al (1983).

It has further been demonstrated that mixed-metal or
"alloy" particles may be prepared via the organometallic
route. This has required the decomposition of heteronuclear
mixed-metal precursors as the simultaneous decomposition of
two different metal carbonyls failed to produce "alloy"
particles. The particles obtained have been found to form
in the ordered or superlattice structure and this may be a
consequence of the preparative route. Magnetic-metal yields
have again been low and in particular it has been observed
th iron is lost to the particles. The success of this
route has been established, however, and has great potential
for preparing many types of new magnetic fluid.

The mean physical particle diameters obtained using the
organometallic route have been found to be in the range
5-10nm in all cases apart from nickel. The particle size
distributions have been found to be Gaussian with standard
deviations of 1.0 to 1.9. Magnetic diameters have been
consistently smaller than physical diameters, typically by
about 1-4nm. This is thought to provide further evidence
for non-magnetic surface layers on particles. It has been
shown that the magnetisation of these fluids has not usually

reached saturation at 1.2T and thus magnetically derived diameters tend to be over-estimates. If the bulk magnetisation assumed for the particles is too large, as will be the case if carbides are present, then the magnetic diameter will be under-estimated. The method of Cahn (1957) together with electron microscopy provides a reasonable characterisation of magnetic particle size. It has been found that most techniques for magnetic particle size estimation provide useful results.

The anisotropy constants of fluids have been derived from torque and magnetisation data. The magnetisation data leads to lower values but the torque data is considered more reliable. Values of the order $10^5 Jm^{-3}$ have been obtained for all the metal systems and $10^4 Jm^{-3}$ for a magnetite system in agreement with previous work. These values are too large to be explained entirely by shape anisotropy and this is an area which requires further investigation.

7.2 Future Work

The immediate extension of this work is to use other heteronuclear organometallics, firstly other dinuclear complexes such as NiCo, Co_3Ni or Fe_2Co and then to use ternary compounds containing Fe, Ni and Co. The inclusion of other, non-ferromagnetic, elements may be desirable, for example chromium/cobalt particles may have several advantages such as enhanced anisotropy and retarded oxidation. In terms of more fundamental research, the preparation of RhFe fine particles would permit an

investigation of the effect of finite dimensionality/surface effects on the ferromagnetic-antiferromagnetic transition temperature. This system would also be useful in examining the effect of interactions in fine particle systems as the dipole-dipole interactions could be "switched" on or off by altering the temperature.

The composition and structure of metallic fine particles requires detailed investigation. This would not be a simple task as the techniques of EXAFS, EDX, Electron Diffraction, Mössbauer and neutron spectrosopy would all be necessary to gain a full insight into particle composition and structure. An ideal experiment would consist of all these measurements performed on the same fluid in the same state of oxidation, which may not be possible. A thorough investigation of anisotropy is also required using as many techniques as possible. The composition and structure will obviously have a strong bearing on this.

From a technological point of view, oxidation remains the major problem. This may be tackled by using different alloys and surfactants. However the author believes that a protective coating of some description is most likely to succeed. This is a problem closely related to particle formation and as this process is still not understood, a full study of this is also necessary. The preparation of particles in low vapour pressure carrier liquids still needs to be examined and will require a more thorough investigation of surfactants.

Much of this work is at present under way at Durham together with a collaborative venture with Dr. P.L. Timms of Bristol University involving the preparation of magnetic fluids by the evaporation of metal atoms into carrier liquid-surfactant solutions. It is the author's belief that this may prove to be an excellent method for preparing metallic fine particle systems.

<u>BIBLIOGRAPHY   AND   REFERENCES</u>

ABELEDO C.R., SELWOOD P.W.
J. Appl. Phys. <u>32</u>, 229 (1961).

AHARONI A.
Phys. Rev. <u>135</u>, 4447, (1964).

AKIMOTO Y., SATO M., HOSHINO Y.
Bull. Tokyo Inst. Technol. <u>108</u>, 141 (1972).

ASIMOW R.M.
Trans. Met. Soc. A.I.M.E. <u>233</u>, 401 (1965).

AYOUB N., KOKUSSI M.A., CHANTRELL R.W., O'GRADY K.,
POPPLEWELL J.
J. Phys. F : Met. Phys. <u>15</u>, 2229, (1985).

BACRI J-C., SALIN D.
J. Physique Lett. <u>45</u>, 558, (1984).

BAGCHI B.
J. Coll. Int. Sci. <u>41</u>, 380, (1972).

BAILEY R.L.
J. Mag. Magn. Mat. <u>39</u>, 178, (1983).

BEAN C.P.
J. Appl. Phys. <u>26</u>, 1381, (1955).

BEAN C.P., JACOBS I.S.
Phys. Rev. <u>27</u>, 1448, (1956).

BECKER J.J.
Trans. A.I.M.E. : J. Met. <u>209</u>, 59, (1957).

BERKOWITZ A., LAHUT J.A., JACOBS I.S., LEVINSON L.M.,
FORESTER D.W.
Phys. Rev. Lett. <u>34</u>, 594, (1975).

BERKOWITZ A., WALKER J.L.
J. Mag. Magn. Mat. <u>39</u>, 75, (1983).

BITTER F.
Phys. Rev. <u>41</u>, 507, (1932).

BLACK W.
"Surface Active Compounds and their Role in pigment
Dispersion"
in "Dispersion of Powders in Liquids"
ed. G. Parfitt, Applied Science, London, (1969).

BLOCH F.
Z. Physik $\underline{57}$, 545, (1929).

BOGARDUS E.H., SCRANTON R., THOMPSON D.A.
IEEE Trans. Mag. $\underline{MAG11}$, 1364, (1975).

BRADBURY A., MENEAR S., CHANTRELL R.W.
J. Mag. Magn. Mat. $\underline{54-57}$, 745, (1986).

BRAGG W.L., WILLIAMS E.J.
Proc. Roy. Soc. (Lon.), $\underline{145}$, 699, (1934).

BRAISFORD F.
"Physical Principles of Magnetism"
van Nostrand, London, (1966).

BROWN W.F. Jr.
Phys. Rev. $\underline{105}$, 1479, (1957)
J. Appl. Phys. supp. to 30, $\underline{30S}$, 130, (1959).
Phys. Rev. $\underline{130}$, 1677, (1963).

BUNGE H.
"Texture Analysis in Materials Science"
Butterworths, London, (1982).

CAHN J.
Trans. A.I.M.E. : J. Met. (Oct. 1957), 1309, (1957).

CASIMIR H.B.G., POLDER D.
Phys. Rev. $\underline{73}$, 360, (1978).

CAYLESS A.T., HOON S.R., TANNER B.K., CHANTRELL R.W.,
KILNER M.
J. Mag. Magn. Mat. $\underline{30}$, 303, (1983).

CEBULA D.J., CHARLES S.W., POPPLEWELL J.
J. Colloid. Poly. Sci. $\underline{259}$, 397, (1981).
J. Mag. Magn. Mat. $\underline{67}$, (1983).

CHANTRELL R.W.
Ph.D. Thesis U.C.N.W., Bangor U.K. (1977).

CHANTRELL R.W., POPPLEWELL J., CHARLES S.W.
Physica $\underline{86-88B}$ 1421 (1977).
IEEE Trans. Mag. $\underline{MAG14}$, 975 (1978)
J. Mag. Magn. Mat. $\underline{15-18}$, 1123, (1980).

CHANTRELL R.W., SIDHU J., BISSELL P.R., BATES P.A.
J. Appl. Phys. $\underline{53}$, 8341, (1982).

CHANTRELL R.W., HOON S.R., TANNER B.K.
J. Mag. Magn. Mat. $\underline{38}$, 83 (1983).

CHANTRELL R.W., WOHLFARTH E.P.
J. Mag. Magn. Mat. 40, 1 (1983).

CHARLES S.W., POPPLEWELL J.
"Ferromagnetic Liquids" Ch. 8. of Vol. 2. of "Ferromagnetic
Materials"
ed. E.P. Wohlfarth, North Holland, Amsterdam (1980).

COWLEY M.D., ROSENSWEIG R.E.
J. Fluid Mech. 30, 671, (1967).

DAVIES H.W., LLEWELLYN J.P.
J. Phys. D. 12, 311, (1979)a
J. Phys. D. 12, 1357, (1979)b
J. Phys. D. 12, 1379, (1979)c
J. Phys. D. 13, 2327, (1980).

DAVIS P.J., RABINOWITZ P.
"Methods of Numerical Integration"
Academic Press, London (1984).

DE BRUYN
Proc. Int. Conf. Rheology, Holland 1948 pII 95, Amsterdam
(1949).

DEBYE P.
Physik Z. 21, 178, (1920).

DE GENNES P.G., PINCUS P.A.
Phys. Kond. Materie. 11, 189, (1970).

DERYUGIN I.A., SIGEL M.A.
Sov. Phys. Sol. State. 4, 359, (1962).

EDELMANN F.H.
"The Preparation and Characteristics of Thin Ferromagnetic
Films"
U.S. Dept. Comm. Report No. PB151525, (1958).

EINSTEIN A.
Kholloid Z. 27, 137, (1920).
Ann. Physk 19, 289, (1906).

EIRICH F., MARGARETHA H., BUNZL M.
Kholloid Z. 75, 20, (1936).

EISENSCHITZ R., LONDON F.
Z. Physik 60, 491, (1930).

ELMORE W.C.
Phys. Rev. 54, 309, (1938)a
Phys. Rev. 54, 1092, (1938)b.

FALK R.B., HOOPER G.D.
J. Appl. Phys. 32, 2536, (1961).   .

FREI E.H., SHTRIKMAN S., TREVES D.
Phys. Rev. 106, 446, (1957).

FRENKEL J., DORFMANN J.
Nature , 126 274 (1930).

GRANDQVIST C.G., BUHRMAN R.A.
J. Appl. Phys. 47, 2200, (1976)a
J. Catalysis 42, 477, (1976)b

HALL W.F., BUSENBERG S.N.
J. Chem. Phys. 51, 137, (1969).

HAMAKER H.C.
Physica 4, 1058, (1937).

HANDRICH K., KOBE S.
Acta Physica Polonica A38, 819, (1970).
* FOR HARTMANN U., MENDE H.H. see after ZULSTRA.
HAYES C.F.
J. Coll. Int. Sci. 52, 239, (1975).

HAYES C.F., HWANG S.R.
J. Coll. Int. Sci. 60, 443, (1977).

HEISENBERG W.
Z. Physik 49, 619, (1928).

HESS P.H., PARKER P.H.
J. Appl. Poly. Sci. 10, 1915, (1966).

HOON S.R., POPPLEWELL J., CHARLES S.W.
IEEE Trans. Mag. MAG14, 981, (1978).
J. Appl. Phys. 50, 7798, (1979).
U.S. Army Report RSG(EUR), Agreement No. DAERO 77-9-037,
(1980)

HOON S.R.
Ph.D. Thesis, U.C.N.W. Bangor, U.K. (1980).

HOON S.R., TANNER B.K., KILNER M.
J. Mag. Magn. Mat. 39, 30, (1983).

HOON S.R., KILNER M., RUSSELL G.J., TANNER B.K.
J. Mag. Magn. Mat. 39, 107, (1983).

HOON S.R., LAMBRICK D.B., PAIGE D.M.
J. Phys. E : Sci. Inst. 18, 389, (1985).

HOON S.R., WILLCOCK S.N.M.
J. Phys. E : Sci. Inst. Submitted 1986 (1986).

ISRAELACHVILI J.N., TABOR D.
Prog. Surf. and Memb. Sci., Acad. Press. $\underline{17}$, 1, (1973).

JACOBS I.S., LUBORSKY F.
J. Appl. Phys. $\underline{28}$, 467, (1957).

KAGAN I. Yu., RYKOV, V.G., YANTOVSKII E.I.
Magnetohydrodynamics $\underline{6}$, 441, (1970).

KAISER R., ROSENSWEIG R.E.
N.A.S.A. Report NASA CR-1407 (1969).

KAISER R., MISKOLCZY D.
J. Appl. Phys. $\underline{41}$, 1064, (1970).

KEESOM W.H.
Physik Z. $\underline{23}$, 225, (1922).

KHALAFALLA S.E., REIMERS G.W.
U.S. Pat. 3764540 (1973).

KILNER M., HOON S.R., LAMBRICK D.B., POTTON J.A.,
TANNER, B.K.
IEEE Trans. Mag. $\underline{MAG20}$, 1735, (1984).

KITTEL C.
Phys. Rev. $\underline{70}$, 965, (1946).

KNELLER E.
"Fine Particle Theory" Ch. 8, Vol. 1 of "Magnetism and
Metallurgy"
ed. A.E. Berkowitz, E. Kneller, Academic Press, London
(1969).

KNIGHT G., under WILSON B.,
Phil. Trans. Roy. Soc. (1779) p.480 (1779)

KOHARA T., YAMAGUCHI M., ASAYAMA K.
J. Phys. Soc. Jpn. $\underline{54}$, 1537, (1985).

KRUEGER D.A.
IEEE Trans. Mag. $\underline{MAG\ 16}$, 251, (1980).
J. Appl. Phys. $\underline{50}$, 8169, (1979).

KRUYT H.R.
"Colloid Science", Elsevier, N.Y., (1952).

KUSAKA K., WADA N., TASAKI A.
Jpn. J. Appl. Phys. $\underline{8}$, 599, (1969).

LAMBRICK D.B., MASON N., HARRIS N.J., HOON S.R., KILNER M.
IEEE Trans. Mag. <u>MAG 21</u>, 1891, (1985).

LAMBRICK D.N., MASON N., HOON S.R., KILNER M.,
J. Mag. Magn. Mat. (In press) (1986).

LANGBEIN D.
J. Adhes. <u>1</u>, 237, (1969).
J. Phys. Chem. Sol. <u>32</u>, 1657, (1971).

LEVI A.C., HOBSON R.F., McCOURT F.R.
Canad. J. Phys. <u>51</u>, 180, (1973).

LIFSHITZ, E.M.
Sov. Phys. JETP <u>2</u>, 73, (1956).

LLEWELLYN J.P.
J. Phys. D. <u>16</u>, 95, (1983).

LONDON F.
Z. Physik. Chem. <u>B11</u>, 222 (1930)a
Z. Physik <u>63</u>, 245, (1930)b
Trans. Farad. Soc. <u>33</u>, 8, (1937).

LUBORSKY F.E., PAINE T.O.
J. Appl. Phys. <u>31</u>, 665, (1960).

MACKOR E.L.
J. Colloid. Sci. <u>6</u>, 492, (1951).

MALLINSON J.
J. Appl. Phys. <u>37</u>, 2614, (1966).

MARIGNIER J.L., BELLONI J., DELCOURT M.O., CHEVALIER J.P.
Nature <u>317</u>, 344, (1985).

MARTINET A.
"Experimental Evidence of Static and Dynamic Anisotropies of
Magnetic Colloids"
in "Thermomechanics of Magnetic Fluids"
ed. B. Berkovsky, Hemisphere, Washington D.C. (1978).

MASON N.
Ph.D. Thesis, Durham University, Durham, U.K. (in
preparation), (1986).

MASSART R.
IEEE Trans. Mag. <u>MAG17</u>, 1247, (1981).

MARUNO S., YUBAKAMI K., SOGA M.
J. Mag. Magn. Mat. <u>39</u>, 187, (1983).

MAYER A., VOGT E.
Z. Natuur. $\underline{7A}$, 334, (1952).

McLACHLAN A.D.
Proc. Roy. Soc. (Lon). $\underline{A271}$, 87, (1963)a
Proc. Roy. Soc. (Lon). $\underline{A274}$, 80, (1963)b
Disc. Farad. Soc. $\underline{40}$, 239, (1965).

McTAGUE J.P.
J. Chem. Phys. $\underline{51}$, 133, (1969).

MENEAR S., BRADBURY A., CHANTRELL R.W.
J. Mag. Magn. Mat. $\underline{43}$, 166, (1984).

MENEAR S., BRADBURY A.
J. Mag. Magn. Mat. $\underline{51}$, 103, (1985).

MIEKLEJOHN W.H., BEAN C.P.,
Phys. Rev. $\underline{102}$, 1413, (1956).

MIEKLEJOHN W.H.
J. Appl. Phys. $\underline{29}$, 454, (1958).

MORIYA T.
J. Mag. Magn. Mat. $\underline{14}$, 1, (1979).

MORRISH A.H., HANEDA K.
J. Mag. Magn. Mat. $\underline{35}$, 105, (1983).

MYALKOVSKII V.V., SHVETS T.M., VASILENKO V.P., MEL'NICHENKO
Z.M.
Trans. Porosh. Metall. $\underline{5}$, 1, (1984).

NEEL L.
C.R. Acad. Sci. $\underline{228}$, 664, (1949)a
Ann. Geophys. $\underline{5}$, 99, (1949)b

O'GRADY K., CHANTRELL R.W., POPPLEWELL J., CHARLES S.W.
IEEE Trans. Mag. $\underline{MAG16}$, 1077, (1980).
IEEE Trans. Mag. $\underline{MAG17}$, 2943, (1981).

O'GRADY K.
Ph.D. Thesis U.C.N.W., Bangor, U.K. (1982).

O'GRADY K., BRADBURY A., CHARLES S.W., MENEAR S., POPPLEWELL
J.
J. Mag. Magn. Mat. $\underline{31-34}$, 958, (1983)a

O'GRADY K., BRADBURY A.
J. Mag. Magn. Mat. $\underline{39}$, 91, (1983)b

O'GRADY K., CHANTRELL R.W., WOHLFARTH E.P.
IEEE Trans. Mag. $\underline{MAG20}$, 1849, (1984).

O'GRADY K., BRADBURY A., POPPLEWELL J., CHARLES S.W.,
CHANTRELL R.W.
J. Mag. Magn. Mat. $\underline{49}$, 106, (1985).

O'KONSKI C.T., YOSHIOKA K., ORTTING W.H.
J. Phys. Chem. $\underline{63}$, 1558, (1954).

PAIGE D.M., TANNER B.K.
J. Phys. E. : Sci. Inst. $\underline{15}$, 128, (1982).

PAIGE D.M.
Ph.D. Thesis, Durham University, Durham, U.K., (1983).

PAIGE D.M., HOON S.R., TANNER B.K., O'GRADY K.
IEEE Trans. Mag. $\underline{MAG20}$, 1852, (1984).

PAPELL S.S.
Space Daily (Nov. 1963), 211, (1963)
U.S. Pat. 3215592 (1965).

PAPIRER E.
C.R. Acad. Sci. $\underline{285}$, 73 (1977).

PAPIRER E., HENRY P., BALARD H., ANTHORPE R., PETIPAS R.,
MARTINET A.
J. Coll. Int. Sci. $\underline{94}$, 207, (1983).

PARPIA D.Y., TANNER B.K., LORD D.G.
Nature $\underline{303}$, 684, (1983).

PAUTHENET R.
J. Appl. Phys. $\underline{53}$, 8187, (1982).

PETERSEN E.A., KRUEGER D.A., PERRY M.P., JONES T.B.
A.I.P. Conf. Proc. $\underline{24}$, 560, (1974).

PETERSEN E.A., KRUEGER D.A.
J. Coll. Int. Sci. $\underline{62}$, 22, (1977).

POPPLEWELL J., CHARLES S.W., HOON S.R.
IEE Conf. Publn. $\underline{142}$, 13, (1976).
IEEE Trans. Mag. $\underline{MAG16}$, 191, (1980).

POTTON J.A.
Ph.D. Thesis, University of Southampton, Southampton, U.K.
(1983)

POTTON J.A., DANIELL G.J., MELVILLE D.
J. Phys. D. $\underline{17}$, 1567, (1984).

RABINOVICI R., BADESCU V.
Rev. Roum. Phys. $\underline{22}$, 891, (1977).

RABINOW J.
Franklin. Inst. 248, 155, (1949).   .

RAIKHER Yu.L.
J. Mag. Magn. Mat. 39, 11, (1983).

ROSENSWEIG R.E., NESTOR J.W., TIMMINS R.S.
A.I. Chem. E. - I. Chem. E. Symposium Series No. 5, 104,
(1965).

ROSENSWEIG R.E., KAISER R., MISKOLCZY D.
J. Coll. Int. Sci. 29, 680, (1969).

ROSENSWEIG R.E.
U.S. Pat. 3917538, (1975).
Adv. Electron. Electron. Phys. 45, 368, (1979).

ROSENSWEIG R.E.
J. Appl. Phys. 57, 4259, (1985).

ROSENSWEIG R.E.
"Ferrohydrodynamics", C.U.P., Cambridge U.K., (1985).

SCHOLTEN P.C.
IEEE Trans. Mag. MAG11, 1400, (1975).
"Colloid Chemistry of Magnetic Fluids"
in "Thermomechanics of Magnetic Fluids"
ed. B. Berkovsky, Hemisphere, Washington D.C.(1978).
IEEE Trans. Mag. MAG16 77, (1980a)
IEEE Trans. Mag. MAG16 221, (1980b)

SHEPHERD P.G., POPPLEWELL J.
Phil. Mag. 23, 239, (1971).

SHEPHERD P.G., POPPLEWELL J. CHARLES S.W.
J. Phys. D. 5, 2273, (1972).

SHLIOMIS M.I.
Sov. Phys. JETP 34, 1291, (1972).
Sov. Phys. Usp. 17, 158, (1974).

SIMHA R.
J. Res. Nat. Bur. Stand. 42, 409, (1949).
J. Coll. Sci. 5, 386, (1950).

SMITH T.W., WYCHICK D.
J. Phys. Chem. 84, 1621, (1980).

SOFFGE F., SCHMIDBAUER E.
J. Mag. Magn. Mat. 24, 54, (1981).

STONER E.C.
Phil. Mag. 15, 1018, (1933).
Proc. Roy. Soc. (Lon.), 165, 372, (1938).
Proc. Roy. Soc. (Lon.), 169, 339, (1939).
Rept. Prog. Phys. 11, 43, (1948).
J. de Physique 12, 337, (1951).

STONER E.C., WOHLFARTH E.P.
Phil. Trans. Roy. Soc. A240, 599, (1948).

STRATTON J.A.
"Electromagnetic Theory", McGraw-Hill, N.Y., (1941).

SZPUNAR B.
J. Mag. Magn. Mat. 49, 93, (1985).

SZPUNAR B., SZPUNAR J.
J. Mag. Magn. Mat. 43, 317, (1984).

TANNER B.K., McCOY J.M., WILLCOCK S.N.M., HETHERINGTON M.G.,
JAKUBOVICS J.P.
J. Mat. Sci. Lett. 5, 296, (1986).

THOMAS J.R.
J. Appl. Phys. 37, 2914, (1966).

VAND V.
J. Phys. Colloid. Chem. 52, 300, (1948).

VAN VLECK J.H.
Rev. Mod. Phys. 25, 220, (1953).

VAN WONTERGHEM J., MORUP S., CHARLES S.W., WELLS S.,
VILLASDEN J.
Phys. Rev. Lett. 55, 410, (1985).

WANG S.C.
Physik Z. 2B, 663, (1928).

WEISS P.
J. de Physique 6, 661, (1907).

WESER T., STIERSTADT K.
Z. Phys. B. (Cond. Matt.), 59, 257, (1985)a
Z. Phys. B. (Cond. Matt.) 59, 253, (1985)b

WEST F.G.
J. Appl. Phys. (Supp.), 32S, 249S, (1961).

WILLCOCK S.N.M.
Ph.D. Thesis, Durham University, Durham, U.K., (1985).

WOHLFARTH E.P.
Proc. Roy. Soc. A232, 208, (1955).
Inst. Phys. Conf. Series No. 55, 161 (Ch. 4), (1981).

ZIJLSTRA H.
in "Experimental Methods in Magnetism" Vol. 1. Generation
and Computation of Magnetic Fields   .
ed. E.P. Wohlfarth, North Holland, Amsterdam, (1967).

HARTMANN U., MENDE H.H.
phys. stat. sol (a) $\underline{82}$ 481 (1984)a
J. Mag. Magn. Mat. $\underline{45}$ 409 (1984)b
Phil. Mag. B $\underline{52}$ 889 (1985)

APPENDIX A

CONTROL PROGRAM FOR SEDOMETER AND VOLTAGE

CONVERTER CIRCUIT

```
10 REM————————————————
20 REM——— SEDOMETER CONTROL ———
30 REM———      PROGRAM        ———
40 REM————————————————
50 :
60 :
70 DIM BIT(7),D1(90),D2(90),U1(90),U2(90)
80 ?&FE62=230:?&FE60=0:?&FE60=2:?&FE60=0
90 XC%=10:YC%=45
100 FOR I%=0 TO 7:BIT(I%)=2↑I%:NEXT
110 :
120 MODE4
130 VDU 23;8202;0;0;0;
140 PROCTitle
150 PROCInstruct
160 PROCOptions
180 PROCGraph
190 REPEAT
200  REPEAT
210   IF NOT FNSwitch_closed THEN PROCMove("Up",100)
220  UNTIL FNSwitch_closed
230 IF NOT FNTop_closed THEN PROCChange_dir_to("Up")
240 UNTIL FNTop_closed
250 PROCChange_dir_to("Down")
260 PROCReadADC
270 PLOT 4,Ch2*700+XC%,YC%:PLOT 21,Ch2*700+XC%,YC%+900
280 PLOT 4,Ch2*700+XC%,YC%
290 J%=0
300 FOR K%=1 TO 83
310 J%=J%+1
320 PROCReadADC
330 D1(J%)=Ch1:D2(J%)=Ch2
340 PROCLines(D2(J%),J%,"Solid")
350 PROCMove("Down",67)
360 NEXT
370 J%=J%+1          ..
380 PROCReadADC
390 D1(J%)=Ch1:D2(J%)=Ch2
400 PROCLines(D2(J%),J%,"Solid")
410 Npts%=J%
420 J%=J%+1
430 FOR K%=1 TO 83
440 J%=J%-1
450 PROCReadADC
460 U1(J%)=Ch1:U2(J%)=Ch2
470 PROCLines(U2(J%),J%,"Dots")
480 PROCMove("Up",67)
490 NEXT
500 J%=J%-1
510 PROCReadADC
520 U1(J%)=Ch1:U2(J%)=Ch2
530 PROCLines(U2(J%),J%,"Dots")
540 PROCStore_data
550 REM CHAIN "P.NEWDUMP"
560 END
570 :
580 :
590 :
600 DEFPROCTitle
610 CLS
```

```
620 VDU23,96,255,0,0,0,0,0,0,0
630 PRINT TAB(17) "'''''''''"
640 PRINT TAB(17) "SEDOMETER"
650 PRINT TAB(17) "_____"
660 VDU10:VDU10
670 PRINT TAB(5) "n.b. The equipment needs to warm up for at least 2 hrs and at best for 24"
680 VDU10
690 PRINT "The Lock-in Amplifier should be used on the 30mV sensitivity"
700 PROCPause(2)
710 ENDPROC
720 :
730 :
740 :
750 DEFPROCPause(Delay)
760 LOCAL T
770 T=TIME
780 REPEAT:UNTIL TIME>T+Delay∘100
790 ENDPROC
800 :
810 :
820 :
830 DEFPROCInstruct
840 CLS
850 PRINT TAB(10) "SETTING UP SEDOMETER"
860 PRINT TAB(10)"_____"
870 PRINT
880 PRINT
890 PRINT "1. Set frequency to approx. 1kHz and amplitude to 10 V":PRINT
900 PRINT "2. Set freq. to minimize signal on oscilloscope":PRINT
910 PRINT "3. Zero PSD (zero check in)":PRINT
920 PRINT "4. Use phase of PSD to minimize PSD output,change phase by 90; use 180 if necessary
930 PRINT "5. Back off PSD using offset control":PRINT
940 PRINT "6. Make sure there is no overload"
950 VDU10:VDU10
960 PRINT "Press R when ready:";:A$=GET$
970 CLS
980 PRINT TAB(10)"Sample data:"
990 PRINT TAB(10)"_____"
1000 VDU10:INPUT "Sample:" SA$
1010 VDU10:INPUT "Date:" DA$
1020 VDU10:INPUT "Time (24 hr clock):" TYD$
1030 VDU10:INPUT "Name of file to store data D." File$
1040 CLS
1050 ENDPROC
1060 :
1070 :
1080 :
1090 DEFPROCOptions
1100 CLS
1110 PRINT "OPTIONS WILL BE HERE"
1120 ENDPROC
1130 :
1140 :
1150 :
1160 DEFPROCTestbit(N)
1170 X=?&FE60
1180 IF(X AND BIT(N)) THEN R=FALSE ELSE R=TRUE
1190 ENDPROC
1200 :
1210 :
```

```
1220:
1230 DEFFNTop_closed
1240 PROCTestbit(4)
1250 =R
1260:
1270:
1280:
1290 DEFFNBot_closed
1300 PROCTestbit(3)
1310 =R
1320:
1330:
1340:
1350 DEFFNSwitch_closed=FNTop_closed OR FNBot_closed
1360:
1370:
1380:
1390 DEFPROCMove(D$,NS%)
1400 LOCAL UD
1410 IF D$="Up" THEN UD=4
1420 IF D$="Down" THEN UD=0
1430 ?&FE62=230
1440 ?&FE60=?&FE60+2
1450 ?&FE60=?&FE60-2
1460 ?&FE60=?&FE60+UD
1470  FOR I%=1 TO NS%
1480 ?&FE6B=128:?&FE66=0
1490 ?&FE67=128:?&FE65=64
1500 TIME=0:REPEAT:UNTIL TIME>3
1510 NEXT
1520 ?&FE60=?&FE60-UD
1530 ENDPROC
1540:           .
1550:           .
1560:
1570 DEFPROCChange_dir_to(Dir$)
1580 LOCAL ND%
1590 IF Dir$="Up" THEN ND%=3
1600 IF Dir$="Down" THEN ND%=4
1610 ?&FE60=?&FE60+2↑(ND%+2)
1620 REPEAT
1630 PROCMove(Dir$,1)
1640 UNTIL FNSwitch_closed=FALSE
1650 ?&FE60=?&FE60-2↑(ND%+2)
1660:           .
1670:
1680:
1690 .DEFPROCReadADC
1700 PROCPause(5)
1710 Ch1=0:Ch2=0
1720 FOR I%=1 TO 10
1730 Ch1=Ch1+ADVAL(1)/16
1740 Ch2=Ch2+ADVAL(2)/16
1750 NEXT
1760 Ch1=Ch1/10:Ch2=Ch2/10
1770 Ch1=FNRound(Ch1):Ch2=FNRound(Ch2)
1780 Ch1=1.8*Ch1/4096:Ch2=1.8*Ch2/4096
1790 ENDPROC
1800:
1810:
```

```
1820:
1830 DEFPROCStore_data
1840 File$="D."+File$
1850 FF=OPENOUT(File$)
1860 FOR I%=1 TO Npts%
1870 PRINT#FF,D1(I%),D2(I%),U1(I%),U2(I%)
1880 NEXT
1890 PRINT#FF,-999,0,0,0
1900 PRINT#FF,SA$
1910 PRINT#FF,DA$
1920 PRINT#FF,TYD$
1930 CLOSE#FF
1940 ENDPROC
1950:
1960:
1970:
1980 DEFPROCGraph
1990 CLG
2000 PLOT 4,XC%,YC%
2010 FOR I%=1 TO 18
2020 PLOT 5,I%*70+XC%,YC%
2030 PLOT 5,I%*70+XC%,YC%-10
2040 PLOT 5,I%*70+XC%,YC%
2050 NEXT
2060 PLOT 4,XC%,YC%
2070 FOR I%=1 TO 22
2080 PLOT 5,XC%,YC%+40*I%
2090 PLOT 5,XC%-8,YC%+40*I%
2100 PLOT 5,XC%,YC%+40*I%
2110 NEXT
2120 VDU 5
2130 PLOT 4,(5*70-48)+XC%,35:PRINT "0.5"
2140 PLOT 4,(10*70-48)+XC%,35
2150 PRINT "1.0"  .
2160 PLOT 4,1112+XC%,25:PRINT "Volts"
2170 BX%=800:BY%=1000
2180 PLOT 4,BX%,BY%:PLOT 5,BX%,BY%-150
2190 PLOT 5,BX%+470,BY%-150
2200 PLOT 5,BX%+470,BY%:PLOT 5,BX%,BY%
2210 PLOT 4,BX%+5,BY%-10
2220 PRINT "Fluid: ";SA$
2230 PLOT 4,BX%+5,BY%-60
2240 PRINT "Date:  ";DA$
2250 PLOT 4,BX%+5,BY%-110
2260 PRINT "Time:  ";TYD$
2270 VDU4
2280 ENDPROC
2290:
2300:
2310:
2320 DEFFNRound(Z)
2330 ZZ=INT(10*Z)-10*INT(Z)
2340 IF ZZ>=5 THEN Z=INT(Z)+1 ELSE Z=INT(Z)
2350 =Z
2360:
2370:
2380:
2390 DEFPROCLines(XA,XB%,T$)
2400 XA=700*XA+XC%:YA=(XB%-1)*9+YC%
2410 IF T$="Solid" THEN PLOT 5,XA,YA
```

```
2420 IF T$="Dots" THEN PLOT 69,XA,YA
2430 ENDPROC
2440:
2450:
2460:
```

FIGURE A1
Voltage converter circuit
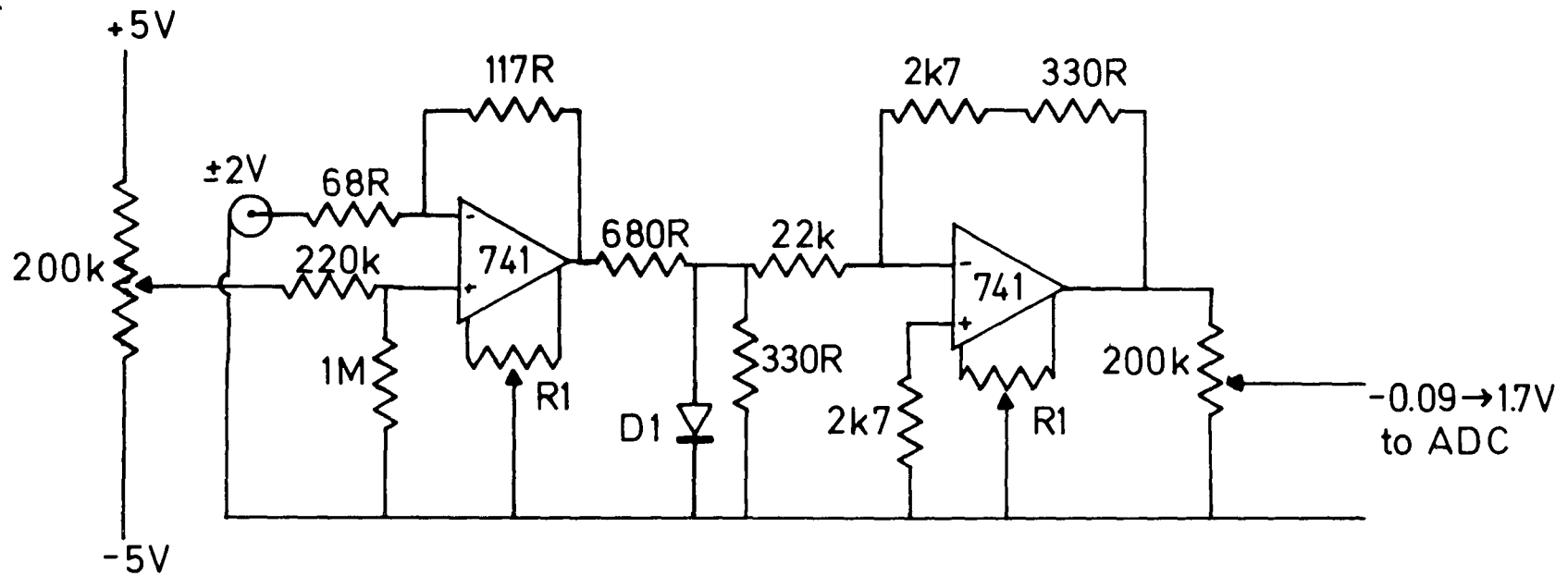
D1-OA202   R1-10k preset

APPENDIX B

IMAGE SIZE ANALYSER SOFTWARE:

(a) Control program

(b) Binning program

(c) Histogram plotting program

```
  10:
  20:
  30REM Particle Size Analyser
  40:
  50:
  60 KP=FALSE
  70 DIM P(700),R(700),D(700)
  80 DIM CP(3),CR(3),CD(3),CS(3)
  90 DIM HC(3)
 100 Np%=0
 110 HC(1)=7:HC(2)=5:HC(3)=4
 120 DDRB=&FE62:IORB=&FE60
 130 ?DDRB=1:?IORB=0
 140 CLS
 150:
 160:
 170:
 180 PROCIntro
 190 PROCCalibrate
 200 REPEAT
 210 PROCOptions
 220 PROCFinish
 230 UNTIL E$="E"
 240 CLS
 250 PROCDown(5)
 260 PRINT TAB(13)"OK - finished "
 270 PROCPause(3)
 280 CLS
 290 END
 300:
 310:
 320 DEF PROCReadADCs
 330 C3=0:C2=0:C1=0
 340 FOR I%=1 TO 10
 350 C3=C3+ADVAL(3)/16
 360 C2=C2+ADVAL(2)/16
 370 C1=C1+ADVAL(1)/16
 380 NEXT
 390 C3=C3/10
 400 C2=C2/10
 410 C1=C1/10
 420 ENDPROC
 430:
 440:
. 450:
 460 DEF PROCRead_point
 470 PROCReadADCs
 480 Np%=Np%+1
 490 P(Np%)=C3
 500 R(Np%)=C2
 510 D(Np%)=C1
 520 ENDPROC
 530:
 540:
 550:
 560 DEF PROCMark_image
 570 ?IORB=1
 580 TIME=0:REPEAT:UNTIL TIME>20
 590 ?IORB=0
 600 ENDPROC
```

```
 610:
 620:
 630:
 640 DEF PROCLogging_data
 650 KeyOK=FALSE
 660 *FX15,1
 670 REPEAT
 680   CLS
 690   VDU10:PRINT TAB(12)"RECORDING DATA"
 700   VDU10:PRINT TAB(12)"_____"
 710   VDU10
 720   VDU10:PRINT " Data point number: ";Np%
 730   VDU10:PRINT "  has values... "
 740   VDU10:PRINT TAB(8)"Pot. (Ch1):";P(Np%)
 750   PRINT TAB(8)"Ref. (Ch2):";R(Np%)
 760   PRINT TAB(8)"Dio. (Ch3):";D(Np%)
 770   VDU10
 780   VDU10:PRINT "To read in a data point, press ......R"
 790   PRINT "  OR press the foot pedal"
 800   VDU10:PRINT "To correct a mistake press .........C"
 810   VDU10:PRINT "To go back to the main menu press ...B"
 820   REPEAT
 830     K$=INKEY$(1)
 840     B1=?IORB AND 2
 850   UNTIL (K$<>"" OR B1=0)
 860   IF (K$="R" OR K$="r") OR B1=0 THEN PROCRead_point:PROCMark_image:KeyOK=TRUE
 870   IF (K$="C" OR K$="c") THEN PROCChange_data:KeyOK=TRUE
 880   IF (K$<>"B" AND K$<>"b") AND NOT KeyOK THEN PROCInstruct
 890 UNTIL (K$="B" OR K$="b")
 900 ENDPROC
 910:
 920:
 930:
 940 DEF PROCIntro
 950 CLS
 960 PRINT TAB(8) "_____"
 970 VDU10:PRINT TAB(8)"Particle Size Analyser"
 980 VDU10:PRINT TAB(8)"_____"
 990VDU10:PRINT TAB(5)"For instructions press... 'I'"
1000 PROCDown(3)
1010 PROCDown(4)
1020 PRINT TAB(4)" otherwise please wait a moment."
1030 K$=INKEY$(500)
1040 IF K$="I" THEN PROCInstruct
1050 ENDPROC
1060:
1070:
1080:
1090 DEF PROCCalibrate
1100 CLS
1110 VDU10:PRINT TAB(14)"CALIBRATION"
1120 PRINT TAB(14)"-----------"
1130 VDU10:PRINT "Place the perspex calibration plate"
1140 PRINT "onto the PSA."
1150 VDU10:PRINT "Now set the light spot equal to each"
1160 PRINT "of the following 3 holes, pressing the"
1170 PRINT "SPACEBAR when you have done so:"
1180 VDU10
1190 FOR J%=1 TO 3
1200 PRINT J%;". The ";HC(J%);"mm hole."
```

```
1210 PROCSpacebar
1220 PROCReadADCs
1230 CP(J%)=C3:CR(J%)=C2:CD(J%)=C1
1240 PROCPause(1)
1250 NEXT
1260 ENDPROC
1270:
1280:
1290:
1300 DEF PROCOptions
1310 REPEAT
1320   KeyOK=FALSE
1330   CLS
1340   VDU10:PRINT TAB(8)"Particle Size Analyser"
1350   PRINT TAB(8)"_____"
1360   VDU10:PRINT "Your options are.."
1370   VDU10:PRINT TAB(5)"Instructions.................I"
1380   VDU10:PRINT TAB(5)"Record data..................R"
1390   VDU10:PRINT TAB(5)"Save data....................S"
1400   VDU10:PRINT TAB(5)"Correct a mistake............C"
1410   VDU10:PRINT TAB(5)"Erase present data...........E"
1420   VDU10:PRINT TAB(5)"Finish & exit................F"
1430   VDU10:PRINT "Please press the relevant key"
1440   REPEAT:O$=INKEY$(1):UNTIL O$<>""
1450   IF O$="I" OR O$="i" THEN PROCInstruct:KeyOK=TRUE
1460   IF O$="R" OR O$="r" THEN PROCLogging_data:KeyOK=TRUE
1470   IF O$="S" OR O$="s" THEN PROCSave_data:KeyOK=TRUE
1480   IF O$="C" OR O$="c" THEN PROCChange_data:KeyOK=TRUE
1490   IF O$="E" OR O$="e" THEN PROCClear_data:KeyOK=TRUE
1500   IF O$="F" OR O$="f" THEN KeyOK=TRUE
1510   IF NOT KeyOK THEN KP=TRUE:PROCInstruct
1520 UNTIL O$="F" OR O$="f"
1530 ENDPROC
1540:
1550:
1560:
1570 DEF PROCInstruct
1580 CLS
1590 PRINT TAB(14)"INSTRUCTIONS"
1600 PRINT TAB(14)"_____"
1610 IF KP THEN 1680
1620 VDU10:PRINT "To operate the particle size analyser,"
1630 PRINT "set the light spot equal to the image"
1640 PRINT "size and then press the foot pedal. The"
1650 PRINT "computer will activate the pen and mark"
1660 PRINT "the image when it has read the image"
1670 PRINT "size."
1680 VDU10
1690 PRINT "If you press a key that is not on a"
1700 PRINT "menu, it will be ignored and you will"
1710 PRINT "be presented with the menu again."
1720 VDU10:PRINT " Press spacebar to continue"
1730 REPEAT:S$=INKEY$(2):UNTIL S$=" "
1740 ENDPROC
1750:
1760:
1770:
1780 DEF PROCFinish
1790 CLS
1800 VDU10:VDU10
```

```
1810 PRINT " Remember you have to save your data"
1820 PRINT " onto disc else you lose it."
1830 VDU10:VDU10:PRINT " To exit program press E otherwise we"
1840 PRINT" will go back to the main options."
1850 E$=INKEY$(400)
1860 ENDPROC
1870 :
1880 :
1890 :
1900 DEF PROCClear_data
1910 CLS
1920 PROCDown(2)
1930 INPUT "Are you sure? (y/n)" YN$
1940 IF YN$<>"Y" AND YN$<>"y" THEN ENDPROC
1950 FOR I%=1 TO Np%
1960 P(I%)=0:R(I%)=0:D(I%)=0
1970 NEXT
1980 Np%=0
1990 ENDPROC
2000 :
2010 :
2020 :
2030 DEF PROCChange_data
2040 REPEAT
2050 CLS
2060 VDU10:PRINT TAB(14)"CORRECTIONS"
2070 PRINT TAB(14)"_____"
2080 VDU10:PRINT "You have recorded ";Np%;" points"
2090 VDU10:PRINT "To delete the last point, press D"
2100 VDU10:PRINT "To return to last menu, press B"
2110 REPEAT:KC$=INKEY$(2):UNTIL KC$<>""
2120 IF KC$="D" AND Np%=0 THEN PRINT CHR$(10);CHR$(10);" ..but there are no points!":PROCPause(2)
2130 IF KC$="D" AND Np%>0 THEN PROCDelete_point
2140 UNTIL KC$="B"
2150 ENDPROC
2160 :
2170 :
2180 :
2190 DEF PROCDelete_point
2200 P(Np%)=0
2210 R(Np%)=0
2220 D(Np%)=0
2230 Np%=Np%-1
2240 ENDPROC
: 2250 :
2260 :
2270 :
2280 DEF PROCSave_data
2290 REPEAT
2300 CLS
2310 VDU10:PRINT TAB(5)"Saving data onto disc"
2320 PRINT TAB(5)"_____"
2330 VDU10
2340 PRINT "Type filename or *CAT for list of files"
2350 VDU10:INPUT "Filename D." Fname$
2360 IF Fname$="*CAT" THEN *CAT
2365 IF Fname$="*CAT" THEN PROCPause(10)
2370 Fname$="D."+Fname$
2380 UNTIL Fname$<>"D.*CAT"
2390 CLS
```

```
2400 VDU10:PRINT "Photograph details:"
2410 PRINT "_____"
2420 PROCDown(2)
2430 INPUT "Sample (material): " SAM$
2440 VDU10:INPUT "Photo no.: " PHN$
2450 VDU10:INPUT "Total magnification: " TMAG
2460 FF=OPENOUT(Fname$)
2470 PRINT#FF,SAM$
2480 PRINT#FF,PHN$
2490 PRINT#FF,TMAG
2500 FOR I%=1 TO 3
2510 PRINT#FF,CP(I%),CR(I%),CD(I%),HC(I%)
2520 NEXT
2530 PRINT#FF,Np%
2540 FOR I%=1 TO Np%
2550 PRINT#FF,P(I%),R(I%),D(I%)
2560 NEXT
2570 CLOSE#FF
2580 CLS
2590 VDU10:VDU10:VDU10
2600 PRINT" Your data has been saved in disc file "
2610 PRINT TAB(16);Fname$
2620 PROCPause(3)
2630 ENDPROC
2640 :
2650 :
2660 :
2670 DEFPROCPause(P%)
2680 TIME=0
2690 REPEAT:UNTIL TIME>P%*50
2700 ENDPROC
2710 :
2720 :
2730 :
2740 DEFPROCDown(D%)
2750 FOR J%=1 TO D%
2760 VDU10
2770 NEXT
2780 ENDPROC
2790 :
2800 :
2810 :
2820 DEFPROCSpacebar
2830 LOCAL SP$
2840 SP$=""
2850 REPEAT
2860  SP$=GET$
2870 UNTIL SP$=" "
2880 ENDPROC
2890 :
2900 :
2910 :
```

```
  10 REM ——————————————————
  20 REM —— This program bins data  ——
  30 REM —— taken on the "BONKER"    ——
  40 REM —— and creates another data ——
  50 REM —— file before chaining the ——
  60 REM —— histogram plotter prog.  ——
  70 REM ——————————————————
  80 :
  90 :
 100 MODE7
 110 DIM P(550),R(550),D(550)
 120 DIM BUpper(600),BLower(600)
 130 DIM Diam(550),Bin(550)
 140 DIM CP(3),CR(3),CD(3),CSize(3)
 150 PROCTitle
 160 PROCReaddata
 170 PROCInfo
 180 PROCCalibrate
 190 VDU10:PRINT "Busy...":VDU10
 200 PROCHist
 210 PROCBin
 220 PROCStats
 230 PROCWritedata
 240 PROCPrint
 250 CHAIN "P.HPLOT"
 260 END
 270 :
 280 :
 290 DEF PROCReaddata
 300 INPUT "Name of disc file D." Fname$
 310 Fname$="D."+Fname$
 320 FILE=OPENIN(Fname$)
 330 INPUT#FILE,SAMPLE$
 340 INPUT#FILE,PHOTO$
 350 INPUT#FILE,MAGNIF
 360 FOR I%=1 TO 3
 370 INPUT#FILE,CP(I%),CR(I%),CD(I%),CSize(I%)
 380 NEXT
 390 INPUT#FILE,Noofpoints%
 400 FOR I%=1 TO Noofpoints%
 410 INPUT#FILE,P(I%),R(I%),D(I%)
 420 NEXT
 430 CLOSE#FILE
 440 ENDPROC
 450 :
 460 :
 470 DEF PROCTitle
 480 CLS
 490 VDU10:VDU10
 500 PRINT TAB(12)"** BINNING DATA **"
 510 VDU10
 520 ENDPROC
 530 :
 540 :
 550 DEF PROCBin
 560 FOR I%=1 TO Noofpoints%
 570 FOR J%=1 TO Nobins%
 580 IF(Diam(I%)>BLower(J%))AND(Diam(I%)<BUpper(J%)) THEN Bin(J%)=Bin(J%)+1
 590 NEXT J%
 600 NEXT I%
```

```
 610 ENDPROC
 620 :
 630 :
 640 DEF PROCHist
 650 LOCAL Diff,DCentre,P,NB%
 660 PROCMaxmin
 670 Nobins%=0:NB%=0
 680 Diff=MX-MN
 690 DCentre=(MN+(Diff/2))
 700 DCentre=FNROUND(DCentre)
 710 REPEAT
 720 P=DCentre-Nobins%*Binw
 730 Nobins%=Nobins%+1
 740 UNTIL P<MN
 750 BMin=DCentre-Nobins%*Binw
 760 REPEAT
 770 P=DCentre+NB%*Binw
 780 NB%=NB%+1
 790 UNTIL P>MX
 800 Nobins%=Nobins%+NB%
 810 FOR II%=1 TO Nobins%
 820 BLower(II%)=BMin+(II%-1)*Binw
 830 BUpper(II%)=BMin+II%*Binw
 840 NEXT
 850 ENDPROC
 860 :
 870 :
 880 DEF PROCMaxmin
 890 MN=Diam(1):MX=0
 900 FOR II%=1 TO Noofpoints%
 910 IF Diam(II%)>=MX THEN MX=Diam(II%)
 920 IF Diam(II%)<=MN THEN MN=Diam(II%)
 930 NEXT
 940 ENDPROC
 950 :
 960 :
 970 DEF FNROUND(X)
 980 DF=INT(100*X)-10*INT(10*X)
 990 IF (DF>=5) THEN ROUND=(10*INT(10*X)+10)/100 ELSE ROUND=(10*INT(10*X))/100
1000 =ROUND
1010 :
1020 :
1030 DEF PROCCalibrate
1040 CK=0
1050 FOR I%=1 TO 3
1060 CK=CK+(CSize(I%)↑2*CR(I%)*PI/(CD(I%)*4))
1070 NEXT
1080 CK=CK/3
1090 FOR II%=1 TO Noofpoints%
1100 Diam(II%)=CK*D(II%)/R(II%)
1110 Diam(II%)=SQR(4*Diam(II%)/PI)
1120 Diam(II%)=Diam(II%)*1E6/MAGNIF
1130 IF LL$="LOG" THEN Diam(II%)=LN(Diam(II%))
1140 NEXT
1150 ENDPROC
1160 :
1170 :
1180 DEF PROCWritedata
1190 INPUT "Filename to store binned data D." Fn$
1200 Fn$="D."+Fn$
```

```
1210 FILE=OPENOUT(Fn$)
1220 PRINT#FILE,SAMPLE$
1230 PRINT#FILE,PHOTO$
1240 PRINT#FILE,MAGNIF
1250 PRINT#FILE,Binw
1260 PRINT#FILE,Nobins%
1270 PRINT#FILE,Mean
1280 PRINT#FILE,Sdev
1290 PRINT#FILE,Noofpoints%
1300 FOR I%=1 TO Nobins%
1310 PRINT#FILE,I%*Binw+BMin-Binw/2,Bin(I%)
1320 NEXT
1330 CLOSE#FILE
1340 ENDPROC
1350 :
1360 :
1370 DEF PROCPrint
1380 CLS
1390 PRINT "Mean=";Mean
1400 PRINT "SDev=";Sdev
1410 PROCMessage(19)
1420 REPEAT:UNTIL GET=32
1430 CLS
1440 PRINT TAB(3); SAMPLE$
1450 PRINT TAB(3); PHOTO$
1460 PRINT TAB(3); MAGNIF
1470 FOR I%=1 TO Nobins%
1480 BSiz=I%*Binw+BMin-Binw/2
1490 PRINT TAB(3);I%;" ",BSiz,Bin(I%)
1500 NEXT
1510 PROCMessage(6)
1520 REPEAT:UNTIL GET=32
1530 ENDPROC
1540 :
1550 :
1560 DEF PROCStats
1570 LOCAL TT,TB
1580 TT=0:TB=0
1590 FOR II%=1 TO Noofpoints%
1600 TT=TT+Diam(II%)
1610 NEXT
1620 FOR II%=1 TO Noofpoints%
1630 TB=TB+Bin(II%)
1640 NEXT
1650 IF TB<>Noofpoints% THEN PRINT "No of points problem"
1660 Mean=TT/TB:Mean=FNROND(Mean)
1670 ST=0
1680 FOR II%=1 TO Noofpoints%
1690 ST=ST+(Diam(II%)-Mean)↑2
1700 NEXT
1710 Sdev=SQR(ST/(Noofpoints%-1)):Sdev=FNROND(Sdev)
1720 ENDPROC
1730 :
1740 :
1750 DEF FNROND(X)
1760 ROND=INT(X*100)/100
1770 =ROND
1780 :
1790 :
1800 DEF PROCMessage(X)
```

```
1810 FOR I=1 TO X
1820 VDU10
1830 NEXT
1840 PRINT " —— press space bar to continue ——"
1850 ENDPROC
1860:
1870:
1880 DEF PROCInfo
1890 VDU10:INPUT "Log or lin binning? "LL$
1900 IF LL$="log" OR LL$="Log" THEN LL$="LOG"
1910 IF LL$="LOG" THEN VDU10:PRINT "A bin size of about 0.1 nm is recommended"
1920 VDU10:INPUT "Bin size required:"Binw
1930 ENDPROC
1940:
1950:
```

```
  10 REM ──────────────────────────────
  20 REM ──   HISTOGRAM PLOTTER FOR   ──
  30 REM ──           BONKER           ──
  40 REM ──────────────────────────────
  50 MODE4
  60 DIM BINS(300),BCen(300),Num(300)
  70 MODE4:SP$="N"
  80 PROCReaddata
  90 VDU10
 100 INPUT "Do you want hardcopy (y/n)?" HC$:IF HC$="y" THEN HC$="Y"
 110 VDU10
 120 IF HC$="Y" THEN INPUT "On serial or parallel printer (s/p)?" SP$
 130 PROCMaxh
 140 PROCSetup
 150 CLS
 160 PROCHisto
 170 PROCGtitle
 180 CLOSE#FF
 190 IF SP$="S" OR SP$="s" THEN PROCSerialprint
 200 REM
 210 REM
 220 REM
 230 *DIR U
 240 IF HC$="Y" THEN CHAIN "P.NEWDUMP"
 250 END
 260 :
 270 :
 280 :
 290 DEF PROCReaddata
 300 CLS
 310 PROCTitle
 320 INPUT "Name of data file D." fn$
 330 fn$="D."+fn$
 340 FF=OPENIN(fn$)
 350 INPUT#FF,SAMPLE$
 360 INPUT#FF,PHOTO$
 370 INPUT#FF,MAG
 380 INPUT#FF,Binw
 390 INPUT#FF,Nobins%
 400 INPUT#FF,Mean
 410 INPUT#FF,SDev
 420 INPUT#FF,Npoints%
 430 FOR I%=1 TO Nobins%
 440 INPUT#FF,BCen(I%),Num(I%)
 450 NEXT
 460 ENDPROC
 470 :
 480 :
 490 :
 500 DEF PROCMaxh
 510 MX=0:MN=Num(1)
 520 FOR I%=1 TO Nobins%
 530 IF Num(I%)>=MX THEN MX=Num(I%)
 540 IF Num(I%)<=MN THEN MN=Num(I%)
 550 NEXT
 560 MH=MX
 570 ENDPROC
 580 :
 590 :
 600 :
```

```
 610 DEF PROCSetup
 620 X%=100:Y%=100:N%=0:B%=0:I%=0
 630 SF=600/MH
 640 BW=INT(1000/Nobins%)
 650 ENDPROC
 660:
 670:
 680:
 690 DEF PROCHisto
 700 PROCaxes
 710 PROCdraw_bins
 715 PROCNormal_dist
 720 ENDPROC
 730:
 740:
 750:
 760 DEF PROCaxes
 770 IF (MH>20 AND MH<40) THEN SK=5
 780 IF (MH<20) THEN SK=2 ELSE SK=10
 790 VDU5
 800 MOVE X%,Y%
 810 DRAW X%+1120,Y%
 820 MOVE X%,Y%
 830 FOR J%=1 TO MH
 840 DRAW X%,Y%+J%*SF
 850 IF (J% MOD SK=0)OR J%=MH THEN DRAW X%-10,Y%+J%*SF
 860 MOVE 19,Y%+J%*SF+12:IF (J% MOD SK=0)OR(J%=MH) THEN PRINT;J%
 870 MOVE X%,Y%+J%*SF
 880 NEXT
 890 DRAW X%,Y%+800
 900 MOVE X%+20,Y%
 910 VDU4
 920 ENDPROC
 930:
 940:
 950:
 960 DEF PROCdraw_bins
 970 VDU5
 980 X%=X%+20
 990 FOR I%=1 TO Nobins%
1000  H=INT(SF*Num(I%))
1010  DRAW X%,Y%+H:X%=X%+BW
1020  DRAW X%,Y%+H:DRAW X%,Y%
1030  MOVE X%-BW/2,Y%:DRAW X%-BW/2,Y%+10
1040  MOVE X%,Y%
1050  IF I%=1 OR I%=Nobins% THEN MOVE X%-BW,90:PRINT;BCen(I%);:IF I%=Nobins% THEN PRINT;"nm"
1060  MOVE X%,Y%
1070 NEXT
1080 VDU4
1090 ENDPROC
1100:
1110:
1120:
1130 DEF PROCTitle
1140 VDU 10
1150 PRINT TAB(10);" ";"** HISTOGRAM **"
1160 VDU 10:VDU 10
1170 ENDPROC
1180:
1190:
```

```
1200:
1210 DEF PROCGtitle
1220 VDU5
1230 MOVE 110,890
1240 PRINT;SAMPLE$
1250 MOVE 110,855
1260 PRINT;PHOTO$
1270 MOVE 110,800
1280 PRINT;Binw;"nm"
1290 MOVE 400,890
1300 PRINT;"Mean=";Mean
1310 MOVE 400,855
1320 PRINT;"S Dev=";SDev
1330 MOVE 800,890
1340 PRINT "Points=";Npoints%
1350 VDU4
1360 ENDPROC
1370:
1380:
1390:
1400 DEFPROCSerialprint
1410 *FX5,2
1420 *FX8,7
1430 *FX6
1440 ENDPROC
1450:
1460:
1470:
1480 DEF PROCNormal_dist
1490 LOCAL I,H,X,Y,FT
1500 MOVE 120,100
1510 SY=(1/Binw)*BW
1515 XS=BCen(1)-.5*Binw
1516 XF=BCen(Nobins%)+.5*Binw
1517 FT=1/((SQR(2*PI)*SDev))
1520 FOR I=XS TO XF STEP .01
1530 H=FT*EXP(-0.5*(((I-Mean)/SDev)↑2))*Npoints%*Binw
1540 Y=H*SF+100
1550 X=(I-XS)*SY+120
1560 IF I=BCen(1) THEN MOVE X,Y ELSE DRAW X,Y
1570 NEXT I
1580 ENDPROC
1590:
1600:
1610:
1620 DEF PROCLog_normal
1630 LOCAL I,H,X,Y,FT
1640 MOVE 120,100
1650 SY=(1/Binw)*BW
1660 XS=BCen(1)-.5*Binw
1670 XF=BCen(Nobins%)+.5*Binw
1680 FT=1/((SQR(2*PI)*0.13))
1690 FOR I=XS TO XF STEP .01
1700 H=FT*(1/I)*EXP(-0.5*(((LN(I)-1.89)/0.13)↑2))*Npoints%*Binw
1710 Y=H*SF+100
1720 X=(I-XS)*SY+120
1730 IF I=BCen(1) THEN MOVE X,Y ELSE DRAW X,Y
1740 NEXT I
1750 ENDPROC
```

APPENDIX C

THE LOGNORMAL DISTRIBUTION AND PASCAL PROGRAM

TO INTEGRATE THE LANGEVIN FUNCTION

THE LOGNORMAL DISTRIBUTION

C1. Definitions and Notation.

Defn: A random variable X has a lognormal
distribution (and is said to be a lognormal
random variate) with parameters μ, σ^2 if and
only if its probability density function is
given by;

$$
f(x) = \begin{cases} \dfrac{1}{\sigma\sqrt{2\pi}} \cdot \dfrac{1}{x} \; \exp\!\left(-\dfrac{1}{2\sigma^2}\left(\ln x - \mu\right)^2\right) & x > 0 \\[20pt] 0 & x \leqslant 0 \end{cases}
$$

This is denoted $X \sim \Lambda(\mu, \sigma^2)$. (As a normal
random variate Y with mean μ, variance σ^2 is
denoted $Y \sim N(\mu, \sigma^2)$.

It must be made clear that μ and σ^2 are not the mean
and variance of the lognormal distribution. This
distribution has the following properties (proofs may be
found in "The Lognormal Distribution" by J.Aitchison and
J.A.C.Brown, C.U.P., Cambridge 1969):

Theorem C1

If $X \sim \Lambda(\mu, \sigma^2)$ and b,c are constants where $c>0$ (say $c=e^a$) then $cX^b \sim \Lambda(a+b\mu, b^2\sigma^2)$.

Theorem C2

If $X_1 \sim \Lambda(\mu_1, \sigma_1^2)$ and $X_2 \sim \Lambda(\mu_2, \sigma_2^2)$ are independent lognormal variables then $Y = X_1 X_2 \sim \Lambda(\mu_1 + \mu_2, \sigma_1^2 + \sigma_2^2)$.

Moments about the origin are given by:-

$$E(X^n) = \exp(n\mu + \tfrac{1}{2} n^2 \sigma^2).$$

In particular the mean and variance of the distribution are:-

$$E(X) = \overline{x} = \exp(\mu + \sigma^2)$$
$$\mathrm{var}(X) = E(X)^2 - E(X^2)$$
$$= \exp(2\mu + \sigma^2)(\exp(\sigma^2) - 1)$$

In addition the mode and median are given by,

$$\mathrm{mode} = \overline{x}_m = \exp(\mu - \sigma^2)$$
$$\mathrm{median} = \overline{x}_{\frac{1}{2}} = \exp(\mu)$$

Deviations from normality are expressed in terms of the

third and fourth moments about the mean;

$$\text{skewness} = \gamma_1 = \sqrt{(e^{\sigma^2} - 1)} \; (e^{\sigma^2} + 2)$$

$$\text{kurtosis} = \gamma_2 = (e^{\sigma^2} - 1)(e^{3\sigma^2} + 3e^{2\sigma^2} + 6e^{\sigma^2} + 6)$$

The lognormal distribution is related to the normal distribution in the following manner;

If X is a positive variate and $Y = \ln(X) \sim N(\mu, \sigma^2)$ then $X \sim \Lambda(\mu, \sigma^2)$. In other words if X is a lognormal variate with parameters μ, σ^2 then its natural logarithm will be normally distributed with mean μ and variance σ^2.

A simple relationship exists between the quantiles of $\Lambda(\mu, \sigma^2)$ and $N(0,1)$. If ξ_q and ν_q are the quantiles of order q of $\Lambda(\mu, \sigma^2)$ and $N(0,1)$ respectively, then;

$$\xi_q = \exp(\mu + \nu_q \sigma)$$

(ξ_q, ν_q = the value of x for which the area under the distribution is q.)

C2 From a distribution of moments to a distribution of diameters.

C2.1 Moment distribution to volume distribution.

Magnetic measurements sample the magnetic moment distribution of a magnetic fluid. The lognormal

distribution has the rare property that if the moment
distribution is assumed to be lognormal then the physical
diameter distribution will also be lognormal. This is shown
below.

It is assumed that the magnetic moments, m, are
distributed as,

$$m \sim \Lambda(\mu', \sigma'^2)$$

and that the magnetic moment of the particles is related
to the volume by

$$m = v_p M_b^\infty$$

thus $v_p = \dfrac{m}{M_b^\infty} = a'm$ and setting $c' = \ln(a')$, theorem C1
gives the volume distribution as,

$$V \sim \Lambda(c' + \mu', \sigma'^2) = \Lambda(\mu'', \sigma'^2)$$

2.2 Volume fraction to number fraction.

It should be noted that magnetisation measurements
obtain the moment per unit volume and thus the moment and
volume distributions above are volume fraction
distributions. That is they represent the fraction of the
total particle volume contributed by particles with volume
(moment) between v and v+dv unlike a number fraction
distribution which gives the fraction of the total number
of particles with volumes in that range. In order to

compare electron microscopy results with magnetic results, the volume fraction distribution must be converted into a number fraction distribution.

The volume fraction is related to the number fraction distribution by,

$$f(v)dv = \frac{N_p}{V_p} vn(v)dv$$

where V_p = total particle volume and N_p is the total number of particles. Now if

$$n(v) = \frac{1}{\sigma_n \sqrt{2\pi}} \frac{1}{v} \exp\left\{-\frac{1}{2\sigma_n^2}(\ln v-\mu_n)^2\right\}$$

then

$$f(v) = \frac{N_p}{V_p} \frac{1}{\sigma_n \sqrt{2\pi}} \exp\left\{-\frac{1}{2\sigma_n^2}(\ln v-\mu_n)^2\right\}$$

but $\dfrac{N_p}{V_p} = \dfrac{1}{\bar{v}_n} = \dfrac{1}{e^{\mu_n+\frac{1}{2}\sigma_n^2}}$ and placing this into the above, expanding the quadratic and writing $\mu_n+\sigma^2$ as μ_v results in

$$f(v) = \frac{1}{\sigma_n \sqrt{2\pi}} \frac{1}{v} \exp\left\{-\frac{1}{2\sigma_n^2}(\ln v-\mu_v)^2\right\}$$

i.e. if the volume fraction distribution is $V \sim \Lambda(\mu'',\sigma'^2)$ then the number fraction distribution is $V_n \sim \Lambda(\mu''-\sigma'^2,\sigma'^2)$ which may be written,

$$V_n \sim \Lambda(\mu''',\sigma'^2)$$

2.3 Volume to diameter distribution.

Application of theorem C1 will provide the diameter distribution where,

$$v_p = \frac{\pi d_p^3}{6} \quad \text{i.e.} \quad d_p = sv_p^{\frac{1}{3}} \text{ and if } t = \ln(s)$$

then

$$D \sim \Lambda(t + \tfrac{1}{3}\mu''', \tfrac{1}{9}\sigma'^2)$$

or $D \sim \Lambda(\mu, \sigma^2)$ where $\mu = \tfrac{1}{3}\mu''' + t$, $\sigma^2 = \tfrac{1}{9}\sigma'^2$. In terms of the original parameters,

$$\mu = \tfrac{1}{3}(\mu'' - \sigma'^2) + \ln(\tfrac{6}{\pi})$$

$$= \tfrac{1}{3}(\ln(\tfrac{1}{M_6^\infty}) + \mu' - \sigma'^2) + \ln(\tfrac{6}{\pi})$$

C3. Dividing by the median.

In order to render the lognormal distribution function amenable to analytic manipulation it is common practice to work with the reduced variate obtained by dividing by the median.

$$\text{i.e.} \quad x \rightarrow x / \overline{x}_{\frac{1}{2}} = x'$$

Then since $\ln(\tfrac{1}{\overline{x}_{\frac{1}{2}}}) = -\mu$,

$$X' \sim \Lambda(0, \sigma^2).$$

i.e. the probability density function is

$$f(x') = \frac{1}{\sigma\sqrt{2\pi}} \frac{1}{x'} \exp(-\frac{1}{2\sigma^2}\ln^2 x').$$

```
(*************************************************************)
(*                                                         *)
(*      Program Llintegration.                             *)
(*      _____                                   *)
(*                                                         *)
(*      This program integrates the Longevin function multiplied *)
(*      by a lognormal or normal dist. of part. diameters. Low   *)
(*      field approximation of the Langevin function is used for *)
(*      b<0.1 and high field for b>6 (b=mH/kT). The integration  *)
(*      is a compound Simpsons Rule (Numerical Integration by    *)
(*      Davis and Rabinowitz ).                           *)
(*                                                         *)
(*                              (c) D.B.Lambrick 1985      *)
(*                                                         *)
(*************************************************************)


program llintegration;

const pi=3.14159265;
      kb=1.3807E-23;
      sent=-999.0;


type
     yv =  array[0..1500] of real;
     data = array[0..400,1..4] of real;
     tstor = array[0..50] of integer;

var
  Xi,Bo,Mbulk,dmed,sigma,intsum,h,ms,mr,vr : real;
  xo,x2n,Minf,alpha,lambda,temp,rhoff,Sinf,b : real;
  i,n,dl,npts,distrb : integer;
  y: yv;
  vsmdata: file of real;
  exdata,thdata : data;
  datout,curvout : text;
  stack : tstor;
  top: 0..50;

function coth(x:real) : real;
begin
  coth:=(exp(2*x)+1)/(exp(2*x)-1);
end;


function lang(x:real) : real;
begin
  if (x=0) then lang:=0.0;
  if (x>0) & (x<=0.1)  then lang:=x/3-x*sqr(x)/45;
  if (x>0.1) & (x<6)   then lang:=coth(x)-1/x;
  if (x>=6)            then lang:=1-1/x;
end;


function ef(x:real) : real;
begin
  if (distrb=1) then ef:=(1/x)*exp(-lambda*sqr(ln(x)));
  if (distrb=2) then ef:=dmed*exp(-lambda*sqr(dmed)*sqr(x-1));
end;
```

```pascal
function g(x:real) : real;
 var
  neg : integer;

begin
 if exdata[i,1]<0 then neg:=-1 else neg:=1;
 exdata[i,1]:=neg*exdata[i,1];
 b:=Xi*exdata[i,1]*x*x*x;
 g:=ef(x)*lang(b);
 exdata[i,1]:=neg*exdata[i,1];
end;

function f(x:real) : real;
begin
  f:=g(x);
end;


procedure yvals;
 var
   j:integer;
 begin
   for j:=0 to 2*n do
     y[j]:=f(xo+j*h);
 end;


procedure integrate;
 var
  oddsum,evensum : real;
   j : integer;

 begin
  oddsum:=0.0;
  evensum:=0.0;
  for j:=1 to (2*n-1) do
   begin
   if odd(j) then oddsum:=oddsum+y[j]
              else evensum:=evensum+y[j];
   end;
  intsum:=(h/3)*(y[0]+4*oddsum+2*evensum+y[2*n]);
 end;



 procedure getdata;
 var
  i,k : integer;
  sample : string(25);

 begin
  reset(input,'unit=scards');
  exdata[0,1]:=0.0;
  i:=0;
  while exdata[i,1] <> -999.0 do
  begin
   i:=i+1;
   for k:=1 to 4 do
```

```pascal
    begin
     read(input,exdata[i,k]);
    end;
  end;
 npts:=i-1;
 read(input,sample);
 read(input,ms,mr,vr,temp);
 close(input);
end;


procedure getinfo;
var
  I,bulkmat : integer;
  msource : text;
begin
  page;
  reset(msource,'file=*msource* interactive');
  writeln('                    Size distribution  integration');
  writeln('                    ——————————————————');
  writeln;
  writeln('  Do you want a lognormal or a Gaussian distribution?');
  writeln;
  writeln('  Type a 1 for a lognormal, 2 for a Gaussian');
  writeln;
  readln(msource,distrb);
  writeln;
  writeln('  Please enter the following :');
  writeln;
  writeln('     The particle material: ');
  writeln;
  writeln('        Choose one of : 1 Fe   2 Co(hex) 3 Co(fcc) 4 Ni');
  writeln('                        5 Fe3O4 6 FeCo   7 FeNi3');
  readln(msource,bulkmat);
  writeln('     The median particle diameter (nm) : ');
  readln(msource,dmed);
  writeln('     The lognormal parameter sigma: ');
  readln(msource,sigma);
  writeln('     The density of the magnetic fluid (kg/m3) : ');
  readln(msource,rhoff);
  writeln('     The magn./unit mass at infinite field of the fluid: ');
  readln(msource,Sinf);
  Minf:=rhoff*Sinf;

  case bulkmat of
    1 : Mbulk:=17.1;
    2 : Mbulk:=14.43;
    3 : Mbulk:=14.92;
    4 : Mbulk:=4.91;
    5 : Mbulk:=4.77;
    6 : Mbulk:=18.99;
    7 : Mbulk:=9.81;
  end;
end;


procedure outinfo;

const zero = 0.0;
```

```pascal
var
  i,k : integer;

begin
 rewrite(curvout,'unit=3');
 writeln(curvout,zero:8:5,zero:8:5,zero:8:5,zero:8:5);
 for i:=1 to npts do
 begin
  for k:=1 to 4 do
   begin
    write(curvout,' ',thdata[i,k]:8:5);
   end;
  writeln(curvout);
 end;
 writeln(curvout,sent:8:3,zero:8:5,zero:8:5,zero:8:5);
 writeln(curvout,'  SIMULATION');
 writeln(curvout,dmed:5:3,' ',sigma:4:2,' ',rhoff:8:4,' ',Sinf:8:5);
 writeln(curvout,Mbulk*1e5:9:1,' ',temp:6:2);
 writeln(curvout,xo:8:5,' ',x2n:8:5,' ',Xi:8:5);
 writeln(curvout,n:3,' ',h:8:5);
 end;



  procedure initialize;

  begin
  xo:=0.32;
  x2n:=5.32;
  alpha:=1/(sqrt(2*pi)*sigma);
  lambda:=1/(2*sqr(sigma));
  Xi:=3.7923*dmed*sqr(dmed)*Mbulk/temp;
  n:=175;
  h:=(x2n-xo)/(2*n);
  thdata[1,4]:=0.0;
  thdata[0,4]:=0.0;
  end;



  procedure quicksort;

  type
   tarr = array[1..4] of real;

  var
   i,j,k,t,first,last,size : integer;
   divlin : real;
   tempo : tarr;

  begin
   size:=npts;
   stack[1]:= 1;
   stack[2]:=size;
   top:=2;
   repeat
    last:=stack[top];
    top:=top-1;
    first:=stack[top];
    top:=top-1;
    i:=first;
```

```pascal
    repeat
     j:=last;
     t:=(first+last) div 2;
     writeln(t:5);
     divlin:=abs(exdata[t,1]);
     repeat
      while abs(exdata[i,1]) < divlin do
       i:=i+1;
      while abs(exdata[j,1]) > divlin do
        j:=j-1;
      if i<=j then
       begin
         for k:=1 to 4 do
          begin
           tempo[k]:=exdata[i,k];
           exdata[i,k]:=abs(exdata[j,k]);
           exdata[j,k]:=abs(tempo[k]);
          end;
         i:=i+1;
         j:=j-1;
        end;
    until i>j;
    if first<j then
     begin
       top:=top+1;
       stack[top]:=first;
       top:=top+1;
       stack[top]:=j;
      end;
    first:=i;
  until first>=last;
 until top = 0;
end;



  (* program  starts *)



 begin
  page;
  getdata;
  getinfo;
  initialize;
(*quicksort;*)
  for i:=1 to npts do
  begin
     yvals;
     integrate;
     thdata[i,3]:=alpha*Sinf*intsum;
     thdata[i,1]:=exdata[i,1];
     if (exdata[i,1]<0) then thdata[i,3]:=-thdata[i,3];
     thdata[i,2]:=0.0;
     thdata[i,2]:=abs(thdata[i,3]-exdata[i,3]);
     thdata[i,4]:=thdata[i-1,4]+thdata[i,2];
  end;
  outinfo;
 end.
```